Spin and Orbital Effects in Antiferromagnetic CoO Thin Films

Dissertation

zur Erlangung des Grades
„Doktor der Naturwissenschaften“
am Fachbereich Physik, Mathematik und Informatik
der Johannes Gutenberg-Universität
Mainz

Christin Schmitt

geb. in Boppard

Mainz, der 4. März 2026

Examination date : 19th February 2026

Berichterstatter: Removed due to data privacy

Anhänge gemäß Prüfungsordnung

I hereby declare that the thesis submitted is my own unaided work. All direct or indirect sources (this also includes AI-based applications or tools) used are acknowledged as references. The thesis, in whole or in part, has never been submitted to any other examination committee that is able to admit a doctoral degree.

Ich versichere, dass ich meine Dissertation selbstständig verfasst und keine anderen als die angegebenen Quellen und Hilfsmittel (dazu zählen auch KI-basierte Anwendungen oder Werkzeuge) benutzt sowie Zitate kenntlich gemacht habe. Die Doktorarbeit ist weder abschnittsweise, noch in der vorliegender Form bei einer anderen Prüfungsbehörde zur Erlangung eines Doktorgrades eingereicht worden.

Mainz, 4. März 2026

Christin Schmitt

Abstract

Antiferromagnetic materials have emerged as key candidates in the field of spintronics due to their intrinsic advantages: zero net magnetic moment, robustness against external magnetic fields, and ultrafast magnetization dynamics in the THz range. These properties highlight their potential to revolutionize information technologies by enabling stable, high-speed, and densely integrated devices. However, the development of efficient mechanisms for writing and reading magnetic information in antiferromagnets remains a significant challenge. Although electrical switching of the Néel vector has been widely studied, it is often dominated by thermal effects that obscure the ultrafast dynamics responsible for the materials' unique appeal. Similarly, conventional readout schemes based on spin currents tend to yield weak signals, limiting their practical applicability. Although readout schemes based on orbital currents exist, the orbital currents themselves cannot be directly utilized because they couple inefficiently to the spin magnetization in magnetic materials. Consequently, they must first be converted into spin currents to be utilized.

This thesis investigates thin films of CoO, a prototypical antiferromagnet with a large, orbital moment, and explores switching and readout mechanisms from a novel perspective. By studying CoO/Pt and CoO/Cu* heterostructures, where Cu* refers to a naturally oxidized Cu layer, this work addresses the central challenges related to the manipulation and detection of antiferromagnetic order in insulating systems.

First, we demonstrate the coexistence of spin-orbit torque-driven switching and thermal switching in ultrathin CoO/Pt films. By correlating the electrical readout with magnetic domain imaging, we demonstrate that the final magnetic state

cannot be accounted for solely by thermomagnetoelastic effects, indicating an additional torque-driven contribution. This finding points to the potential for ultrafast, current-induced manipulation and switching in ultrathin antiferromagnetic layers.

Second, we present the first (to our knowledge) experimental evidence of a purely orbital interaction mechanism in antiferromagnets using CoO/Cu* bilayers. By combining orbital currents with the orbital-dominated magnetization of CoO, we achieve a two-order-of-magnitude enhancement in a magnetoresistance signal. Notably, the absence of a heavy metal layer, and thus the absence of a conventional spin current source, excludes spin-based mechanisms as the dominating origin of the observed signal. Instead, Cu* is known to generate significant orbital currents, and we demonstrate that the enhanced readout signal arises from the coupling of these currents to the large orbital moment in CoO. This finding provides compelling evidence that orbital currents can serve as an efficient and robust readout mechanism, marking a paradigm shift from spin-based approaches and opening a new frontier in antiferromagnetic orbitronics.

Third, comparative studies on CoO/Cr and CoO/Cu/Pt trilayers show that the effect is robust and not limited to the oxidation of the Cu. Because the surface oxidation of Cu is difficult to control, it is essential to identify mechanisms and materials that are suitable for real-world applications. In CoO/Cr, we find that the readout signal is enhanced by a factor of five compared with measurements on CoO/Pt. Moreover, the enhanced readout signal in CoO/Cu/Pt bilayers indicates that the effect can as well originate from interface-driven orbital-current generation, rather than solely from oxidation of the Cu layer or other extrinsic effects. This result demonstrates the feasibility of manufacturing stable, oxidation-free devices and lays the groundwork for further investigations into interface effects and the precise readout mechanism.

By demonstrating spin-orbit-torque-based switching and introducing a novel readout mechanism based on orbital currents, this work constitutes a paradigm shift in our understanding of spin- and orbital-driven phenomena in antiferromagnets. These results open new avenues for the field of orbitronics and establish orbital angular momentum as a critical tool in developing faster, more energy-efficient, and scalable magnetic technologies.

Kurzzusammenfassung

Antiferromagnetische Materialien haben sich aufgrund ihrer intrinsischen Eigenschaften - kein Nettomagnetmoment, Robustheit gegenüber externen Magnetfeldern und ultraschnelle Magnetisierungsdynamiken im THz-Bereich - als wichtige Kandidaten im Bereich der Spintronik etabliert. Diese Eigenschaften unterstreichen ihr Potenzial, Informationstechnologien durch stabile, schnelle und kompakt integrierte Bauelemente zu revolutionieren. Die Entwicklung effizienter Mechanismen zum Schreiben und Auslesen magnetischer Informationen in Antiferromagneten stellt jedoch weiterhin eine große Herausforderung dar. Obwohl elektrische Schaltprozesse des Néel-Vektors intensiv untersucht wurden, werden sie häufig von thermischen Effekten dominiert, die die ultraschnellen Dynamiken überlagern, welche die Materialien besonders attraktiv machen. Ebenso führen herkömmliche Ausleseverfahren, die auf Spinströmen basieren, meist zu schwachen Signalen, was ihre praktische Anwendbarkeit einschränkt. Zwar existieren bereits Auslesekonzepte auf Basis von Orbitalströmen, die Orbitalströme selbst können jedoch nicht direkt genutzt werden, da sie nur ineffizient mit der Spinmagnetisierung in magnetischen Materialien koppeln. Folglich müssen sie zunächst in Spinströme umgewandelt werden, bevor sie genutzt werden können.

In dieser Arbeit werden CoO-Dünnschichten untersucht und Schalt- sowie Auslesemechanismen aus einer neuen Perspektive betrachtet. CoO ist ein prototypischer Antiferromagnet mit großem Bahndrehmoment, und durch die Untersuchung von CoO/Pt- und CoO/Cu*-Heterostrukturen - wobei Cu* eine natürlich oxidierte Cu-Schicht bezeichnet - werden zentrale Herausforderungen im Zusammenhang mit der Manipulation und Detektion antiferromagnetischer Ordnung in isolierenden Systemen adressiert.

Zunächst demonstrieren wir die Koexistenz von Spin-Bahn-Drehmoment-getriebenem Schalten und thermisch induzierten Effekten in ultradünnen CoO/Pt-Systemen. Durch die Korrelation elektrischer Auslesedaten mit Abbildungen magnetischer Domänen zeigen wir, dass der endgültige magnetische Zustand nicht allein durch thermomagnetoelastische Effekte erklärt werden kann, sondern auf die Existenz eines drehmomentgetriebenen Mechanismus hinweist. Dieses Ergebnis weist auf das Potenzial ultraschneller, strominduzierter Manipulation und Schaltvorgänge in ultradünnen antiferromagnetischen Schichten hin.

Zweitens präsentieren wir den ersten (nach unserem Kenntnisstand) experimentellen Nachweis eines rein orbitalen Wechselwirkungsmechanismus in Antiferromagneten anhand von CoO/Cu*-Zweischichtsystemen. Durch die Kombination orbitaler Ströme mit dem orbitaldominierten Magnetisierungsmoment von CoO erreichen wir ein um zwei Größenordnungen verstärktes Magnetwiderstandssignal. Hervorzuheben ist, dass keine Schwermetallschicht verwendet wurde und somit konventionelle spinbasierte Mechanismen für das beobachtete Signal ausgeschlossen werden können. Stattdessen ist bekannt, dass Cu* signifikante orbitale Ströme erzeugt, und wir zeigen, dass das verstärkte Auslesesignal aus der Kopplung dieser orbitalen Ströme an das große Bahndrehmoment von CoO resultiert. Dieses Ergebnis liefert überzeugende Belege dafür, dass orbitale Ströme als effiziente und robuste Auslesemechanismen dienen können und markiert einen Paradigmenwechsel gegenüber spinbasierten Ansätzen - ein Schritt, der ein neues Kapitel der antiferromagnetischen Orbitronik eröffnet.

Drittens zeigen vergleichende Studien an CoO/Cr- und CoO/Cu/Pt-Dreischichtsystemen, dass der Effekt robust ist und nicht auf oxidiertes Cu beschränkt bleibt. Da die Oberflächenoxidation von Cu schwer kontrollierbar ist, ist die Identifikation von Mechanismen und Materialien entscheidend, die für reale Anwendungen geeignet sind. In CoO/Cr beobachten wir eine fünffache Verstärkung des Auslesesignals im Vergleich zu Messungen an CoO/Pt. Darüber hinaus deutet das verstärkte Auslesesignal in CoO/Cu/Pt-Schichtsystemen darauf hin, dass der Effekt auch von einer schnittstellengetriebenen Erzeugung orbitaler Ströme herrühren kann und nicht ausschließlich aus einer Oxidation von Cu oder anderen extrinsischen Effekten. Dieses Ergebnis demonstriert die Machbarkeit der Herstellung stabiler, oxidationsfreier Bauelemente und bildet die Grundlage für weiterführende Untersuchungen zu Grenzflächeneffekten und zum genauen Auslesemechanismus.

Zusammenfassend widmet sich diese Arbeit direkt den zentralen Herausforderungen der Manipulation und Auslese antiferromagnetischer Ordnung in isolierenden Dünnschichtsystemen. Durch den Nachweis von spin-orbit-drehmomentbasiertem Schalten und der Einführung eines neuartigen, auf Orbitalströmen beruhenden Auslesemechanismus stellt diese Arbeit einen Paradigmenwechsel in unserem Verständnis spin- und orbitalgetriebener Phänomene in Antiferromagneten dar. Diese Ergebnisse eröffnen neue Wege für das Forschungsfeld der Orbitronik und etablieren den orbitalen Drehimpuls als ein entscheidendes Werkzeug für die Entwicklung schnellerer, energieeffizienterer und skalierbarer magnetischer Technologien.

Contents

Abbreviations

AFM	antiferromagnet
AHE	anomalous Hall effect
AMR	anisotropic magnetoresistance
DC	direct current
EBL	electron beam lithography
EELS	electron energy loss spectroscopy
fcc	face-centered cubic
FM	ferromagnet
GMR	giant magnetoresistance
HM	heavy metal
iSHE	inverse spin Hall effect
LH	linear horizontal
LV	linear vertical
MR	magnetoresistance
OAM	orbital-polarized angular momentum
OHE	orbital Hall effect
OMR	orbital magnetoresistance
OQP	orbital quadrupole
OREE	orbital Rashba Edelstein effect
PEEM	photoemission electron microscopy
PHE	planar Hall effect
RF	radio frequency
S-domain	spin-domain
SHE	spin Hall effect

SMR	spin Hall magnetoresistance
SOC	spin-orbit coupling
SOT	spin-orbit torque
SREE	spin Rashba Edelstein effect
STEM	scanning transmission electron microscopy
STT	spin-transfer torque
T-domain	twin-domain
TMR	tunnel magnetoresistance
UV	ultraviolet
XAS	X-ray absorption spectroscopy
XMD	X-ray magnetic dichroism
XMCD	X-ray magnetic circular dichroism
XMLD	X-ray magnetic linear dichroism
XNCD	X-ray natural circular dichroism
XNLD	X-ray natural linear dichroism
XRD	X-ray diffraction
XRR	X-ray reflectometry

1 Introduction

Information is often treated as an abstract entity, detached from the constraints of the physical world. Yet, as Rolf Landauer famously emphasized, *information is physical* [1]. Every bit stored, transported, or erased requires energy and time [2, 3]. As modern computing approaches the fundamental limits of charge-based electronics [4], this realization is no longer philosophical but the need to find alternative ways to charge based information processing becomes a guiding principle.

Today, the urgency of this task is amplified by the massive energy demands of artificial intelligence and a data-driven society. Modern data centers already consume a substantial fraction of the world's electricity [5, 6], and the rapid expansion of artificial intelligence workloads is further accelerating that demand [5]. A central challenge arises from Joule heating in silicon-based semiconductor technology: in contemporary data centers, the majority of energy consumption stems not from computation itself, but from the cooling required to dissipate the heat generated by resistive charge currents [7, 8]. Beyond the technical inefficiencies, the environmental impact cannot be ignored: every joule consumed by computation and cooling can have ecological consequences [9, 10]. This highlights the need for information-processing technologies that inherently reduce Joule heating and required computation power.

This energy crisis is compounded by the fact that the long-standing trajectory of performance improvement, embodied in Moore's Law, is faltering as transistors approach atomic dimensions and conventional scaling strategies lose effectiveness [4, 11]. Without new physical mechanisms to sustain progress, further increases in computing capacity risk becoming energetically and economically un-

sustainable.

These challenges compel us to rethink computing fundamentally. Electrons in solid-state devices are not mere carriers of electric charge; they are quantum objects endowed with additional internal degrees of freedom, such as spin and orbital-polarized angular momentum (OAM) [12]. Rather than attempting to extend the scaling of charge-based electronics beyond its practical limits, it is necessary to consider whether these alternative quantum degrees of freedom can support more efficient information processing. In this context, spintronics and orbitronics provide promising avenues [13–16]. By exploiting the electron's spin, its intrinsic angular momentum, and its orbital motion, information can be encoded and manipulated with significantly lower energy dissipation than in conventional charge-based devices [17–19]. These quantum degrees of freedom thus enable device concepts that are not merely incremental extensions of existing technologies, but represent qualitatively new paradigms for information processing.

The transformative potential of spintronics first became evident with the discovery of giant magnetoresistance (GMR) [20, 21] and tunnel magnetoresistance (TMR) [22], which revolutionized read-head technology and enabled modern magnetic hard drives. These discoveries demonstrated that spin-dependent transport phenomena could directly translate into technological impact. More recently, the emergence of spin-transfer torque based magnetic tunnel junctions and magnetic random-access memory has strengthened spintronics as a key field for future memory and storage technologies [23–26].

While the focus of early spintronics research was largely on ferromagnets (FMs), attention has increasingly shifted toward antiferromagnets (AFMs) [27]. AFMs offer several intrinsic advantages: the absence of net magnetization eliminates stray fields, enabling dense integration [28]; their dynamics, governed by strong exchange interactions, reach the THz regime, far beyond FM limits [29, 30]; and their robustness against external magnetic perturbations leads to stability of the encoded bits [31, 32].

Yet, despite these advantages, AFMs come with significant challenges that have slowed their technological adoption. Their compensated magnetic structure, while beneficial for integration and stability, also makes them inherently difficult to manipulate and read out [27, 31, 33, 34]: the absence of a net magnetization suppresses conventional magnetic signals, and the responses tend to be weak. As a result,

both writing and detection in AFMs often require large current densities, complex interface engineering, or indirect probing schemes, limiting efficiency and scalability. Overcoming these limitations has therefore become one of the central goals of modern AFM spintronics.

In this context, orbitronics provides a particularly promising route forward. Theoretical work predicts that orbital Hall conductivities can exceed spin Hall conductivities by orders of magnitude in many systems [35–41], suggesting that OAM currents could in principle drive more efficient and more powerful device functionalities than their spin-based counterparts. These large orbital currents offer an attractive path toward enhanced manipulation and readout of magnetic order.

However, despite this promise, a practical bottleneck remains: dynamic OAM (orbital current) couples only inefficiently to spin-based magnetic order in conventional materials [42, 43]. For this reason most orbitronic device concepts rely on converting orbital current into spin current via the weak relativistic spin-orbit coupling (SOC), and it is the resulting spin current that interacts with the magnetization based on spin [44–46]. That intermediate conversion step reintroduces the inefficiencies and limitations of small SOC-based effects, that orbitronics aims to overcome.

To address the challenges of electrically manipulating and reliably reading out the Néel vector, this thesis focuses on insulating CoO thin films and heterostructures from both, a spintronic and an orbitronic perspective. Although initial reports have demonstrated current-induced switching of insulating AFMs using adjacent heavy metal (HM) layers [47–49], the observed effects have been dominated by thermally driven mechanisms [50, 51]. As a consequence, they have not provided access to the ultrafast intrinsic dynamics of AFMs that underpin their technological appeal. In this work, we revisit the problem using ultrathin CoO films, in which interfacial torques, rather than bulk thermal processes, are expected to play a more prominent role [49]. By combining electrical measurements and magnetic imaging, we can separate thermal from non-thermal contributions and show that the dominating switching mechanism is of thermomagnetoelastic origin. However, local changes within the current-carrying regions reveal a concurrent spin-orbit torque (SOT)-driven Néel-vector reorientation.

Secondly, to tackle the practical challenge posed by the small read-out signals that currently hinder device-level operation, we investigate a complementary or-

bitronic approach in which externally generated orbital currents from oxidized Cu are used as the readout probe. By exploiting the large, unquenched orbital moment of CoO, these orbital currents can couple efficiently to the AFM order, resulting in a roughly two-orders-of-magnitude enhancement in the measured magnetoresistance (MR) compared with conventional spin-based schemes, without the need for orbital-to-spin conversion. Thus, offering a robust and highly sensitive electrical readout channel.

Taken together, these two strategies, torque-based manipulation in ultrathin films and orbital-current-based readout, address two unresolved issues in insulating AFMs. The identification of interfacial torques in ultrathin CoO provides evidence for a non-thermal switching pathway in systems where such mechanisms have long been debated, marking an important step toward accessing their intrinsic ultrafast dynamics. In contrast, the orbital readout concept introduced here has broader significance: demonstrating that pure orbital currents can directly couple to OAM magnets, and can enhance readout signals by two orders of magnitude, establishes a general orbitronic mechanism applicable well beyond CoO. In doing so, the two strategies reconnect AFM spin- and orbitronics to the broader challenges information technology is facing.

As we observe unprecedented demands for speed, density, and energy efficiency, advancing physical principles that enable ultrafast control and low-loss readout becomes essential. By demonstrating viable pathways towards both, this thesis contributes to the development of magnetic device concepts that are compatible with the needs of a data-intensive, artificial intelligence-driven, and energy-constrained world.

This thesis is structured as follows: Ch. 2 provides a foundational overview of magnetism in solids. The various energy terms defining the magnetic state of a solid are discussed. It introduces AFMs, the primary material class of interest, and discusses the formation of AFM domains. The chapter concludes with a brief treatment of the effects of large applied magnetic fields on such systems. Moving on, Ch. 3 reviews the current-induced phenomena exploited throughout this thesis. It begins with mechanisms for spin current generation and spin Hall magnetoresistance (SMR), followed by orbital current generation and orbital magnetoresistance (OMR). The chapter also covers spin torques and thermal effects, including Joule heating and thermomagnetoelastic switching. An introduction to the main

AFM material of interest for this work, CoO, comes in Ch. 4 alongside an introduction to the experimental techniques regarding sample deposition, fabrication, characterization and measurement techniques used in this thesis. The experimental results are presented across three chapters. Ch. 5 details the structural and magnetic characterization of the CoO thin films used in this work. It examines the influence of growth parameters, optical domain nucleation, and AFM shape anisotropy. The electrical switching of ultrathin CoO films is shown in Ch. 6.1, where the presence of a SOT based switching mechanism coexisting with a thermomagnetoelastic switching mechanism is shown by using the combination of electrical measurements and optical imaging of the AFM domain structure. Ch. 7 then demonstrates electrical readout of the Néel vector state in CoO using purely orbital means. Unlike prior approaches, which rely on orbital-to-spin conversion, this method directly couples OAM, generated in oxidized Cu, to the unquenched orbital moment in CoO, yielding a two-order-of-magnitude enhancement in readout signal. Furthermore, we show that this mechanism is not restricted to oxidized Cu: it is also observed when using for example Cr as the OAM generator, suggesting broader applicability. Finally, Ch. 8 summarizes the principal findings of this thesis and outlines potential directions for future research.

2 Concepts of Magnetism

This chapter presents the theoretical background of fundamental concepts in magnetism that are essential for understanding the experimental results discussed in this thesis. First, an overview of the different classes of magnetism in solids is provided, followed by an introduction to magnetic free energy, exchange interactions, and magnetic anisotropy. Subsequently, an overview of AFMs is given, including the various types of AFMs, a model to describe their magnetic ordering, domain formation, and the influence of strain and magnetic fields on AFM ordering.

2.1 Magnetism in Solids

The magnetic behavior of materials originates from the collective interactions of atomic magnetic moments, which arise from the spin and orbital angular momentum of electrons [12]. Depending on the interaction and alignment of these moments, various types of magnetic order can be distinguished, each characterized by a distinct response to an externally applied magnetic field $\boldsymbol{H}$. The induced magnetization $\boldsymbol{M}$ in the material is related to $\boldsymbol{H}$ through the magnetic susceptibility $\chi = \boldsymbol{M}/\boldsymbol{H}$ [12, 52].

All materials exhibit *diamagnetism*, a weak and universal response due to induced currents that oppose the applied magnetic field, resulting in a small negative susceptibility. This effect becomes significant primarily in systems without unpaired electrons [53]. In contrast, *paramagnetic* materials possess partially filled electron shells, which give rise to a net magnetic moment μ. Paramagnets show a positive susceptibility, and their magnetic moments align with an external magnetic field [52]. In both diamagnetic and paramagnetic materials, magnetization

responds linearly to the applied magnetic field. However, in the absence of an external magnetic field, thermal fluctuations prevent any spontaneous magnetic ordering [12, 52].

When the exchange interaction (see Sec. 2.2.1) between neighboring spins is sufficiently strong, spontaneous magnetic ordering can emerge. In a *FM*, this interaction favors parallel alignment of all spins, both with respect to each other and to an applied magnetic field, resulting in a large net magnetization [12, 54]. FMs exhibit characteristic features such as magnetic domains and hysteretic behavior, whereby the material maintains a net magnetic moment even after the external field is removed. This remanent magnetization depends on the history of the applied magnetic field [55]. FMs form the foundation of most classical magnetic technologies.

On the other hand, when the exchange interaction favors antiparallel alignment, *AFM ordering* arises [56, 57]. In conventional AFMs, neighboring magnetic moments cancel out each other, leading to zero net magnetization despite the presence of an ordered spin structure. In a simple picture one can understand a collinear AFM as a superposition of two oppositely aligned FM sublattices, as illustrated in Fig. 2.1. Each sublattice has an individual magnetic moment $|\boldsymbol{M_1}| = |\boldsymbol{M_2}| = M_0$. The overall net magnetization vanishes in equilibrium $\boldsymbol{M} = \boldsymbol{M}_1 - \boldsymbol{M}_2 = 0$. Magnetic order in AFMs can be characterized by the Néel vector, and is defined as $\boldsymbol{n} = (\boldsymbol{M}_1 - \boldsymbol{M}_2)/2M_0$ [58, 59].

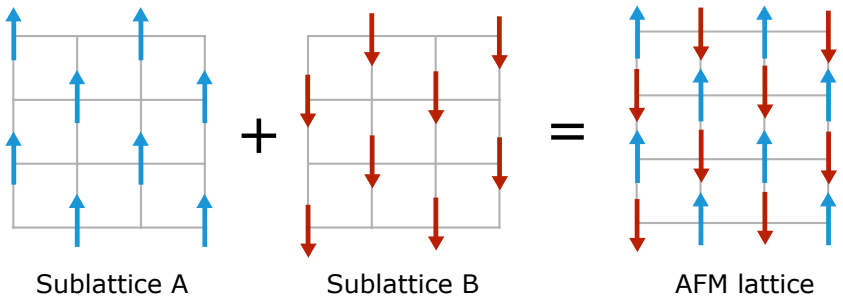

Figure 2.1: Schematic of a collinear AFM with two FM sublattices (red, blue) with antiparallel magnetization as indicated by the direction of the arrows.

Ferrimagnets consist of opposing magnetic moments, similar to AFMs, however, these moments are unequal in magnitude or number, resulting in an incomplete cancellation and a finite net magnetization, as in FMs [60]. Beyond these well-established magnetic phases, recent theoretical and experimental advances

have led to the identification of *altermagnetism*, a novel, symmetry-defined form of collinear magnetic order [61–63].

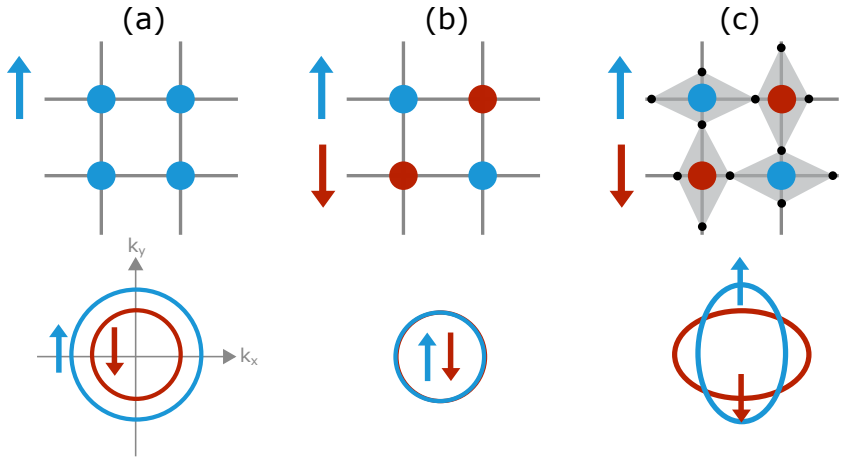

Figure 2.2: Schematic illustration of real-space (upper panel) and momentum-space (lower panel) spin configurations for (a) ferromagnetism with all magnetic moments aligned parallel to each other and spin splitting in reciprocal space. (b) AFM ordering with two magnetic sublattices (red and blue) and no spin splitting. (c) Altermagnetic order with two magnetic sublattices and a non-isotropic local crystallographic environment due to non-magnetic atoms (black) in real space and spin splitting in reciprocal space.

Altermagnets, like conventional AFMs, possess no net magnetization in equilibrium due to a fully compensated arrangement of opposing magnetic moments. However, the opposite spin sublattices in altermagnets are coupled by rotational symmetry and break time-reversal symmetry. As a consequence, altermagnets break spin-degeneracy in the electronic band structure due to their distinct magnetic space group symmetries. This spin degeneracy lifting gives rise to spin-split bands, similar to those found in FMs, enabling altermagnets to host spintronic phenomena traditionally associated with systems possessing a net magnetization [61]. Figure 2.2 compares the spin structure and spin polarization in FMs, AFMs and altermagnets.

2.2 Magnetic Free Energy

The *magnetic free energy* $\mathcal{F}$ of a system determines its magnetic ground state in equilibrium [64]. The free energy is composed of the sum of various intrinsic and extrinsic energy contributions [12, 52, 65]:

$$\mathcal{F} = \int_V f(\boldsymbol{r}) dV = \int_V \left(f_{\text{ex}}(\boldsymbol{r}) + f_{\text{ani}}(\boldsymbol{r}) + f_{\text{Z}}(\boldsymbol{r}) + f_{\text{me}}(\boldsymbol{r}) + \ldots \right) dV. \tag{2.1}$$

The energy terms discussed here are limited to those relevant for the magnetic ordering of the AFM materials studied in this thesis. These include the exchange interaction f_{ex}, which couples atomic magnetic moments and the crystalline anisotropy f_{ani}, which aligns magnetic moments along preferred crystallographic directions. Both are crucial in determining the magnetic ground state. Furthermore, the Zeeman energy f_{Z} describing the coupling between magnetic moments and an external magnetic field, is discussed in the following section. The magnetoelastic energy f_{me}, which couples magnetic moments to mechanical strain in the material and plays a key role in the formation of AFM domains [65, 66], will be addressed in the context of AFM domain formation in Sec. 2.3.2.

2.2.1 Exchange Energy

Long-range magnetic order in solids arises from *exchange interactions*, which constitute an important contribution to the magnetic free energy and play a central role in determining the magnetic structure of AFMs. Exchange interactions act between pairs of spins, coupling them and thereby stabilizing ordered magnetic states. The origin of the exchange interaction lies in both classical and quantum mechanical principles: the Coulomb repulsion between the electrons and the Pauli exclusion principle. The latter requires the total wavefunction of a system of identical fermions to be antisymmetric under particle exchange.

In the following, we first introduce the concept of direct exchange interaction [67–69], following the description in Refs. [12, 52]. We then discuss the superexchange interaction [70], which is particularly relevant for the strong AFM coupling observed in CoO.

2.2.1.1 Direct Exchange

Although magnetic ordering is observed as a macroscopic phenomenon, its origin is fundamentally quantum mechanical, arising from the overlap of electron wavefunctions.

In the simplest case, we consider two electrons with overlapping wavefunctions, both occupying the 1*s* orbital, such as in a hydrogen molecule (H_2). The spatial part of the wavefunctions is denoted by $\psi_1(\boldsymbol{r}_1)$ and $\psi_2(\boldsymbol{r}_2)$, and the spin

parts by $\chi_1(s_1)$ and $\chi_2(s_2)$. The total wavefunction of the two-electron system is then given by

$$\Psi(1,2) = \psi(\boldsymbol{r}_1, \boldsymbol{r}_2) \cdot \chi(s_1, s_2). \tag{2.2}$$

The total wavefunction of the two-electron system must be antisymmetric under exchange of the two particle:

$$\Psi(1,2) = -\Psi(2,1). \tag{2.3}$$

To satisfy the antisymmetry requirement of the total wave function, the spin and spatial components must possess complimentary symmetry. This results in two distinct configurations: a singlet state with total spin $S = 0$ (antisymmetric spin state χ_a, symmetric spatial state ψ_s) and a triplet state with total spin $S = 1$ (symmetric spin state χ_s, antisymmetric spatial state ψ_a).

The energy difference between the singlet and triplet states is given by $2J$, where J is the exchange integral.

The exchange energy of neighboring electrons, with dimensionless spin operators $\hat{\boldsymbol{S}}_1$ and $\hat{\boldsymbol{S}}_2$, can be expressed by the Heisenberg Hamiltonian [12, 52]

$$\mathcal{H}_{\text{ex}} = -2J\, \hat{\boldsymbol{S}}_1 \cdot \hat{\boldsymbol{S}}_2. \tag{2.4}$$

This can be generalized to a lattice of interacting spins, yielding

$$\mathcal{H}_{\text{ex}} = -2 \sum_{i>j} J_{ij}\, \hat{\boldsymbol{S}}_i \cdot \hat{\boldsymbol{S}}_j. \tag{2.5}$$

The sign of the exchange integral J determines the preferred type of magnetic ordering: a positive value of J favors FM alignment, whereas a negative J favors AFM order.

In systems containing a large number of interacting spins, a full quantum mechanical description becomes computationally infeasible. To address this, a continuum approximation is employed, in which the local magnetization $\boldsymbol{M}(\boldsymbol{r})$ is described as a continuous vector field [52]. Its magnitude is assumed constant and equal to the saturation magnetization M_s. One then defines the unit vector

$$\boldsymbol{m}(\boldsymbol{r}) = \frac{\boldsymbol{M}(\boldsymbol{r})}{M_s}. \tag{2.6}$$

The exchange energy density in the continuum model is given by [52]

$$f_{\mathrm{ex}} = A(\nabla \boldsymbol{m}(\boldsymbol{r}))^2, \tag{2.7}$$

where A is the exchange stiffness, a material-dependent and temperature-sensitive constant. The exchange energy penalizes spatial variations in the magnetization, thereby favoring the formation of smooth magnetic textures and large magnetic domains [52].

2.2.1.2 Superexchange

The interaction mechanism relevant to the materials investigated in this thesis is indirect *superexchange*. In $3d$ transition metal oxides, electrons are strongly localized, resulting in minimal overlap between the $3d$ orbitals [71]. Consequently, direct exchange interactions between these orbitals are negligible due to the short-range nature of the exchange mechanism. Instead, magnetic ions interact via non-magnetic atoms, such as oxygen, which mediate the exchange interaction [12, 72, 73].

The underlying principle of this mechanism is illustrated in Fig. 2.3(a) for CoO. In this system, the exchange interaction between unpaired $3d$ electrons of Co ions is facilitated through the hybridization with the $2p$ orbitals of the intermittent oxygen atom. This interaction occurs via a virtual exchange process: two electrons from the oxygen $2p$ orbital are transferred to the unoccupied $3d$ orbitals of adjacent Co ions, resulting in a long-range coupling between the magnetic ions.

As shown in Fig. 2.3(b), the Pauli exclusion principle suppresses such virtual electron hopping in the case of FM alignment of the Co moments, since parallel spins prohibit an orbital overlap. In contrast, AFM alignment permits electron delocalization throughout the system, reducing the total kinetic energy and making the AFM configuration energetically favorable [12]. However, electron hopping also increases the on-site Coulomb repulsion, confining it to a virtual process. As a result, most AFM oxides are electrical insulators [12, 52].

In systems containing magnetic ions with unequal valencies, FM coupling may become energetically favorable due to the double exchange mechanism [12]. This effect arises when electron hopping is favored between ions of different oxidation states, thereby stabilizing a FM alignment of the spins.

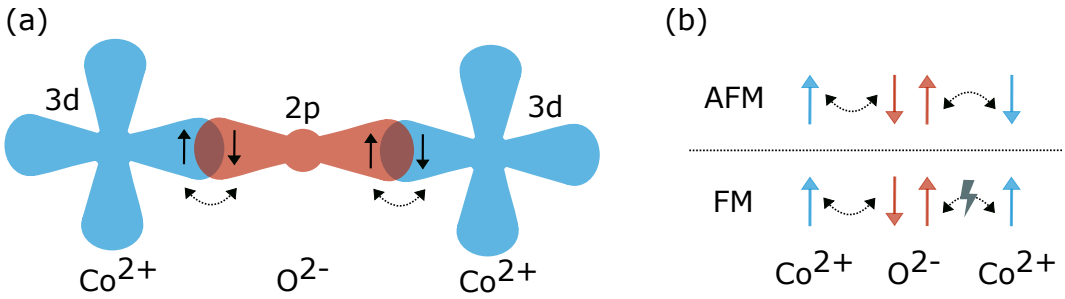

Figure 2.3: (a) Illustration of the indirect superexchange mechanism in CoO. The coupling between the Co 3*d* atomic orbitals is mediated by the 2*p* atomic orbital of the oxygen atom. (b) AFM ordering is preferred due to the Pauli exclusion principle. Blue arrows represent the spin orientation of the Co 3*d* electron spins, red arrows the oxygen 2*p* electron spins mediating the exchange.

2.2.2 Magnetic Anisotropy

The Heisenberg exchange energy is invariant under the rotation of the spin coordinate system and depends solely on the relative orientation between neighboring spins. However, experimental studies have revealed that magnetic moments in many material systems preferentially align along specific crystallographic directions [52]. This directional dependence arises from the underlying crystal structure of the material. The coupling between the lattice and orbital moments via SOC alters the wavefunction overlap between neighboring spins, resulting in direction-dependent energy variations [74, 75]. This phenomenon, known as *magnetocrystalline anisotropy*, gives rise to energetically favorable directions for the alignment of magnetic moments, termed *easy axes*, and energetically unfavorable directions, called *hard axes* [75]. To reorient the magnetization from an easy axis direction to another crystallographic direction, external work must be performed by a magnetic field [52].

The magnetocrystalline anisotropy reflects the symmetry properties of the crystal lattice. Specifically, symmetry operations that leave the crystal lattice invariant also leave the magnetic anisotropy energy of the system unchanged. For instance in a cubic system, the directions [100], [010] and [001] are symmetry-equivalent. In such a case, the cubic anisotropy energy density can be expressed as [12, 52]

$$E_\mathrm{a} = K_1(T)(\alpha_1^2\alpha_2^2 + \alpha_2^2\alpha_3^2 + \alpha_3^2\alpha_1^2) + K_2(T)(\alpha_1^2\alpha_2^2\alpha_3^2) + \ldots, \tag{2.8}$$

here $K_1(T)$ and $K_2(T)$ are temperature-dependent anisotropy constants that approach zero as the system approaches the magnetic transition temperature [12, 52, 76], and α_i denote the direction cosines of the magnetization vector with respect to the crystallographic axes.

When $K_1 > 0$ and $K_2 \approx 0$, the easy axes directions are aligned along the three equivalent {100} directions, as is the case in base-centered cubic Fe. In contrast, for face-centered cubic (fcc) ordered Ni, where $K_1 < 0$ and $K_2 > 0$, the easy axes lie along the four {111} cube diagonals [12].

In magnetic thin films, if the domains differ only in their in-plane ordering, the magnetocrystalline anisotropy can be simplified. For a film exhibiting fourfold in-plane symmetry, the magnetocrystalline anisotropy energy can be approximated as [77, 78]

$$f_{\text{ani}} = -\frac{1}{4}k\cos\theta, \tag{2.9}$$

where k is the anisotropy constant, and θ is the angle between the magnetization and the in-plane easy axes [65].

In FM materials, anisotropy can also arise from the geometry of the sample, known as shape anisotropy [79, 80]. The source are dipole-dipole interactions. However, in AFMs, shape anisotropy is generally negligible due to the absence of a net magnetization and, hence, negligible dipolar interactions.

2.2.3 Zeeman Energy

The *Zeeman energy* refers to the potential energy associated with the interaction between a magnetic moment and an external magnetic field. It quantifies how much the energy of a system shifts when placed in a magnetic field [52].

When a single magnetic dipole $\boldsymbol{\mu}$ is placed in a static magnetic field $\boldsymbol{H}$, it experiences a torque Γ that tends to align the dipole moment with the magnetic field,

$$\Gamma = \boldsymbol{\mu} \times \boldsymbol{H}. \tag{2.10}$$

The general expression for the potential energy U of a single magnetic dipole in an external magnetic field is obtained by integrating the torque over all angles between the dipole and the field [52]:

$$U = -\boldsymbol{\mu} \cdot \boldsymbol{H}. \tag{2.11}$$

For a magnetic material, the Zeeman interaction energy is the total interaction energy of the magnetization $\boldsymbol{M}$, defined as the average magnetic moment per unit volume, with external magnetic field. This leads to the local Zeeman energy density

$$f_{\mathrm{Z}}(\boldsymbol{r}) \propto -\boldsymbol{M}(\boldsymbol{r}) \cdot \boldsymbol{H}(\boldsymbol{r}). \tag{2.12}$$

This equation shows that, in a FM, the energy is minimized when the magnetization aligns parallel to the external magnetic field.

In contrast, in a perfect collinear AFM with two sublattices, the Zeeman energy is minimized when the Néel vector aligns perpendicular to the applied magnetic field, and the sublattice magnetizations cant in the direction of the magnetic field. Like this the Zeeman energy of the two sublattices is minimized simultaneously [52].

2.3 Antiferromagnetism

AFMs were first proposed independently by Landau and Néel in the 1930s [56, 60, 81, 82]. Both researchers observed anomalous magnetic behavior in materials previously thought to be paramagnetic and suggested a new form of magnetic ordering.

The first experimental confirmation of AFM order came from Shull and Smart, who used neutron scattering to demonstrate that the magnetic unit cell of MnO is twice the size of its crystallographic unit cell [83]. Since then, numerous AFM configurations have been discovered across metallic, semiconducting, and insulating materials [31, 33].

Although all AFMs exhibit no net macroscopic magnetization in equilibrium, the microscopic spin arrangement within the magnetic unit cell can vary widely. AFM order occurs not only in three-dimensional lattices but also in lower-dimensional systems such as one-dimensional spin chains [84], two-dimensional layers [85, 86], and two-dimensional magnetic lattices [87–89].

The specific type of AFM coupling depends strongly on the underlying crystallographic structure [12].

In a cubic system, three common types of ordering are observed: A-type, C-type and G-type. Landau first proposed the A-type AFM ordering [81], where magnetic moments are ferromagnetically coupled within a plane (e.g. the (100)

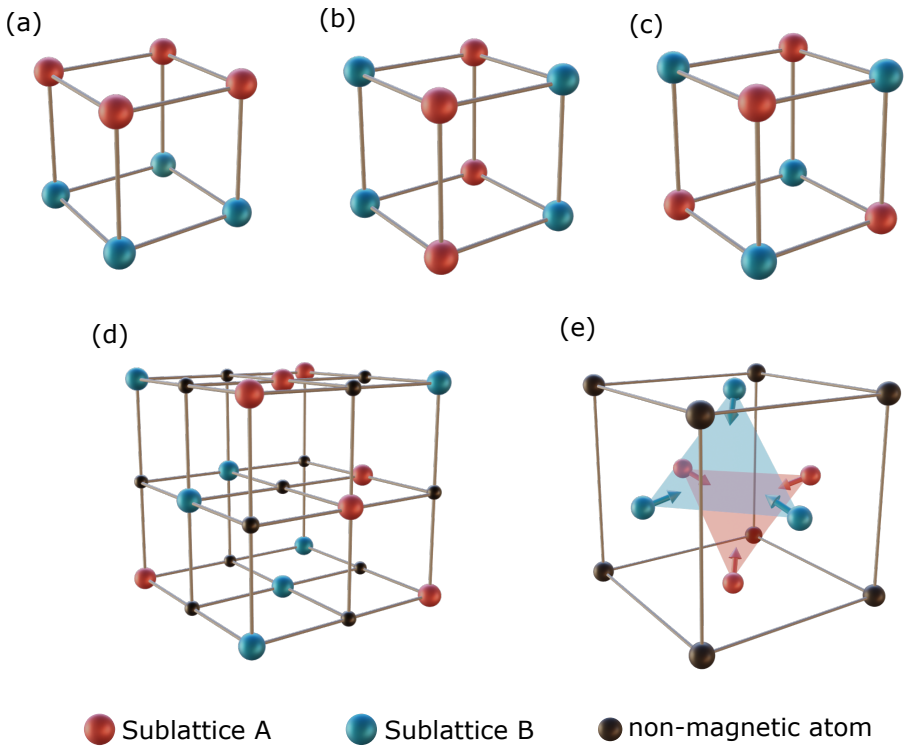

Figure 2.4: Comparison of different types of AFM ordering. (a) A-type ordering with layers of ferromagnetically ordered moments. (b) C-type ordering with AFM coupling of the moments along two directions. (c) G-type ordering with AFM coupling along three directions. (d) Type-II AFM coupling in an fcc ordered crystal as found e.g. in CoO and (e) non-collinear AFM ordering with the spins within one sublattice rotated 120° relative to each other.

plane), and adjacent planes are coupled antiferromagnetically [12], as illustrated in Fig. 2.4(a). In contrast, C-type ordering arises when adjacent planes are ferromagnetically coupled while the inter-plane coupling is antiferromagnetic (Fig. 2.4(b)). The third common ordering, G-type, originally proposed by Néel [56, 60, 82], involves AFM coupling both inter-plane and intra-plane (Fig. 2.4(c)).

Transition metal oxides such as CoO crystallize in a rock-salt (NaCl-type) structure. Here, FM coupling occurs within the (111) planes, while adjacent planes couple antiferromagnetically [90–92], as shown in Fig. 2.4(d). This type of ordering is referred to as a type-II AFM order. Although geometrically similar to G-type ordering, type-II is specifically defined for cubic structures like rock-salt.

The AFM structures discussed so far are all examples of collinear AFMs, where the magnetic moments lie along a common axis and two magnetic moments can-

cel each other out. Similar collinear coupling can also be engineered in synthetic AFMs [93, 94]. In addition, non-collinear AFM order exists, such as for example found in the triangular structure of $Mn_3Ni_{0.35}Cu_{0.65}N$ or $IrMn_3$ [95, 96]. In these materials, magnetic moments are rotated by 120° relative to each other, forming an AFM structure composed of three coupled moments, as depicted in Fig. 2.4(e).

The work shown in this thesis focuses on collinear type-II AFMs, and therefore, the following sections will focus on the description and properties of collinear AFMs.

2.3.1 Weiss Model of Antiferromagnetism

The Weiss model for AFMs [56, 60, 82], is a mean-field theory that extends the original Weiss molecular field model for FMs [54, 97]. It was developed by Louis Néel, a PhD student of Pierre Weiss [98], to describe the interaction between the two sublattices $\boldsymbol{M}_1$ and $\boldsymbol{M}_2$, under the influence of a negative exchange interaction, characteristic for AFMs. Here, we present the core concepts of the model, following Refs. [12, 52].

In this framework, the molecular field acting on each sublattice depends on the magnetization of the other sublattice [12]:

$$\boldsymbol{H}_{M_1} = -\lambda_{11}\boldsymbol{M}_1 - \lambda_{12}\boldsymbol{M}_2, \tag{2.13}$$

$$\boldsymbol{H}_{M_2} = -\lambda_{21}\boldsymbol{M}_1 - \lambda_{22}\boldsymbol{M}_2, \tag{2.14}$$

the coefficients λ_{ij} are proportionality constants. Specifically, λ_{11} and λ_{22} describe the molecular field contributions for next-nearest-neighbor intra-sublattice interactions, while λ_{12} and λ_{21} are the molecular field constants for nearest-neighbor inter-sublattice interactions. For the simplest case, in which the atoms on both sublattices are of the same type, $\lambda_{11} = \lambda_{22} = \lambda_{ii}$ and $\lambda_{12} = \lambda_{21}$.

When a small external magnetic field $\boldsymbol{H}$ is applied, Eqs. 2.13 and 2.14 become,

$$\boldsymbol{H}_1 = \boldsymbol{H} + \boldsymbol{H}_{M_1}, \tag{2.15}$$

and,

$$\boldsymbol{H}_2 = \boldsymbol{H} + \boldsymbol{H}_{M_2}. \tag{2.16}$$

In thermal equilibrium the magnetization of each sublattice can be expressed by

the Brillouin function B_J [52]

$$\boldsymbol{M}_{1,2} = \frac{ng\mu_\mathrm{B}J}{2} B_J(x_{1,2}), \tag{2.17}$$

with the number of magnetic atoms per sublattice $n/2$, the Landé factor g, the Bohr magnetron μ_B and the total angular momentum J, including spin and orbital angular momentum. The Brillouin function depends on the dimensionless quantity $x_{1,2}$, representing the ratio of the Zeeman energy to the thermal energy for each sublattice

$$x_{1,2} = \frac{g\mu_\mathrm{B}J}{k_\mathrm{B}T} \boldsymbol{H}_{1,2}, \tag{2.18}$$

where k_B is the Boltzmann constant and T is the absolute temperature.

Analogous to FMs, AFMs exhibit a critical temperature known as the Néel temperature T_N, above which the thermal energy overcomes the exchange interaction, resulting in vanishing sublattice magnetizations. In this paramagnetic regime ($T > T_\mathrm{N}$), the application of a small external magnetic field induces a small magnetization aligned with the field.

To derive the magnetic susceptibility χ just above the Néel temperature, we expand the Brillouin function in the limit of small x. Using the linear approximation [12, 52]

$$\chi \propto \frac{1}{T + \theta_\mathrm{P}}, \tag{2.19}$$

where θ_P defines the paramagnetic temperature of the AFM

$$\theta_\mathrm{P} = \frac{1}{2} C(\lambda_{ii} + \lambda_{12}), \tag{2.20}$$

with C being the Curie constant. If $\theta_\mathrm{P} > 0$, the material exhibits FM ordering, and θ_P corresponds to the Curie temperature T_C. If $\theta_\mathrm{P} < 0$, the material orders antiferromagnetically, and in the absence of a external magnetic field, the Néel temperature T_N is given by

$$T_\mathrm{N} = \frac{1}{2} C(\lambda_{12} - \lambda_{ii}). \tag{2.21}$$

This relation shows that a strong intra-sublattice exchange λ_{12}, combined with a weak inter-sublattice exchange λ_{ii}, leads to a higher Néel temperature.

2.3.2 Domain Formation

In FM materials, the total magnetic free energy (see Sec. 2.2) can be reduced by domain formation [54]. These domains help to reduce the magnetostatic energy associated with stray and demagnetizing fields generated by the sample [12, 52].

FM domain formation can be illustrated using the example of a rectangular shaped element, as shown in Fig. 2.5 [65].

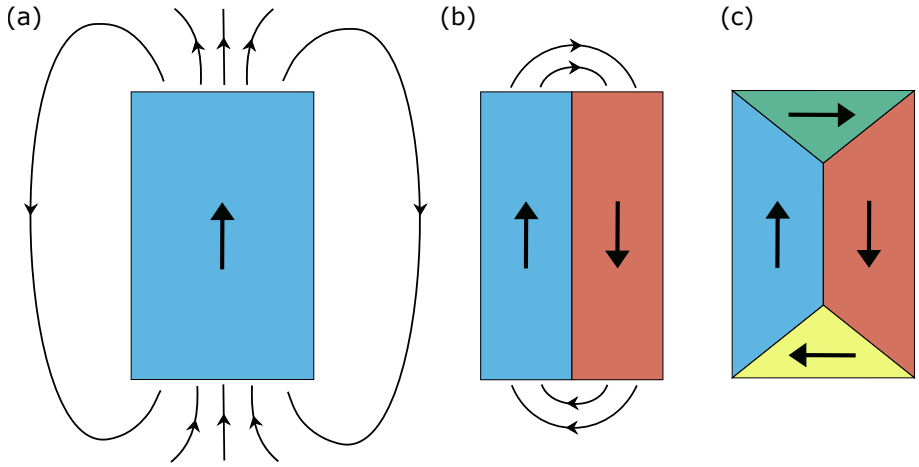

Figure 2.5: Schematic of the domain structure with the magnetic stray field of (a) a single domain and (b) a two domain state with antiparallel Néel vector orientation. (c) The total energy can be reduced and stray fields suppressed when closure domains are formed.

In the absence of an external magnetic field, and considering only contributions from exchange energy and magnetocrystalline anisotropy, a uniform magnetization state aligned along a crystalline easy axis represents the energetically favorable configuration in a FM (compare Fig. 2.5(a)). However, such a monodomain state maximizes the demagnetization energy through significant stray fields. Introducing an additional domain with antiparallel magnetization reduces this demagnetization energy, as shown in Fig. 2.5(b). Stray fields can be entirely suppressed through the formation of closure domains at the edges of the rectangle, illustrated in Fig. 2.5(c).

Within each domain, magnetization remains uniform, while the transition between the domains occurs across domain walls, where the magnetization gradually rotates [99, 100]. This rotation increases the exchange energy due to the nonparallel alignment of neighboring spins. Ultimately, an equilibrium state is estab-

lished in which the reduction in demagnetization energy balances the increase in exchange energy [12, 52]. AFMs do not possess a net magnetic moment, and thus, the formation of a multidomain structure is not expected from energetic considerations alone. Nevertheless, multidomain states have been experimentally observed in a variety of AFM materials [91, 101–108].

One proposed explanation involves a competition between the increase in entropy, associated with greater disorder introduced by domain formation, and the exchange energy cost associated with domain walls. However, the resulting change in entropy has been shown to be too small to compensate for the increase in exchange energy [109, 110]. While the formation of domains can to some extend be attributed to defects or pinning effects [109, 111], multidomain states have also been observed in annealed AFM films [91].

To understand the emergence of multidomain states in AFMs, it is essential to consider the role of strong magnetoelastic coupling and the influence of strain.

2.3.2.1 Magnetoelastic Energy

In materials with strong magnetoelastic coupling, the magnetic order is intimately linked to the crystal lattice [112, 113]. The elastic properties of such materials can be altered by external magnetic fields, and conversely, the magnetization can be affected by lattice deformations, which introduce strain into the system and contribute to the magnetic free energy.

In FMs, magnetoelastic coupling originates primarily from SOC: lattice strain modifies the atomic orbital environment, thereby altering the electrostatic potential and influencing the orientation of magnetic moments. In AFMs, additional contributions to magnetoelastic coupling arise from exchange coupling, as the coupling constant J is sensitive to lattice distortions [74, 114].

In the case of an uniaxial FM, one may observe either an elongation or a contraction of the material along the direction of an applied magnetic field, depending on the sign of the magnetoelastic coupling constant λ [52], as shown in Fig. 2.6. Magnetoelastic coupling plays a crucial role in the formation of magnetic domains, particularly in AFMs [64]. Due to the magnetoelastic coupling, any redistribution of magnetic domains is accompanied by a corresponding redistribution of strain within the material [91]. The magnetostriction depends on the orientation of the Néel vector relative to the crystallographic axes. The magnetoelastic contribution

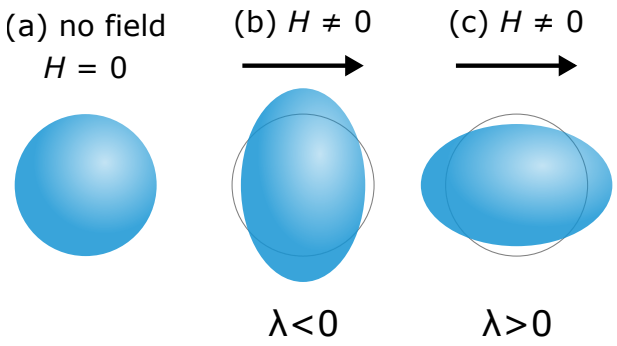

Figure 2.6: Illustration of the effect of an applied magnetic field on a magnetoelastic material with (a) negative and (b) positive magnetoelastic coupling constant [52].

to the magnetic free energy density can be expressed as [115]

$$f_{\text{me}} = \lambda_{ijkl} u_{ij} n_k n_l, \tag{2.22}$$

where the magnetoelastic coupling constant λ_{ijkl} is a tensor relating the strain u to the Néel vector $\mathbf{n}$.

To model the domain structure in the AFM thin films studied here, we can consider an isotropic crystal and neglect contributions from the out-of-plane Néel vector component n_z [115]. Under these assumptions, the magnetoelastic energy density simplifies to

$$f_{\text{me}} = \lambda[(u_{xx} - u_{yy})(n_x^2 - n_y^2) + 4 n_x n_y u_{xy}], \tag{2.23}$$

where u_{xx} and u_{yy} represent normal strain and u_{xy} is a shear strain. Alternatively, the magnetoelastic energy density can be expressed in terms of the angle ϕ between the Néel vector and the crystallographic axes [77, 78]

$$f_{\text{me}} = \lambda[\cos(2\phi)(u_{xx} - u_{yy}) + 2\sin(2\phi) u_{xy}]. \tag{2.24}$$

Strain in the AFM system, whether introduced by the thin-film growth on a substrate or by intrinsic defects and pinning sites, therefore contributes to the magnetoelastic energy density and can promote the formation of AFM domains, in order to redistribute and minimize the introduced strain.

2.3.3 Effect of a Large Applied Magnetic Field

In a collinear AFM, the magnetic susceptibility χ below the Néel temperature T_N depends on whether a magnetic field is applied parallel or perpendicular to the Néel vector [12, 52]. The two branches of susceptibility are illustrated in Fig. 2.7.

When a magnetic field is applied perpendicular to the AFM axes, the sublattice magnetizations cant by a small angle δ towards the field direction. This canting angle increases until the rise in exchange energy balances the reduction in Zeeman energy. As a result, a small net magnetic moment develops along the direction of $\boldsymbol{H}$. Since thermal fluctuations reduce both the exchange and Zeeman energy in a similar fashion, the perpendicular susceptibility $\chi_\perp$ remains temperature independent below T_N.

In contrast, when a magnetic field is applied parallel to the AFM axes, the susceptibility $\chi_\parallel$ is zero at $T = 0\,\mathrm{K}$, as both sublattices are fully saturated and the magnetic field does not have any additional effect. However, as the temperature approaches T_N, thermal fluctuations reduce the magnitude of the sublattice magnetizations, weakening the exchange coupling and thereby allowing the magnetic field to induce a finite response. Consequently $\chi_\parallel$ increases with temperature [12, 52].

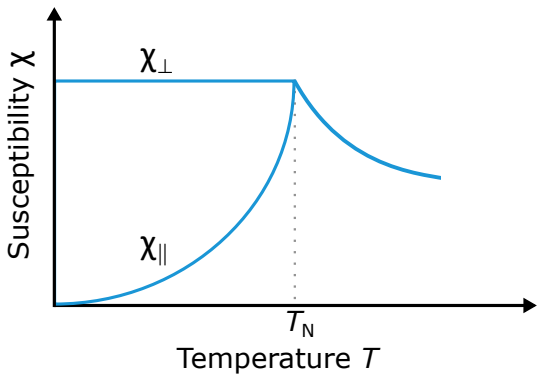

Figure 2.7: Susceptibility of an AFM as a function of temperature for a magnetic field applied parallel ($\chi_\parallel$) and perpendicular ($\chi_\perp$) to the AFM spin axes.

Depending on the strength of the applied magnetic field, the response of the AFM can vary. Below T_N, the magnetic susceptibility parallel to the Néel vector is smaller than the susceptibility perpendicular to it $\chi_\parallel < \chi_\perp$. As a result, a perpendicular alignment of the sublattice magnetizations relative to the applied magnetic field is, in principle, energetically favorable [12, 52].

However, when considering the state with lowest magnetic free energy, the

magnetocrystalline anisotropy must also be considered. This anisotropy favors alignment of the magnetic moments along the easy axes of the sample.

Therefore, if the magnetic field is applied along such an easy axis and is relatively weak, the system minimizes its total magnetic free energy by maintaining the magnetizations aligned parallel to the easy axis, despite the lower magnetic susceptibility in that configuration. At a critical field strength H_{sf}, the energy cost associated with keeping the spins aligned along the easy axis becomes equal to the gain in Zeeman energy achieved by reorienting the spins perpendicular to the field. Below this field strength the sublattice magnetizations will be collinear with the easy axis and the applied field and for $\boldsymbol{H} > H_{sf}$, the AFM sublattices reorient such that their magnetizations are nearly perpendicular to both the applied magnetic field and the easy axis (compare Fig. 2.8(b)), leading to the formation of a canted spin structure. This field-induced reconfiguration is known as a *spin-flop* transition. The critical spin flop field is given by [52]

$$H_{sf} = \sqrt{\frac{2K}{\chi_\perp - \chi_\parallel}}, \tag{2.25}$$

where K is a constant of the anisotropy energy.

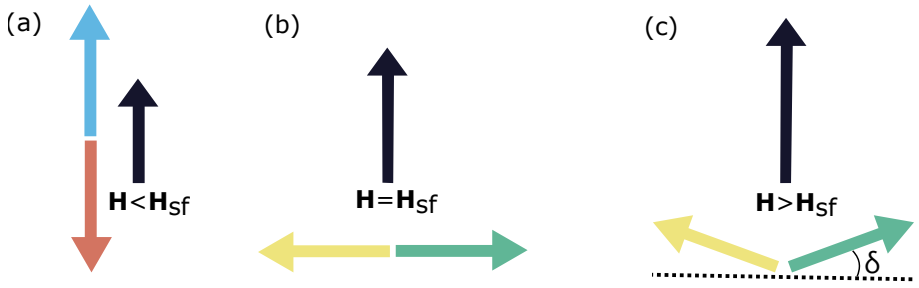

Figure 2.8: Effect of an increasing magnetic field on the sublattice magnetization: (a) Is the magnetic field $\boldsymbol{H}$ applied parallel to the sublattice magnetization, (b) above a critical field it comes to a rotation of the magnetic moments perpendicular to the applied magnetic field, the so called spin flop transition. (c) Further increasing the magnetic field, now perpendicular to the sublattice magnetization, leads to a canting of the magnetic moments.

If the magnetic field is applied perpendicular to the sublattice magnetizations, either after the spin-flop transition or because this geometry was chosen initially, the canting angle δ between the sublattices increases with increasing magnetic

field strength. As the field grows stronger, the Zeeman energy gain eventually becomes large enough to overcome the AFM exchange interaction, which initially maintains the antiparallel alignment of the sublattice magnetizations. At this point, all spins align parallel to the magnetic field, resulting in a spin-flip transition. However, because the exchange interaction in AFMs is typically large, very strong magnetic fields are required to induce this transition [52].

A spin-flop transition was first experimentally observed in $CuCl_2 \cdot 2H_2O$ [116, 117] and has since been reported in a variety of AFMs [118–120], including CoO [50, 121]. When experimentally accessible, the spin-flop transition provides a valuable tool for controlling the orientation of the Néel vector, thereby enabling more detailed insights into the magnetic structure and facilitating improved interpretation of experimental results.

3 Current-Induced Effects

The research fields of insulator spintronics and orbitronics exploit the transfer of spin and orbital angular momentum of electrons for information processing and related technological applications. A charge current flowing through a non-magnetic layer, can generate spin and orbital currents. While for the generation of spin currents a HM layer is needed, orbital currents can be generated in light metals.

In the following section, we outline current-induced phenomena that are relevant to the experimental investigations presented in this thesis. In particular, we first discuss the underlying mechanisms to generate spin and orbital current from charge current. The spin and orbital currents can be utilized to read the orientation of the order parameter in adjacent insulating AFM layers, such as CoO, through the SMR and OMR mechanisms. Next, we introduce the concept of spin torques, which have been predicted to enable the switching of AFM order. Finally, we address thermal effects arising from the applied charge currents.

3.1 Spin and Orbital Transport Effects

In 1879 Edwin Hall discovered the Hall effect: the generation of a transverse voltage in a conductor or semiconductor when an electric current flows through it in the presence of a perpendicularly applied magnetic field due to the Lorentz force [122]. Since its discovery, numerous related phenomena, collectively referred to as Hall effects, have been identified, including the spin Hall effect (SHE) and the orbital Hall effect (OHE) [40, 123–127]. These effects extend the original concept to the conversion of a charge current into spin-polarized or OAM currents. Such

charge-to-spin or charge-to-orbital conversion mechanisms are of central importance to the fields of spintronics and orbitronics, and the experimental investigations presented in this thesis are based on these principles.

3.1.1 Spin Hall Effect and Spin Rashba Edelstein Effect

The SHE enables the conversion of charge to spin current, which is a prerequisite for many spintronics applications, as the generation and detection of pure spin currents are key requirements [128]. When a charge current flows through a conductor with strong SOC, such as a HM, the electrons experience spin-dependent deflection. This results in a net transverse flow of spin current, as illustrated in Fig. 3.1(a). In this way, a pure spin current $\boldsymbol{j}_s$ can be generated, flowing perpendicular to both the charge current $\boldsymbol{j}_c$ and the spin polarization vector $\boldsymbol{\sigma}$. The SHE, therefore, provides an entirely electrical means of generating a pure spin current.

The reciprocal process, the inverse spin Hall effect (iSHE), enables the conversion of a spin current into a charge current [129], see Fig. 3.1(b). This charge current can then be detected electrically in measurements.

Detailed reviews on the SHE are given in [128, 130]. Here, only an overview of the main concepts will be given.

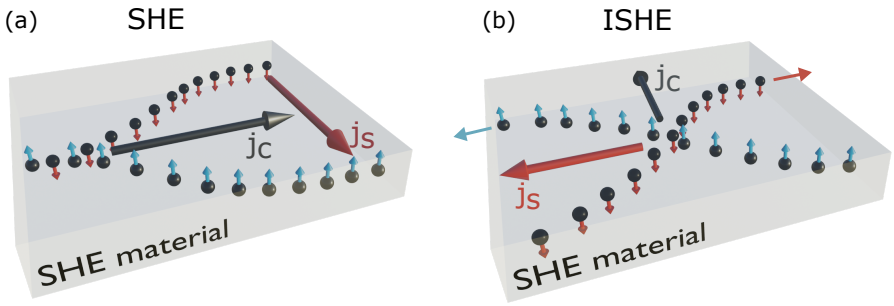

Figure 3.1: (a) Schematic of the SHE. A flowing charge current $\boldsymbol{j}_c$ is converted into a polarized spin current $\boldsymbol{j}_s$ in the transverse direction due to the spatial separation of electrons with opposite spin. (b) iSHE: A spin current $\boldsymbol{j}_s$ is converted into a transverse charge current $\boldsymbol{j}_c$.

The SHE was first predicted theoretically in 1971 by D'yakonov and Perel, who predicted the spatial separation of electrons in semiconductors as a function of their spin polarization [131]. Their description based on the concept of Mott scattering, laid the groundwork for later developments. More than two decades later, Hirsch [132] and Zhang [133] extended the idea to paramagnetic metals, establish-

ing a broader theoretical framework.

In the early theoretical works, considerable debate arose regarding the origin of the SHE. Extrinsic mechanisms, arising from Mott scattering off impurities, such as skew scattering [134], were considered, as well as other extrinsic effects like the side-jump mechanism [135]. In parallel, intrinsic contributions, originating from the relativistic band structure, were proposed for semiconductors [136, 137] and $3d$, $4d$ and $5d$ transition metals [35]. According to this mechanism, electrons acquire a momentum-space Berry phase, leading to a spin-dependent, anomalous velocity.

The first direct experimental demonstrations of the SHE were reported in 2004 using the magneto-optical Kerr effect [127], with the observed effect attributed to extrinsic scattering effects. Shortly thereafter, the intrinsic SHE was claimed based on photoluminescence measurements [138]. The reciprocal iSHE was observed in 2006 via FM resonance measurements of a $Y_3Fe_5O_{12}$/Pt bilayer. In this experiment spin pumping from the magnetic insulator into the Pt layer generated a measurable voltage via the iSHE [129].

The interconversion between a charge current $\boldsymbol{j}_c = \boldsymbol{j}_\uparrow + \boldsymbol{j}_\downarrow$ ($\boldsymbol{j}_{\uparrow/\downarrow}$ denote the spin-up and spin-down electron currents, respectively) and a spin current $\boldsymbol{j}_s = \boldsymbol{j}_\uparrow - \boldsymbol{j}_\downarrow$ via the SHE and its reciprocal iSHE can be expressed as

$$\boldsymbol{j}_c \propto \theta_{\mathrm{SH}}(\boldsymbol{\sigma} \times \boldsymbol{j}_s), \tag{3.1}$$

$$\boldsymbol{j}_s \propto \theta_{\mathrm{SH}}(\boldsymbol{\sigma} \times \boldsymbol{j}_c). \tag{3.2}$$

The efficiency of charge-to-spin interconversion in the SHE and iSHE is characterized by the spin Hall angle, $\theta_{\mathrm{SH}} = \boldsymbol{j}_s/\boldsymbol{j}_c$, defined as the ratio between generated spin current and applied charge current. It provides a measure of a materials efficiency of spin-current generation [128]. θ_{SH} scales approximately with Z^4, where Z is the atomic number, reflecting the fundamental role of SOC in the SHE [139]. Reported values of θ_{SH} can be either positive or negative, depending on the material [128].

Pt is among the most widely used materials for spin-current generation, owing to its large positive spin Hall angle [128] and high electrical conductivity, which is a prerequisite for energy efficient device application. However, experimentally reported values of $\theta_{\mathrm{SH,Pt}}$ vary significantly from 0.5% to 11% [128], reflecting both the challenges in determining this quantity with high precision and the variations

in material properties. These discrepancies arise in part from the complexity of the experimental techniques, which often require the determination or estimation of additional parameters, such as the spin-mixing conductance, in order to extract θ_{SH}. Moreover, the relative contributions of extrinsic and intrinsic SHE have been shown to depend on the resistivity of the transition metal, introducing further uncertainty [140–143].

One has to consider, that when using Pt as a spin-current source there is the possibility of proximity induced magnetization, when Pt is placed in contact with a magnetic layer, as Pt is close to the Stoner criterion for the onset of ferromagnetism [144, 145]. In conductors, the magnitude of the induced Pt moment scales with the saturation magnetization M_s of the adjacent layer, and a detectable magnetic proximity effect is observed only when the interfacial moment exceeds a threshold of roughly $0.3\,\mu_B$ per magnetic atom [146]. In contrast, Pt in contact with insulating magnetic oxides, including YIG, $NiFe_2O_4$ and $CoFe_2O_4$, shows no measurable proximity-induced magnetization [147–151]. Therefore, for Pt/CoO one does not expect a magnetic proximity effect unless the CoO interface contains metallic, ferromagnetic Co with a sufficiently large interfacial moment.

In addition to the SHE, another mechanism for spin accumulation generation is the spin Rashba Edelstein effect (SREE), which originates from broken structural inversion symmetry and strong SOC at interfaces or surfaces [152–154]. In systems with Rashba-type SOC [152], such as HM/oxide [155] or metal/semiconductor interfaces [156, 157], the electron bands exhibit spin-momentum locking: each momentum state is associated with a specific spin orientation due to the Rashba effect. When a charge current is applied, this results in an imbalance of occupation in momentum space, generating a non-equilibrium spin density oriented perpendicular to both the current direction and the interface normal as shown in Fig. 3.2. This interfacial spin polarization can diffuse into adjacent magnetic layers, effectively enabling charge-to-spin conversion without requiring a bulk SHE [153]. The SREE has been observed in various heterostructures, including Bi/Ag [155], $\alpha-$Sn [158], and $LaAlO_3/SrTiO_3$ [159] interfaces, as well as in topological insulator surface states, where strong SOC and broken inversion symmetry are intrinsic features [160]. Unlike the bulk SHE, which generates a spin current in the transverse direction, the SREE produces a non-equilibrium spin density localized at the interface.

The two mechanisms can coexist in multilayer systems and may contribute simultaneously to SOT phenomena, complicating the interpretation of experimental results [154, 161, 162]. Although the SREE plays a critical role in certain device geometries and material systems, it is not directly relevant for the experiments presented in this thesis, which rely on the bulk SHE in Pt for spin current generation, but is presented here only for completeness.

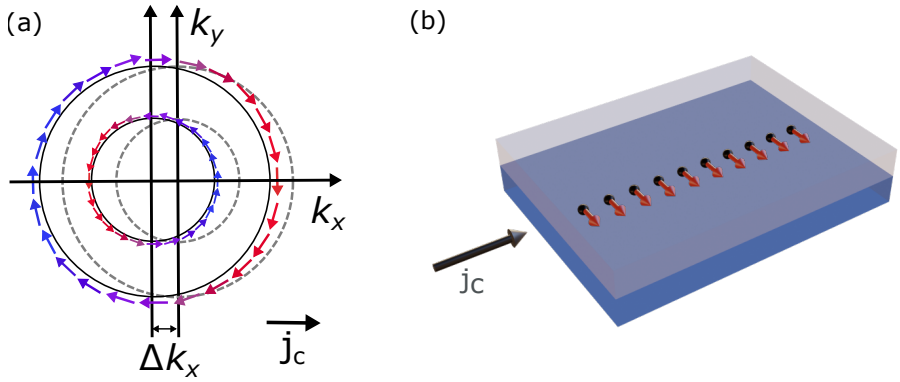

Figure 3.2: (a) Principle of the Edelstein effect at a Rashba interface. (b) Schematic of the SREE where a specific momentum state is associated with a specific spin orientation due to spin momentum locking.

3.1.2 Spin Hall Magnetoresistance

MR refers to the change in electrical resistance of a metallic magnetic material due to the presence or orientation of a magnetic field [163]. Several microscopic mechanisms can give rise to MR, depending on the material system. A notable example relevant to this work is the SMR, first reported in 2013 in bilayer systems composed of a normal metal with strong SOC and an adjacent magnetic insulator [145, 164]. The SMR enables the electrical detection of the magnetic orientation in bilayers consisting of a HM and a magnetic insulator. In such systems, the resistance measured in the HM layer varies systematically with the relative orientation between the magnetization of the magnetic insulator and the applied charge current [165].

The SMR arises from the combined action of the SHE and the iSHE in the HM, together with angular momentum transfer across the HM/magnetic insulator interface. When a charge current $\boldsymbol{j}_c$ is injected into the HM layer, the SHE generates a transverse spin current $\boldsymbol{j}_s$, as discussed in Sec. 3.1.1, and a spin accumulation $\boldsymbol{\sigma}$ builds up at the interface between the HM and the magnetic insulator. Depending

on the relative alignment of $\boldsymbol{\sigma}$ and the order parameter, i.e. magnetization $\boldsymbol{M}$ or the Néel vector $\boldsymbol{n}$ of the adjacent magnetic insulator, the spin accumulation can either be reflected or absorbed. In case of a parallel alignment $\boldsymbol{\sigma} \parallel \boldsymbol{M}$ ($\boldsymbol{\sigma} \parallel \boldsymbol{n}$), the generated spin accumulation is predominantly reflected at the interface and converted back into a charge current via the iSHE, enhancing the net current in the HM and thereby reducing the measured resistance as illustrated in Fig. 3.3(a). For a perpendicular alignment, $\boldsymbol{\sigma} \perp \boldsymbol{M}$ ($\boldsymbol{\sigma} \perp \boldsymbol{n}$), the spin accumulation can transfer angular momentum to the magnetization via spin-transfer torque (STT), leading to partial absorption of the spin current. This reduces the spin accumulation available for back-conversion to a charge current, lowering the net current and increasing the measured resistance as shown in Fig. 3.3(b). Since $\boldsymbol{\sigma} \perp \boldsymbol{j}_c$, the result is an enhanced resistivity for $\boldsymbol{M} \perp \boldsymbol{j}_c$ ($\boldsymbol{n} \perp \boldsymbol{j}_c$) and a reduce resistivity for $\boldsymbol{M} \parallel \boldsymbol{j}_c$ ($\boldsymbol{n} \parallel \boldsymbol{j}_c$) [165].

The theoretical framework developed for describing the SMR in AFMs [166–168] predicts for the longitudinal (ΔR_{xx}) and transverse (ΔR_{xy}) resistance changes

$$\frac{\Delta R_{xx}}{\bar{R}} \propto \frac{\Delta\rho}{\rho}\langle n_y^2 \rangle, \tag{3.3}$$

$$\frac{\Delta R_{xy}}{\bar{R}} \propto \frac{\Delta\rho}{\rho}\langle n_x n_y \rangle. \tag{3.4}$$

$\bar{R}$ is the mean longitudinal resistance value to normalize the changes, x denotes the direction parallel to the applied charge current and y the in-plane direction perpendicular to the current. The quantities n_x and n_y are the respective components of the Néel vector $\boldsymbol{n}$, and $\langle ... \rangle$ denotes an average over the probed magnetic domain structure [167]. The SMR coefficient $\frac{\Delta\rho}{\rho}$ is a measure for the SMR response of a system with resistivity ρ. Within the framework of spin-diffusion theory, it can be modeled as

$$\frac{\Delta\rho}{\rho} = \theta_{\mathrm{SH}}^2 \frac{\lambda_S}{d} Re\left[\frac{2\lambda_S G_{\uparrow\downarrow} \tanh^2(\frac{d}{2\lambda_S})}{\sigma + 2\lambda_S G_{\uparrow\downarrow} \coth^2(\frac{d}{\lambda_s})}\right]. \tag{3.5}$$

It depends on the electrical conductivity σ, the spin Hall angle θ_{SH}, the spin-diffusion length λ_s, the metallic layer thickness d, and the spin mixing conductance $G_{\uparrow\downarrow}$, which quantifies the efficiency of spin transport across the metal/magnet interface [165].

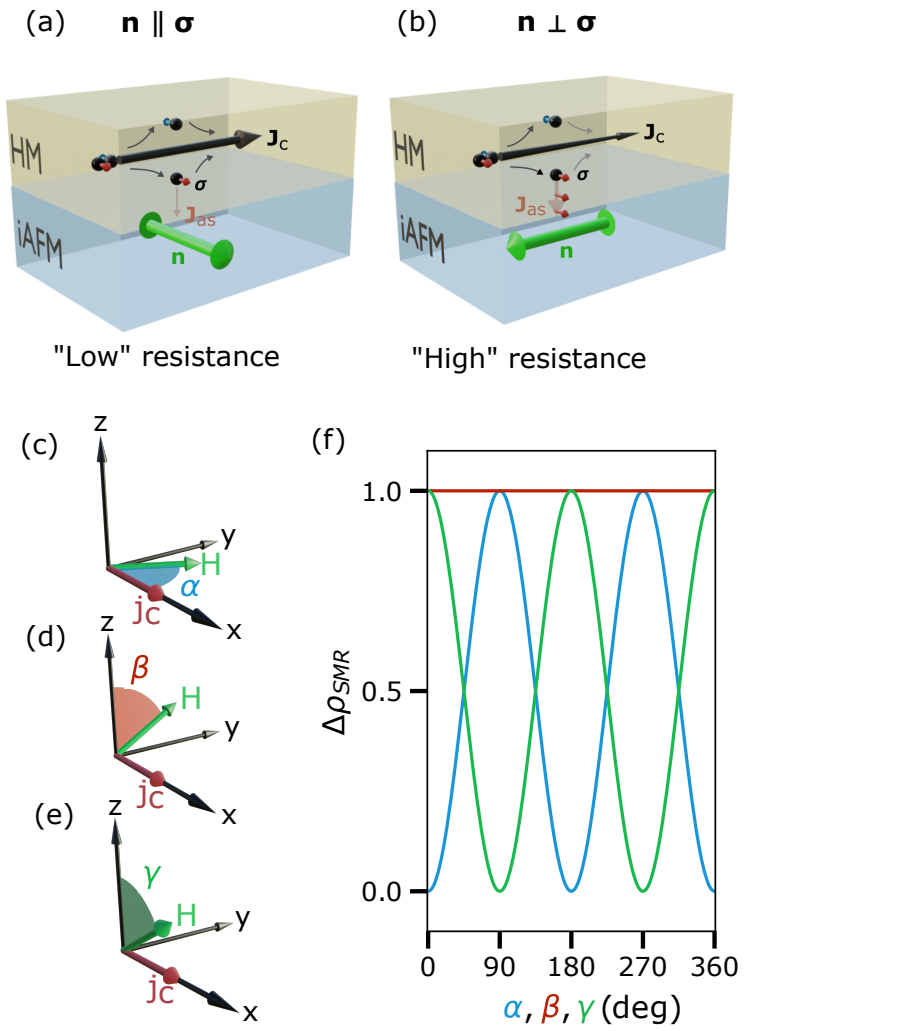

Figure 3.3: Illustration of the SMR effect in a HM/AFM insulator bilayer. A charge current $\boldsymbol{j}_c$ in the HM generates a transverse spin current $\boldsymbol{j}_s$ and a non-equilibrium spin accumulation $\boldsymbol{\sigma}$ at the interface to the magnetic insulator via the SHE, if the metal shows sufficiently strong SOC. (a) In the case of parallel alignment of electron spin accumulation $\boldsymbol{\sigma}$ and Néel vector $\boldsymbol{n}$, the spin current is reflected and contributes to the total charge current $\boldsymbol{j}_c + \boldsymbol{j}_c^*$ (low resistive state). (b) For a perpendicular alignment of $\boldsymbol{\sigma}$ and $\boldsymbol{n}$, the spin current is absorbed via STT and $\boldsymbol{j}_c^*$ is suppressed (high resistive state). (c) - (e) Definition of the $\alpha-$, β and $\gamma-$rotation angles, defining rotations in the xy-, yz- and xz-planes, respectively. (f) Ideal angular dependence of $\Delta\rho_{SMR_{xx}}$ in the three rotation planes for an AFM insulator as a function of the angle between the charge current and the magnetic order parameter.

The spin mixing conductance is generally complex, $G_{\uparrow\downarrow} = G_r + iG_i$. The real part G_r describes the dissipative absorption of spin current by the magnetic layer and is, therefore, the quantity that determines the observable SMR signal. In contrast, the imaginary part G_i represents a reactive, phase-shifting component that does not lead to net spin absorption and thus has no significant impact on the measured resistivity, but only on the phase of the spin accumulation.

Since the minimum in magnetic free energy arises for the Néel vector being oriented perpendicular to the applied magnetic field, the SMR is expected to show a 90° phase shift relative to the case of FM insulators. This prediction, however, assumes that the Néel vector can freely rotate with the applied magnetic field $\boldsymbol{H}$.

By convention, the SMR is defined as *positive* if it follows the same angular dependence as in YIG/Pt bilayers, where the effect was first observed [145], a behavior commonly found in most FMs. On the other hand, if the angular dependence is shifted by 90°, the effect is referred to as *negative* SMR [166]. Experimentally both cases have been reported in AFMs: positive SMR with a FM-like signature [169] as well as negative SMR with an AFM-like signature [168, 170]. The ideal negative SMR response of an AFM for a rotation of the magnetic field is shown in Fig. 3.3(f), while the the $xy-$, $yz-$ and $xz-$ rotation planes are defined in Figs. 3.3(c)-(e).

3.1.3 Orbital Angular Momentum Manipulation

Analogous to the spin current generation mechanisms (see Sec. 3.1.1), orbital angular momentum current can also be generated from charge current via the OHE and the orbital Rashba Edelstein effect (OREE). Despite the theoretical predictions of large orbital effects [171], the field has attracted significant attention only recently, due to experimental observations of large torques and magnetoresistance effects that cannot be explained within the framework of spin-based mechanisms [44, 172], yet they emerge from the orbital part of the electronic degrees of freedom.

OAM is an intrinsic property of electrons associated with circulating motion around the atomic nucleus, and within the atomic center approximation, each atomic site serves as a local center for orbital quantization. Transport of OAM in solids can thus be understood as the hopping of electrons between these sites, where both the local atomic character and the band structure contribute to the orbital angular momentum [173].

In crystalline solids, the electrostatic potential from surrounding atoms produces crystal field effects that strongly influence the OAM. These crystal fields lift the degeneracy of the atomic orbitals, tending to align the OAM along specific crystallographic axes and often leading to orbital quenching, in which the net orbital moment is reduced because the angular momentum of electrons averages to zero across the split orbitals [174, 175].

However, in certain materials, the orbital moment is only partially quenched. In CoO, for example, the Co^{2+} ions have incompletely filled t_{2g} orbitals, which retain some degeneracy. Combined with moderate SOC and small lattice distortions that do not fully lift this degeneracy, this allows a substantial residual orbital moment to persist [176–178].

3.1.3.1 Orbital Hall Effect

The OHE is a transport phenomenon in which an applied charge current generates a transverse flow of OAM without any accompanying charge current $\boldsymbol{j}_c$ or net charge displacement. This effect was first theoretically predicted in 2005 for Si [171]. Unlike the SHE, which relies on SOC to connect the spin of charge carriers to their motion, the crystal momentum of electrons naturally couples to their OAM. As a result, the generation of orbital currents does not require strong SOC and can, therefore, occur even in materials composed of light elements where SOC is weak [35, 39, 171].

The OHE can be defined within the framework of orbital textures in Bloch bands [37, 38]. In formal terms, the OHE is understood as a transverse orbital current response to a longitudinal electric field (see Fig. 3.4), with the orbital Hall angle θ_{OH} describing the proportionality between the two [35, 37, 39]:

$$\boldsymbol{j}_o \propto \theta_{\mathrm{OH}} \left(\boldsymbol{\sigma}_o \times \boldsymbol{j}_c \right), \tag{3.6}$$

where $\boldsymbol{j}_o$ denotes the transverse orbital current and $\boldsymbol{\sigma}_o$ is the unit vector along the orbital polarization direction. The orbital Hall angle is a function of the orbital Hall conductivity σ_{OH} and the conductivity σ of a material $\theta_{\mathrm{OH}} = \frac{\sigma_{\mathrm{OH}}}{\sigma}$.

Orbital Hall conductivities were theoretically calculated for various elemental materials across the periodic table [39]. The results indicate that significant orbital Hall conductivities are not limited to HM elements with strong SOC, but are instead widespread among transition metals and other materials. Notably, θ_{OH}

values are predicted to be one to two orders of magnitude larger than spin Hall conductivities [39].

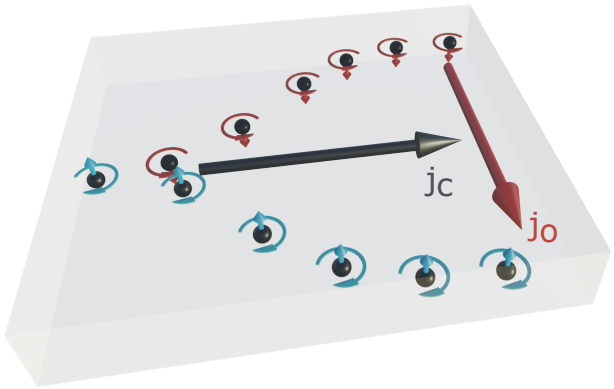

Figure 3.4: Illustration of the orbital Hall effect. A flowing charge current $\boldsymbol{j}_c$ is converted into a transverse orbital current $\boldsymbol{j}_o$.

Microscopically, the OHE can originate from orbital hybridization in the electronic band structure. In materials with strong mixing of atomic orbitals, such as *p*-*d* or *d*-*d* hybridization, the resulting Bloch states display a momentum-dependent orbital texture, meaning that the expectation value of the OAM, $\langle L_z \rangle(\boldsymbol{k})$, varies across the Brillouin zone [37, 38]. This orbital texture is often odd in momentum

$$\langle L_z \rangle(\boldsymbol{k}) = -\langle L_z \rangle(-\boldsymbol{k}), \tag{3.7}$$

as a consequence of time reversal symmetry, which reverses both momentum and orbital angular momentum. When an electric field is applied, the distribution of the occupied states in momentum space is shifted, creating an imbalance between states carrying opposite OAM. This imbalance results in a net transverse orbital current $\boldsymbol{j}_o$, the signature of the OHE. This Berry curvature-based view effectively describes the intrinsic clean-limit OHE and allows for first-principles predictions of large orbital Hall conductivities [37, 38].

Within the framework of gauge-invariant quantum kinetic theory for multiband electron systems [179], orbital currents arise both from the intrinsic Berry curvature of Bloch bands as well as from interband quantum coherences generated by spatial or temporal gradients of the carrier distribution. This framwork promises to be applicable to realistic device structures, as it naturally incorporates

the effects of weak disorder, finite-size geometry, and boundary conditions [180]. In systems with time reversal and inversion symmetry, quantum kinetic theory reveals that the physically measurable OHE current is purely intraband and describes actual orbital transport in the bulk. Observed orbital accumulation at the edges of such samples arises predominantly from locally generated interband quantum coherences, processes unrelated to the diffusion of a bulk OHE current. In this model edge OAM accumulation does not, in general, serve as direct evidence for the presence of a bulk orbital Hall current [180].

Thus, while Berry curvature models associate edge effects intimately with a bulk OHE, the quantum kinetic approach demonstrates that edge accumulation and Hall current are, in general, distinct phenomena and only carefully designed experimental probes can distinguish between true orbital Hall transport and boundary-induced edge effects [180]. Thus, further experimental studies are required to understand the origin of orbital current.

3.1.3.2 Orbital Rashba Edelstein Effect

The OREE describes the generation of a non-equilibrium OAM from an applied charge current in systems with broken inversion symmetry [181]. Analogous to the SREE, the OREE originates from a momentum-dependent orbital texture in the band structure, which arises from inversion-symmetry breaking and is further influenced by interfacial electric fields [181]. While the SREE relies on SOC to lock spin to momentum, the OREE stems from momentum-orbital locking that can exist even in materials with weak SOC [41, 182].

At an interface, inversion symmetry breaking produces an interfacial electric field, similar to the situation in the SREE. This field modifies the mixing between atomic orbitals (hybridization), leading to a momentum-dependent orbital polarization as shown in Fig. 3.5. Such hybridization can involve s-p character [183] or p-d character [184]. The orbital Rashba coupling strength depends sensitively on the orbital composition of the interfacial states and is often enhanced at interfaces with oxides due to their large difference in electronegativity and the resulting strong potential gradient [184].

Cu/CuOx interfaces have been theoretically predicted to induce a pronounced OREE [184]. In this system, the interfacial orbital texture originates from p-d hybridization between oxygen and copper states, which is strongly modified by the

presence of the interfacial electric field. It was shown that a large OREE can occur under the assumption of fcc metallic Cu covered by a single oxygen monolayer [184]. Theoretical models suggest that such a configuration yields substantial orbital Rashba splitting, enabling the efficient conversion of charge current into orbital polarization.

Experimental evidence for orbital currents was reported in Cu/CuOx in 2020 [44], supporting the idea that interfaces between low-SOC metals and oxides can serve as efficient orbital current sources.

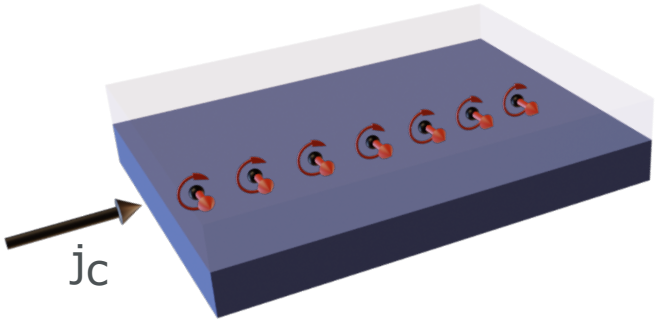

Figure 3.5: Schematic of the OREE. A charge current $\boldsymbol{j}_c$ is converted into an orbital momentum accumulation due to inversion symmetry breaking at the interface.

3.1.4 Orbital Magnetoresistance

In direct analogy to the SMR (see Sec. 3.1.2), the concept of OMR has recently emerged as a novel mechanism by which OAM current may influence charge transport in magnetically ordered systems. In this context, the OHE or OREE generate an orbital accumulation at the interface between a nonmagnetic metal and a magnetic insulator, which can interact with the magnetization and yield a magnetization-dependent resistance [185].

The microscopic mechanism underlying the coupling between OAM and the magnetic layer is an active area of research. In principle, the accumulated OAM may couple directly to either spin or orbital moments within the magnetic layer [185, 186]. This interaction is expected to become particularly relevant in materials with a significant orbital contribution to the total magnetization, such as rare-earth elements [187, 188], or in cases where orbital quenching is suppressed, such as in CoO [176–178]. To date, a direct orbital-to-orbital coupling has not been unambiguously observed, and its precise mechanism remains unclear.

Thus, the interaction of OAM with magnetic layers has primarily been observed via an orbital-to-spin interconversion process [44, 46]. In systems with finite SOC, the orbital accumulation can be partially converted into spin angular momentum through SOC, which subsequently interacts with the magnetic moment via the conventional SMR mechanism. This orbital-to-spin conversion may occur in a strong SOC interlayer such as Pt [44, 46], within the magnetic material itself [46], or across an AFM CoO layer that efficiently transmits and converts orbital angular momentum into spin torque [189].

3.1.5 Other Magnetoresistance Effects

In addition to the SHE and OHE and their associated magnetoresistance phenomena, other Hall- and magnetoresistance-related effects may also contribute to the measured signal, each modifying the electrical resistance in distinct ways. These effects exhibit different symmetries with respect to the magnitude and direction of the applied magnetic field as well as the magnetization direction of the material. The ordinary Hall effect, for example, depends directly on the applied magnetic field.

Other effects depend indirectly on the magnetization of the material, such as the anisotropic magnetoresistance (AMR), planar Hall effect (PHE) and the anomalous Hall effect (AHE) [123]. All occur in materials with FM moments. In materials with in-plane magnetized moments, an in-plane charge current will cause a longitudinal and a transverse Hall-like effect via the AMR and PHE, respectively. These effects originate from spin-dependent scattering of charge carriers, which depends on the in-plane angle between the magnetization and the charge current direction [190].

AHE arises from the combined action of SOC and spontaneous magnetization and was first observed in out-of-plane magnetized iron [123]. Even in the absence of an external magnetic field, a transverse voltage can be generated, which reverses sign when the magnetization of the iron is inverted [123]. This causes variations in the longitudinal resistance and can coexist with SHE- or OHE-induced signals.

A further effect to consider is the Hanle MR. It is observed in nonmagnetic conductors with strong SOC. In this case, a transverse magnetic field modulates the spin accumulation via the Hanle precession mechanism [191], producing characteristic magnetoresistive signatures even in the absence of magnetic order. The

application of a large magnetic field perpendicular to the spin polarization yields a precession of the spin moments at the edges of the layer and as a consequence a dephasing of the spin moments.

The relative magnitudes of these additional effects depend strongly on material properties, sample geometry, and measurement configuration. In some cases, they may superimpose upon or obscure the desired SHE- or OHE-related signals. Consequently, careful experimental separation of contributions, through material characterization, optimized measurement geometry and symmetry analysis is essential for the accurate interpretation of magnetotransport measurements in SOC systems.

3.2 Spin Torques

Over the past decade, the electrical switching of AFMs via spin torques has been the subject of intense investigation [47–49, 192]. In the context of spin-torque-driven switching in AFMs, two distinct types of torques must be distinguished.

Staggered torques act with opposite sign on the two magnetic sublattices. Staggered bulk torques are crucial for the electrical switching of metallic AFMs with broken inversion symmetry, such as Mn_2Au and CuMnAs [30, 193, 194].

In contrast, in insulating AFMs, such as CoO, non-staggered interfacial torques can induce a reorientation of the Néel vector. These torques act individually on both sublattices. A SOT acting on sublattice $\boldsymbol{M}_1$ can be expressed as [33]

$$\boldsymbol{\tau} = \tau_{\parallel}^{1}\boldsymbol{M}_1 \times (\boldsymbol{\sigma} \times \boldsymbol{M}_1) + \tau_{\perp}^{1}\boldsymbol{M}_1 \times \boldsymbol{\sigma}, \tag{3.8}$$

where $\boldsymbol{\sigma}$ represents the spin polarization direction, $\tau_{\parallel}^{1}$ ($\tau_{\perp}^{1}$) represents the magnitude of the torque component parallel (perpendicular) to the ($\boldsymbol{M}_1$; $\boldsymbol{\sigma}$) plane.

The first term in Eq. 3.8 corresponds to the antidamping-like torque, while the second term corresponds to the field-like torque. Their respective influence on the AFM order is illustrated in Fig. 3.6 [33].

A field-like torque acting equally on both sublattices has an effect equivalent to an external magnetic field applied perpendicular to the Néel vector (Fig. 3.6(a)). This induces a canting of the AFM order without a net reorientation. In this case, the torques τ_{H} exerted by the external field on $\boldsymbol{M}_1$ and $\boldsymbol{M}2$ are opposite in sign and exactly cancel the exchange torque τ_{Ex} between the sublattices. On the other

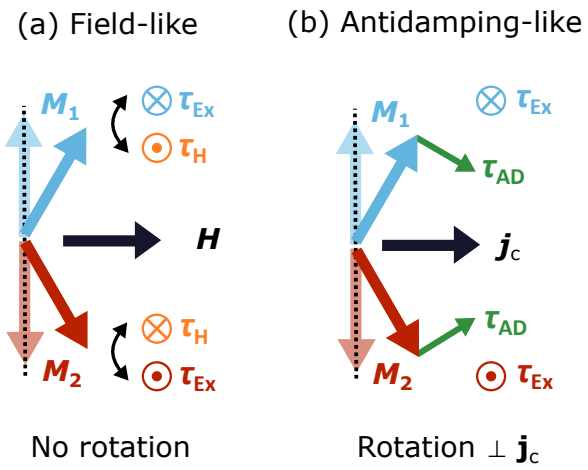

Figure 3.6: Mechanisms of (a) field-like and (b) antidamping-like torques acting on a collinear AFM with magnetic moments $\boldsymbol{M}_1$ and $\boldsymbol{M}_2$. Here, τ_{H} denotes the torque exerted by an external magnetic field, τ_{AD} represents the effect of the antidamping-like torque, and τ_{Ex} corresponds to the exchange torque arising from the mutual interaction between the two sublattice magnetizations.

hand, an antidamping-like torque ($\propto \boldsymbol{M}_1 \times (\boldsymbol{\sigma} \times \boldsymbol{M}_1)$) also cants the sublattice moments, but here τ_{Ex} does not compensate the torque (Fig. 3.6(b)). As a result, a rotation of the AFM order becomes possible [33]. In AFM/HM bilayers, such non-staggered antidamping-like torques are predicted to enable a reorientation of the Néel vector [192, 195]. As discussed in Sec. 3.1.1, a charge current in the HM layer is converted into a transverse spin current via the SHE. Part of this spin current is absorbed by the magnetic layer. The absorption of the spin components perpendicular to the sublattice magnetization $\boldsymbol{M}_i$, exerts a damping-like spin torque acting on the sublattice magnetizations [165, 196]. The direction of the acting torque is fixed by the orientation of $\boldsymbol{\sigma}$, implying that electrical switching of the AFM order is unidirectional with respect to the applied current pulse $\boldsymbol{j}_c$.

For switching driven by antidamping-like torques, several microscopic mechanisms have been proposed. These include coherent rotation of the Néel vector and current-induced domain wall motion [48, 192]. Another possibility is a combined effect in which the antidamping-like spin torque acts directly on the domain wall while the spin current modifies the effective anisotropy. This anisotropy change creates an energetic imbalance between domains, leading to a ponderomotive force that pushes domain walls toward the energetically unfavorable domain orienta-

tion [49]. Chirality-dependent switching has also been suggested [197]. However, high-resolution imaging experiments have so far found no evidence of chiral domain walls in these systems [198].

3.3 Thermal Effects

An electrical current flowing through a material with finite resistance inevitably generates heat, which can give rise to thermally induced effects. In the following, we first discuss the concept of Joule heating and its influence on electrical measurements in AFM/HM bilayers. We then address thermomagnetoelastic switching, a mechanism by which thermal effects can induce a reorientation of the Néel vector in electrical switching experiments.

3.3.1 Joule Heating

The electrical manipulation of insulating AFMs requires large current densities on the order of $10^{11}\ \frac{\mathrm{A}}{\mathrm{m}^2}$ in the adjacent HM layer [199]. Such high current densities cause significant Joule heating, as part of the electrical energy of the charge carriers is dissipated as heat due to scattering processes at crystal defects, interfaces, and phonons. The dissipated power P scales with [200]

$$P \propto \boldsymbol{j}_c^2 R, \tag{3.9}$$

where $\boldsymbol{j}_c$ is the applied charge current and R the device resistance. Joule heating can, on one hand, assist electrical switching by thermally overcoming anisotropy barriers between magnetic states [201], but on the other hand may also lead to irreversible device degradation through electromigration and material diffusion [199, 202].

These non-magnetic effects from heating in the adjacent HM layer can strongly influence the measured resistance in switching experiments [203, 204]. It is, therefore, essential to characterize and subtract the non-magnetic background changes to the resistivity signal in order to isolate the purely magnetic signal. For the CoO/Pt films investigated in this thesis, the non-magnetic contribution was found to scale linearly with the number of applied current pulses, in agreement with observations for NiO/Pt [205]. By subtracting this linear contribution from the measured SMR response, the purely magnetic contribution can be extracted.

It should be emphasized, however, that this linear approximation is a simplification of the complex underlying processes and may no longer be valid at very high current densities close to the device breakdown limit [205]. Thus, for the analysis of experimental results, it is best to limit the applied current pulses to a regime where no irreversible changes are caused.

3.3.2 Thermomagnetoelastic Switching

In materials exhibiting strong magnetoelastic coupling, electrical current pulses with high current densities can induce switching of the Néel vector via a thermomagnetoelastic mechanism, distinct from the SOT-driven switching discussed in Sec. 3.2.

The applied electric current pulses do not only generate Joule heating within the structured HM layer but also produce inhomogeneous distributions of heat and strain within the AFM layer [200]. Such strain gradients break the degeneracy between different magnetic easy axes, thereby facilitating the reorientation of the Néel vector [51]. However, it is important to emphasize that inhomogeneous strain alone is insufficient to drive the switching process. Adequate heating is also necessary to overcome the magnetic anisotropy barriers [51].

Unlike SOT-induced switching, which denotes on interfacial effects and scales inversely with the thickness of the AFM layer, thermomagnetoelastic switching is a bulk phenomenon insensitive to the layer thickness.

The spatial distribution of strain is determined both by the device geometry and the direction of the applied current pulse [50, 51, 200]. Consequently, the switching direction is determined not only by the current direction, as in SOT-based switching, but also by the complex spatial distribution of current-induced heat and strain [51]. This can lead to striking phenomena such as opposite switching signs arising from different contact geometries despite identical current flow directions at the device center, as illustrated in Fig. 3.7. Furthermore, thermomagnetoelastic switching can vary spatially within a single device, producing regions with different switching behavior. Notably, if heat and strain gradients are sufficiently strong, switching can even be induced in areas where no current is flowing [51].

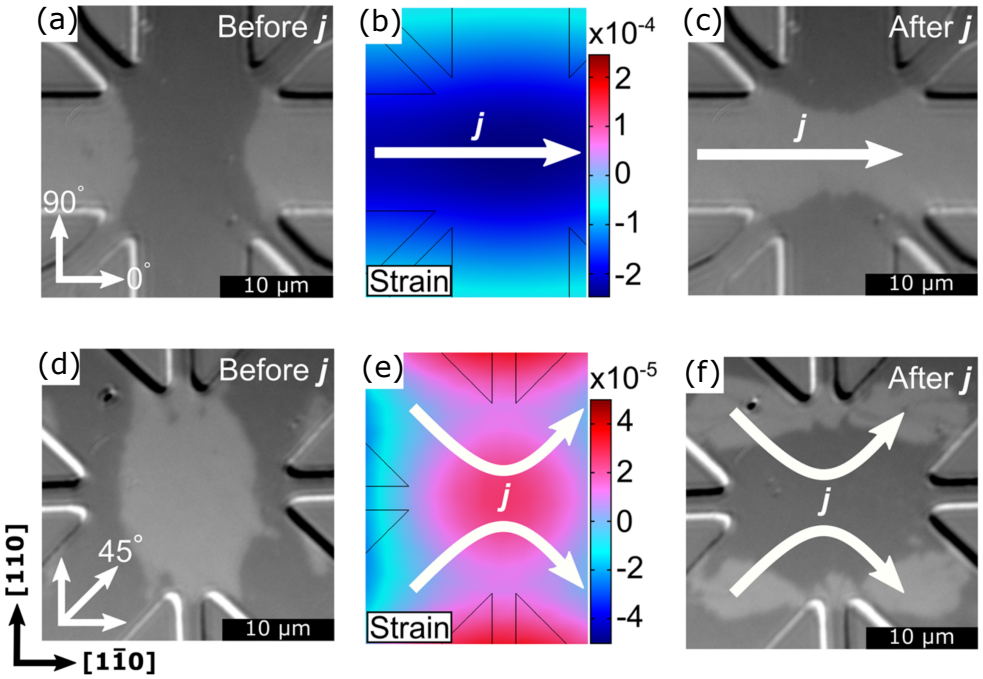

Figure 3.7: Comparison of the switching between different geometries. (a) Initial domain structure in the [110] star device and (b) simulations of the current-induced strain ϵ differences between the easy axes ($\epsilon_{[1\bar{1}0]} - \epsilon_{[110]}$) for a straight pulse along [1$\bar{1}$0] direction resulting in the domain structure shown in (c) after the application of five pulses in the direction indicated by the arrow. (d) The initial domain structure in a [100] star device and (e) the strain difference for X-shaped pulses along [1$\bar{1}$0], resulting in the domain structure shown in (f) after the application of five pulses. Adapted with permission from Ref. [51]. Copyright 2020 American Chemical Society.

4 Material and Experimental Methods

The investigation of spin and orbital effects in AFM thin-film systems requires the growth and fabrication of high quality films and advanced techniques to characterize, electrically measure and image the films.

This chapter first introduces CoO as a material system and discusses the sample fabrication and characterization. Then electrical measurements are discussed and the measurement setup is introduced before the imaging of the AFM texture by X-ray based microscopy is discussed.

The methods described in this chapter follow established procedures outlined in several prior theses and reviews [34, 206–212]; these sources have served as the foundation for the methodological approach adopted here.

4.1 CoO

CoO is an insulating 3*d* transition metal oxide, ordered in the NaCl crystal structure which consists of a diatomic base with an fcc lattice structure. Its properties have been extensively investigated since the mid-20$^{\text{th}}$ century [176, 213–216]. Early neutron diffraction experiments indicated a magnetic structure similar to those of other well-known 3*d* transition metal oxides such as NiO [71]. However, it is now understood that CoO exhibits different magnetic properties in several aspects, such as structure, domain formation and orbital quenching [70, 71, 177, 217].

In its bulk form, CoO has a Néel temperature close to room temperature (291 K) [213, 218, 219]. Experimental research on the crystallographic structure has revealed a 1.2% tetragonal distortion of the fcc lattice below the Néel temperature [213, 220–222]. However, the exact spin structure of CoO remains a topic of ongoing

debate. Neutron diffraction measurements have not provided definitive evidence, leading to the proposal of various models [223]. Initially, a collinear spin structure was proposed analogous to NiO, with FM spin coupling within the {111}-planes and AFM coupling between neighboring planes [71, 213, 224] as shown in Fig. 4.1. However, the observed tetragonal distortion of the lattice led to the consideration of a non-collinear spin structure within a multi-spin-axis model [225–227]. Later studies demonstrated that a tetragonal distortion can occur even in a collinear spin alignment, provided that an additional monoclinic distortion is present [70, 219]. After this monoclinic distortion was experimentally observed in CoO, the collinear magnetic structure became widely accepted [90, 219, 228–230]. Nevertheless, there are still new studies proposing a non-collinear spin structure [92, 231, 232].

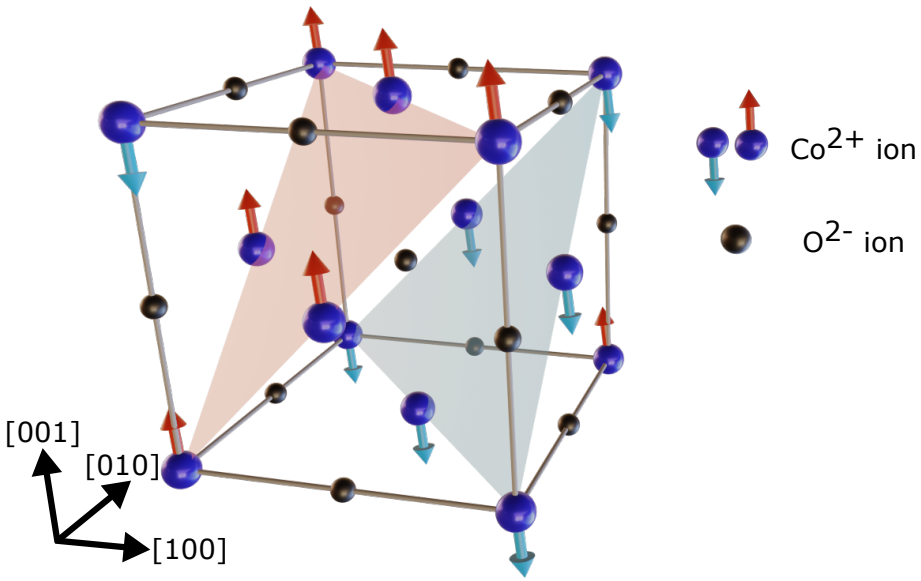

Figure 4.1: Illustration of the spin structure of CoO. The spins are coupled ferromagnetically within the {111}-planes and antiferromagnetically between the planes. The individual spins are aligned along the [117] direction.

Due to the tetragonal distortion along one of the three cubic axes, three distinct {111}-planes, referred to as twin-domains (T-domains), can form in CoO [103]. Within each of these T-domains, the spins can align into one of three equivalent ⟨117⟩ directions, forming spin-domains (s-domains) [213], as exemplarily shown for [117] in Fig. 4.1. The exact magnetic structure, especially when investigating CoO thin films, depends on the growth conditions as well as on the chosen substrate material and orientation, and the resulting induced strain. [103, 233]. While

compressive strain on CoO(001) favors in-plane spin alignment, tensile strain induces out-of-plane canting [234, 235]. When CoO with a lattice parameter of 426 pm is grown on an MgO(001) substrate, the +1.2% lattice mismatch results in a compressive strain on the CoO layer [234, 236]. This leads to spin moments aligning along the ⟨110⟩ directions, forming a fourfold in-plane magnetic anisotropy [50, 237, 238], while also increasing the Néel temperature to above 300 K [50].

In addition to its spin degree of freedom, CoO exhibits an orbital degree of freedom. Theoretical studies indicate that the OAM of the Co^{2+}-ions is only partially quenched by the cubic crystal field, resulting in an effective OAM of $\boldsymbol{L} = 1$ [177]. Several studies predict that the orbital moment is sizable in comparison to the spin moment, with values ranging from 0.5 to 2.05 μ_B, accounting for up to 45% of the total moment per Co atom [176–178]. X-ray experiments report an L/S ratio of up to 0.95 [239]. The presence of unquenched OAM in CoO contributes to both the staggered magnetization and magnetic anisotropies [121]. However, the relative orientation of the orbital and spin moments remains debated, with theoretical studies predicting both parallel and antiparallel alignment [240, 241].

4.2 Sample Fabrication and Characterization

The growth of materials is often challenging and depends on numerous factors [242]. While commercially available samples and companies specializing in materials growth do exist, obtaining non-standard samples or thin films with specific thicknesses and tailored properties often requires growing them independently. To achieve the desired properties and appropriately adjust the growth parameters, it is necessary to repeatedly characterize the crystallographic and magnetic properties of the films. A common set of tools for this purpose includes X-ray analysis techniques such as X-ray reflectometry (XRR) and X-ray diffraction (XRD). Preparation of optimized films for subsequent measurements involves patterning of structures.

The following section provides a brief overview of the principles of sputter deposition, with a particular focus on the growth of the CoO thin films used in this thesis. Subsequently, the employed X-ray analysis techniques are discussed, followed by an introduction to the structuring of thin films via optical lithography and electron beam lithography (EBL).

4.2.1 Sputter Deposition of Thin Films

A widely used technique for preparing high-quality thin film samples for research and industrial applications is *sputtering* [243–245]. It is favored for its high deposition rates [206, 245, 246]. However, the growth of high-quality thin films remains challenging due to the numerous process parameters that must be carefully optimized [242]. In the context of this work, such optimization is crucial for the formation of large AFM domains [49, 247] and the ability to manipulate them.

Sputtering relies on the ablation of material from a target, followed by the deposition of the ejected target atoms onto a substrate [206, 246]. The process takes place under vacuum conditions to avoid contaminations in order to improve film quality. The most basic variant of this technique is direct current (DC) sputtering. Figure 4.2(a) shows a schematic of a DC sputtering setup. During the process, a noble gas, typically argon, due to its chemical inertness and high sputter yield (rate at which material is removed from the target), is introduced into the vacuum chamber [248]. A large DC voltage of 200 V is applied between the target (cathode) and the substrate (anode), accelerating free electrons. These electrons collide with Ar atoms, leading to ionization and photon emission, which generates a plasma [249]. The resulting Ar^+ ions, being positively charged, accelerate toward the negatively charged target. Upon impact, they initiate a collision cascade at the target surface, ejecting atoms [250, 251]. These atoms are emitted radially and partially deposit on the substrate surface.

Despite its simplicity, DC sputtering has limitations, including a relatively low sputter yield and surface charging effects when used with insulating targets [251]. These issues can be mitigated by replacing the DC voltage with an alternating voltage, as in radio frequency (RF) sputtering, which typically operates at a RF of 13.56 MHz [246, 252]. The alternating electric field increases the collision rate between electrons and Ar atoms, thereby enhancing ionization and improving the sputter yield. This results in higher deposition rates and allows the process to operate at lower gas pressures [253].

An even higher sputter rate can be achieved via magnetron sputtering, in which magnetic fields are used to trap electrons near the target [206, 246]. A basic magnetron sputtering chamber is shown in Fig. 4.2(b). In this configuration, permanent magnets generate a magnetic field that confines electrons in circular orbits above the target surface, further increasing their collision rate [206]. However,

this setup leads to inhomogeneous target erosion, with material being preferentially ablated along the electron path [206]. Additionally, magnetic targets can interact with the applied magnetic field, reducing the efficiency of the magnetron sputtering process. This issue can be addressed by using more advanced magnet geometries [252].

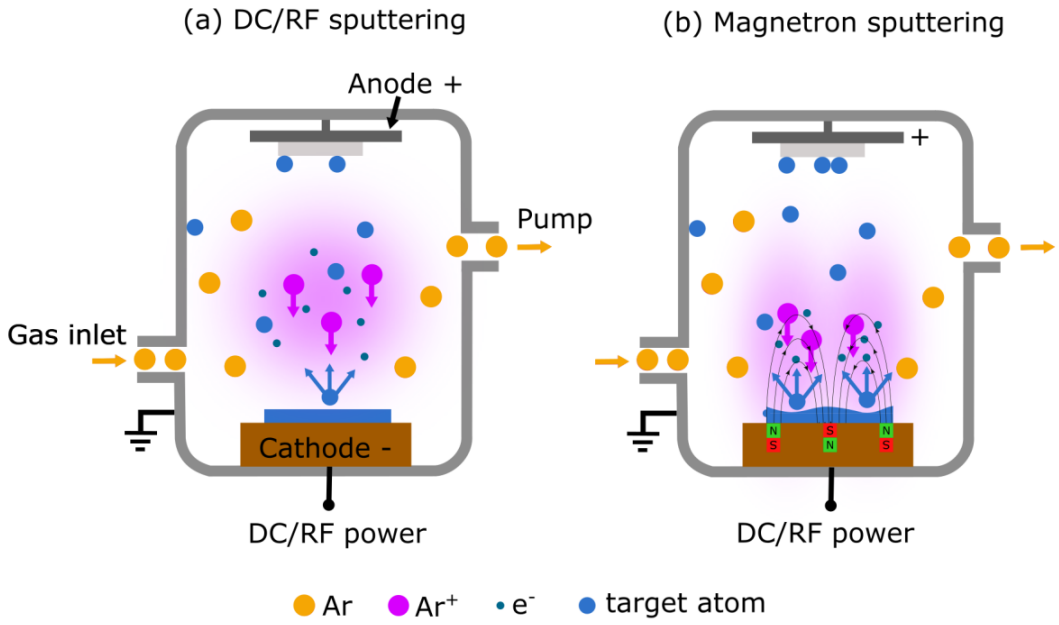

Figure 4.2: Schmatic of different sputtering principles. (a) Basic DC/RF sputtering in which DC or RF voltages can be applied to the target cathode and Ar atoms (orange) are ionized and a plasma is formed. (b) In a magnetron sputtering system a magnetic field confines the Ar^+-ions (pink) and electrons (black), leading to an increased sputter yield, and increases the deposition of target atoms (blue) on the substrate.

4.2.1.1 CoO/Pt Thin Film Growth

The growth of CoO/Pt, CoO/Cu, CoO/Cr, CoO/Ti and CoO/Cu/Pt thin film multilayers is carried out using the ULVAC QAM-4 automated sputtering system of the research group of Prof. Dr. Eiji Saitoh at Tokyo University, Japan. The system enables automated growth of multilayer structures and features separate chambers for the sputtering of magnetic and non-magnetic materials to prevent cross-contamination. It also includes an automated transfer mechanism for moving samples between chambers.

The AFM CoO layer is deposited via reactive magnetron sputtering from a Co

target, with oxygen gas being introduced into the sputtering chamber in addition to Ar [254, 255]. The oxygen flow rate controls the thin-film growth rate, influences the film structure and affects adatom diffusivity [255]. During the deposition process, Co oxidizes with O_2 at the cathode surface and the substrate to form CoO [206, 252]. An illustration of the sputtering chamber for magnetic materials is shown in Fig. 4.3.

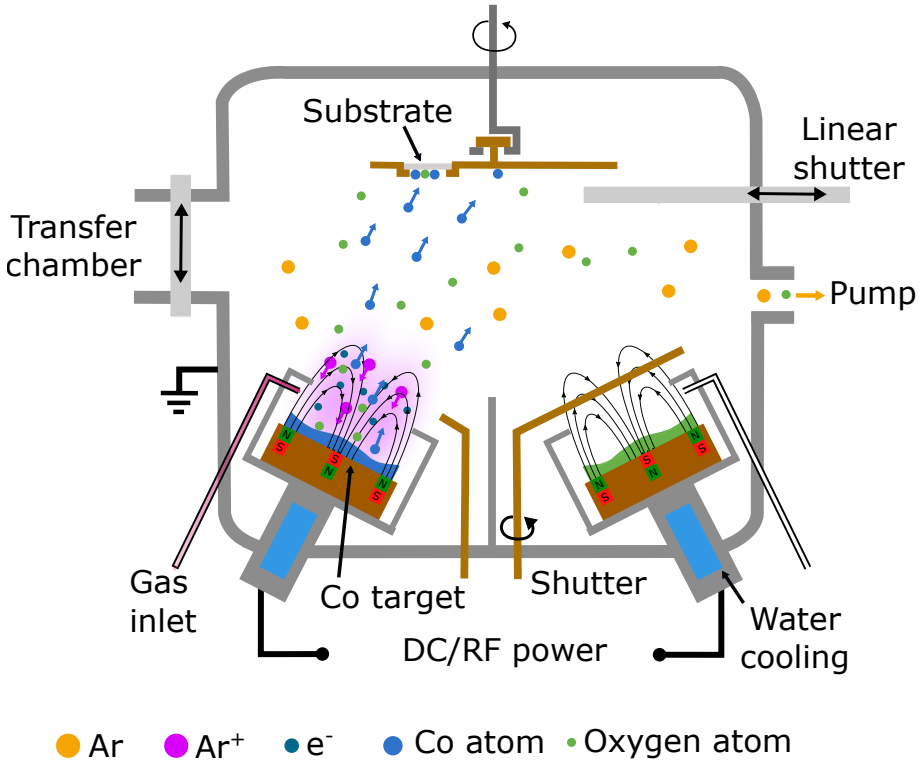

Figure 4.3: Sketch of the sputter chamber for magnetic materials of the ULVAC QAM-4 automated sputtering system of the research group of Prof. Dr. Eiji Saitoh at Tokyo University, Japan.

The substrates are positioned face-down on a rotating copper holder above the sputter targets. The sample holder temperature is adjustable to optimize growth conditions. The chamber contains four magnetic sputter targets, all arranged at an oblique angle to minimize surface roughness in the deposited films [252]. The target holders can operate with either DC or RF voltage. Deposition times are automatically controlled using shutters positioned above the targets. When varying film thicknesses on a single substrate (preparation of wedges), a linear shutter can be placed in front of the substrate, in which case the rotation of the substrate

holder must be disabled. The magnetic sputtering chamber is connected to a similar chamber dedicated to non-magnetic materials via a transfer chamber. This allows for the sequential deposition of layers such as Pt, Cu, Cr or Ti. Detailed process parameters and growth recipes are provided in the Appendix A.1.

4.2.2 X-ray Analysis

The crystallographic order, lattice parameter and mosaicity of the thin films can be analyzed using XRD. For this purpose, a Bruker D8 DISCOVER X-ray diffractometer was used [256], equipped with a parallel monochromatic Cu K_α X-ray beam of wavelength $\lambda(K_\alpha) = 0.154\,\text{nm}$ [257]. The incident X-rays, characterized by a wave vector $\boldsymbol{k}_i$, strike the sample at an incidence angle θ with respect to an atomic plane, as illustrated in Fig. 4.4(a). The X-rays are reflected by the sample, resulting in a wave vector $\boldsymbol{k}_r$. The reflected X-rays are detected at the same angle of reflection as the angle of incidence, on the opposite side of the sample. The angle between the extension of the incident X-rays and the reflected X-rays is given by the scattering angle 2θ. When the scattering vector $\boldsymbol{Q} = \boldsymbol{k}_r - \boldsymbol{k}_i$ equals a reciprocal lattice vector $\boldsymbol{G}$, diffraction peaks become visible [258]. By varying the angle of incidence in a $2\theta - \theta$ scan, the crystal orientation can be identified [258]. The precise positions of the diffraction peaks in the spectrum are related to the lattice constant via the Bragg condition for constructive interference

$$n\lambda = 2d_{hkl}\sin(\theta), \tag{4.1}$$

with n being the diffraction order and d_{hkl} representing the lattice plane spacing associated with the Miller indices (hkl). Further characterization of the diffraction peaks can be performed using a *rocking curve* measurement. In this technique, the scattering angle 2θ, thus the angle between X-ray source and detector is kept constant, while the incident angle and the detection angle are varied. The width of the resulting peak provides information on the mosaicity and overall crystal growth quality [259].

For XRR, the sample is also irradiated by an X-ray beam, but under grazing incidence. In this case, smaller angles are used because the measurement probes interference from scattering centers that are farther apart. While XRD investigates the interference of adjacent atomic planes, XRR measures the interference of adjacent interfaces. If the atomic planes are not perfectly parallel to the interfaces, for

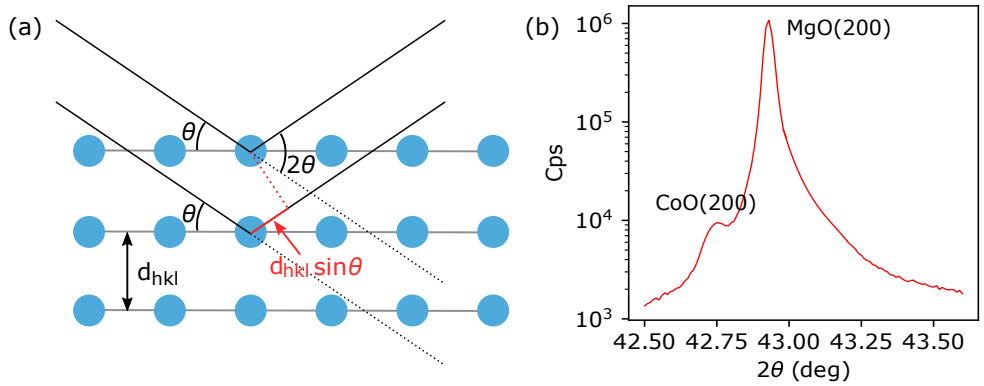

Figure 4.4: (a) Illustration of XRD from the crystal lattice including the definitions of angles and lattice spacing used to determine the condition of constructive interference. (b) Typical XRD scan for CoO grown on an MgO substrate.

example, in the case of vicinal surfaces, the sample orientation (i.e., the θ-2θ condition) must be adjusted when switching between XRR and XRD measurements. Below a critical angle θ_{crit}, the beam experiences total reflection. At angles slightly larger than θ_{crit}, the X-rays partially penetrate the material and may be reflected multiple times before exiting the material. The detected intensity exhibits an oscillatory behavior as a function of θ, known as Kissing fringes. The Kissing fringes are related to the film thickness as well as to the surface and interface roughness. Constructive interference of the reflected and refracted beams leads to intensity maxima, while destructive interference results in minima. Therefore, the oscillation width provides information about the film thickness, and both the amplitude of the Kissing fringes and the overall signal decay yield insights into the roughness of the film surface and the film/substrate interface.

The XRR data were fitted using the noncommercial software GenX, which applies the Parratt recursive method [260] in combination with the Névot-Croce roughness model [261].

4.2.3 Structuring of Thin Films

Defined micro- and nanometer-scale structures, required for the research presented in this work, necessitate the patterning of thin films following their deposition. This is achieved through *lithography*, meaning the transfer of a design onto a thin layer of photoresist [262]. Lithography can be performed using either optical lithography or EBL. The choice of photoresist depends on the type of ra-

diation used: ultraviolet (UV) light for optical lithography or electrons for EBL. For industrial applications, optical lithography has been optimized using extreme UV light, enabling the fabrication of structures down to 3 nm [263]. In contrast, university research typically employs EBL for patterning structures smaller than 1 µm.

The fundamental lithography process is illustrated in Fig. 4.5. First, the sample undergoes a multi-step cleaning process to remove any surface contamination. A polymer resist is then applied via spin-coating to achieve a thin, uniform layer (Fig. 4.5(a)). This is followed by a baking step at elevated temperatures to remove solvent residues and cross-link the polymer chains. For EBL on insulating substrates, an additional conductive resist layer is applied to mitigate charging effects.

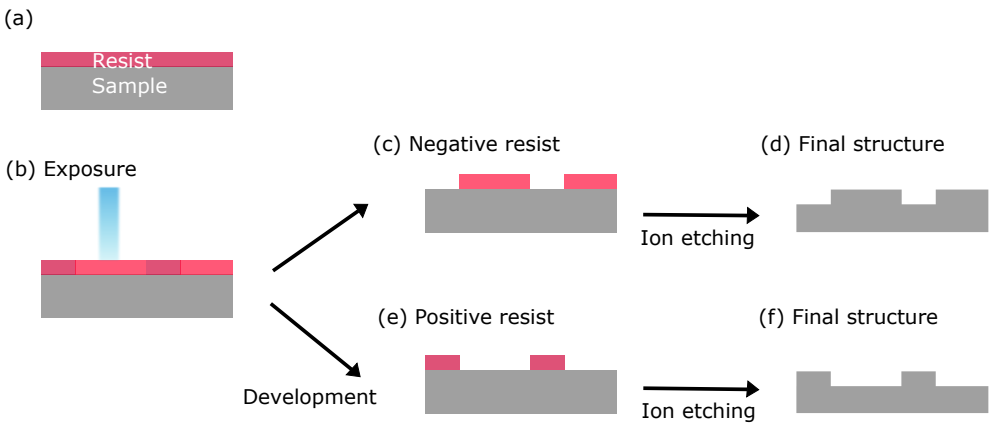

Figure 4.5: Cartoon sketch of the lithography process. A sample is (a) coated with resist and (b) exposed to electrons or light. (c) If negative resist is used, the unexposed regions of the resist are removed during development. (d) In an ion etching process argon plasma is used to etch regions not protected by resist anymore, resulting in the desired structure. (e) When positive resist is used the exposed regions of resist are removed in the development process resulting in a different structure (f) after ion etching.

Next, as shown in Fig. 4.5(b), the desired pattern is imprinted on the polymer. In optical lithography, this can be achieved using a structured glass mask with Cr patterns, which is placed in contact with the photoresist. When exposed to UV light, the exposed areas of the photoresist undergo a chemical reaction, while the unexposed regions remain unaffected. This method has a resolution limit of approximately 2 µm. A more advanced approach utilizes the Durham Magneto Optics Microwriter ML3 lithography system, equipped with a 385 nm photodiode [264].

This system enables patterning with resolutions down to 1 µm by directly projecting the desired pattern onto the photoresist using computer-controlled optics. In EBL, patterning is performed similarly using a focused electron beam that scans the sample surface along the defined pattern. By optimizing parameters such as acceleration voltage, with EBL we can achieve resolutions as fine as 100 – 200 nm.

The third step of the patterning process involves developing the exposed resist. The chemical reactivity of the exposed regions differs from that of the unexposed regions when interacting with the developer. For a *negative resist*, the developer removes the resist from the unexposed areas (see Fig. 4.5(c)), whereas for a *positive resist*, the exposed areas are removed (see Fig. 4.5(e)).

In the final step, the structured thin films undergo further processing. An inert gas plasma, such as Ar-ion plasma, can be used to etch the unprotected regions of the sample (Figs. 4.5(d), (f)). Alternatively, additional material layers can be deposited and subsequently removed, along with the remaining resist, in a *lift-off* process. The lithography recipes used for the work in this thesis are presented in Appendix A.2.

4.3 Electrical Measurements

A main obstacle for the use of AFM materials is the ability to easily read and write their AFM order. As AFMs, unlike their FM counterparts, do not posses any macroscopic magnetization, it is more challenging to detect their magnetic order [33, 34]. One way to read the AFM domain structure is by means of electrical measurements. It was first shown in metallic AFMs, that the Néel vector can be detected via AMR measurements [194, 265, 266] and set via staggered Néel SOTs or thermal effects [30, 193, 194, 201, 267–270]. Later the concept was extended to insulating AFMs: Making use of an adjacent HM layer, one can detect the Néel vector via SMR and set the magnetic order via SOTs and thermal effects [47, 48, 51, 145, 167, 168, 170, 192, 271]. The following section gives a brief overview over the two different measurement geometries utilized for reading and writing the Néel order; local MR measurements and electrical switching experiments. Then the experimental setup itself is introduced.

4.3.1 Local MR Measurements

For the local MR measurements, Hall bar structures were utilized. The structures consist of a central 6 µm-wide bar that carries the sensing current. Two additional channels, each 2 µm wide and oriented perpendicular to the central bar, allow for the measurement of longitudinal and transverse voltage. A schematic of the Hall bar device, including the electrical contact scheme, is shown in Fig. 4.6.

The sensing current is provided by a Keithley model 6221 [272] operating in Delta Mode, while the voltage is detected using a Keithley model 2182A nanovoltmeter [273]. When operating in Delta Mode, the current source and nanovoltmeter are internally coupled. A direct current is applied and inverted at a frequency of 12 Hz, such that the current traces a square wave. The Keithley model 2182A nanovoltmeter measures the voltage at the same frequency, averaging the values for positive and negative currents. This internal coupling enhances measurement speed, enabling the acquisition of many data points within a short period, thereby reducing noise to approximately $1-2$ nV at 200 K and an integration time of 20 ms per voltage reading with 100 readings combined into each data point.

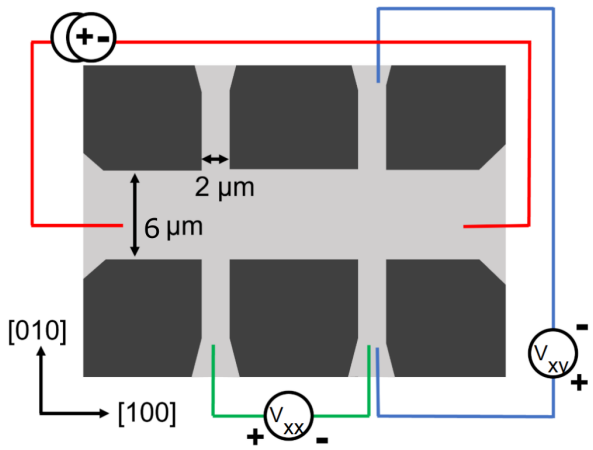

Figure 4.6: Schematic of a Hall bar including the connection scheme used for longitudinal V_{xx} and transverse V_{xy} voltage measurements.

4.3.2 Electrical Switching Measurements

For the electrical switching measurements, two types of devices were utilized: Hall cross and Hall star devices, as shown in Figs. 4.7(a) and (b), respectively. Both devices consist of two 10 µm-wide, perpendicular channels for the application of

current pulses with a current density on the order of $10^{11}\,\mathrm{Am}^{-2}$.

The Hall cross devices are aligned with the [100] and [010] crystallographic axes of the sample, whereas the Hall star devices are oriented along the [110] and [$\bar{1}$10] direction. The latter also include two additional 2 µm-wide channels along the crystallographic ⟨100⟩ in-plane axes for the application of sensing current and transverse voltage detection. This design allows for the measurement of the Néel vector orientation in the same geometry as the Hall bar devices. Additionally, in this configuration, the reading current is aligned at 45° with respect to the in-plane magnetic easy axes of CoO, thereby maximizing the MR signal according to Eq. 3.3 [167].

The current pulse channels of the two devices are rotated by 45° relative to each other to facilitate the use of different switching geometries. To observe switching effects and compare the final orientation of the Néel vector with respect to the applied current pulses, the pulse direction at the center of the Hall device must be aligned along the ⟨110⟩ magnetic easy axes of the sample. Consequently, different pulsing geometries are employed, either applying pulses around an edge of the Hall cross or directly along the Hall star, when utilizing different devices.

Current pulses are applied using a Keithley model 6221 alternating-current current source, which supplies a maximum voltage of 105 V with a minimum pulse duration of 10 µs, allowing for the application of comparatively short pulses [272]. However, due to the current's rise time of approximately 0.1 ms, only longer 1 ms pulses are used. This approach ensures a more reliable comparison of changes as a function of current density while allowing the rise time to be neglected.

Since switching measurements require frequent reconfiguration of the electrical connections, a Keysight 34970A+ data logger [274] equipped with a Keysight 34904A 4×8 matrix module is used. This setup enables computer-controlled (re)routing of contacts, streamlining the measurement process.

The Néel vector orientation is determined electrically via a charge current supplied by a Keithley model 2400 sourcemeter [275], while the transverse voltage is detected using a Keithley model 2182A nanovoltmeter [273]. To improve the signal-to-noise ratio and eliminate thermal contributions, the current direction is alternated, and five measurements are averaged for both positive and negative current directions.

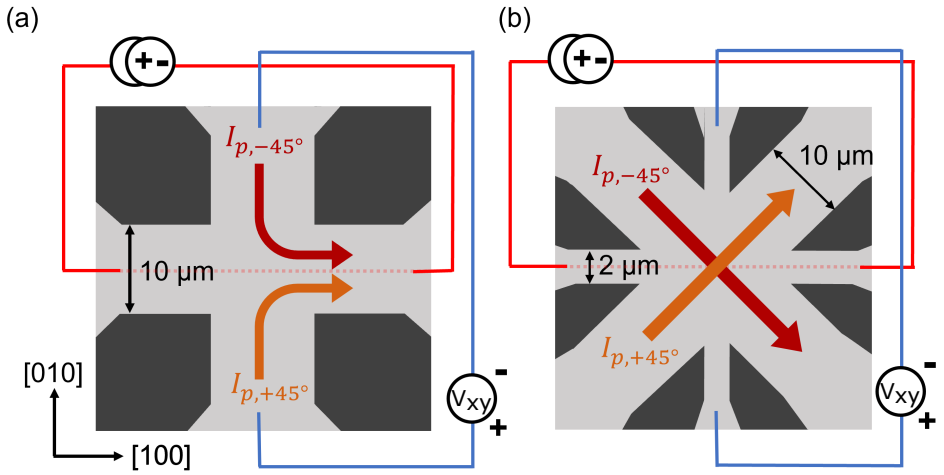

Figure 4.7: (a) Schematic of a Hall cross device including the connection scheme used for transverse resistance measurements. The channels of the cross are oriented along the crystallographic axes and the current pulses are applied along two neighboring arms of the cross. In comparison the Hall star device in (b) is rotated 45° compared to the Hall cross. Here, the large channels along which current pulses are applied, are aligned along the two in-plane ⟨110⟩ directions.

4.3.3 Experimental Setup

For the electrical measurements, the samples were installed inside the variable temperature insert of a superconducting cryostat. In the course of this thesis, two different cryostats were employed.

The first was an Oxford Instruments VSM MagLab cryostat, capable of generating magnetic fields up to 12 T and operating at temperatures ranging from 300 K down to 1.9 K via liquid helium cooling. The second was an Oxford Instruments low loss dewar, equipped with a superconducting magnet that, in standard operation, can generate magnetic fields up to 15 T. When operated in Lambda mode, wherein the coils are cooled to 2.2 K, magnetic fields of up to 17 T are achievable.

Temperature control was managed using a LakeShore Model 335 Temperature Controller [276], which was connected to a LakeShore Cernox 1050 sensor.

Although the magnets used in the cryostats are solenoidal, the samples could be mounted in either an in-plane or out-of-plane configuration using a piezo-rotating element (ANRv51/RES/LT) [277], which was controlled by an ANC350 [278] from Attocube. This piezo-rotator enables continuous 360° rotation in high magnetic

fields and at cryogenic temperatures. However, a full rotation is impractical due to the risk of entangling and severing the electrical connections necessary for signal readout. Additionally, the encoder exhibits a blind spot between 320° and 360°, restricting the accessible angular range to $0° - 320°$. To obtain measurement data for a complete 360° rotation in the magnetic field, it is necessary to invert the magnetic field direction. A reversal of the magnetic field by 180° corresponds to an angle between the magnetic field and the applied current of $\alpha' = \alpha + 180°$. When combined with a subsequent rotation back to 0°, this procedure enables access to all angles.

Rotation is achieved by applying a brief DC voltage pulse to the piezo-rotating element rather than a continuous voltage, which could otherwise lead to excessive heating and potential damage to the component. Each voltage pulse induces an incremental stepwise rotation, exhibiting a ratcheting motion. The rotational speed is governed by both the magnitude of the applied voltage and the frequency of its application. Typically, a voltage of 35 V at a frequency of 4 Hz is used, as this provides a balance between efficient rotation and the mechanical integrity of the positioner. In high magnetic fields, each voltage pulse induces a small torque on the positioner's cables, potentially leading to solder joint failure.[1] Moreover, the rotational speed is temperature-dependent, decreasing at lower temperatures.

The piezo-rotating element accommodates two different sample boards, which enable sample rotation in three orthogonal planes. On the in-plane sample board, the sample is mounted such that the applied field lies within the sample plane, permitting rotation within the xy-plane. Conversely, on the out-of-plane sample board, the sample is oriented such that the field is perpendicular to the sample plane, allowing for rotation within the xz- or yz-plane while being subjected to a static magnetic field.

4.4 X-ray Based Magnetic Imaging

X-ray-based techniques provide powerful tools for magnetic imaging, offering several advantages over methods that rely on visible light. They enable non-invasive, element-specific investigations and achieve spatial resolutions well beyond those of conventional optical approaches [279], reaching down to about 5 nm [280, 281]. Moreover, X-ray based imaging can offer magnetic sensitivity when using polar-

[1] Operation is save up to voltages of ≈ 40 V applied with a frequency of 4 Hz.

ized mono-chromatic X-rays, as the absorption and dispersion of X-rays depends on the orientation of magnetization within a material [282, 283].

The following section first provides a short overview on X-ray absorption spectroscopy and its interaction with AFM materials. The second part focuses on the generation of polarized X-rays in a synchrotron, as well as on photoemission electron spectroscopy, including the experimental setups and procedures used in this thesis.

4.4.1 X-ray Absorption Spectroscopy

X-ray absorption spectroscopy (XAS) is a powerful element-specific technique to investigate material properties. The energy-dependent absorption of monochromatic X-rays by a material provides insights into magnetic ordering, electronic structure, and the oxidation state of the material under investigation [284].

One common method to determine the energy-dependent X-ray absorption cross section σ is to perform scanning transmission X-ray microscopy measurements. The transmission of X-rays through a sample of thickness d [284] can be expressed as

$$I = I_0 \cdot \exp\left(-\rho\sigma d\right), \tag{4.2}$$

with I_0 being the initial intensity, which is attenuated to I after passing through the sample, ρ being the atomic density of the material, and σ being the interaction cross section. Since the resulting intensity strongly depends on the sample thickness d, transmission experiments require very thin films, typically on the order of a few hundred nanometers [285]. Alternatively, X-ray absorption can be studied by measuring the secondary photons emitted from the sample (fluorescence) [286] or the electrons emitted from the sample upon X-ray irradiation (electron yield) [284]. The latter was used to investigate the CoO thin films in this work.

When a sample is irradiated with photons, core-level electrons can be excited into unoccupied valence states, as illustrated in Fig. 4.8(a). The recombination of these excited electrons with core holes can lead to the excitation of other electrons above the vacuum energy E_{Vac}, which are ejected from the atom (Fig. 4.8(b)). These emitted electrons are known as Auger electrons. Inelastic scattering of Auger electrons can lead to the emission of secondary electrons from the sample, as shown in Fig. 4.8(c). Which can be detected [284, 287, 288], as discussed in Sec. 4.4.2.2.

The probing depth is typically limited by the escape distance of secondary elec-

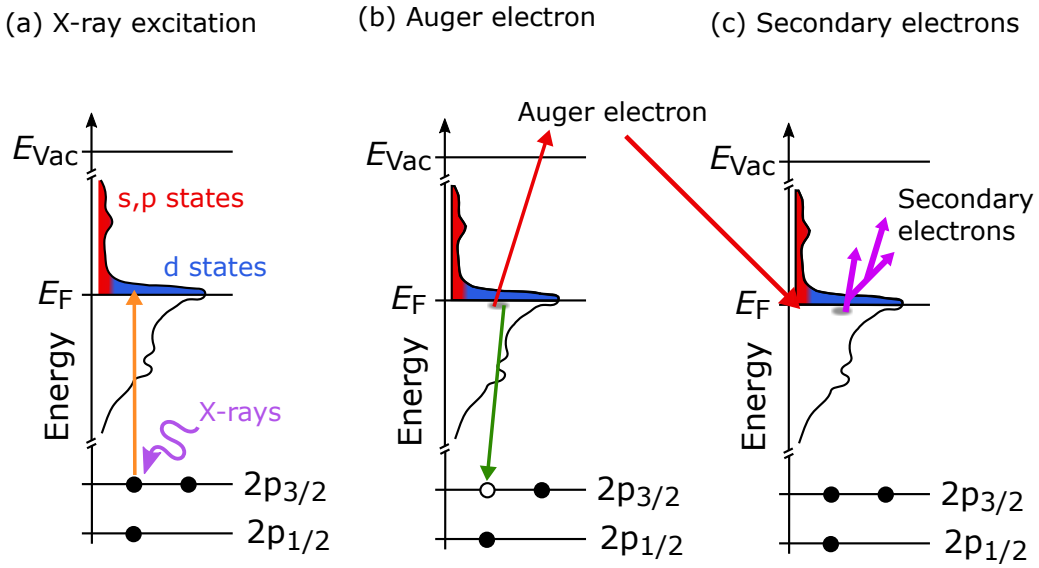

Figure 4.8: Sketch of the creation of secondary electrons from X-ray irradiation. (a) The absorption of photons excites core level electrons from p states into empty d states close to the Fermi level E_F. (b) The subsequent relaxation of electrons can excite further electrons above the vacuum energy E_{Vac} and thus lead to an ejection from the atom. These electrons are called Auger electrons. (c) Inelastic scattering of the Auger electrons can induce emission of secondary electrons [210, 212, 288].

trons, whereas the photon penetration depth is much greater, although it depends on the incident photon energy [289]. Due to the short electron escape depth, this technique is particularly surface sensitive. The measured intensity of the emitted electrons I_e can be described by

$$I_e = I_{e,0} \cdot \left(1 - \exp\left(-\frac{d}{z}\right)\right), \tag{4.3}$$

with the phenomenological parameter z representing the secondary electron escape distance, at which the initial electron intensity $I_{e,0}$ has decayed to approximately 37% of its original value. Despite this limitation, absorption can still be detected in layers up to a thickness of approximately $3z$ [290]. Typical values of z are $z_{Co} = z_{Ni} = 2.5\,\text{nm}$ [289]. Insulators typically exhibit longer secondary electron escape depths compared to metals [291].

By tuning the X-ray energy to the absorption edge of a material, element-specific information can be obtained. For $3d$ transition metals such as Co, the L-edge exhibits two distinct peaks due to the spin-orbit splitting of the core level

into $2p_{1/2}$ and $2p_{3/2}$. While transitions from the core level to unoccupied s- and p-states are possible, the XAS spectrum is primarily dominated by transitions from the $2p$ core level to unoccupied $3d$ states [284, 292]. The shape of the XAS spectrum provides valuable information about the chemical composition of the material; for instance, oxidized material may cause the appearance of an additional shoulder in the spectrum for many elements [293].

XAS spectra obtained for different X-ray polarizations can vary significantly due to *dichroism*, a phenomenon for which the X-ray absorption cross section of a material differs for two perpendicular polarization states of the incident X-rays. Dichroism arises only when the symmetry of the interaction between the X-rays and the material is broken. This symmetry breaking can occur due to the intrinsic structure of the material (natural or structural dichroism) [294, 295] or due to magnetic ordering (magnetic dichroism) [296, 297].

Depending on the X-ray polarization used, four distinct types of dichroism can be identified:

- X-ray natural linear dichroism (XNLD) [284, 294]
- X-ray magnetic linear dichroism (XMLD) [296, 298]
- X-ray natural circular dichroism (XNCD) [295]
- X-ray magnetic circular dichroism (XMCD) [297]

The forms of X-ray magnetic dichroism (XMD) arise from modifications in a material's electronic structure due to magnetic ordering, which in turn affect its interaction with X-ray photons. XMD is a resonant effect that occurs predominantly within the near-edge X-ray absorption fine structure of magnetic atoms [284].

In FMs, XMCD is commonly used to investigate the magnetic ordering [297]. Circularly polarized photons carry angular momentum and are, therefore, sensitive to the direction of magnetic ordering [284]. XMCD originates from the spin-orbit interaction in the core-level states, leading to different transition probabilities for left- and right-circularly polarized light [299]. Its sensitivity to both spin and orbital magnetic moments makes XMCD a valuable tool in analyzing SOC and magnetic anisotropy, with quantitative interpretation enabled by established XMCD sum rules [299]. In contrast, compensated collinear AFMs, such as CoO,

exhibit no net magnetic moment and thus show no XMCD effect. To investigate collinear AFMs, linearly polarized X-rays are used, as in the XMLD effect orientational but no directional sensitivity is found [296].

When interpreting the magnetic signal, it is important to distinguish magnetic from non-magnetic origins of linear dichroism. XNLD can result from charge anisotropies caused by the surrounding crystal field, leading to polarization-dependent absorption [300]. XNLD can occur in both magnetic and non-magnetic materials [294].

In a non-magnetic cubic system without charge anisotropy, XNLD vanishes, and X-rays of different polarizations are absorbed equally [284]. The coupling of X-rays to electronic states depends on the X-ray polarization, meaning that absorption of photons is related to the number of valence states along the direction of the electric field $\boldsymbol{E}$ [284]. In an uniaxially aligned system, the intensity of the XNLD signal depends on the angle β between the electric field vector and the symmetry axes [284]

$$I(\beta) = I_{\parallel} \cos^2(\beta), \tag{4.4}$$

with $I_{\parallel}$ being the intensity for $\beta = 0$.

Crystal field effects are particularly pronounced in thinner films, for which a lattice mismatch of film and substrate breaks the crystal symmetry, and can give rise to XNLD [301, 302]. These non-magnetic contributions can produce dichroic signals that, if not carefully accounted for, may lead to a misinterpretation of the underlying magnetic order [301, 303, 304].

4.4.1.1 X-ray Magnetic Linear Dichroism

The XMLD effect can be employed to investigate collinear AFMs [298, 305]. Since linear polarization possesses axial, but no directional, properties, XMLD is observed in AFMs, FMs, and ferrimagnets alike. However, XMLD is a second-order effect, scaling with $\langle M_{\parallel}^2 \rangle$, and is, therefore, often significantly weaker than XMCD in ferromagnetically ordered systems [298]. The XMLD effect originates from a non-spherical distortion of atomic orbitals caused by SOC, and depends on the magnetic ordering within the material [298], as illustrated in Fig. 4.9.

The absorption of X-rays differs depending on whether they are polarized parallel or perpendicular to the spin direction and also varies between different spin

orientations (i.e., magnetic domains). To date, XMLD has firmly established itself as a technique for studying many collinear AFM materials and investigate their magnetocrystalline anisotropy and AFM domain structure [299].

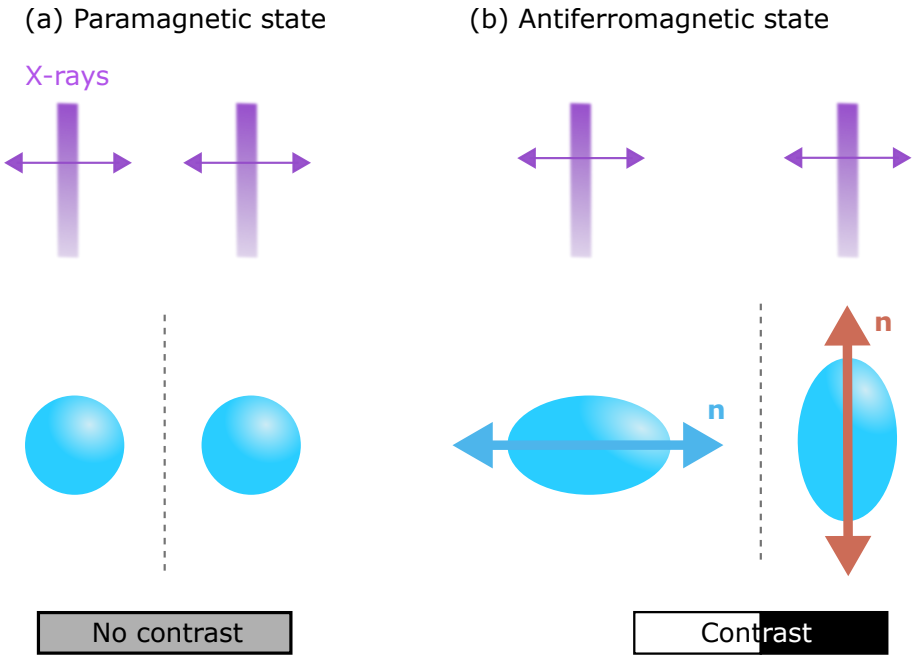

Figure 4.9: Schematic of the contrast change of an AFM in (a) paramagnetic state with a spherically symmetric charge density (blue) in comparison to (b) the AFM state with a distorted charge density.

The XMLD signal can be determined either from the difference in absorption between linearly horizontally (LH) and linearly vertically (LV) polarized X-rays, or from the difference in absorption of polarized light at two distinct photon energies. In collinear AFMs, such as CoO, significant absorption differences arise between LH and LV polarized X-rays, as well as between different X-ray energies, as illustrated in Fig. 4.10.

A rigorous theoretical description of the XMD effects is inherently complex and depends on the electronic structure of the magnetic material. Accurate modeling typically requires approaches such as band structure calculations [306] and a complete magnetic multipole framework that accounts for higher-order magnetic tensor components beyond the net magnetization [299]. The necessity of this complex theory is underscored by the observation of XMCD in altermagnetic systems [307]. The presence of XMCD, under the absence of a net magnetic moment, shows that

the emergence of XMCD is not governed by the spin configuration, but rather by the symmetry of magnetic dipole moments permitted by the crystal and magnetic structure. Optical responses such as XMCD and XMLD do thus not directly probe the magnetization, but reflect the underlying magnetic multipole symmetry of the system [299]. Consequently, oversimplified models and analogies [288, 308] are often misleading and fail to capture the true physical mechanisms.

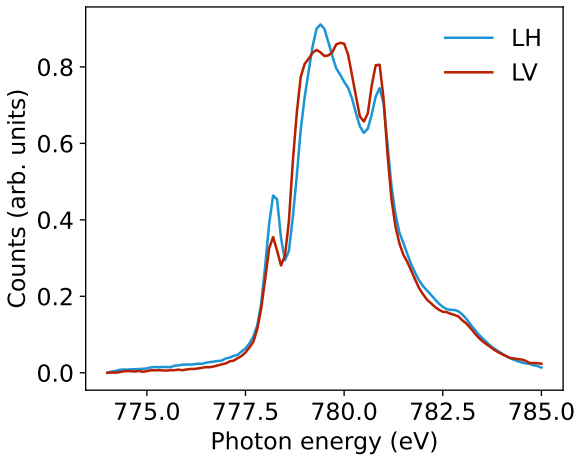

Figure 4.10: X-ray absorption spectrum at the Co L_3 peak for LH (blue) and LV (red) polarized X-rays.[2]

In this context, particular attention must be paid to the decomposition of X-ray linear dichroism into its spinless and spinful components. The spinless contributions correspond to XNLD effects, as discussed in Sec. 4.4.1 and arise from anisotropic charge distributions caused by the surrounding crystal field. These non-magnetic effects can lead to polarization-dependent absorption even in non-magnetic materials and must be carefully disentangled from the magnetic signal. In contrast, the spinful component originates from the underlying magnetic ordering and is associated with rank-2 magnetic multipole moments, notably the anisotropic magnetic dipole operator $\langle T^{(2)} \rangle$. This magnetic contribution is what encodes information about the direction and symmetry of the magnetic order.

In AFM materials, it is specifically the in-plane spinful XMLD component that is sensitive to variations in the orientation of the magnetic order parameter, such

[2]The CoO data has been measured on an MgO(001)/CoO(4 nm)/Pt(2 nm) sample by Dr. Adithya Rajan, Aditya Kumar, Grischa Beneke and Tobias Sparmann under the guidance of the author during a beamtime at the ALBA synchrotron.

as the Néel vector. Because linear polarization possesses axial, but not directional, symmetry, this XMLD component varies with the relative angle between the polarization vector and the spin orientation. As a result, it enables detection of changes in magnetic orientation across different crystallographic or magnetic domains, even in systems without net magnetization and can be exploited to determine the three-dimensional orientation of the Néel vector in various magnetic domains within a sample [210, 309, 310].

To quantitatively analyze XMLD and isolate the magnetic contributions, recent theoretical developments, such as those by Yamasaki et al. [299], have introduced sum rules based on a complete magnetic multipole basis. In this formalism, the XMLD intensity is expressed as a weighted sum of expectation values of magnetic multipole operators:

$$I_{\mathrm{XMLD}} \propto \sum_{k=2,4,\ldots} \langle T^{(k)} \rangle \cdot P^{(k)}, \tag{4.5}$$

with $\langle T^{(k)} \rangle$ being the multipole moments and $P^{(k)}$ being the polarization-dependent geometrical coefficients. This approach captures contributions beyond the net magnetization and is essential for correctly interpreting XMLD spectra.

4.4.2 Polarized X-ray Radiation

Dichroism is a powerful tool for probing the magnetic properties of materials. However, it requires monochromatic X-rays with tunable polarization. Such X-rays can be generated using a synchrotron light source [281]. Synchrotron radiation, also known as magnetobremsstrahlung, is electromagnetic radiation emitted by a charged particle undergoing radial acceleration in a magnetic field while traveling at velocities close to the speed of light. The emission mechanism is analogous to dipole radiation [311]. Although originally regarded as an unwanted energy loss, synchrotron radiation is now valued for its exceptionally high spectral brilliance (photon flux per area and opening angle of the source) which makes it a crucial tool in modern X-ray spectroscopy and microscopy [281, 284]. The following section introduces the fundamental principles of synchrotron radiation, the process of its generation, and the basic operating principles of photoemission electron microscopy (PEEM).

4.4.2.1 Synchrotron Radiation

A synchrotron light source generates highly collimated, coherent X-ray beams with an intensity that is six to twelve orders of magnitude greater than that of conventional laboratory sources [311]. These X-rays exhibit tunable polarization and energy, along with exceptionally high brilliance. This makes synchrotron radiation ideally suited for a wide range of experiments, enabling higher energy resolution in spectroscopy, greater angular resolution in diffraction studies, and improved spatial resolution in imaging applications [311]. The layout of a typical synchrotron light source is illustrated in Fig. 4.11 [281].

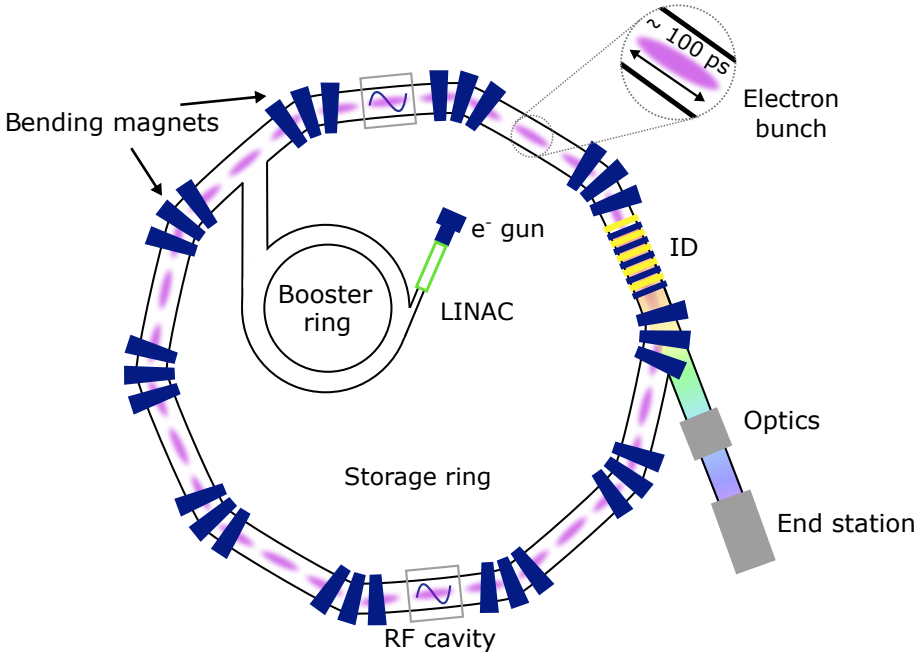

Figure 4.11: Schematic of a synchrotron with its key components. Electrons are generated in a source. They are accelerated in the linear accelerator (green), connected to the booster ring where they are boosted in energy and then injected into the storage ring. RF cavities (grey squares) maintain the electron energy. Bending magnets (dark blue) and insertion devices (yellow and blue) steer and oscillate the high-energy electron bunches, producing synchrotron radiation. The emitted X-rays are directed through beamline optics to the end stations. For simplicity only one insertion device and end station are shown.

Electrons are initially generated by a source and subsequently accelerated by a linear accelerator before being injected into a booster ring. In the booster ring, the electrons are further accelerated to velocities close to the relativistic limit and

then transferred into the storage ring. Within the storage ring, electrons circulate at energies of several GeV. In each loop the electrons loose energy, which must be replenished. To compensate for this energy loss, RF cavities are installed in at least one part of the ring to boost the electrons' energy.

The entire electron path is enclosed within an evacuated vessel to prevent beam degradation due to collisions with gas molecules. Nevertheless, occasional collisions with residual particles still occur and lost electron bunches are continuously replenished to maintain a stable beam current.

Although commonly referred to as a "ring," the actual shape of the storage ring is not perfectly circular, but rather resembles a polygon composed of straight sections connected by curved segments [281]. In the curved sections, one or more bending magnets are used to deflect the electron beam and guide it along the closed trajectory. These bending magnets produce X-rays with a broad energy spectrum and a wide opening angle, resulting in relatively low brilliance.

In the straight sections of the ring, insertion devices are installed [281]. These are periodic magnetic arrays, typically composed of permanent magnets with alternating polarity, that perturb the electron path. As the electrons pass through an insertion device, they undergo a slalom-like motion around the central axis, emitting high-brilliance photons with specific properties tunable by the insertion device setting at each bend [312, 313]. When the electron oscillations are small and remain close to the central axis, the emitted radiation from each bend adds coherently, leading to constructive interference and intensity peaks at specific X-ray energies. Insertion devices that operate in this regime are referred to as undulators [312, 313]. The X-ray energies at which the intensity peaks occur, as well as the polarization of the emitted radiation, are determined by the spacing (gap), strength, and periodicity (phase) of the magnetic arrays, all of which can be tuned to suit experimental needs [312, 313].

The emitted X-rays are guided to individual beamlines and experimental end stations, at which they are used for a wide range of scientific applications [281].

4.4.2.2 Photoemission Electron Microscopy

Combining the concept of dichroism with PEEM enables element-specific imaging of local magnetic (domain) structures on the sample surface by mapping the electrons emitted from the sample surface [314]. PEEM operates analogously to

an optical microscope, but uses electrons and electrostatic lenses instead of visible light and glass optics, thereby achieving superior spatial resolution.

In PEEM, the detected signal originates not from the incoming photons but from secondary electrons emitted via Auger processes as described in Sec. 4.4.1. To obtain a good image, the sample surface must be electrically conductive, and the incident X-ray wavelength must be appropriate for exciting the core electrons of the material under investigation [288].

Figure 7.5 shows a typical PEEM setup utilizing grazing-incidence X-rays at an angle of 16°. High-resolution imaging requires electrons with sufficiently high kinetic energy. To achieve this, a strong electric field of 10-20 kV is applied between the sample surface and the objective lens to accelerate the emitted electrons. These electrons are focused by the objective lens and pass through a contrast aperture, which limits the emission angle of the electrons. Subsequently, the electrons are guided through a series of magnetic lenses and into an energy analyzer. After passing through an energy-selective slit, electrons within the desired energy range are focused onto a detector by projection lenses. Since only the emitted secondary electrons are used for imaging, the resolution of PEEM is not limited by the wavelength of the incident X-rays. Instead, it is constrained by the performance of the electron optics and by factors such as spherical and chromatic aberrations, as well as electron diffraction [281, 290]. Furthermore, PEEM is inherently surface-sensitive, and imperfections or defects on the sample's surface can distort the local electric field, thereby affecting electron trajectories and image quality.

When PEEM is combined with XMCD or XMLD contrast mechanisms, it enables imaging of the magnetic domain structure of a sample. These techniques are referred to as XMCD-PEEM and XMLD-PEEM, respectively. In this work, XMLD-PEEM was primarily employed, as the materials under investigation exhibit AFM order.

To obtain an XMLD-PEEM image, either polarization-dependent or energy-dependent imaging can be performed [267, 282, 315]. This means that PEEM images are acquired using either two orthogonal linear polarizations, or two distinct photon energies are combined to reveal magnetic contrast. The XMLD-PEEM images presented in this work were obtained by subtracting images acquired at two

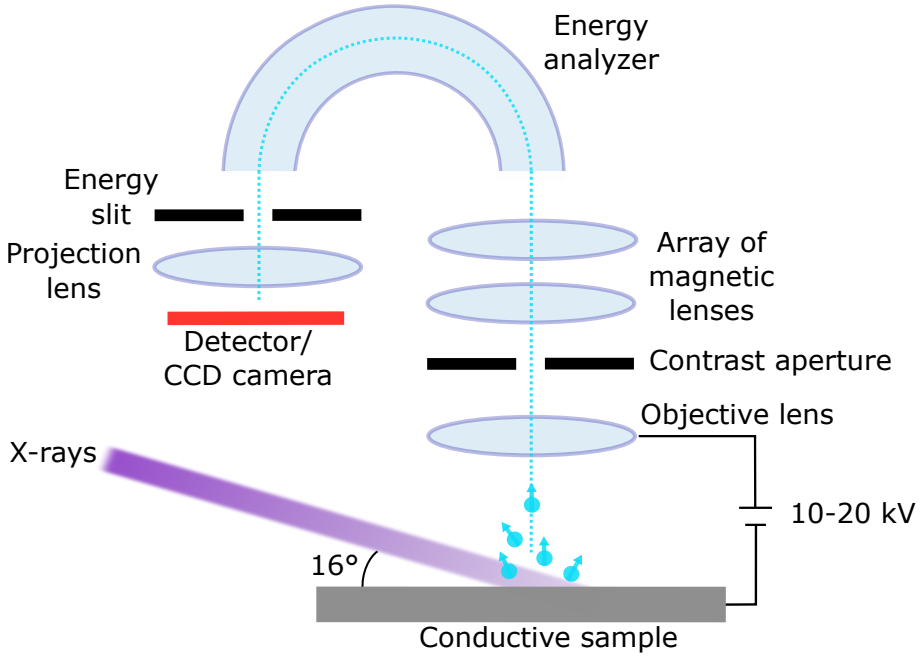

Figure 4.12: Schematic of a PEEM setup with grazing incidence of the X-rays as found e.g. at the CIRCE beamline at ALBA. The X-rays illuminate the conductive sample, causing the emission of electrons (cyan) at random angles. These electrons are accelerated by a high voltage towards the electron optics, where they are first focused by an objective lens, then pass through a contrast aperture and an array of magnetic lenses. An energy analyzer and energy slit enable energy-filtered imaging before the electrons are projected onto a detector/CCD camera.

different photon energies (E_1 and E_2) at the Co L_3 absorption edge:

$$\mathrm{XMLD}_{\mathrm{Image}} = \frac{I(E_1) - I(E_2)}{I(E_1) + I(E_2).} \tag{4.6}$$

Here, the denominator minimizes the effect of non-magnetic contributions, such as surface roughness, on the XMLD-PEEM images.

Despite the increased spatial resolution of PEEM compared to optical microscopy, a significant drawback is that imaging is limited to conducting samples. This limitation arises because, in the absence of conductivity, the removal of electrons would result in a net positive charge on the sample [316]. This charge accumulation would shift the work function, making it more difficult for the emitted electrons to reach the detector.

Additionally, external electric and magnetic fields, aside from those within

the lens system of the microscope, perturb the electron trajectories [317]. Consequently, the system must be well shielded, and the in-situ use of electric and magnetic fields is restricted to very small fields. This constraint limits experiments on AFM materials to those that do not require large magnetic fields.

The high voltage required to accelerate the electrons can generate substantial electric fields, which can lead to rapid electric discharges between the sample and the microscope [316]. These discharges cause a drop in high voltage, preventing electrons from reaching the detector. Locally, this can result in a large charge current flowing through the sample, potentially causing damage. To minimize the risk of discharge, maintaining a high vacuum and a flat sample surface is essential.

4.4.3 Experimental Setups

For the work presented in this thesis primarily three different PEEM setups at synchrotron facilities in Europe have been used: The BL24-CIRCE beamline at ALBA (Spain) [318], the UE49-PGM SPEEM beamline at Bessy II (Germany) [319, 320] and the MAXPEEM beamline at MAX IV (Sweden) [321]. The main characteristics of these setups are discussed in Tab. 4.1.

4.4.3.1 Data Acquisition and Image Processing

For the dichroism images, stacks of individual images were acquired. Depending on the observed contrast and the signal-to-noise ratio, between 20 and 500 images, each with a 1 s averaging time, were acquired for each of the two energies.

Before the final dichroic images were calculated, according to Eq. 4.6, several image processing routines were performed. First, camera artifacts were removed through image normalization. This process included a flat-field correction, appropriate scaling of the intensity of the central columns and rows, and dead pixel removal, which replaces missing values with the average value of the nearest neighbors. All the individual images acquired for a dichroism image needed to be aligned with respect to each other. The so-called *drift correction* compensates for thermal drift and small system vibrations during the acquisition. The images were all aligned with respect to the first image in the stack.

Image normalization, drift correction, dichroism calculation, and additional post-processing (such as adjustment of the intensity range, further drift correction, and averaging of several XMLD-PEEM images) were performed using either Igor Pro 8 or ImageJ Fiji with routines written and provided by the beamline sci-

entists of the corresponding beamlines.

Table 4.1: Comparison of the BL24-CIRCE (ALBA), UE49-PGM SPEEM (BESSY II), and MAXPEEM (MAX IV) PEEM setups and their main characteristic features.

Feature	**BL24-CIRCE (ALBA)**	**UE49-PGM SPEEM (BESSY II)**	**MAXPEEM (MAX IV)**
Instrument	Elmitec LEEM/PEEM III	Elmitec SPEEM	Elmitec SPLEEM (aberration-corrected)
Detector	Not specified	TimePix3 (1.6 ns time resolution)	CMOS (4096 × 4096 px)
Spatial Resolution	20 nm	30 nm	20 nm
Energy Range	100–2000 eV	100–1800 eV	30–1200 eV
Energy Resolution	0.2 eV	0.07 eV at 700 eV	< 0.2 eV
X-ray Incidence Angle	16° grazing incidence	16° grazing incidence	Normal incidence
Polarization Control	Full polarization control	Full polarization control	In-plane rotation
Temperature Range	Standard: ambient temperature; can be cooled down to ∼ 100 K (LN_2)	Standard: ambient temperature; can be cooled down to 45 K (LHe), limits azimuthal rotation (±90°)	Standard: ambient temperature; can be cooled down to ∼ 90 K (LN_2)
Special Features		Time-resolved imaging (1.6 ns); vertical cartridge geometry	Maximized XMLD for in-plane Néel vectors

5 Characterization of CoO Thin Films

AFM thin films can exhibit magnetic properties that differ significantly from those of their bulk counterparts, owing to strain, defects, or chemical bonding effects introduced during growth on a substrate or within a multilayer structure [322, 323]. Magnetic parameters affected by this can include, among others, the Néel temperature, the size of magnetic domains, and the magnetic anisotropy [324–327]. While bulk CoO has been intensively studied since the 1950s and is still not fully understood [70, 213, 219, 222, 224–228], thin AFM CoO layers have been barely studied. Before performing experiments to electrically read and write the Néel vector, i.e. by the application of an electrical current, it is of key importance to carefully characterize the magnetic properties of the AFM thin films to facilitate the interpretation of the experimental results. In Sec. 5.1, the effect of different growth parameters on the quality of the CoO thin films is investigated. And in Sec. 5.2 and Sec. 5.3, the influence of laser pulses and patterned shapes on the domain structure is investigated, respectively.

5.1 Growth Parameter Optimization

By varying the growth parameters, one can vary the magnetic behavior of FMs and AFMs in a controlled fashion or optimize specific material properties for targeted applications [328–332].

Strain induced during the growth process plays a particularly important role in determining the properties of AFM thin films, especially in materials with large magnetostrictive coefficients, such as CoO [213, 333]. By selecting appropriate growth conditions, one can tailor the strain state of the film, thereby influenc-

ing the AFM domain size, the equilibrium orientation of the Néel vector, and the strength of the magnetic anisotropy [334]. Optimizing these parameters not only enables the realization of CoO thin films with desired magnetic characteristics but also ensures the reliability, reproducibility, and consistency of experimental results.

The correlation between structural and magnetic properties of CoO thin films and their respective growth conditions was systematically investigated by - and - during their Bachelor theses [335, 336], under supervision of the author.

Their studies reveal that the oxygen flow rate during deposition has a significant impact on the lattice parameter of the CoO thin films and hence on the strain imposed by the MgO(001) substrate. This relationship is characterized using XRD measurements. A shift in the CoO (200) peak is observed as a function of oxygen flow rate, as illustrated in Fig. 5.1(a).

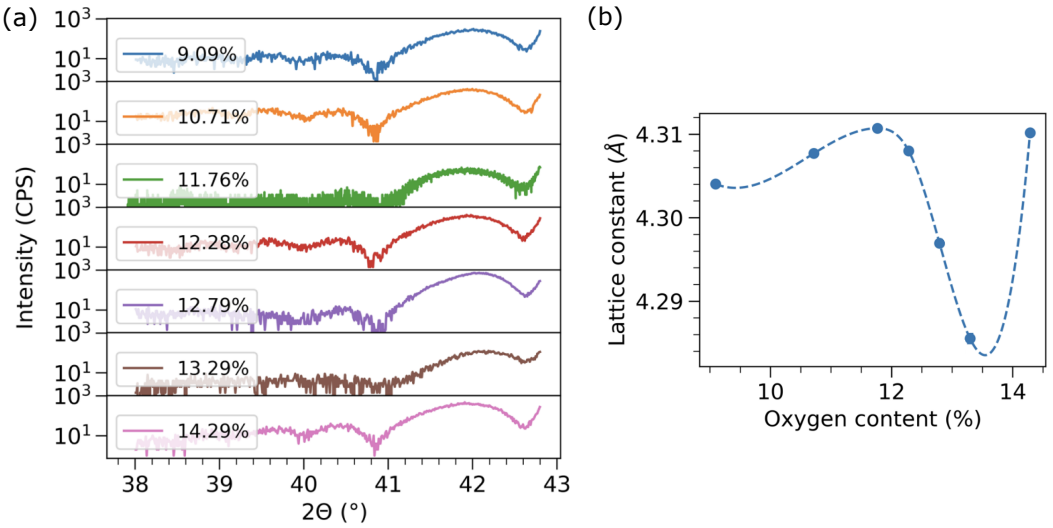

Figure 5.1: (a) XRD spectra around the CoO (200) peak for samples deposited with variable oxygen flow and deposition time in order to yield samples of approximately the same thickness. (b) Impact of the oxygen flow during deposition on the lattice constant, and consequently strain, in the thin films. The error bars are smaller than the symbol size. Data points are connected by cubic interpolation. Reprinted with permission from Ref. [335].

A lack or excess of O_2 during sputtering leads to a higher concentration of defects in the crystal structure. These defects introduce additional intrinsic strain, impeding relaxation of the upper atomic layers and preventing the lattice constant

from approaching its bulk value. The optimal oxygen flow rate was identified to lie in the range of 12-14% of the total gas flow, as determined from the XRD data. Figure 5.1(b) illustrates the lattice parameter determined for the individual samples, showing a significant reduction in lattice parameter within this range. While variations in sputtering power or total gas pressure during deposition also influence film quality, their impact is found to be less significant compared to the effect of oxygen flow.

Furthermore, a reduction in strain is found to correlate with a decrease in magnetic anisotropy and an increase in AFM domain size. These effects are attributed to a reduction in the number of pinning sites within the film, which are typically introduced by lattice defects and local strain variations. The ability to tune these parameters via growth conditions underscores the importance of precise control over the deposition process when engineering CoO thin films for AFM spintronic applications.

5.2 Optical Domain Nucleation

One of the primary advantages of AFMs lies in their intrinsic THz spin dynamics, offering significant potential for ultrafast spintronic applications [29]. To fully exploit these dynamics, particularly for achieving ultrafast switching in AFMs, a transition from current-induced manipulation of the Néel vector to optically-induced control is essential.

In ferri- and FM systems, laser-induced all-optical switching has been extensively investigated and helicity-dependent switching was observed [337–341].

In contrast, studies on optically-induced phenomena in AFM materials have primarily focused on the excitation of magnon modes [342–347], demonstrating that laser irradiation can effectively excite AFM order. Some experimental reports further suggest the possibility of optically inducing AFM domains and domain-walls [348, 349]. Although these processes are typically thermally driven, non-deterministic, and helicity-independent, recent evidence points to helicity-dependent optical switching of AFM domains via laser optical torques in Mn_2Au [350].

Notably, even the thermally-induced processes yield valuable insights into the AFM ordering and contribute to a deeper understanding of the material system because driving it away from equilibrium can expose characteristic coupling mechanisms, and domain dynamics that are otherwise hidden in equilibrium.

In this study, we investigate the impact of laser irradiation on the domain and domain wall structure of CoO thin films. The sample under investigation is a CoO(10 nm)/ Pt(2 nm) bilayer grown on MgO(001). Illumination was performed in the Group of - by -. An ultrafast amplified laser system with a central wavelength of 800 nm and a repetition rate of 1 kHZ was used. Each laser spot was exposed for 1 s and a pulse length of 42 fs was used. The band gap of CoO is ≈ 2.5 eV [351], exceeding the photon energy of the laser (1.55 eV). For different irradiation spots, the polarization of the laser beam was varied (C^-, lin, C^+) as well as the laser pump power, ranging from 40 µW to 100 µW in 20 µW increments. Irradiation was conducted ex-situ at room temperature.

Following irradiation, the illuminated areas were imaged using XMLD-PEEM at the Co L_3 absorption edge at the MAXPEEM beamline at MAX IV.

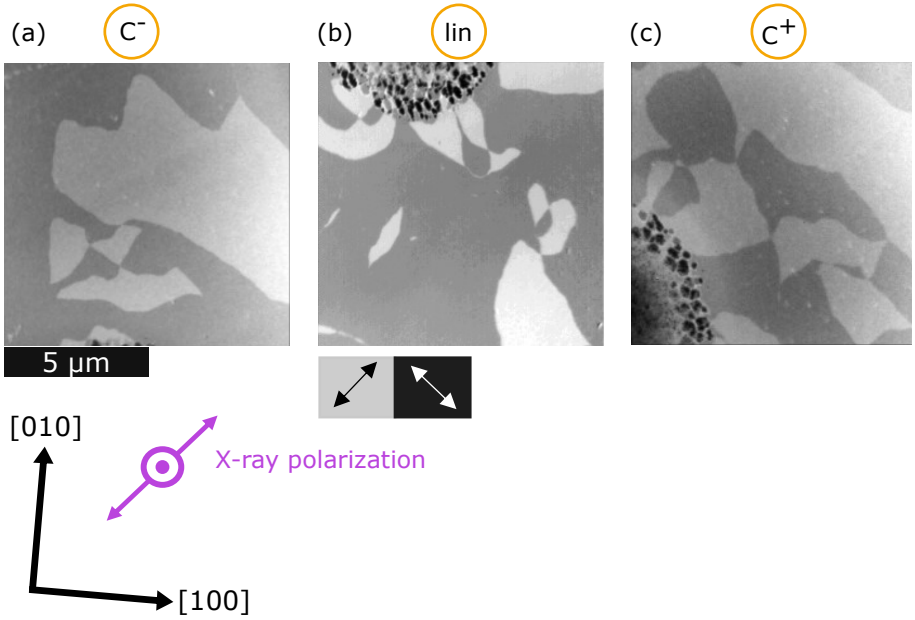

Figure 5.2: Example of the domain structure of an MgO(001)//CoO(10 nm)/Pt(2 nm) sample after irradiation with 1000 42 ± 4 fs laser pulses at 80 µW pump power and (a) circular left (C^-) polarized light, (b) linearly polarized light and (c) circular right (C^+) polarized light. Note that at the edge of the XMLD-PEEM images one can see the heating-induced ablation of the Pt layer where the laser pulse was focused to.

Exemplary XMLD-PEEM images obtained at a laser power of 80 µW for different light polarizations are presented in Fig. 5.2. In the irradiated regions, magnetic domain structures are observed surrounding a central area in which the Pt layer has been structurally changed due to the accumulated heat (visible as small

black and white speckles at the edges of the XMLD-PEEM images). While the regions farther from the illuminated area retain an almost monodomain state, the illuminated zones consistently exhibit a multidomain state for all three laser polarizations (C^-, lin, C^+), characterized by magnetic domains with two orthogonal Néel vector orientations. No systematic differences are observed as a function of the light polarization at any of the tested laser powers, indicating that domain formation in CoO is thermally driven rather than helicity-dependent, similar to previous observations in NiO [349]. Furthermore, domains are present across the entire range of pump powers investigated, with no clear correlation between the laser power and either the domain size or density. This behavior is attributed to the fact that irradiation was performed at room temperature, which is close to the Néel temperature T_N of CoO. Even low-power laser pulses can locally raise the temperature above T_N, and during subsequent cooling and relaxation, a multidomain state is generated.

A closer inspection of the induced domain structures reveals that the spatial orientation of the domain walls is anisotropic. Instead of forming circular domains, the walls exhibit straight edges and linear features, indicating preferred orientations with respect to the magnetic hard and easy axes.

Theoretical studies predict that the spatial configuration of domain walls in AFMs is influenced by magnetoelastic effects [78]. In the absence of such effects, domain walls tend to form isotropic, circular patterns. However, when magnetoelastic coupling is strong, domain walls preferentially align along the magnetic hard axes because this orientation minimizes the magnetoelastic strain energy associated with the rotation of the Néel vector across the wall. Aligning along hard axes reduces the elastic distortions induced by magnetoelastic coupling, making such domain-wall configurations energetically favorable [78].

To qualitatively determine the strength of the magnetoelastic effects, we extract the spatial orientation of the domain walls by extracting the angle between each domain wall segment and the crystallographic [100] direction. This analysis allows us to infer whether the magnetoelastic effects in our samples are sizable or not. The directionality of the domain walls is determined using the *Directionality* plugin in ImageJ - Fiji [352]. First, the XMLD-PEEM images are converted into binary format, as illustrated in Fig. 5.3(a), using the image shown in Fig. 5.2(b) as an example. Next, domain walls are extracted at the color boundaries, as shown

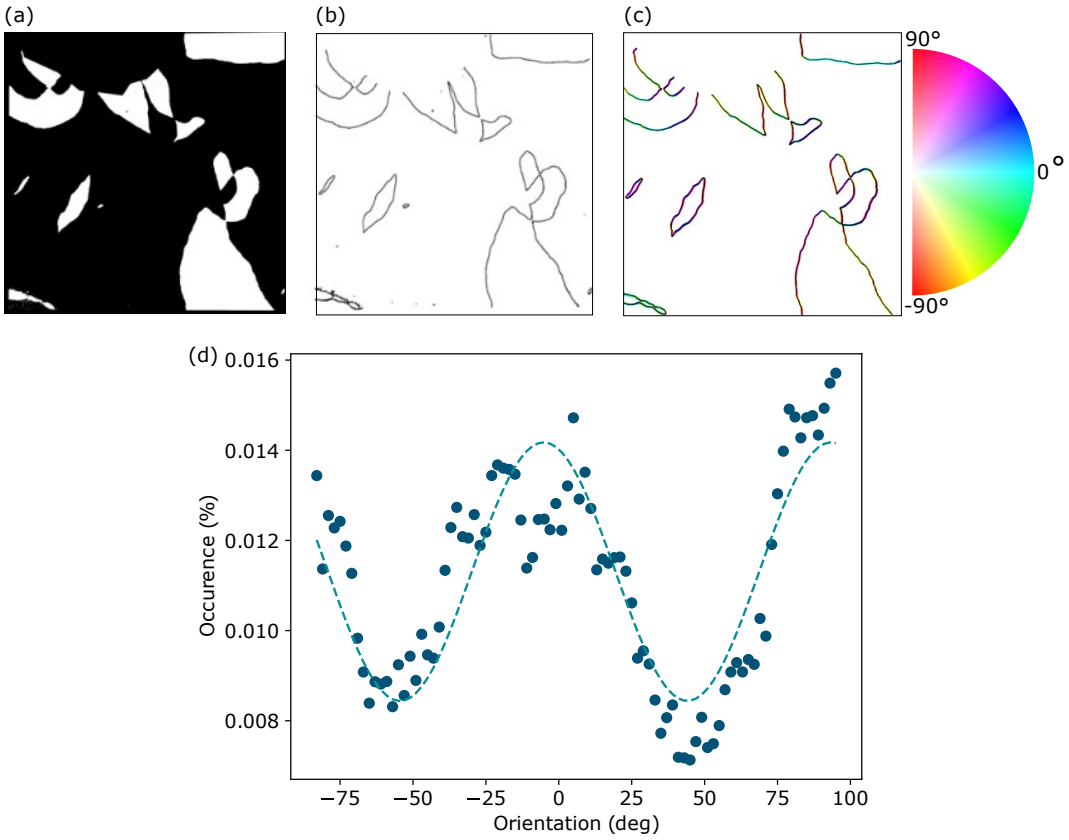

Figure 5.3: The directionality of the domain walls at each point can be determined. The XMLD-PEEM image is first converted into a binary image (a) and then the domain wall is extracted at the color edge (b). (c) The directionality of the domain wall is determined with respect to the horizontal direction of the images and color-coded according to the scale on the right. (d) The occurrence of a certain domain wall directionality as a function of the angle with the [100] direction of the CoO sample.

in Fig. 5.3(b). The *Directionality* function then evaluates the orientation of each wall segment relative to the horizontal axis of the image, yielding a color-coded map of domain wall orientations (Fig. 5.3(c)) and a corresponding histogram of the angular distribution.

The resulting occurrence of domain wall orientations relative to the [100] di-

rection (corrected for the slight misalignment of the crystallographic axes and the linear horizontal X-rays polarization) is depicted in Fig. 5.2(d), averaged over all laser polarizations and pump powers. The data reveals an anisotropic distribution of domain wall orientations. We find distribution maxima at −90°, 0°, and 90°, which correspond to the magnetic hard axes, and minima near the magnetic easy axes. Fitting a $\sin^2(\alpha)$ function to the angular distribution indicates a deviation from perfect 90° symmetry. This anisotropic distribution of domain wall orientations suggests sizable magnetoelastic contributions in our CoO thin films. Additionally, the deviation from fourfold symmetry points to the presence of a uniaxial anisotropy in thin films, superimposed on the expected cubic magnetic symmetry.

5.3 Antiferromagnetic Shape Anisotropy

In FM devices a common method for manipulating magnetic domains is via shape-induced anisotropy [65]. Altering the shape of a FM structure can lead to changes in its magnetic domain configuration. In the absence of an external magnetic field, FM materials often exhibit multidomain states governed by a balance between exchange interaction, dipolar interaction, and anisotropy. In very small structures, dipolar interactions can dominate, leading to shape-dependent domain formation [52].

Although collinear AFMs do not posses dipolar interactions due to the absence of a demagnetization field, multidomain states are still commonly observed [91, 103, 105, 106], as discussed in Sec. 2.3.2. In AFM materials with strong magnetoelastic interactions, shape-dependent effects, analogous to FM shape anisotropy, can emerge in finite-size elements [77, 111, 353]. Given the sizable magnetoelastic effects identified in our thin films (compare Sec. 5.2), it is essential to understand the influence of patterning-induced effects, particularly near edges, and shape-induced effects on the long-range domain structure. This is especially relevant for further experiments requiring patterning of the thin films, which could unintentionally tailor the domain configuration.

To investigate shape- and patterning-induced effects on the domain structure of thin-film CoO, various geometrical elements with different orientations were patterned into a CoO(10 nm)/Pt(2 nm) bilayer using optical lithography. As shown in Fig. 5.4, we have etched away the CoO, Pt and part of the MgO substrate in

the area surrounding the geometrical element. A 1 nm ruthenium layer was subsequently deposited to ensure electrical conductivity and mitigate discharge risks during PEEM imaging. To allow magnetic moment reorientation after patterning, the sample was annealed in vacuum at 350 K, above the Néel temperature, for 10 min.

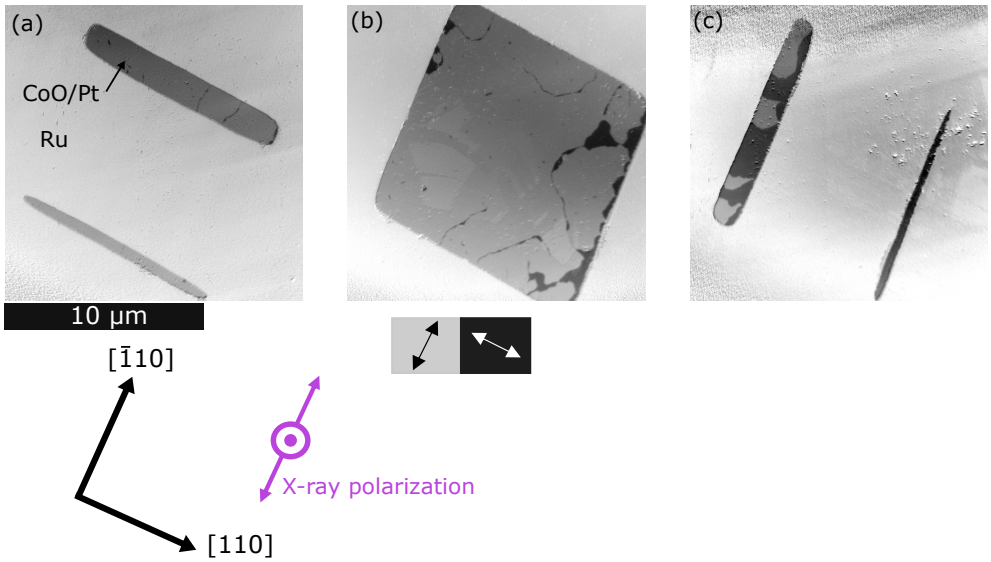

Figure 5.4: XMLD-PEEM images of the AFM domain structure in MgO(001)//CoO(10 nm)/Pt(2 nm) bilayers with patterned rectangular elements. The aspect ratio of the rectangles is varied and the long axis is oriented along the [110] direction in (a), it shows a square shape in (b) and the long axis is oriented along [1̄10] in (c). Note that the slightly brighter areas within the rectangle in (b) are of non-magnetic origin, but rather some photoresist residuals.

PEEM imaging was performed at normal incidence at the MAXPEEM beamline at MAX IV, providing high sensitivity to the in-plane Néel vector orientation. Figure 5.4 displays the domain configurations of rectangular shaped patterns oriented along the magnetic easy axes direction. The aspect ratio of the rectangles was varied from 1 µm × 14 µm to 14 µm × 1 µm. In Fig. 5.4(a), the long axis of the geometrical element is aligned along the [110] direction; Fig. 5.4(b) shows a square element; and in Fig. 5.4(c) the long axis is aligned along the [1̄10] direction. Across all patterns, we can identify the two orthogonal AFM domains typical for CoO thin films [50, 237, 238]. In Fig. 5.4(a), the domain configuration is largely uniform, with one dominant domain type. In contrast, Fig. 5.4(b) reveals the formation of a darker domain within a narrow ≈ 0.5 µm – 1 µm wide region near the patterning-

edge aligned along the [$\bar{1}$10] direction. As the rectangle becomes narrower along the [110] direction, this darker domain becomes increasingly prominent and eventually stabilizes across the entire area in the 1 µm wide structure.

We find that the Néel vector within the dark domain in Fig. 5.4(b) and (c) is oriented orthogonal to the patterning edge. This can be attributed to localized modifications of the surface anisotropy near the edges, introduced during the patterning process leading for instance to strain variations. However, the broadening of the dark domain in narrower rectangles oriented along the [$\bar{1}$10] direction cannot be explained by local anisotropy changes alone. Instead, this behavior points to the influence of long-range magnetoelastic interactions [77]. That the broadening of the domain from one side of the device to the other is only observed in rectangles with a width less than 2 µm suggests that, in contrast to materials such as NiO [77] or CuMnAs [353], the magnetoelastic effects in CoO are not sufficient to overcome the material's stronger intrinsic anisotropy over larger distances away from the edge. In NiO and CuMnAs, shape-anisotropy-induced domain configurations were observed even in elements up to 5 µm in width [77, 353].

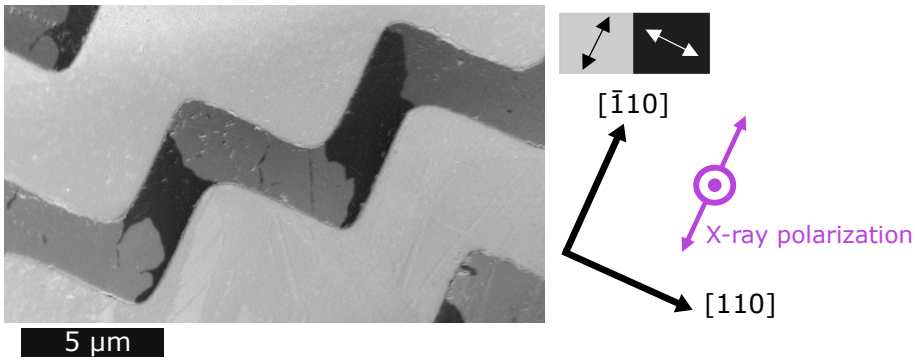

Figure 5.5: XMLD-PEEM image of a zigzag-shaped patterning, showing a preferential formation of different domains at different edges of the patterning.

When examining the zigzag pattern shown in Fig. 5.5, we observe domain formation trends similar to those seen in the rectangular elements. Specifically, we find a preferential formation of bright domains along edges aligned with the [$\bar{1}$10] direction, and dark domains along edges aligned with the [110] direction. As in the rectangular geometries, these results indicate a consistent tendency for the Néel vector to align perpendicular to the respective patterning edge.

Overall, our results demonstrate that patterning- and shape-induced effects in

CoO give rise to an effective AFM shape anisotropy. However, these effects are relatively weak compared to the magnetocrystalline anisotropy and are only able to locally overcome the intrinsic anisotropy near the patterned edges. As such, they are unlikely to significantly impact the outcomes of future experiments on patterned films.

5.4 Conclusion

The AFM properties of thin-film CoO differ significantly from those of bulk CoO. As demonstrated throughout this chapter, careful optimization of the growth parameters is crucial to tailoring the material properties to specific experimental requirements. In particular, as discussed in Section 5.1, the oxygen flow during the sputtering process plays a key role in determining the lattice parameter of the CoO film, which in turn governs the strain state of the material. This strain directly influences the orientation of the Néel vector, the magnetic anisotropy, and the resulting domain structure, including domain size and stability.

Furthermore, in Section 5.2, we have investigated optically induced magnetic effects in CoO/Pt bilayers. The formation of magnetic domains was found to be primarily thermally driven rather than helicity-dependent, for all laser polarizations and pump powers. A closer analysis of the domain wall orientations revealed a distinct anisotropy in their spatial distribution, which indicates the presence of considerable magnetoelastic coupling within the CoO thin films.

Additional studies presented in Section 5.3 explored the impact of lithographic patterning and geometric confinement. These revealed that while magnetoelastic effects do influence domain configurations, particularly near patterned edges, their overall impact remains modest. Unlike in other AFM materials such as NiO or CuMnAs, for which shape-induced anisotropy can dominate over larger scales, the intrinsic magnetocrystalline anisotropy in CoO remains the prevailing factor. Consequently, although shape- and strain-related effects are clearly present, they are unlikely to significantly interfere with, or limit future experimental applications.

6 Current-Induced Switching of CoO/Pt Bilayers

The development of spintronic devices employing AFMs as active components relies critically on efficient and reliable techniques for reading and writing the Néel vector [33]. In conventional FM-based devices, current-induced switching via STTs is a well-established approach to manipulate magnetic order and is commonly employed in STT-magnetoresistive random-access memory [354–356]. However, the current-induced switching of AFMs remains comparatively less explored and poses greater challenges due to the absence of magnetic stray fields and net magnetic moments [33, 34].

Initial studies on the electrical switching in metallic AFMs, such as CuMnAs and Mn_2Au, demonstrated the possibility of electrical manipulation of the AFM Néel vector via staggered bulk field-torques (compare Sec. 3.2) [30, 194, 269, 270]. These efforts were later extended to insulating AFMs, for which an adjacent HM layer acts as the charge carrier. Several works experimentally demonstrated the electrical switching of the Néel vector in AFM CoO, NiO and $\alpha - Fe_2O_3$ via non-staggered interfacial antidamping-like torques [47–51, 238, 302, 357–360].

However, multiple mechanisms contribute to the switching and their effects need to be separated. While early research primarily attributed the switching mechanism to interfacial, non-staggered SOTs [47–49], later works pointed to thermomagnetoelastic effects as the dominant process in thicker films with strong magnetostriction [50, 51, 200, 361]. Since non-staggered SOTs are interfacial effects and scale with the inverse of the AFM thickness, they are expected to become more relevant in ultrathin layers [49]. Most previous studies, have focused on AFM layers of 10 nm thickness or more [47, 49, 51].

The study of ultrathin CoO/Pt bilayers, presented in Section 6.1, addresses this gap. The results are based on the first-author publication of the author of this thesis in Ref. [247], which investigates the switching mechanisms in the ultrathin limit using a combination of electrical measurements and direct magnetic domain imaging.[1]

6.1 Electrical Switching in Ultrathin CoO/Pt Bilayers

In terms of applications, it is of paramount importance to be able to perform the read-out and writing operations in AFMs quickly, efficiently and deterministically. In order to address the latter, the underlying switching mechanism needs to be understood. It has been established that for insulating AFMs, electrical currents in an adjacent HM layer can be used to read out the orientation of the Néel vector via SMR [167, 170]. Electrical writing of information has been reported via current pulses which can induce a reorientation of the AFM order, both in metallic AFMs [30, 194, 269] and bilayers of insulating AFMs and HMs [47–49]. The switching mechanism in the latter case is, however, being debated in terms of origin and efficiency. While SOTs have been proposed as the primary driving force in AFM/HM bilayers [47–49, 197, 357, 358], the observation of switching in tens of nanometer-thick films, for which SOTs are less effective, suggests a contribution from thermomagnetoelastic effects, particularly in materials with strong magnetostriction [50, 51, 200]. Given that SOT efficiency scales with $1/d$, with d being the thickness of the AFM layer [49], ultrathin AFM films are an ideal platform for exploring the electrical switching.

Thin film CoO grown under compressive strain on MgO(001) substrates (lattice mismatch 1.1%) [234, 236], shows a fourfold in-plane magnetic anisotropy with two orthogonal stable states [50, 121, 237]. This configuration is ideal for electrical switching experiments and reading the Néel vector via SMR [48, 145, 167] in order

[1] The following Sec. 6.1 and its subsections and figures were transcribed and adapted from Ref. [247] and its supplementary information, with the first author of this reference being the author of this thesis. Individual contributions are detailed in Appendix C.1. Reprinted with permission from Nano Lett. 2024, 24, 5, 1471-1476; Publication Date: January 12, 2024; https://doi.org/10.1021/acs.nanolett.3c02890. Copyright ©2024 American Chemical Society.

to identify the underlying switching mechanism and to understand if competing mechanisms are present simultaneously.

6.1.1 Electrical Switching Experiments

To investigate the current-induced effects on the AFM domain structure, we have grown epitaxial CoO(d)/Pt(2 nm) bilayers on MgO(001) substrates with d = 4 nm and 2 nm. Using Ar ion beam etching, we have patterned Hall cross structures with a channel width of 10 µm, aligning the arms of the cross parallel to the [100] and [010] sample edges (hard axes), as shown in Fig. 6.1.

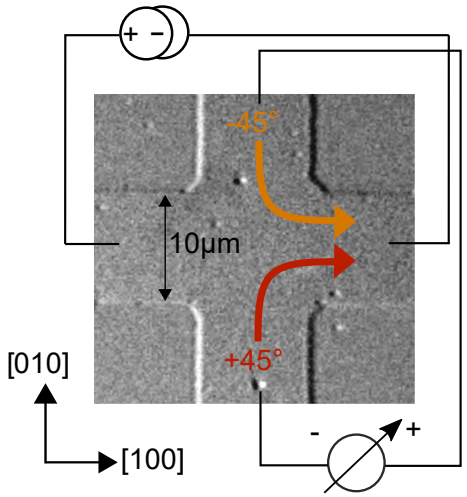

Figure 6.1: Device and contact scheme used for the electrical measurements. The measurement current is applied along the [100] direction while the transverse voltage is read in the two arms along the [010] direction. The current pulses are in a next step applied along either -45° or +45° direction with respect to the measurement current, indicated by the orange and red arrows, respectively. Adapted with permission from Ref. [247]. Copyright 2024 American Chemical Society.

Edge pulses around the corners of the cross result in current directions $\boldsymbol{j}$ in the center of the device parallel or perpendicular to the two magnetic easy axes ([110] and [1$\bar{1}$0]). The layout allows for a reproducible switching between two orthogonal Néel vector orientations. 1 ms long current pulses of varying current density are applied to the device. The resulting magnetic state can be read electrically via the SMR mechanism [167]. The transverse signal is proportional to the in-plane Néel vector components $n_x \cdot n_y$ [167], and thus can distinguish between two orthogonal Néel vector orientations, such as in CoO thin films.

To calibrate the signal, we first apply a strong magnetic field, above the spin-flop field, to set the whole device in a well defined starting state with a known Néel vector orientation along the $[1\bar{1}0]$ orientation. Next we perform a magnetic field sweep along the perpendicular direction. With increasing magnetic field, this induces a spin-flop in our CoO thin films that exhibit a pronounced four-fold anisotropy, and thus a reorientation of the Néel vector, as shown in Fig. 6.2. At zero magnetic field, one consequently observes a splitting of the electrically read values: one corresponding to a Néel vector orientation along $[1\bar{1}0]$ (higher resistivity value), and one, after the spin-flop, corresponding to a Néel vector orientation in the whole device along [110] (lower resistivity value). The difference in the transverse SMR values at zero field thus corresponds to a full magnetic switching of the Hall cross device from one Néel vector orientation to a perpendicular one. A resistivity value between these maximum and minimum values indicates that part of the device has a Néel vector orientation along the $[1\bar{1}0]$ magnetic easy axis, and another part has an orientation along the [110] magnetic easy axis.

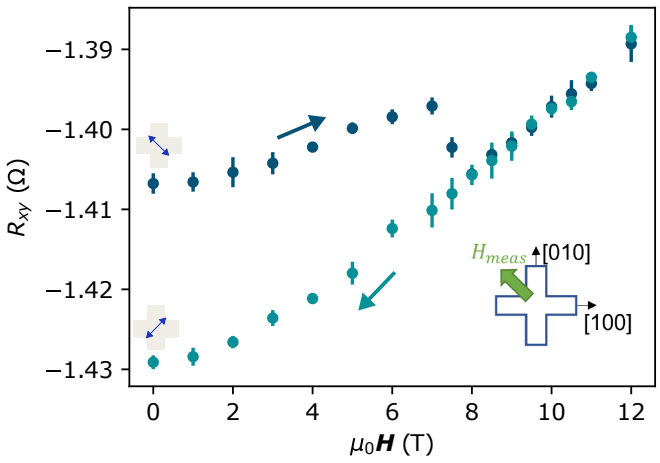

Figure 6.2: Field-induced spin flop at 200 K, read by SMR in the presence of a magnetic field applied along the $[1\bar{1}0]$ direction. A 12 T field was previously applied along the orthogonal direction to set a well-defined starting state. Adapted with permission from Ref. [247]. Copyright 2024 American Chemical Society.

First, we investigate switching in a CoO(4 nm)/Pt(2 nm) film at 200 K. Before the measurements, a magnetic field $\mu_0 \boldsymbol{H}_{\text{before}} = 12$ T is applied along the [110] direction to set the Néel vector $\boldsymbol{n}$ into a defined starting state along the $[1\bar{1}0]$ direction (blue double arrow in Fig. 6.3). Subsequently, five pulses at -45° ($[1\bar{1}0]$) and five

pulses at +45° ([110]), with respect to the measurement current direction, are applied. We note that transport experiments are prone to artifacts [203–205]. Therefore, we have checked, that for the current densities used, we are in a regime with no significant electromigration effects [205].

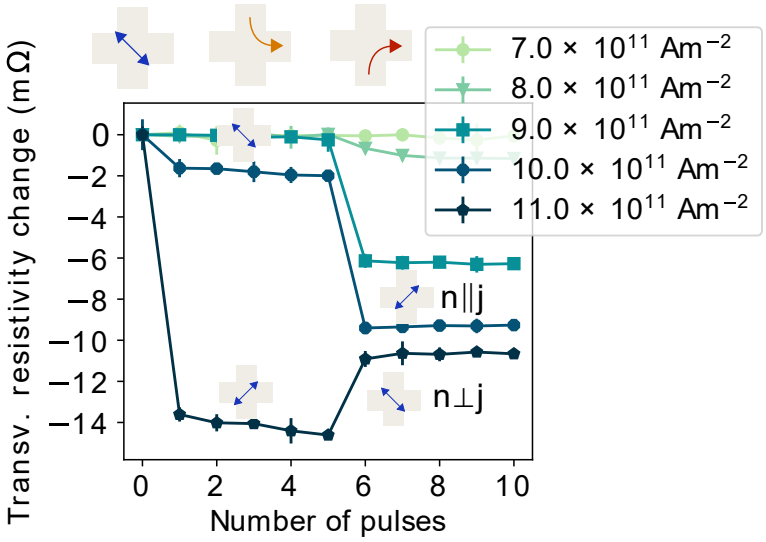

Figure 6.3: Current density-dependent switching of the Néel vector $\boldsymbol{n}$ with respect to the current direction $\boldsymbol{j}$ in CoO(4 nm)/Pt(2 nm) thin-films showing two different switching regimes. The pulsing directions for -45° (pulse 1-5) and +45° pulses (pulse 6-10) are indicated by the orange and red arrow, accordingly. The blue arrows indicate the orientation of the Néel vector before and after the pulses. For low current densities $\boldsymbol{n}$ switches parallel to $\boldsymbol{j}$. For high current densities $\boldsymbol{n}$ switches perpendicular to $\boldsymbol{j}$. Adapted with permission from Ref. [247]. Copyright 2024 American Chemical Society.

At low current densities $j_{\text{pulse}} \leq 8 \times 10^{11}\,\text{Am}^{-2}$, no current-induced switching is detected in the SMR signal (Fig. 6.3). Increasing the current density to $j_{\text{pulse}} = 9 \times 10^{11}\,\text{Am}^{-2}$ shows no change in SMR signal after five pulses at -45°, but a decrease in transverse SMR signal after the first pulse along +45°, indicating a partial switching of the magnetic structure with a final state of the Néel vector $\boldsymbol{n} \parallel \boldsymbol{j}$ (along [110]). $j_{\text{pulse}} = 10 \times 10^{11}\,\text{Am}^{-2}$ shows a small decrease in the transverse resistivity after the first -45° pulse, consistent with a reorientation of $\boldsymbol{n}$ (final state [110]) perpendicular to the current direction ($\boldsymbol{j} \parallel [1\bar{1}0]$). The SMR signal after the first +45° pulse decreases further, indicating larger device areas switching into the [110] direction and an opposite switching sign with $\boldsymbol{n} \parallel \boldsymbol{j}$, as the -45° and +45° pulses are perpendicular to each other. Increasing the current density further

to $\boldsymbol{j}_{\text{pulse}} = 11 \times 10^{11}\,\text{Am}^{-2}$ results in a more pronounced effect after a -45° pulse and a large decrease in transverse resistivity signal can be observed, indicating a reorientation of $\boldsymbol{n} \perp \boldsymbol{j}$. However, a +45° pulse at this current density leads to an increase in the transverse SMR signal. This change in SMR indicates a rotation of parts of the device back into the original $[1\bar{1}0]$ direction and thus a switching of the Néel vector final state $\boldsymbol{n} \perp \boldsymbol{j}$.

Overall, we observe two different switching signs at low and high current densities, implying the presence of two electrical switching regimes with opposite Néel vector final states in ultra-thin CoO(4 nm)/Pt(2 nm) bilayers. This observation suggests that different switching mechanisms dominate at different pulse current densities.

6.1.1.1 Switching in Thinner Samples

Given the scaling of SOT strength with layer thickness, stronger SOT-induced switching is expected for thinner films [49]. Therefore, we also investigate an ultra-thin CoO(2 nm)/Pt(2 nm) sample.

First, field sweep measurements along the two magnetic easy axes were performed. To obtain a well-defined initial state with $\boldsymbol{n} \parallel [110]$, a magnetic field of $\mu_0 \boldsymbol{H} = 11\,\text{T}$ was applied along the $[\bar{1}10]$ direction. The subsequent field sweep along the [110] direction, up to $\mu_0 \boldsymbol{H} = 11\,\text{T}$ at $T = 200\,\text{K}$, is shown in Fig. 6.4(a). A spin-flop transition is observed for magnetic fields in the range $\mu_0 \boldsymbol{H} = 8\,\text{T} - 10\,\text{T}$. In a second step, a field sweep along the $[\bar{1}10]$ direction was conducted. As shown in Fig. 6.4(b), the spin-flop transition for this direction occurs at $\mu_0 \boldsymbol{H} = 7\,\text{T} - 9\,\text{T}$. The difference in spin-flop fields indicates that aligning the Néel vector along [110] is energetically more favorable than along $[\bar{1}10]$. This behavior suggests the presence of a cubic anisotropy defining two magnetic easy axes, superimposed with an uniaxial anisotropy, as we also observed it in Sec. 5.2. Consequently, reversible switching between two orthogonal Néel vector states is hindered. Instead, we employ a switching geometry that combines current-induced switching with the application of a magnetic field of variable strength. When a magnetic field is applied along [110] during the electric pulse application, switching of the Néel vector away from its preferred direction is facilitated.

Figure 6.4(c) presents the variation of the transverse resistance R_{xy} as a function of the number of +45° pulses for various switching current densities, with a static

magnetic field of 5 T applied along [110]. Before each measurement, the system was reset to a reproducible starting state by applying a magnetic field of 11 T along [$\bar{1}$10]. All measurements were conducted at T = 205 K.

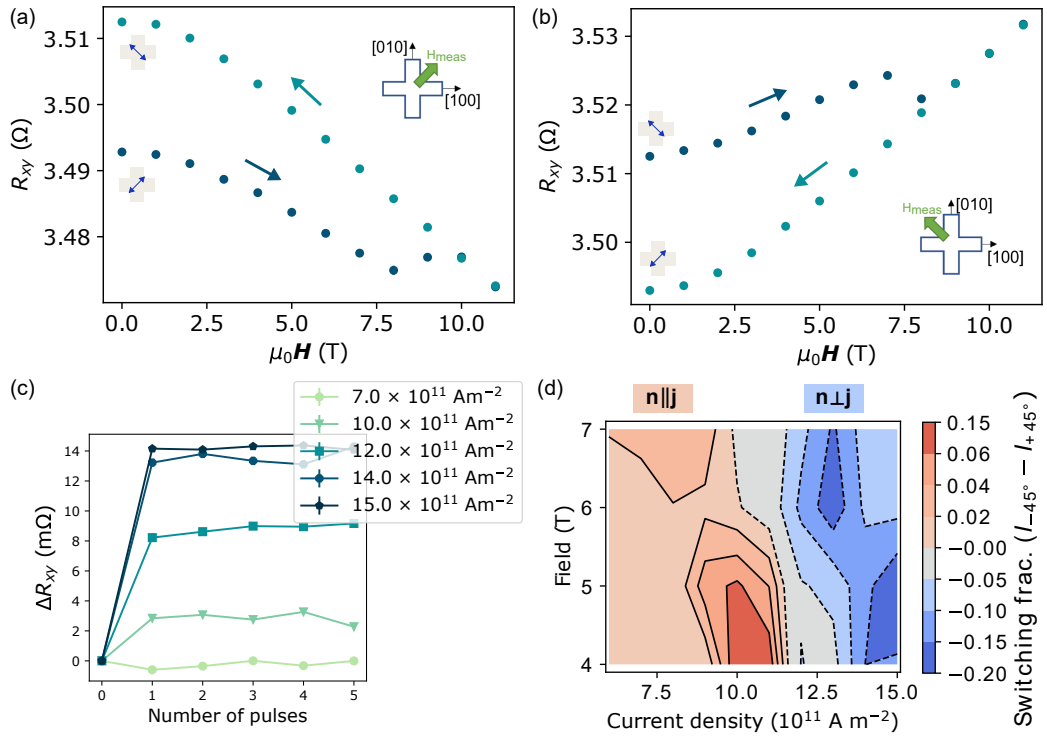

Figure 6.4: (a) Field-induced spin flop at 200 K, read by SMR in the presence of a magnetic field applied along the [110] direction in CoO(2 nm)/Pt(2 nm). A 11 T magnetic field was previously applied along the orthogonal direction to set a well-defined starting state. (b) Field-induced spin flop with orthogonal field direction ([$\bar{1}$10]) compared to the previous scan. (c) Transverse resistance variation versus pulse current density, probing the threshold and saturation of the switching. Before the measurements, a reset field ($\mu_0 \boldsymbol{H}_{\text{reset}}$ = 11 T) was applied along [$\bar{1}$10], followed by five pulses along +45° direction while a static magnetic field of 5 T was applied along [110]. (d) Difference of the switching fraction after -45° and +45° pulses as a function of the applied field and pulse current density. The lines are contour plots with constant switching efficiency. Red and blue as well as solid and doted lines represent the low- and high-current density regimes for which -45° and +45° pulses are dominating, respectively. Adapted with permission from Ref. [247]. Copyright 2024 American Chemical Society.

Below the threshold current density ($\boldsymbol{j}$ = 7 × 10^{11} Am^{-2}), no change in resistance is observed. Increasing the pulse current density leads to an increasing

change in R_{xy}, indicating that $\boldsymbol{n}$ is being switched away from the [110] direction. Field sweeps along the two magnetic easy axes provide reference resistance values corresponding to full switching between the two magnetic easy axes. This enables the quantification of the switching fraction in electrical measurements, assuming a proportionality between resistance change and switched volume.

Using this framework, switching experiments with both -45° and +45° pulses were conducted, and the resulting switching fractions were compared. It is important to note that -45° and +45° pulses are expected to result in orthogonal Néel vector orientations. However, the static magnetic field also contributes to the switching, especially at elevated pulse current densities, for which Joule heating enhances the effect of the magnetic field. This favors alignment of the Néel vector perpendicular to the applied magnetic field. As a result, switching fractions increase with current density for both pulse directions. Nevertheless, slight differences in switching fraction reveal which pulse direction is more effective. The pulse direction that aligns the Néel vector with the direction favored by the magnetic field yields a slightly higher switching fraction.

To compare the effects of the two pulse directions, Fig. 6.4(d) plots the difference in switching fractions ($I_{-45^\circ} - I_{+45^\circ}$) as a function of pulse current density and magnetic field. As observed in thicker CoO(4 nm) films, two distinct switching regimes are evident. At low current densities, -45° pulses yield larger switching fractions than +45° pulses (red regions), indicating that in this regime, $\boldsymbol{n}$ tends to align parallel to the current direction ($\boldsymbol{n} \parallel \boldsymbol{j}$). In contrast, at higher current densities, +45° pulses become more effective (blue regions), suggesting that the Néel vector prefers to align perpendicular to the current direction ($\boldsymbol{n} \perp \boldsymbol{j}$).

Beyond the observation of two switching regimes, however, no further insights into the switching mechanisms in AFM thin films can be easily obtained from the transport study of this sample so that in the following we focus on spatially resolved imaging of switching in the 4 nm thick sample.

6.1.2 Optical Imaging of the Switching

To address the open question of whether two different mechanisms are causing the Néel vector switching in these ultra-thin CoO samples, imaging of the AFM domain structure is essential. Especially, since transport signals can be affected by issues such as spatially varying sensitivity of the Hall cross device [362] or

due to non-magnetic contributions to the SMR signal, from e.g. electromigration effects [205]. By correlating the effect of electrical current pulses on the domain structure by imaging, we can gain insights into the mechanisms and the origin of the distinct switching regimes.

By comparing the electrical signal with the changes in domain structure, we can directly conclude which of the switching signs and regimes is consistent with which proposed switching mechanism for insulating AFM/HM bilayers [51].

To image the AFM domain structure, we use PEEM for the contrast generation the XMLD effect, at the CIRCE beamline at ALBA, Spain. We image the AFM domain structure using energy-dependent XMLD-PEEM at the Co L_3 edge using two energies $E_1 = 777.9\,\text{eV}$ and $E_2 = 779.0\,\text{eV}$. Figure 6.5(a) shows the investigated Hall bar region. Prior to the imaging, a magnetic field above the spin-flop ($\mu_0 \boldsymbol{H}_{\text{before}} = 12\,\text{T}$) was applied along the [110] direction at 300 K, to set the Néel vector in the same starting state as in the transport measurements with $\boldsymbol{n} \parallel [1\bar{1}0]$ (indicated by the blue double arrow). The sample was cooled down to 220 K for the imaging and pulse application. It needs to be noted, that the dark stripes in the center of the Hall cross structure are non-magnetic and arise from surface inhomogeneities. Since the values of the resistance in the Hall cross are comparable for all measured devices, we can conclude that the surface inhomogeneities do not affect the path of the current pulses.

When applying a -45° pulse, indicated by the orange arrow in Fig. 6.5(b), with $\boldsymbol{j}_{\text{pulse}} = 8.5 \times 10^{11}\,\text{Am}^{-2}$, no significant change in the magnetic domain structure is observed, consistent with the low current regime in the electrical measurements, for which a -45° pulse does not lead to an observable change in transverse Hall resistivity. However, a +45° pulse with the same current density induces a reorientation of the Néel vector in the region of the Hall cross through which the current is flowing, as it is shown in Fig. 6.5(c). This magnetic change is consistent with a switching of $\boldsymbol{n} \parallel \boldsymbol{j}$, in agreement with the low current density regime in the electrical measurements.

Before the next current pulses are applied, the magnetic state of the sample was brought back into the approximately monodomain state with $\boldsymbol{n} \parallel [1\bar{1}0]$ by heating it in-situ above its Néel temperature (Fig. 6.5(d)). The subsequent application of a single pulse with $\boldsymbol{j}_{\text{pulse}} = 11.5 \times 10^{11}\,\text{Am}^{-2}$ along the -45° direction induces a change of the AFM domain structure in the arms opposite to those to which the current

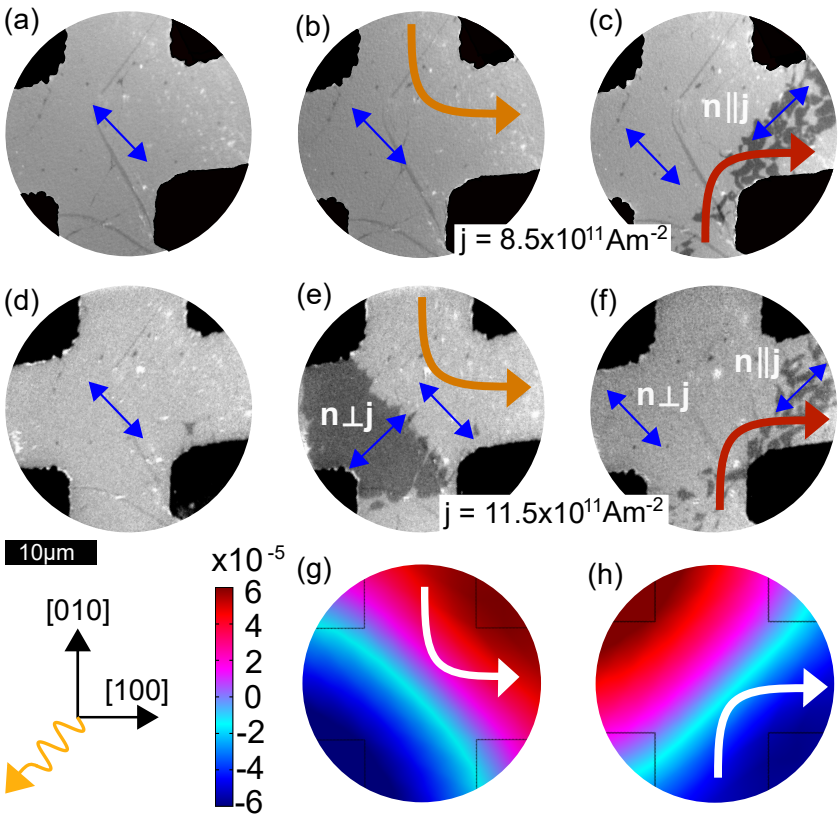

Figure 6.5: XMLD images of a CoO(4 nm)/Pt(2 nm) film. (a) The AFM domain structure is in a saturated nearly monodomain state after the application of a magnetic field of 12 T at 300 K in the [110] direction. The Néel vector orientation is indicated by the blue double arrow. (b) Domain structure after the application of a -45° pulse (orange) with $\boldsymbol{j}_{\text{pulse}} = 8.5 \times 10^{11}\,\text{Am}^{-2}$. (c) The application of a +45° pulse induces some reorientation of the Néel vector with $\boldsymbol{n} \parallel \boldsymbol{j}$. (d) Heating up the sample above Néel temperature restores the almost monodomain state with $\boldsymbol{n} \parallel [1\bar{1}0]$. (e) The application of a -45° pulse ($\boldsymbol{j}_{\text{pulse}} = 11.5 \times 10^{11}\,\text{Am}^{-2}$) induces a change of the AFM domain structure. (f) Magnetic state after a +45° pulse with $\boldsymbol{j}_{\text{pulse}} = 11.5 \times 10^{11}\,\text{Am}^{-2}$. (g) Calculated strain profile for a pulse along the -45° direction. (h) Calculated strain profile for a pulse along the +45° direction. Adapted with permission from Ref. [247]. Copyright 2024 American Chemical Society.

pulse is applied. Figure 6.5(e) shows the resulting magnetic state. The Néel vector in the switched region is oriented perpendicular to the current direction in the center of the device ($\boldsymbol{n} \perp \boldsymbol{j}$). This is in agreement with the sign of the switching observed in the high current density regime in the electrical measurements. A pulse with equal current density but perpendicular direction (+45°), as shown in Fig. 6.5(f), erases parts of the previously nucleated domain structure and generates

a magnetic state similar to that created by applying a smaller current density. In this case, however, the switching sign can not be uniquely determined. In the arms of the cross, opposite those to which the current pulse was applied, the final state of the Néel vector is $\boldsymbol{n} \perp \boldsymbol{j}$, consistent with the observations in the electrical measurements. On the other hand, in the arms through which the current pulse was applied the final state is $\boldsymbol{n} \parallel \boldsymbol{j}$. Thus, the microscopic measurements reveal that different switching behavior can be observed in different parts of the sample and that there are also differences depending on the current density.

To infer the switching mechanism, we compare the XMLD-PEEM images with the predicted switching sign for SOTs in CoO and with the difference in strain distribution resulting from the current-induced heat, which we simulated with COMSOL [363]. For the simulations in Fig. 6.5(g) and (h) we plot the difference between the strain along the two magnetic easy axes $\epsilon[1\bar{1}0] - \epsilon[110]$. A positive strain difference (red), indicates a larger expansion of the CoO along $[1\bar{1}0]$ compared to [110], while a negative strain difference (blue) indicates larger strain along the orthogonal direction. The strain is caused by the expansion of the CoO lattice due to the applied current in the Pt, leading to inhomogeneous Joule heating and thus inhomogeneous expansion. Figure 6.5(g) and (h) show the resulting strain-distributions for the pulses along the -45° and +45° direction, respectively. Comparing these strain profiles with the XMLD-PEEM images in the low current-density regime indicates that after a -45° pulse (Fig. 6.5(b)), no switching is observed. In the region close to the applied current pulse, with sufficient heat and strain present, the Néel vector is already oriented along the [110] direction, the axis along which a stronger expansion of the CoO is observed (red). In the arms opposite those to which the current pulse is applied, the strain is in the orthogonal direction, which could lead to a reorientation of the Néel vector. However, this is not observed, suggesting that the heat in this area may not be sufficient to trigger a switching of the Néel vector [51]. For a +45° pulse, on the other hand, the region with stronger expansion of the CoO along $[1\bar{1}0]$ (blue) is in the arms of the cross through which the current pulse is applied, and the heating is stronger. Here, a switching of the Néel vector can be observed.

The observed behavior in the low current-density regime is consistent with a thermomagnetoelastic switching mechanism. Checking the high current-density regime, we find that the changes in the Néel vector also align with a thermomag-

netoelastic switching mechanism. Specifically, for the -45° pulse there is a reorientation of the Néel vector in the arms opposite to those to which the current pulse is applied, which can be attributed to increased heating in that region (Fig. 6.5(e)). For the +45° pulse the resulting domain structure in the arms, through which the current pulse is applied, switches into the $[1\bar{1}0]$ direction, consistent with the strain in $[1\bar{1}0]$ direction, while in the opposite part, it switches back into the [110] direction, following the strain in [110] direction (red). So this shows that the transport signals can be difficult to interpret if not complemented by direct imaging.

Most importantly, not all observed changes in the domain structure can be solely attributed to the thermomagnetoelastic switching mechanism. The domain structure for +45° pulses, with the change of the Néel vector occurring in regions through which the current pulses are applied, is different from that for -45° pulses, for which the change occurs in the opposite arms. For +45° pulses, the resulting domain structure appears less homogeneous and requires a different explanation. This observation indicates the presence of different switching mechanisms.

To investigate the potential presence of a SOT-based mechanism in the arms through which the pulses are applied, we compare the experimentally observed switching sign with the theoretical predictions for the SOT-based switching mechanism in CoO. SOTs in AFMs are predicted to be caused by the spin accumulation at the AFM/HM interface, induced by the SHE in the HM [48]. The corresponding torques create staggered fields which remove the degeneracy between the two orthogonal magnetic easy axes, resulting in a current-induced energy term, which competes with the magnetic anisotropy [49]. In order to minimize this contribution, the predicted final state of switching in CoO is $\boldsymbol{n} \parallel \boldsymbol{j}$ [50].

For the -45° pulses, we do not observe switching at the locations of the current pulse, in agreement with a SOT switching mechanism, since the Néel vector orientation is already parallel to the current direction in the center of the Hall cross. However, for +45° pulses, we observe a switching of $\boldsymbol{n} \parallel \boldsymbol{j}$, in line with what is expected from a SOT-based switching mechanism.

As a result, we conclude that switching in ultra-thin AFM films is governed by a combination of two mechanisms: a thermomagnetoelastic switching mechanism and a SOT-based mechanism. The SOT mechanism occurs in the areas where the current pulse is applied, while the thermomagnetoelastic mechanism dominates in regions without current flow, so that there cannot be SOTs but for which inhomo-

geneous strain distributions persist, and sufficient heating facilitates the process.

We have carried out additional experiments with the Néel vector aligned along the [110] direction, perpendicular to the Néel vector starting state along [1$\bar{1}$0] as discussed before. These experiments enable further insights into the relative strength of the SOT effect and the thermomagnetoelastic effect. We performed in particular switching experiments with slightly larger current densities.

While the imaging was carried out by birefringence imaging with a resolution limited by optical resolution compared to Fig. 6.5 that was measured by PEEM, the switching of the magnetic domains and the relevant variation in magnetic contrast can be observed clearly, as illustrated in Fig. 6.6. We set the magnetic starting state of the sample by applying 12 T along the [1$\bar{1}$0] direction. This results in a Néel vector orientation along [110] (Fig. 6.6(a)). One expects intuitively that for increased current density the thermomagnetoelastic switching mechanism dominates (scaling with the heating that scales with j^2). So here, we applied a -45° pulse with an orientation in the center of the Hall cross perpendicular to the original Néel vector orientation. Figure 6.6(b) shows that this results in a switching of the magnetic state according to the strain distribution in Fig. 6.6(h) and in accordance with a thermomagnetoelastic switching mechanism.

The perpendicular +45° pulse leads to a partial switching of the Néel vector back into the [110] direction. But only in the regions close to the trajectory of the current in which heating contributions are sufficiently large. In an even higher current density regime, the switched regions become larger, and the second +45° pulse completely reverses the effect of the perpendicular -45° pulse, aligning all regions of the Hall cross according to the strain distributions. We note that the switching is not exactly symmetric because the anisotropy is not completely fourfold but on top there is a small uniaxial magnetic anisotropy that makes the two magnetic easy axis slightly different.

From these experiments we can conclude that there is a subtle interplay between the two mechanisms that leads to one or the other dominate. For a more quantitative understanding, one would require a systematic analysis of different current flow geometries, current amplitudes and temperatures, which goes beyond the scope of this current work. For thinner samples in particular one would expect a more pronounced effect of the SOT mechanism.

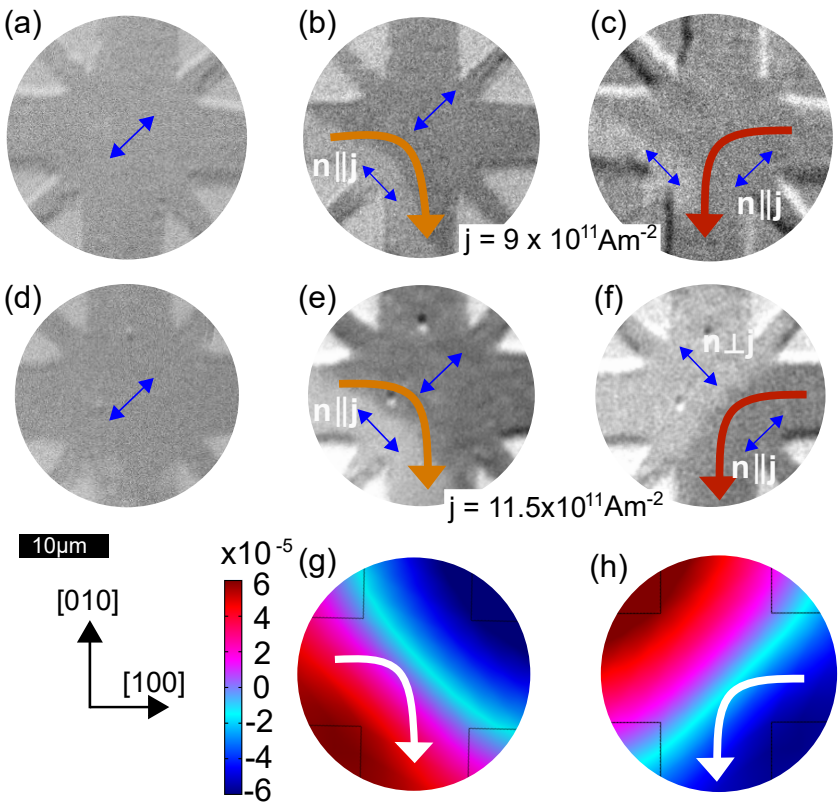

Figure 6.6: Birefringence images of a CoO(4 nm)/Pt(2 nm) film. (a) A saturated nearly monodomain state is set in [110] direction by the application of a magnetic field of 12 T at 300 K. The Néel vector orientation is indicated by the blue double arrow. Domain structure after the application of (b) a -45° pulse (orange) and (c) a +45° pulse (red) with $j_{\mathrm{pulse}} = 9 \times 10^{11}$ Am^{-2}. (d) The starting state is reset by the application of a magnetic field. (e) The magnetic structure after the application of a -45° pulse ($j_{\mathrm{pulse}} = 11.5 \times 10^{11}$ Am^{-2}) and (f) a +45° pulse. (g) Strain profile for a pulse along the -45° direction. (h) Strain profile for a pulse along the +45° direction. Adapted with permission from Ref. [247]. Copyright 2024 American Chemical Society.

6.2 Conclusion

In conclusion, we have investigated current-induced switching of the Néel vector in ultra-thin CoO/Pt bilayers and revealed the interplay of SOT and thermomagnetoelastic switching mechanisms.

In transport measurements, we find that electrical pulses along the same current path can show opposite sign for the switching-induced change of the SMR signal, depending on the current density. However, by comparing these results

with the XMLD-PEEM imaging of the domain structure, we demonstrate that the current-induced switching leading to the different sign of the SMR can be explained by the action of a single heat-assisted thermomagnetoelastic switching mechanism at all current densities. This highlights the importance of magnetic imaging to reveal the full changes in the AFM domain structure, since electrical data itself can be misleading.

Most importantly, we identify the presence of a SOT-based mechanism, which explains the differences in domain structure between the regions through which the current pulse is applied and those opposite to it. It is expected that such a SOT-based mechanism becomes most relevant for thinner films, compared to previous reports of tens of nanometer-thick films for which only thermomagnetoelastic switching mechanisms could be identified.

These findings demonstrate the interplay of the different switching mechanisms and thus motivate further research into thinner AFM films, offering promising opportunities for utilizing AFMs in applications for which electrical reading and efficient writing through SOTs is key. In particular, SOTs provide access to the intrinsic THz dynamics of AFMs, which cannot be realized through thermomagnetoelastic switching, as it is inherently a thermally driven process.

7 Giant Orbital Magnetoresistance Driven by Dynamic Orbital Angular Momentum Interaction

In recent years, the quest for faster, more energy-efficient electronic devices has driven researchers to explore new electronic degrees of freedom in charge-based systems. The interaction between static magnetization and the flow of spin angular momentum (spin currents) through *s-d* exchange has been the key mechanism to detect and control the magnetic state of FMs. This interaction has enabled major applications, ranging from giant magnetoresistance sensors [364, 365] to SOT magnetic random-access memory [366, 367], chiral skyrmion-based racetrack memory [368, 369], logic devices [370], and neuromorphic applications [371–373]. AFMs can likewise be manipulated using electrical currents and the magnetic state can be detected using spin currents, as demonstrated in Sec. 6.1. However, the generation of spin current relies heavily on the SOC of the materials, which is a weak relativistic effect that limits the efficiency and constrains the choices of materials [196].

More recently, the out of equilibrium OAM has emerged as a promising alternative for manipulating magnetization more efficiently when a charge current is applied, even without the need of SOC [37, 38, 44, 374]. Orbital Hall conductivities are predicted to surpass spin Hall conductivities by several orders of magnitude, implying the potential for significantly enhanced orbital-current generation. [35–41]. The two predicted mechanisms of orbital current generation are the OHE in the bulk [35–37] and the OREE at interfaces [41, 375], as introduced in Sec. 3.1.3.

Unlike spin currents, orbital currents can be directly generated from charge currents because the crystal momentum of charge carriers (e.g., electrons) can conceptually directly couple to OAM. This results in a potentially orders-of-magnitude larger generation of current-induced OAM (orbital currents), even in light, abundant, inexpensive and environmentally friendly materials [37, 39, 40, 182, 376, 377].

Despite these advantages, the fundamental limitation in utilizing orbital currents for device applications lies in their low interaction efficiency with magnetization, that in conventional transition metals is carried by spin angular momentum [42, 43]. While spin currents interact efficiently with magnetization (or spin moments) via strong *s-d* exchange interactions, orbital currents cannot couple in conventional magnetic materials with nearly quenched OAM by any strong exchange interaction and, therefore, one cannot make use of the large orbital currents to effectively interact with conventional spin-based magnets.

The study of CoO/dynamic OAM generator bilayers, presented in the following addresses this knowledge gap. The results in Sec. 7.1 and 7.2 are based on a first-author work of the author of this thesis, currently under review, which investigates the giant OMR resulting from the combination of OAM-dominated materials, such as CoO, and OAM current generators such as Cu* and Cr.[1] Sec. 7.3 focusses on CoO/Cu/Pt trilayers to investigate the interplay of SMR and OMR and the generation mechanism of OAM in CoO/Cu. This section is based on a work currently under preparation.[2]

7.1 Giant Orbital Magnetoresistance in CoO/Cu* Bilayers

Orbitronics research promises larger current-induced torques than conventional spintronics, due to the predicted large orbital Hall conductivities. Since the torque increases with the amount of angular momentum transferred from the current to the magnetic system, a stronger orbital response enables more efficient and effective control of magnetic order. [380]. However, the full potential of giant or-

[1] The following Secs. 7.1 and 7.2 and their subsections and figures were transcribed and adapted from Ref. [378] and its supplementary information, with the first author of this reference being the author of this thesis. Individual contributions are detailed in Appendix C.1.

[2] Sec. 7.3 and its subsections and figures was transcribed and adapted from Ref. [379] and its supplementary information, with the first author of this reference being the author of this thesis. Individual contributions are detailed in Appendix C.1.

bital currents has not yet been realized due to the afore mentioned weak coupling of dynamic OAM with conventional spin-based magnets. To address this issue of inefficient interaction with conventional magnets, the mitigation strategy has been the conversion of orbital currents into spin currents to interact with the spin-dominated magnetization of ordinary magnets. The usual remedy is to employ a material with strong SOC to mediate orbital-to-spin conversion [44, 46]. However, this approach yields only a modest, few-fold increase in torque efficiency [44, 381–383], far below the orders-of-magnitude improvement predicted for pure orbital currents, because the conversion still relies on the relatively weak relativistic SOC.

To exploit the potential of large orbital currents more efficiently, one needs to directly couple them to a magnetization carried by unquenched OAM (orbital magnetism), thus bypassing the need for the inefficient orbital-to-spin conversion step.

AFM CoO is an ideal platform to investigate this direct interaction between static orbital magnetization and dynamic orbital magnetization. CoO combines a large unquenched orbital magnetization with the advantages of AFMs such as THz spin dynamics [29, 347], immunity to external magnetic fields and low damping, which allows for the transport of angular momentum over long distances [384, 385]. The OAM of each Co atom is sizeable ($\approx$ 2.05 μ_B/atom) [177], unlike in 3d transition metal FMs for which orbital moments are nearly fully quenched due to the crystal field ($<$ 0.1 μ_B/atom) [386, 387]. The unquenched OAM in CoO contributes to both the staggered magnetization and magnetic anisotropies [121]. Further, the insulating nature of CoO is particularly suitable as it allows to rule out effects of current flow in the magnet such as self-torques or anisotropic MR effects [388, 389]. Thus CoO serves as an ideal system to investigate the interaction between orbital currents and orbital magnetization and to distinguish it from spin magnetization effects. The collinear magnetic and crystallographic structure of thin film CoO is shown in Fig. 7.1(a) (compare Sec. 4.1).

7.1.1 Sample Preparation and Characterization

We deposited epitaxial CoO(5 nm)/Pt(2 nm) and CoO(5 nm)/Cu*(6 nm) thin films on MgO(001) substrates using reactive magnetron sputtering (compare Sec. 4.2.1.1). Here, '*' denotes the natural oxidation of Cu, which serves as an orbital current

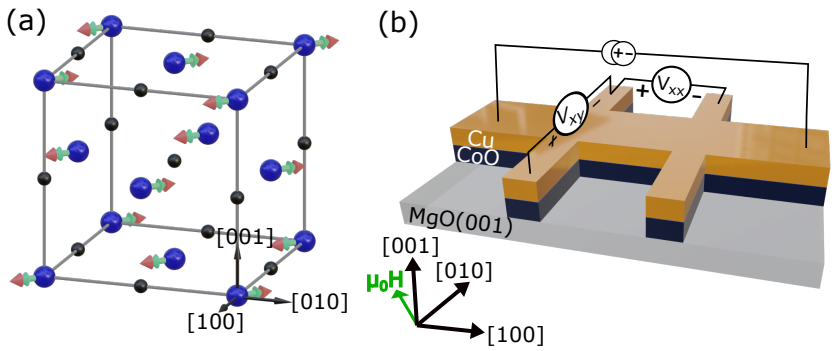

Figure 7.1: (a) Illustration of the magnetic and crystallographic structure of CoO with in-plane magnetocrystalline anisotropy, showing the Néel vector easy axis along the $[\bar{1}10]$ axis. The Co and O atoms are represented by blue and black solid spheres, respectively. The red and green arrows denote the spin and orbital angular momenta of each Co atom, respectively. (b) Schematic of the transverse MR measurement scheme with electrical contacts in the CoO/Cu* structure, including the magnetic field sweep direction $[1\bar{1}0]$, shown by a green arrow.

generator [44, 184], while Pt generates a spin current via the SHE [366]. As shown in Fig. 7.1(a), the CoO thin films exhibit a four-fold in-plane magnetocrystalline anisotropy with two magnetic easy axes of the Néel vector $\boldsymbol{n}$ oriented along the [110] and $[\bar{1}10]$ crystallographic axes [50, 121, 247].

To determine the crystallographic orientation, the lattice constant and the growth quality of our CoO thin films, we performed XRD measurements. Figure 7.2(a) shows the coupled $\theta - 2\theta$ scan for MgO(001)//CoO(5 nm)/Cu(6 nm). The observed peak position for CoO is consistent with the CoO(002) direction, in alignment with the orientation of the MgO(001) substrate. The position of CoO(002) is slightly shifted relative to the expected bulk value, indicating that the CoO thin film is strained. This strain arises from a lattice mismatch of 1.1% between the bulk lattice constants of the MgO substrate ($a = 0.4212$ nm) and CoO ($a = 0.4260$ nm). The growth induced strain shifts the Néel temperature (T_N) of our thin films to approximately ≈ 300 K, which is slightly higher than that of bulk CoO ($T_N = 291$ K for bulk CoO [213, 219]). Figure 7.2(b) presents the rocking curves for the CoO(002) thin film and MgO(002) substrate peaks. Both curves exhibit similar full-width-at-half-maximum values, indicating the high crystalline quality of the CoO film, with minimal dislocations, mosaicity, and defects. Moreover, the CoO peak is centered at the expected position of the film's Bragg reflection, highlighting the excellent

lattice alignment between the film and substrate.

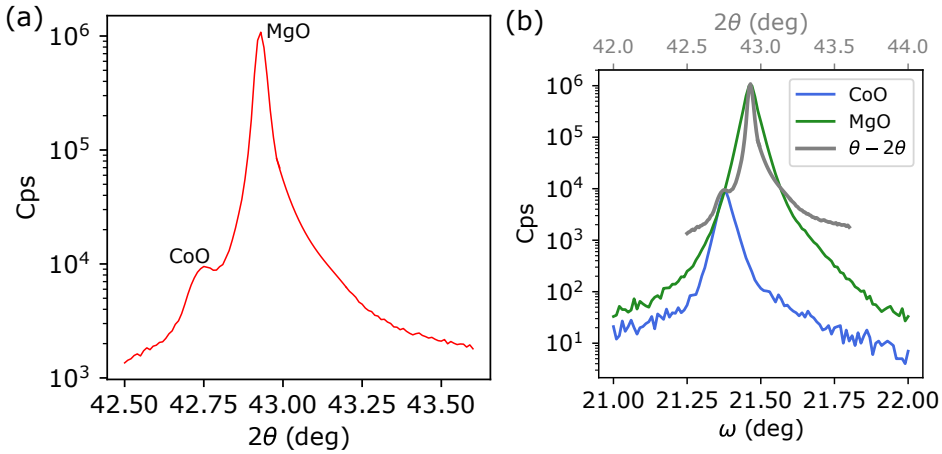

Figure 7.2: (a) $\theta - 2\theta$ XRD scan showing the (001) alignment of the CoO(5 nm)/Cu(6 nm) film on an MgO(001) substrate. (b) XRD rocking-curves of CoO(002) and MgO(002) planes on top of the $\theta - 2\theta$ scan (grey) from panel (a).

To assess the structural quality of the CoO/Cu* heterostructure, scanning transmission electron microscopy (STEM) with a high angle annular dark-field detector and electron energy loss spectroscopy (EELS) measurements were performed.[3]

The STEM image in Fig. 7.3(a) reveals coherent epitaxial growth of the CoO layer on the MgO substrate, confirming its high crystalline quality. The fast Fourier transform pattern in the inset of Fig. 7.3(a) shows that the Cu layer also maintains an epitaxial relationship with the underlying CoO layer indicating a sharp, clean and well-defined interface that facilitates the epitaxial growth on top of the CoO. The observed peak splitting indicates a relaxation of the epitaxial strain in the Cu layer. The map in Fig. 7.3(b) shows the variation of the horizontal lattice spacing in the stack, obtained through geometrical phase analysis of the image in (a) calculated with respect to the MgO substrate. To accomodate the strain arising at the CoO/Cu* interface, lattice dislocations with a periodicity of approximately 1.3 nm arise.

Figures 7.4(a,b) show EELS elemental maps and corresponding atomic fraction profiles extracted along the growth direction. The O-map and profile (green) confirm a strongly oxidized region at the sample surface, with an estimated oxidation depth of 2.3 ± 0.3 nm, accompanied by a noticeable reduction in the Cu signal near

[3]The STEM and EELS measurements were performed by - and -.

the top of the Cu layer (turquoise curve in Fig. 7.4(b)).

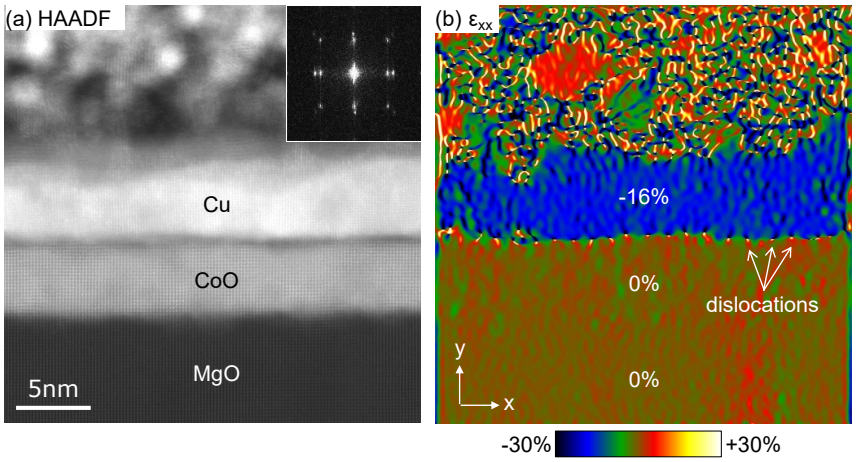

Figure 7.3: (a) STEM image with corresponding fast Fourier transform in the inset showing epitaxial alignment. (b) Horizontal deformation map calculated via geometric phase analysis. The deformation is calculated with respect to the lattice spacing of the MgO substrate following $\epsilon = (d - d_{\mathrm{MgO}})/d_{\mathrm{MgO}}$, for which d is the local lattice spacing.

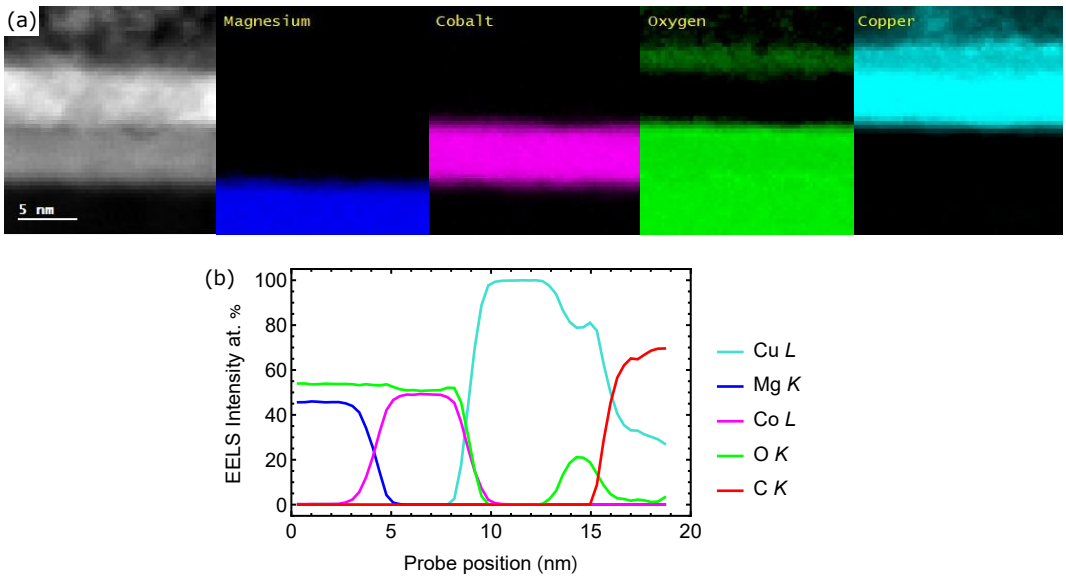

Figure 7.4: (a) STEM image and corresponding elemental EELS maps of Mg (blue), Co (pink), O (green) and Cu (turquoise). (b) Atomic fraction profiles along the growth direction.

Further, to confirm the existence of an orbital moment in our CoO thin films, we performed XMLD-PEEM measurements. A direct experimental quantification of orbital moments in AFM oxides is very challenging. As CoO is an ordered AFM and a correlated Mott insulator, the $2p \longrightarrow 3d$ transitions exhibit strong multiplet splitting due to intra-atomic Coulomb and exchange interactions. Therefore, the XMCD and XMLD sum rules are not applicable (compare Sec. 4.4.1.1). Moreover, the Co ions experience a strong octahedral crystal field in the lattice, which mixes the spin and orbital characters in the ground state. In addition, hybridization between Co *3d* and O *p* states delocalizes the magnetic charge, making the sum rules also not applicable.

Therefore, we used an inverse approach to quantify the unquenched orbital moment in our CoO thin films. We measured energy-dependent XAS in the CoO thin films and compared these experimental results with multiplet calculations of the $2p \longrightarrow 3d$ transition and simulations of the expected XMLD signal for different spin and orbital moments. Such calculations can be found in literature and have been conducted, for example, by S.I. Csiszar et al. [234], and in R. Abrudan et al. they also find a large orbital moment in their CoO films [390].

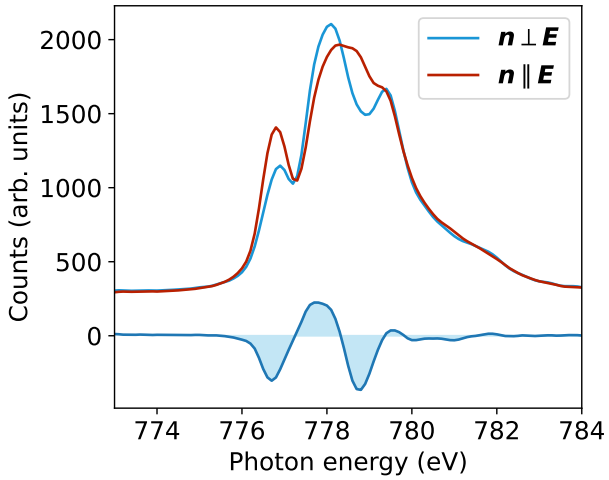

Figure 7.5: XAS measurements at the Co L_3 edge for two 90° different orientations of the Néel vector $\boldsymbol{n}$ with respect to the X-ray polarization $\boldsymbol{E}$.

We show our XAS data in Fig. 7.5. The dichroic signal reflects how crystal field splitting and SOC mix otherwise degenerate *d*-orbitals. When the orbital moment is fully quenched ($L = 0$), the XMLD spectrum is smooth and only shows basic

anisotropy of the L_3 edge. But if SOC and incomplete crystal field quenching allow for a residual OAM, transitions into spin-orbit coupled multiplets create interference ("beating") patterns in the spectrum [391, 392]. These modulations lead to non-monotonic variations in the intensities between 776.0 eV and 779.5 eV at the L_3 edge of Co in our measurements, which serve as a sensitive fingerprint of large unquenched OAM, since XMLD directly probes anisotropic charge and spin-orbit distributions rather than net magnetization. Comparing the data with the XMLD spectrum measured by Abrudan et al. [390], we find the same key features, underlining the existence of a large unquenched orbital moment in our thin films (larger than 1 μ_B/atom).

To investigate the interaction between orbital current and static OAM, we fabricated Hall bar structures consisting of a 6 µm wide bar and two 2 µm wide wires perpendicular to it, separated by 6 µm and patterned along the sample's magnetic hard axes (see Fig. 7.1(b) for the example of CoO/Cu*). For the CoO(5 nm)/Cu(6 nm) sample we grow CoO(5 nm)/Cu(6 nm)/Pt(2 nm) and prior to the measurements remove the Pt by argon etching for 8 s.

When a charge current $\boldsymbol{j}_c$ is injected into the Hall bar, it generates orbital current in Cu* via OHE and/or OREE. A non-equilibrium orbital density μ_o then builds up at the CoO/Cu* interface. Analogous to the SMR mechanism [145], OMR refers to the change in electrical resistance of a non-magnetic material due to the interaction of orbital currents with the magnetization of an adjacent magnetic layer. The change arises from the absorption or reflection of the orbital currents at the interface, depending on the magnetic configuration of the AFM, which in our case is governed by the orientation of the Néel vector.

7.1.2 Zero-Field Magnetoresistance Measurements

Although SMR has been studied in Pt adjacent to a range of materials, including 3d FMs and insulating magnets [145, 393], the reported pure OMR remains weak for the materials under investigation [185], primarily due to the lack of direct coupling to conventional spin-dominated magnetization in these materials. We first consider a device of CoO/Pt to check the interaction of spin currents with CoO to compare it to the interaction of orbital currents in CoO/Cu*. Initially, we apply an external magnetic field of 13 T along the [110] direction of CoO to align the Néel vector along the well-defined [$\bar{1}$10] magnetic easy axis [50]. We then sweep the

magnetic field along the $[\bar{1}10]$ direction and probe the orientation of Néel vector by measuring the transverse resistance (R_{xy}) at $T(< T_N) = 150\,\mathrm{K}$. R_{xy} exhibits different behavior when the magnetic field is swept upward and downward in the range of $7.5 - 9\,\mathrm{T}$ as shown in Fig. 7.6(a). This change in R_{xy}, normalized by the mean longitudinal resistance $\bar{R}$, represents the spin-flop transition and rotation of the Néel vector by 90°, i.e., from $[\bar{1}10]$ to $[110]$ in this case. The orientation of the Néel vector remains unchanged upon reduction of the magnetic field to zero [50]. Therefore, the difference in R_{xy} at zero fields, before and after the magnetic field sweep, effectively probes the two perpendicular Néel vector orientations, providing a measure of SMR amplitudes:

$$\Delta R_{xy}/\bar{R} = [R_{xy}(\boldsymbol{n}_2) - R_{xy}(\boldsymbol{n}_1)]/\bar{R} \tag{7.1}$$

where $\boldsymbol{n}_{1,2}$ are the two orthogonal Néel vector orientations along the two magnetic easy axes $[1\bar{1}0]$ and $[110]$, respectively. $\bar{R}$ is the longitudinal resistance averaged for the two states. The measurements are performed with the electrical current $\boldsymbol{j}_c \parallel [100]$ crystallographic direction. The sign of the MR is defined as positive if upon reorientation of the Néel vector from $[\bar{1}10]$ to $[110]$, the transverse resistance increases, while a decrease in transverse resistance upon reorientation is defined as a negative MR.

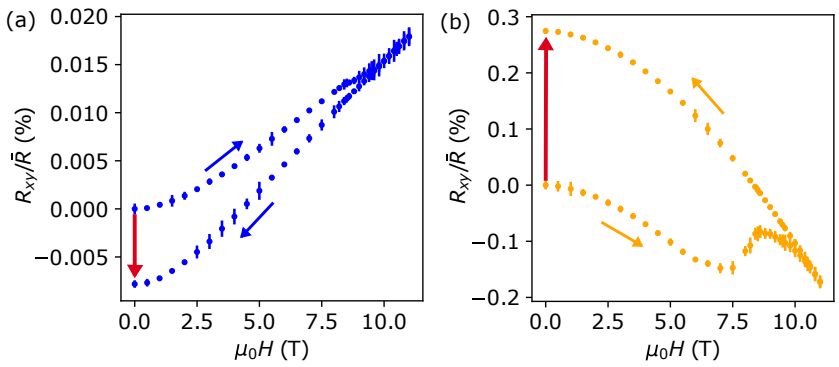

Figure 7.6: Magnetic field-sweep measurements on (a) CoO(5 nm)/Pt(2 nm) and (b) CoO(5 nm)/Cu*(6 nm) samples, respectively. Both samples exhibit a spin-flop transition between 7.5 T – 9 T. The change in transverse resistance corresponding to the two perpendicular Néel vector orientations is indicated by the red arrow. The measurements are performed at $T = 150\,\mathrm{K}$.

Since the MR is estimated from resistance measurements taken at zero magnetic fields, additional contributions to the MR from the metallic layers, such as Hanle MR [191] and ordinary Hall effect, can be ruled out. The amplitude of SMR ($\Delta R_{xy}/\bar{R}$) in CoO/Pt at 150 K is found to be $-0.0078 \pm 0.0001\%$. This amplitude of the SMR is in the order of what is found for all combinations of Pt with magnetic insulators with spin-based magnetization such as NiO, YIG and α-Fe_2O_3 (hematite) [145, 170, 394].

We now compare this to OMR measurements on the CoO/Cu* sample. Figure 7.6(b) shows the transverse resistance R_{xy}, normalized by the longitudinal resistance, as a function of the magnetic field measured at $T = 150$ K (below T_N). The magnetic field protocol is the same as that for the measurements in Fig. 7.6(a). An abrupt change in R_{xy} is observed at the spin-flop field, which occurs at approximately $7.5-9$ T. This value is similar to the spin-flop field observed for CoO/Pt, indicating that the magnetocrystalline anisotropy of CoO remains largely unaffected by the choice of metallic layer on top. The observation of MR in the absence of any significant spin current source indicates the presence of orbital currents originating from Cu*, consistent with previous observations of OMR in Cu* adjacent to metallic FMs [185]. Most importantly, we observe a change in the sign of R_{xy} at the spin-flop field compared to the CoO/Pt structure. This result represents a unique characteristic of orbital current interaction with the unquenched orbital moment in CoO. Such an interaction has not been reported in previous studies on $3d$ transition metal FMs with quenched OAM [185]. The most striking result is the OMR magnitude of $0.2752 \pm 0.0005\%$, which is approximately 36 times larger than the SMR observed in CoO/Pt.

Although Cu* has been recently identified as an efficient source of orbital current [44, 381], an increase of MR in CoO/Cu* by two orders of magnitude cannot be explained solely by the large orbital currents, as the magnitude of OMR in previous experiments on NiFe/Cu* (0.05 %) is found to be significantly smaller than the OMR in our CoO/Cu* [185]. Furthermore, torque experiments reveal that the torques on magnetic layers, in which the OAM is quenched, are not enhanced by two orders of magnitude, since the orbital currents from Cu* need to be converted into spin currents via the weak SOC of Pt [44, 381].

Our experimental results thus suggest that additional factors or mechanisms must contribute to the giant amplitude of the MR in the CoO/Cu* system. Specifi-

cally, our findings provide strong evidence that while spin currents from Pt interact with the spin magnetization in CoO via via *s*-*d* exchange coupling, in which the spin-polarized conduction electrons from Pt interact with the localized *d*-electron moments in CoO, the orbital current from Cu* interacts strongly with the large unquenched component of the orbital magnetization in CoO. This interaction is dominant in CoO/Cu* samples in which no significant source of spin current is present, and is thus responsible for the giant OMR compared to the conventional CoO/Pt.

Additionally, the opposite sign of MR in the two systems indicates the different origin of the two signals. The sign of the spin current from Pt and the orbital current from Cu* is theoretically predicted [39] and experimentally found to be the same, as confirmed by the same sign of SMR and OMR in NiFe/Pt and NiFe/Cu* systems [185]. One possible explanation is that the unquenched OAM of CoO can give rise to an orbital quadrupole (OQP) moment [395]. Our results indicate that the dynamics of the OQP moment in CoO are fundamentally different from the classical dynamics of FMs. A similar difference to quadrupole moment dynamics in FMs has recently been experimentally demonstrated [396].

To understand the underlying mechanisms for the large MR magnitude and its sign, we compare the temperature dependence of the MR in the two systems. Figure 7.7(a) shows the evolution in MR as a function of temperature in CoO/Cu* (top panel) and CoO/Pt (bottom panel). The sign of MR in CoO/Cu* remains opposite to that of CoO/Pt throughout the measured temperature range. However, the magnitude does vary. In CoO/Cu*, the MR signal increases initially, from 0.15% at 275 K to a peak of 0.28% at 150 K, followed by a slight decrease as the temperature is further lowered to 75 K. For comparison, we have also measured the temperature dependence of MR in CoO/Pt, which shows a similar trend of the magnitude with temperature, but with an opposite sign and a two-order of magnitude lower amplitude compared to CoO/Cu*. Remarkably, the ratio of MR amplitude in the CoO/Cu* sample compared to the CoO/Pt sample increases further at lower temperatures, as shown in Fig. 7.7(b). At $T = 200$ K, the MR in CoO/Cu* is a factor 35 larger than in CoO/Pt. At $T = 75$ K the ratio increases to a factor of more than 150. Although a similar temperature dependence has been previously observed in studies of SMR and torques in YIG/Pt bilayers [394], as well as in FM/Pt bilayers, the increase in the ratio of OMR in CoO/Cu* to SMR in CoO/Pt suggests that

two different mechanisms are involved. We attribute this temperature dependence primarily to angular momentum relaxation mediated by phonon scattering, which likely plays a significant role for SMR [394] but OAM is not prone to these damping mechanisms.

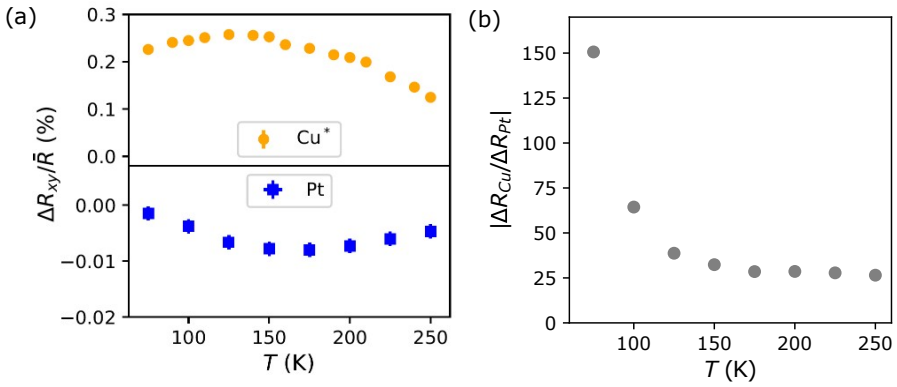

Figure 7.7: (a) The difference in OMR as a function of temperature. The top panel presents the results for CoO/Cu* (in orange), while the bottom panel shows the results for CoO/Pt (in blue). (b) The ratio of MR in CoO/Cu* vs. CoO/Pt as a function of temperature.

The observed orbital current could have its origin primarily in either the bulk Cu* via OHE or at the surface via an OREE. To determine the origin, we perform Cu* thickness-dependent measurements of OMR in CoO/Cu*(t) samples at 150 K. To ensure maximum comparability of the Cu* thickness dependence on OMR, all Cu* thickness dependence measurements were performed on the same Hall bar device. This approach minimizes the impact of any potential variation arising from the CoO/Cu* interface due to growth conditions on the measured OMR. Therefore, we progressively reduce the Cu* layer thickness using an Ar^+ ion milling technique, followed by exposure to air for 12 hours after each etching step. The remaining Cu* thickness after each etching step was estimated by measuring the sheet resistance of the Cu* layer and comparing it with the sheet resistances of as-grown films of known Cu* thicknesses. For the as-grown samples with varying Cu* thicknesses, we used the Van der Pauw method [397] to determine the sheet resistance (R_S). For the etched Hall bar structure, we measured the longitudinal resistance at room temperature and accounted for the device geometry ($w = 8\,\text{nm}$, $l = 6\,\text{nm}$) by dividing it by a factor of 1.33. Figure 7.8(a) shows the sheet resistance as a function of etch time. In Fig. 7.8(b), we show how the sheet

resistances of the etched films are matched to those of the as-grown samples. It is worth noting that a Cu* layer with a thickness of 2 nm was already fully oxidized, rendering the sheet resistance measurement impossible.

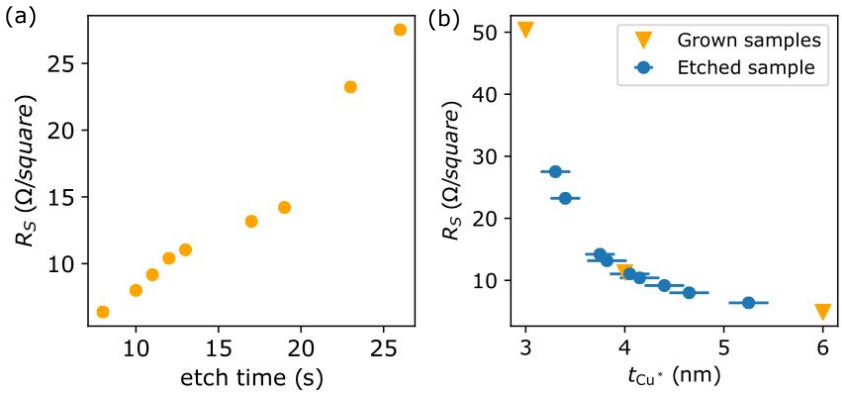

Figure 7.8: (a) Sheet resistance R_S of the etched Hall bar device as a function of etch time. (b) Comparison of sheet resistance of as-grown films with varying Cu* thickness and the sheet resistance of a Cu* layer after several Ar-ion etching steps to calibrate the thickness of the etched Cu* sample.

In Fig. 7.9, we show the Cu* layer thickness dependence of the OMR. The results reveal that the OMR remains nearly constant at approximately 0.32 % for Cu* thicknesses ranging from 3.7 to 5.5 nm. When the Cu* thickness is reduced further to 3.2 nm, the OMR decreases slightly, from 0.32 % to 0.22 %. For Cu* thicknesses below 3.2 nm, the sample becomes insulating, making it impossible to measure any OMR. This observed trend suggests that the orbital current responsible for the OMR in our samples predominantly originates at the surface of the Cu layer. The pronounced oxidation of the Cu layer detected in the EELS measurement likely facilitates orbital current generation. Even the presence of a very thin layer of oxygen at a Cu surface can give rise to an OREE [38]. The large OMR signal can thus result from the efficient generation of large orbital currents at the oxidized Cu surface by OREE. Furthermore, the nearly constant OMR observed in the thickness range of 3.7-5.5 nm indicates that the underlying mechanism remains stable within this regime. Although the OMR originates from a surface effect, a minimum Cu thickness is required to maintain a consistent Cu* layer while preserving a thin region of unoxidized Cu underneath. Within this thickness range, the Cu volume is sufficient to maintain an oxygen gradient and an uniform Cu* thickness, which supports robust orbital current generation and transport, making it more suitable

for practical applications.

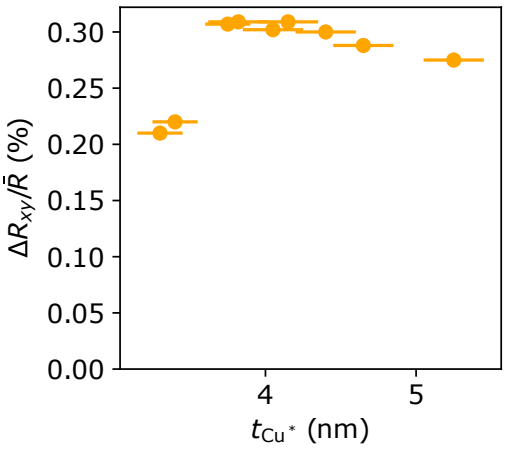

Figure 7.9: The difference in transverse resistance for two perpendicular Néel vector states at zero field as a function of Cu-layer thickness in CoO/Cu*(t). The measurements were performed at a constant temperature of $T = 150$ K.

7.1.3 Angular Dependent Magnetoresistance Measurements

To doublecheck that the observed effect originates from the magnetic properties of the CoO layer, we measure the angular-dependence of R_{xy} for different magnetic field amplitudes. We performed these angular-dependent MR measurements on CoO/Pt and CoO/Cu* at various external magnetic fields, ranging from below to above the spin-flop fields of CoO. A static magnetic field of up to 11 T was applied at a temperature of 200 K, and the samples were rotated in the xy-plane to vary the in-plane angle between the applied electric current and the magnetic field. The angle was varied over a range of 300° in steps of 1°. The MR in the xy-plane for CoO/Pt and CoO/Cu* is shown in Fig. 7.10(a) and (b), respectively.

Our measurements reveal that, for externally applied magnetic fields below the spin-flop field (7 T), the angular scans in the xy-plane exhibit a sinusoidal variation in transverse resistance. However, when the in-plane magnetic field exceeds the spin-flop field, additional hysteresis loops emerge, centered around the hard-axis directions ([100], [010], and [$\bar{1}$00]) of the sample. These hysteresis loops can be attributed to field-induced anisotropy arising from the unquenched OAM in CoO [121]. The different behavior of the two signals raises questions about their origin and their respective contributions to the overall MR. To address this, we

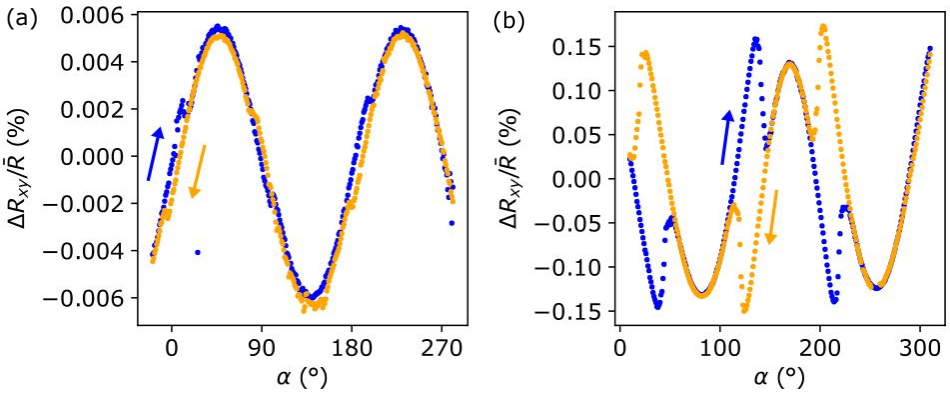

Figure 7.10: Angular dependence of transverse MR in (a) CoO/Pt and (b) CoO/Cu* at 200 K for an applied magnetic field of 11 T. The blue and orange data points represent two different rotation directions, as indicated by the colored arrows.

analyzed the magnetic field dependence of the transverse resistance in the xy-plane by separating the sinusoidal and hysteretic components. We first calculated the required shift to align one branch of the hysteresis curve with the other. The magnitude of this shift corresponds to the amplitude of the hysteretic signal. Subsequently, we fitted a $\sin^2(\alpha)$ function to the shifted signal to represent the data without the hysteretic contribution, thereby determining the amplitude of the sinusoidal component. The two steps are illustrated in Fig. 7.11(a, b).

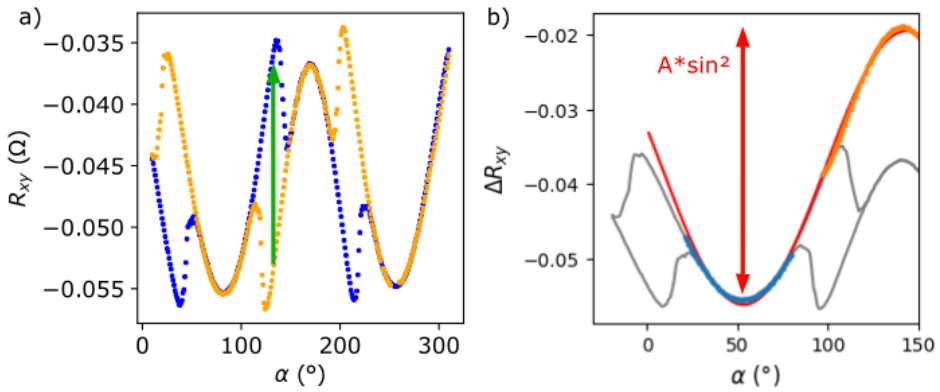

Figure 7.11: Exemplary data of CoO/Cu* to show how the two contributions to the signal can be disentangled. (a) The amplitude of the hysteretic signal can be determined by shifting one angle sweep direction (orange) of the hysteresis to the second one (blue), as shown by the green arrow. (b) By fitting a $\sin^2(x)$-function (red) to the minimum and maximum for positive and negative sweep direction (blue and orange) the amplitude of the sinusoidal signal is determined.

Figure 7.12 shows that the amplitude of the hysteretic signal is nearly zero for magnetic field strengths below the spin-flop transition for both samples. As the magnetic field is increased beyond the spin-flop field (8 − 9 T), the MR signal saturates, confirming that the observed effect is field-independent and ruling out the contribution from other spurious signal origins.

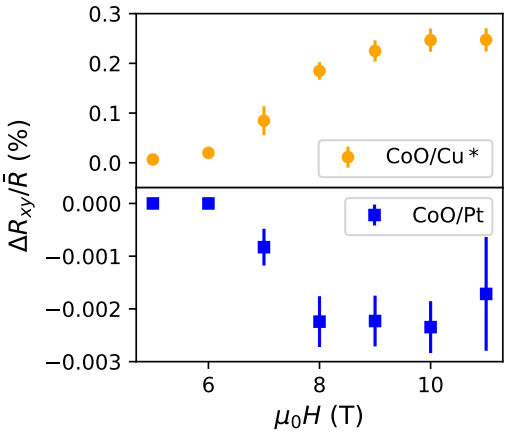

Figure 7.12: The change in transverse MR for CoO(5 nm)/Cu*(6 nm) and CoO(5 nm)/Pt(2 nm) as a function of applied magnetic field at $T = 200$ K.

In contrast, the sinusoidal contribution increases with the applied magnetic field as shown in Fig. 7.13. The magnetic field range, for which a hysteretic signal is observed without reaching the saturated amplitude yet, corresponds well to the range of magnetic field strengths in Fig. 7.6(a, b) for which the spin-flop transition is observed. Thus, indicating that the hysteresis in the MR signal corresponds to the switching of the Néel vector. The magnitude of the hysteretic component quantifies the MR amplitude. At 200 K, the extracted MR values for the CoO/Cu* and CoO/Pt samples are 0.25% and 0.002%, respectively. These values are consistent with those obtained using the zero-field approach (see Fig. 7.6(c)). Consequently, the observed hysteresis in the transverse MR not only confirms the presence of significant unquenched OAM in our samples but also provides a reliable measure of the MR amplitude through the height of the hysteretic component. On the other hand, the sinusoidal signal likely arises as an artifact due to MR contributions from the Cu layer and is not of magnetic origin from the CoO.

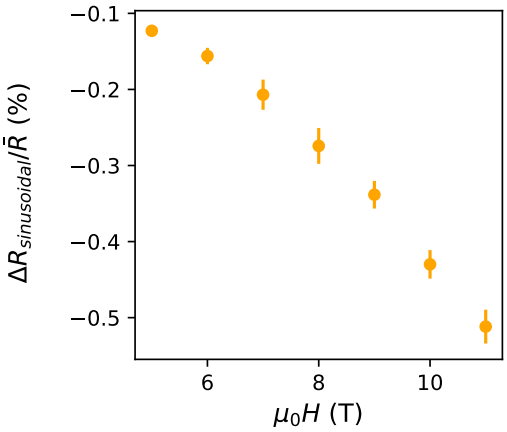

Figure 7.13: Amplitudes of the spurious sinusoidal signal as a function of applied magnetic field strength in CoO(5 nm)/Cu*(6 nm).

7.1.4 Theoretical Explanation of the Observed Giant Orbital magnetoresistance

The theoretical explanation of the observed giant OMR signal in CoO/Cu* compared to the ordinary SMR in CoO/Pt, including all calculations and simulations mentioned in the following, was provided by _____, _____ and _____ (all Forschungszentrum Jülich and JARA), _____ and _____ (Johannes Gutenberg University Mainz) and _____ (École Polytechnique Paris) [378].

CoO is known for its uncompensated, atomic-like orbital magnetism of d-electrons which arises as a result of a combination between the crystal field, band filling and electron-electron correlation of t_{2g}-electrons [241, 398]. First-principles calculations for CoO with the experimentally measured lattice parameters predict the value of the band gap on the order of 2.5 eV, with the magnitude of local spin and orbital moments on the order of 2.70 μ_B and 1.2 μ_B. The spin and orbital moments preserve their magnitude once the effect of SOC is gradually switched off in electronic structure calculations, proving it is intrinsic to CoO's electronic structure. While the spin degree of freedom is coupled to the orbital moments via relatively weak SOC, the effect of significant orbital splitting among the states with opposite orbital polarization, which accounts for the order of the band gap, can be perceived in the orbital channel only as a result of an effective orbital exchange term in

the Hamiltonian which signifies the repulsion energy between orbitally-polarized states.

To probe the response of CoO to injected spin and orbital currents, first-principles linear-response calculations were performed. These calculations determine how the spin moments (S_i), orbital moments (L_i), and OQP moments ($\{L_i, L_j\}$) change when spin- and orbital-dependent exchange fields are applied. Such exchange fields mimic the effect of spin and orbital currents on the electronic structure of bulk CoO in case of CoO/Pt and CoO/Cu* interfaces.

The calculations of the corresponding response tensors for the [110] and [1$\bar{1}$0] directions of the Néel vector within the band gap of CoO reveal that the response to the induced orbital fields is orders of magnitude larger than the response to spin exchange fields – an effect that clearly originates from the unquenched orbital momentum of Co atoms. Moreover, the spin and orbital response tensors exhibit a much stronger anisotropy with respect to the direction of $\boldsymbol{n}$ when perturbed by an orbital field, whereas the response to injected spin is only very weakly anisotropic. This behavior is expected, since the response to an orbital perturbation directly reflects the intrinsic anisotropy of the magnetic structure in CoO. This intrinsic anisotropy is evident, for example, in the dependence of the orbital moments and crystal-field splittings on the direction of $\boldsymbol{n}$, that are observed in the calculations. Overall, we can conclude that driving spin-and-orbital dynamics through orbital injection from the CoO/Cu* interface leads to a more complex, more anisotropic, and more pronounced dynamical response of the coupled Co spin and orbital moments.

Building on this strong orbital sensitivity, CoO's response to injected OAM can give rise to a giant OMR amplitude, for example through modifications of the anisotropy profile caused by the large, non-vanishing current-induced OQPs $\langle\{L_i, L_j\}\rangle$. Recently, the currents of OQP moments, coupled to spin via the SOC of Pt, have been shown to mediate the injection of a magnetic octupole into altermagnetic materials. This injection induces a novel type of torque on the Néel vector $\boldsymbol{n}$ via the linear coupling between $\boldsymbol{n}$ and the magnetic octupole moment [399]. In CoO, it has been recently shown that the OQP moment, arising from a combined action of an externally applied magnetic field and SOC, plays a key role in driving intricate spin-orbital dynamics via the energy term that couples components of $\boldsymbol{n}$ and $\langle\{L_x, L_y\}\rangle$ [121]. Due to this coupling of the OQP and the spins, the induced

quadrupole moment generates a strongly anisotropic torque on the Néel vector, thus inducing coupled spin-orbital dynamics resulting in energy losses and an increase in the MR signal.

Since the orbital dipole-to-quadrupole conversion does not, in principle, require SOC, the effective OQP torques generated by orbital injection from Cu* are expected to be very efficient, ultimately leading to strong absorption of the electrically generated OAM. Note that the large orbital moments and OQPs in CoO are key to producing such torques.

One remarkable feature of CoO, compared to other materials of this kind, are strong orbital exchange interactions. Ab-initio calculations of the spin and orbital dipole and quadrupole exchange couplings in CoO reveal that isotropic AFM next-nearest-neighbor spin-spin exchange interaction is by far the largest (about 90 meV). However, among the nearest-neighbor exchange interactions, the largest magnitudes appear in the orbital quadrupole-quadrupole sub-block, with the strongest coupling on the order of 12 meV. This provides an additional, purely orbital channel for energy dissipation by low-energy excitations of the orbital degrees of freedom when their corresponding dynamics is driven by the orbital current generated at the CoO/Cu* interface. To show this, we consider the absorptive part of the susceptibility of CoO and compute it along high-symmetry directions of the parent fcc Brillouin zone. These computations reveal that, within the considered range, two broad groups of excitation bands are present: a lower band lying between 20 and 45 meV, and an upper band extending beyond 60 meV. While the exact energetic position of the excitation bands depends sensitively on the structural details of the film and its interfacial properties, the relative energy difference between the lower and upper bands arises from the qualitatively different interactions that define them. We find that the lower band (20-45 meV) is mainly of orbital-quadrupole character, whereas the upper band is mainly due to spin excitations.

Consequently, the efficient excitation of orbital modes by the injected orbital current, in addition to the coherent torques, can lead to the significantly stronger orbital-current absorption in CoO/Cu* compared to the spin-current-driven dynamics in Pt-based bilayers, thereby explaining the experimental findings.

To summarize, in the context of the measured OMR, the large, unquenched orbital dipole moments L_i on Co underlie the strong and highly anisotropic response

of CoO to injected OAM, making the material particularly susceptible to orbital-current-induced torques. The induced OQP moments, in turn, generate strongly anisotropic torques on the Néel vector via the coupling term $\boldsymbol{n} \cdot \langle \{L_i, L_j\} \rangle$ and can efficiently couple to low-energy orbital-quadrupole modes, providing an important dissipation channel that contributes substantially to the enhanced OMR signal.

7.2 Magnetoresistance in Systems with Different Dynamic Orbital Angular Momentum Sources and Orbital-Quenched Magnets

The generation of orbital currents is not confined to the OREE observed in Cu/Cu* systems. Recent theoretical studies have predicted that a broad class of materials can exhibit substantial orbital Hall conductivities, particularly transition metals with intrinsically weak SOC, such as Cr, Ru, and Ti [39]. This raises the fundamental question if the effective coupling between dynamic OAM and orbital momentum dominated magnetic order is a general phenomenon, or rather is restricted to a specific material combination.

We, therefore, extend our analysis beyond the naturally oxidized CoO/Cu* system to evaluate the universality of giant OMR and to determine whether it can be realized in materials more suitable for practical applications, specifically, those that do not rely on oxidation.

Further, to validate our interpretation, we expand our study to materials for which the static OAM is quenched and does not contribute significantly to the magnetization to check for the absence of a MR signal.

7.2.1 Orbital Magnetoresistance Measurements on CoO with Cr and Ti as Orbital Angular Momentum Generating Materials

To assess whether the observed OMR mechanism is specific to oxidized Cu or can also be realized using other OAM-generating materials, we conducted additional experiments employing the weak-SOC transition metals Cr and Ti. The multilayer stacks CoO(5 nm)/Cr(13 nm)/Al_2O_3(5 nm) and CoO(5 nm)/Ti(9 nm)/Al_2O_3(5 nm) were fabricated on MgO(001) substrates, with Al_2O_3 capping layers preventing

additional oxidation. The CoO thickness was chosen to match that used in the CoO/Cu* reference samples, while the Cr and Ti thicknesses were selected based on their orbital diffusion lengths of approximately 6.5 nm [376] and 4-5 nm [40, 400], respectively. Both Cr and Ti are theoretically predicted to exhibit large orbital Hall conductivities but negligible spin Hall conductivities [39, 382].

When Cr serves as the OAM source, a pronounced MR signal is observed that cannot be attributed to the SHE. Following the same measurement protocol as used for the CoO/Cu* and CoO/Pt systems (see Sec. 7.1.2), the transverse resistance R_{xy} normalized by the longitudinal resistance is plotted as a function of in-plane magnetic field in Fig. 7.14(a). At $T = 250\,\mathrm{K}$, an abrupt change in R_{xy} occurs near 11 T, corresponding to the CoO spin-flop transition. The slightly higher spin-flop field compared to CoO/Pt and CoO/Cu* is attributed to differences in film deposition conditions leading to higher anisotropies of the CoO. Above $T = 300\,\mathrm{K}$, this feature disappears, confirming its magnetic origin. Although the raw data (inset of Fig. 7.14) displays a substantial background signal arising from the ordinary Hall effect and possibly other parasitic contributions, the zero-field extraction procedure ensures that these effects do not influence the interpretation.

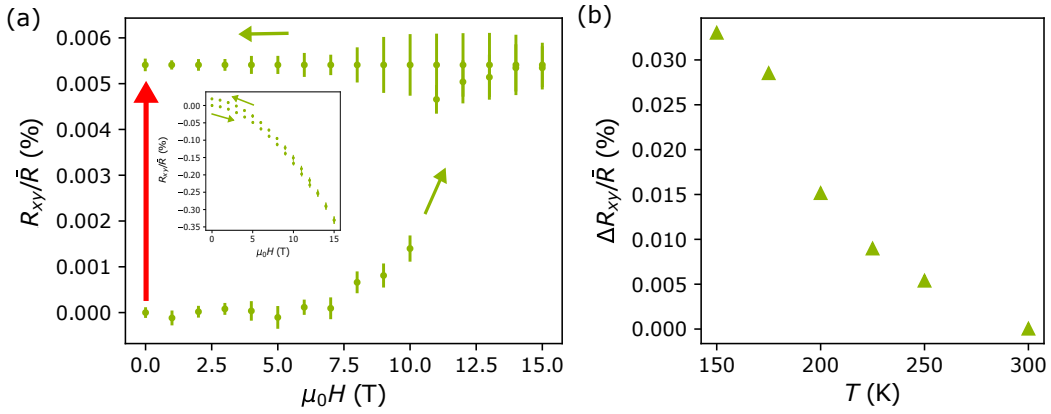

Figure 7.14: (a) Normalized $R_{xy}/\bar{R}$, i.e., OMR, as a function of in-plane magnetic field in a CoO/Cr sample at a temperature, $T = 250\,\mathrm{K}$. The $R_{xy}/\bar{R}$ exhibits abrupt changes at ≈11 T field, corresponding to the spin-flop field of CoO. The inset shows the raw data with a parabolic background signal from Cr. (b) The OMR in CoO/Cr as a function of temperature.

The temperature dependence of the OMR in CoO/Cr, shown in Fig. 7.14(b), reveals a monotonic increase of $R_{xy}/\bar{R}$ upon decreasing the temperature, reaching 0.033% at $T = 150\,\mathrm{K}$, approximately five times larger than the SMR amplitude

observed in CoO/Pt. Given the weak SOC and negligible spin Hall conductivity of Cr [39, 382], this enhancement must arise from the interaction between the orbital current generated in Cr and the orbital magnetization of CoO. The OMR in CoO/Cr exhibits the same sign as in CoO/Cu*, in contrast to the reversed sign of SMR observed for CoO/Pt.

These findings demonstrate that the substantial enhancement of the OMR does not rely on the oxidation of Cu or on poor metallic conductivity. Instead, it represents a more general characteristic of orbital-current-driven magnetotransport in systems with unquenched orbital moments. This makes the orbital-orbital coupling more appealing for applications, given that Cu oxidation is difficult to control.

To probe the universality of the orbital-orbital coupling in systems of orbital dominated magnetism and weak-SOC metals with substantial orbital Hall conductivity, we now extend our investigation to Ti to evaluate whether the observed effects are material-independent or if differences depending on the orbital current generator arise.

Measurements on the MgO//CoO(5 nm)/Ti(9 nm)/Al_2O_3(5 nm) stack reveal similar magnetic-field-dependent features, including a clear spin-flop transition at $T = 200\,\mathrm{K}$ near 4 T, as shown in Fig. 7.15(a). The background signal is notably smaller than in Cr, likely due to the higher resistivity of Ti, while the reduced spin-flop field again reflects variations in the growth conditions. The zero-field OMR amplitude at $T = 200\,\mathrm{K}$ is smaller than that in CoO/Pt and exhibits the same sign as the spin-based MR. Since Ti possesses a negligible and negative spin Hall conductivity, opposite to that of Pt, the observed consistency in sign indicates that the response cannot originate from spin currents. It may instead arise from orbital effects, even though the MR amplitude is small. The somewhat lower amplitude in Ti compared with Cr suggests that the efficiency of orbital-current generation or transmission at the CoO/metal interface may differ between materials. Material-dependent factors such as orbital polarization, interfacial coupling symmetry, or the orbital diffusion length could underlie this contrast, but further experiments are required to precisely determine the origin.

Figure 7.15(b) shows the temperature dependence of the MR in CoO/Ti. Owing to the reduced spin-flop field in this sample, a wider temperature range could be explored. The MR amplitude vanishes above the Néel temperature and increases

continuously upon cooling down to 25 K, emphasizing its distinct mechanism compared to conventional spin-based SMR systems, where the signal typically shows a maximum at intermediate temperatures (compare Fig. 7.7 for CoO/Pt) and decreases at low temperature as the spin modes freeze out.

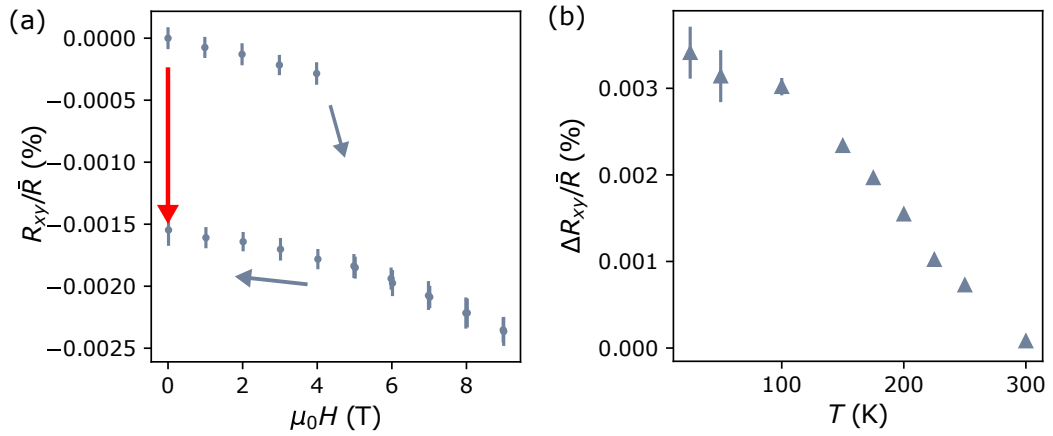

Figure 7.15: (a) Normalized $R_{xy}/\bar{R}$ as a function of in-plane magnetic field in a CoO/Ti sample at a temperature, $T = 200$ K. The $R_{xy}/\bar{R}$ exhibits abrupt changes between 4 and 5 T magnetic field, corresponding to the spin-flop field of CoO in this sample at 200 K. (b) The MR in CoO/Ti as a function of temperature.

A comparison of the MR signals in CoO combined with Pt, Cu*, Cr, and Ti at $T = 150$ K is summarized in Fig. 7.16. The conventional SMR in CoO/Pt serves as a reference. The OMR in CoO/Cu* is enhanced by more than two orders of magnitude and exhibits an opposite sign. CoO/Cr shows an enhancement by a factor of approximately four to five with the same sign as CoO/Cu*, whereas CoO/Ti yields a smaller signal, reduced by roughly a factor of three compared to the SMR in CoO/Pt, preserving the same sign as CoO/Pt. These results indicate that the sign of the orbital signal is strongly influenced by the choice of OAM-generating material, even though Cr and Ti exhibit orbital Hall conductivities of the same sign [39].

The differences between Cr and Ti likely reflect variations in orbital polarization, such as magnitude of orbital accumulation or symmetry of the occupied orbital states, or in the efficiency and symmetry of interfacial coupling to CoO. The dominant coupling mechanism may differ across materials. Differences in the orbital diffusion length may also contribute to the observed material dependence of the OMR amplitude. These hypotheses warrant further investigation on the

different sample systems to unambiguously identify the mechanism.

Overall, these results not only confirm the generality of orbital-current-driven magnetotransport in CoO but also reveal a rich variety of interfacial coupling mechanisms that depend sensitively on the electronic structure and orbital character of the OAM source. Understanding these interactions and their dependence on material selection, orbital polarization, and interfacial structure represents a promising direction for future research in the emerging field of orbitronics.

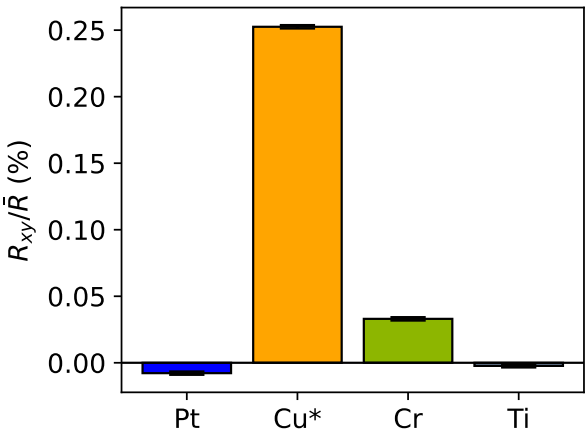

Figure 7.16: Comparison of MR at a temperature of $T = 150\,\mathrm{K}$ in CoO thin films with different capping layers for spin and orbital current generation.

7.2.2 Measurements on Materials with Quenched Orbital Angular Momentum

To validate our interpretation of the OMR effects observed in CoO, we performed control experiments on systems with quenched OAM to distinguish orbital from spin-related contributions.

As a reference, we investigated α-Fe_2O_3, an antiferromagnetic insulator with nearly quenched OAM [401] that is expected to show negligible response to orbital currents.

We performed SMR measurements on a 100 nm c-cut α-Fe_2O_3 film using a spin current generated in Pt, as shown in Fig. 7.17(a). A small SMR signal on the order of $\sim 3 \times 10^{-4}$ was detected at low magnetic fields when performing field-sweep measurements at 175 K in the easy-axis phase, in agreement with previous observations [402]. The Hall bars were patterned equivalently to those used for the

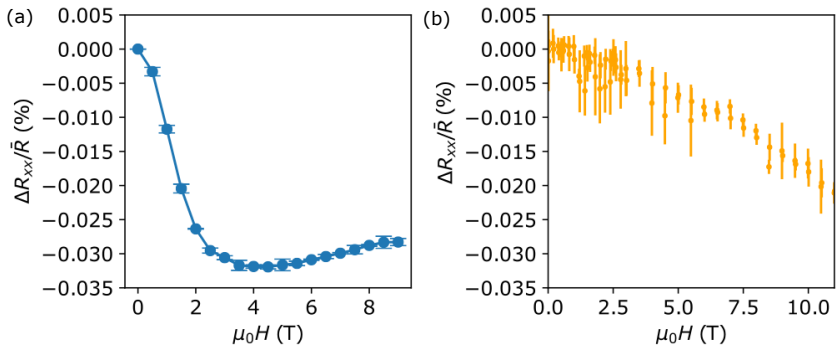

Figure 7.17: Interaction of spin and orbital currents with spin-dominated AFM $\alpha - Fe_2O_3$. (a) Longitudinal resistance of $\alpha - Fe_2O_3$/Pt and (b) $\alpha - Fe_2O_3$/Cu* bilayers at 175 K in the easy-axis phase for a magnetic field applied along the current direction.

CoO measurements, and electrical currents up to 1 mA were applied to ensure a good signal-to-noise ratio. To check for possible orbital contributions, we compared these results to MR measurements on the very same sample but this time interfaced with a 5 nm Cu* layer and found that the OMR was negligible. With the magnetic field oriented parallel to the current direction, no significant resistance change was observed at low magnetic fields (up to 2 T). Only at higher magnetic fields did a minor resistance change of about $\sim 0.2\%$ appear. However, since this field strength exceeds the spin-flop field of α-Fe_2O_3/Cu*, the origin of this signal cannot be related to the orientation of the Néel vector. Because the insulating nature of hematite prevents orbital-to-spin conversion, no SMR is expected in this sample, thus supporting our interpretation that the effects we observed in CoO originate from orbital physics.

In addition, we carried out control experiments on yttrium iron garnet YIG/Pt, YIG/Cu*, and YIG/Ru heterostructures to check if orbital current can give rise to a MR effect in magnets with fully quenched orbital moments. YIG is an insulating ferrimagnetic oxide in which the OAM is completely quenched, making it an ideal reference. Figure 7.18 shows that in the YIG/Ru and YIG/Cu* cases, no measurable MR signal was detected over a wide temperature range (from room temperature down to 7 K). In contrast, YIG/Pt exhibits the expected SMR and its well-known temperature dependence [145, 394]. These observations are consistent with previous studies [44, 381], which demonstrated that enhanced SOTs appear only when a Pt interlayer is present, an essential condition for converting orbital currents

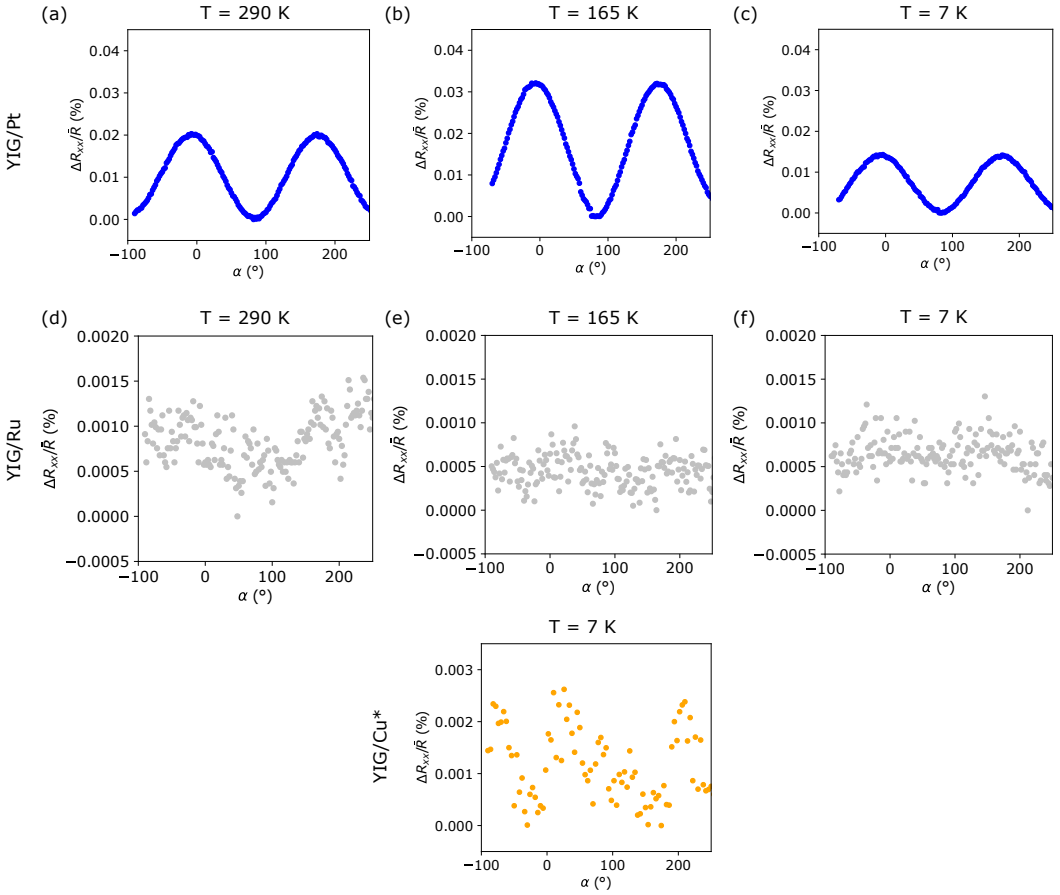

Figure 7.18: SMR measurements in YIG/Pt (top panel), YIG/Ru (middle panel), YIG/Cu* (bottom panel) for several temperatures. As expected, YIG/Pt shows sizable SMR at all temperatures, whereas YIG/Ru and YIG/Cu* do not show any MR behavior. All the measurements were performed by rotating the samples in the presence of a 0.1 T magnetic field, which is enough to saturate the YIG magnetization.

into spin currents. In YIG/Cu*, where no Pt is included, no measurable torques were detected, confirming that dynamic OAM does not efficiently couple to the spin-based magnetization.

Taken together, these comprehensive control experiments on α-Fe_2O_3 and YIG-based systems demonstrate that the MR effects observed in CoO are of orbital origin. The absence of OMR signals in materials with quenched orbital moments, combined with the necessity of a Pt interlayer for orbital-to-spin conversion as observed in previous studies, provides compelling evidence that the observed phenomena in CoO arise from the dynamics of orbital currents rather than from con-

ventional spin-based mechanisms.

7.3 Generation of Orbital Accumulation at the CoO/Cu Interface

As demonstrated in Secs. 7.1 and 7.2, OAM currents can couple directly to orbital-dominated magnetic systems, enabling efficient magnetization control without the need for spin-orbit conversion. This paradigm opens promising avenues for the development of low-power, high-efficiency magnetic devices and highlights the potential of direct orbital-orbital coupling to overcome limitations inherent to weak SOC and inefficient spin-current conversion.

However, a critical limitation remains in the CoO/Cu* system, in which the largest MR signal was observed: the dependence on uncontrolled natural oxidation of Cu renders such systems impractical for real-world applications. Such oxidation is neither reproducible nor stable under ambient or operational conditions.

Recent experimental work has shown that the Co/CoO/Cu* heterostructure exhibits large orbital torques, with torque efficiency preserved even upon capping the Cu layer. Hence, orbital currents may be generated directly at the CoO/Cu interface and natural oxidation is not required [189].

In the following section, we therefore address the central question of whether orbital currents can be generated at the CoO/Cu interface, and whether a stable, engineered source of orbital current can be realized, without dependence on uncontrolled oxidation. We further investigate the interplay between SMR and OMR contributions in systems that contain both, a spin current as well as an orbital current generator.

7.3.1 Angular-Dependent Measurements in CoO/Cu/Pt Trilayers

We fabricate MgO(001)//CoO(5 nm)/Cu(t)/Pt(2 nm) heterostructures, for which the thickness t of the Cu layer is varied between 0 nm and 25 nm. Both the Cu and Pt layers are deposited in-situ without breaking the vacuum, to ensure clean, well-defined interfaces.

Given that interface quality critically influences the signal fidelity in SMR measurements [403–406], we first characterize the structural integrity of the interfaces

using XRR. This step ensures that all samples are comparable in terms of interfacial sharpness and layer continuity prior to transport characterization.

Figure 7.19 presents XRR data for two representative samples with Cu interlayer thicknesses of 2 nm and 25 nm. Both samples exhibit smooth, well-defined interfaces, with a surface/interface roughness of the CoO and Cu layers below 0.4 nm. This interfacial quality ensures minimal defect- and boundary-induced scattering, enabling robust spin- and orbital-current transfer between layers and establishing sample-to-sample comparability. Furthermore, the Pt layer exhibits a maximum roughness of 0.3 nm, confirming continuous film growth that effectively passivates the Cu interlayer against ambient oxidation.

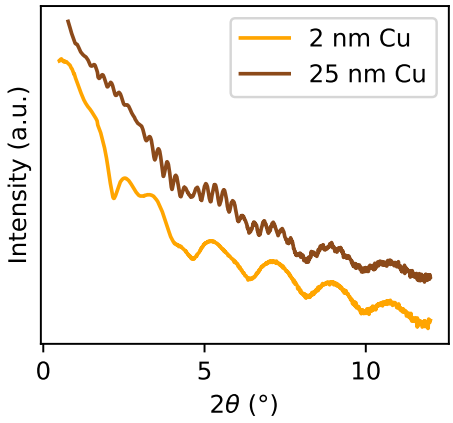

Figure 7.19: (a) XRR data for two CoO(5 nm)/Cu(d)/Pt(2 nm) films with d = 2 nm and 25 nm.

For electrical characterization, Hall bar devices (6 µm width) oriented along the [100] crystallographic direction were patterned, consistent with those in the prior sections. We first investigate the magnetic anisotropy in the pure spin-current system CoO(5 nm)/Pt(2 nm) using angular-dependent MR measurements at 200 K under an applied magnetic field of $\mu_0 \boldsymbol{H}$ = 11 T, which is sufficient to overcome the spin-flop field [50]. We rotate the magnetic field within the sample plane and vary the angle α between the applied charge current and the magnetic field, as defined in Fig. 3.3(c) in Sec. 3.1.2.

Consistent with Sec. 7.1.3, the measured transverse resistance R_{xy} consists of two distinct contributions: (i) a hysteretic component around the magnetic hard axes, correlated with a negative SMR signal (Fig. 7.20(a)) [50, 121]. This feature

confirms the fourfold in-plane magnetic anisotropy of the CoO layer, induced by substrate strain, with two easy axes in the (001) plane ([110] and [$\bar{1}$10]) and an out-of-plane hard axis along [001]; and (ii) a non-hysteretic sinusoidal background signal, correlated with a positive SMR.

The longitudinal SMR signal R_{xx} (Fig. 7.20(b)) exhibits a pure $\sin^2(\alpha)$ dependence without hysteretic features near the magnetic hard axes.

Upon insertion of a Cu interlayer between the AFM CoO and the spin-current source Pt, both the amplitude and functional form of the magnetoresistance signals evolve systematically with Cu thickness t. For the transverse component (Figs. 7.20(c) and (e)), the sinusoidal signal reverses sign as t increases: at $t = 0$ nm, R_{xy} exhibits a maximum when $\boldsymbol{H} \parallel [110]$ ($\alpha = 45°$); at $t = 3$ nm, the sinusoidal component nearly vanishes, producing a flat response around $\alpha = 45°$; and at $t = 6$ nm, a minimum replaces the initial maximum at the same angle. Systematic measurements of R_{xy} across intermediate Cu thicknesses (Appendix A) reveal a continuous evolution: the positive sinusoidal amplitude decreases monotonically with increasing t, vanishes near $t \approx 3$ nm, and transitions to a progressively stronger negative amplitude for $t > 3$ nm.

An analogous sign inversion occurs in the longitudinal component (Figs. 7.20(d) and (f)), with the signal amplitude vanishing at $t \approx 3$ nm. Further, we note that for $t = 3$ nm and 6 nm sharp peaks can be observed in the R_{xx} signal. The angle of the peaks coincide with the angle of the hysteretic component in the transverse R_{xy} measurement, indicating that the observed peaks can be correlated with the spin-flop transition in CoO, which according to Eq. 3.3 in the longitudinal measurement only induces a change while the Néel vector is reorienting from one magnetic easy axis to the perpendicular one. The two magnetic easy axis themselves yield the same MR value.

Considering the hysteretic signal, we find that in the transverse MR configuration it becomes more pronounced upon insertion of a Cu layer. Moreover, the sign of the hysteretic component reverses with the introduction of a thin Cu interlayer, and the amplitude of this inverted hysteretic signal further increases with increasing Cu thickness. The evolution of the signal can be understood as the superposition of two MR contributions arising from distinct mechanisms. By comparing the OMR signal in pure CoO/Cu*, shown in Fig. 7.10(b), with the transverse MR signal observed here (Fig. 7.20(e)), we find that the CoO(5 nm)/Cu(6 nm)/Pt(2 nm) sample

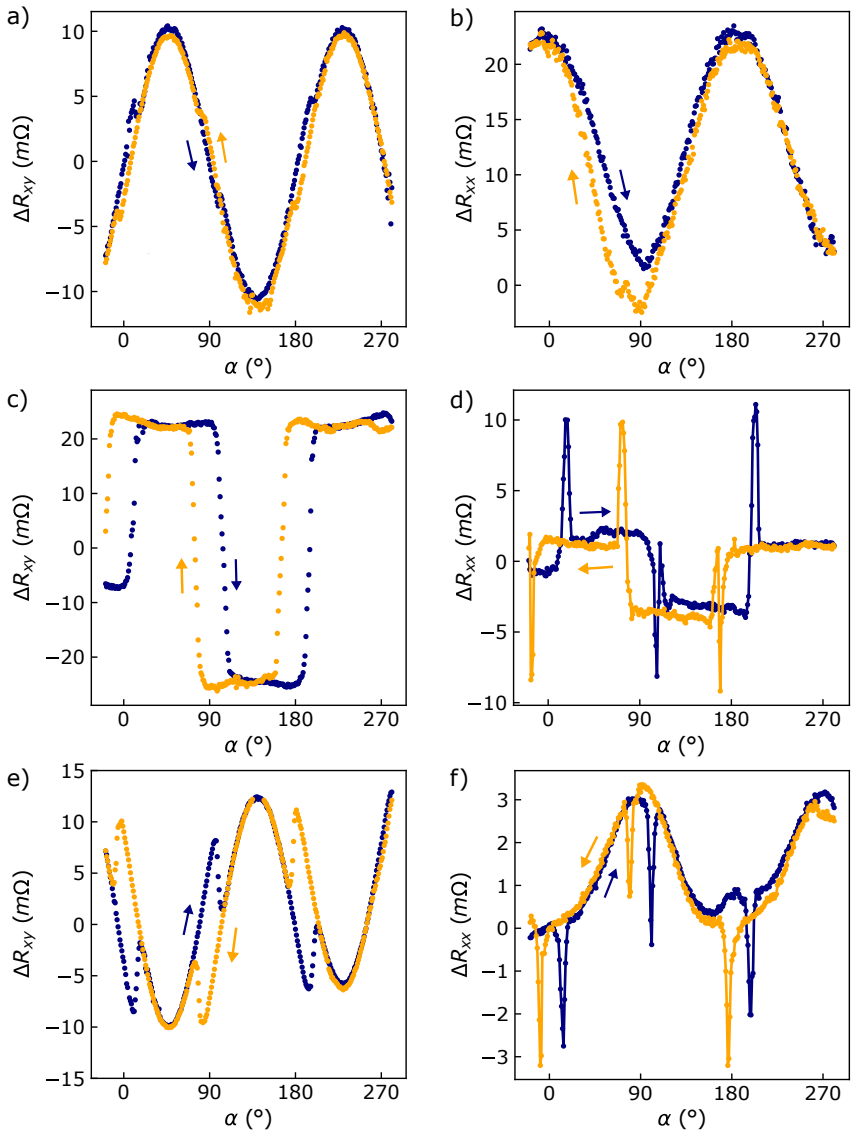

Figure 7.20: Transverse and longitudinal MR measurements for CoO(5)/Pt(2) (a) and (b), CoO(5)/Cu(3)/Pt(2) (c) and (d) and CoO(5)/Cu(6)/Pt(2) (e) and (f), respectively.

exhibits sinusoidal and hysteretic components whose amplitude ratio closely resembles that of the pure OMR observed in CoO(5 nm)/Cu(6 nm). The absolute magnitude of the resistance change is comparable in both cases; however, the longitudinal resistance of the sample containing the additional Pt layer is slightly smaller, leading to a somewhat larger relative change. Notably, the hysteretic component associated with the spin-flop transition remains consistent across both systems.

The similarity of the MRs observed in the two samples indicates that, in addition to the SMR signal and the spin current generated in the HM Pt, an orbital current originating from the Cu interlayer and consequently an OMR contribution are also present, even in the absence of intended surface oxidation. By varying the Cu and Pt thicknesses, the current distribution among the layers, and thus the relative contributions of SMR and OMR, can be tuned. Consequently, the overall MR response, resulting from the combination of these two contributions, evolves accordingly.

7.3.2 Comparison of Contributions Related and Unrelated to the Magnetization Configuration in CoO

Since the OMR in CoO/Cu* was found to be significantly stronger than the SMR in CoO/Pt, we extracted the amplitudes of both the hysteretic and sinusoidal components as a function of Cu interlayer thickness, according to Sec. 7.1.3. This analysis aims to determine whether the amplitude increases with the fraction of current flowing through the Cu layer, as expected for an enhanced OMR contribution.

The results, presented in Fig. 7.21, show that both signal amplitudes increase with Cu thickness up to 6 nm. This trend is in agreement with the hypothesis that the overall MR signal strengthens due to enhanced coupling of the OAM to the orbital moments in CoO as a larger portion of the current shunts through the Cu layer.

To quantify this behavior, we applied the Fuchs-Sondheimer model, which describes the thickness-dependent resistivity of thin metallic films by accounting for surface scattering of conduction electrons [407, 408]. From this model, we estimated the size-dependent resistivities and sheet resistances to calculate the expected current distribution between the Cu and Pt layers. Here, we employ a simplified linear approximation, which, for ultrathin films with thicknesses smaller than the electron mean free path, tends to underestimate the resistance increase. Consequently, the current fraction in Cu is likely slightly underestimated, whereas the current fraction in Pt is slightly overestimated.

For the calculations the resistivities of bulk Cu and Pt were considered as $\rho_{\mathrm{Cu,bulk}} = 1.68 \times 10^{-8}$ Ωm and $\rho_{\mathrm{Pt,bulk}} = 1.06 \times 10^{-7}$ Ωm, respectively [409]. The electron mean free path ℓ for Cu is $\ell_{\mathrm{Cu}} = 39$ nm [410] and for Pt $\ell_{\mathrm{Pt}} = 10$ nm [411].

For a metallic film of thickness t, bulk resistivity ρ_0, and electron mean free path

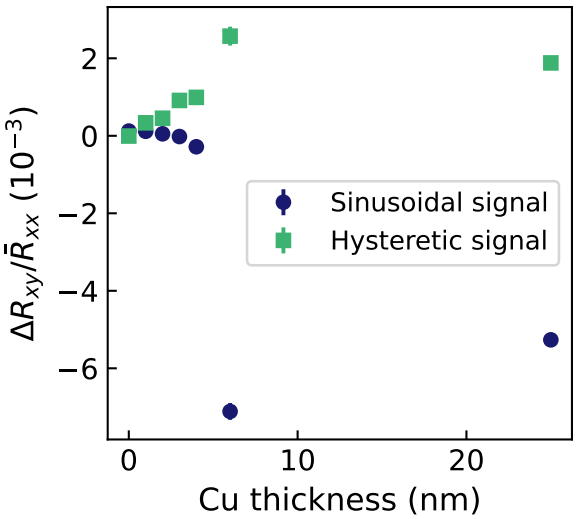

Figure 7.21: Separated amplitudes of the hysteretic and sinusoidal signal components as a function of Cu interlayer thickness.

ℓ, the simplified Fuchs-Sondheimer expression describing the thickness-dependent increase in resistivity is given by:

$$\rho(d) = \rho_0 \left(1 + \frac{3\ell}{8t}\right). \tag{7.2}$$

This relation assumes fully diffuse surface scattering. Using this expression, we calculate the resistivity for Cu interlayers with thicknesses of 3 nm and 6 nm, as well as for the 2 nm Pt layer, yielding:

$$\rho_{\mathrm{Cu}}(6\,\mathrm{nm}) = 5.8 \times 10^{-8}\,\Omega\mathrm{m},$$

$$\rho_{\mathrm{Cu}}(3\,\mathrm{nm}) = 9.9 \times 10^{-8}\,\Omega\mathrm{m},$$

$$\rho_{\mathrm{Pt}}(2\,\mathrm{nm}) = 3.0 \times 10^{-7}\,\Omega\mathrm{m}.$$

For comparison, we determined the resistivities experimentally using CoO(5 nm)/Cu(6 nm), CoO(5 nm)/Cu(3 nm), and CoO(5 nm)/Pt(2 nm) bilayers:

$$\rho_{\mathrm{Cu,Exp}}(6\,\mathrm{nm}) = 4.9 \times 10^{-8}\,\Omega\mathrm{m},$$

$$\rho_{\mathrm{Cu,Exp}}(3\,\mathrm{nm}) = 50.4 \times 10^{-8}\,\Omega\mathrm{m},$$

$$\rho_{\mathrm{Pt,Exp}}(2\,\mathrm{nm}) = 23.5 \times 10^{-8}\,\Omega\mathrm{m}.$$

These values, however, cannot be directly compared to the CoO/Cu/Pt trilayers studied here, since in the calibration samples the Cu layer was uncapped and therefore subject to oxidation. The resistivities of Pt and Cu(6) remain reasonably close to the theoretical predictions (within ~20%), but the Cu(3) film exhibits a drastically increased resistivity due to the oxidation of a significant part of the ultrathin layer. Because of this effect we rely on the theoretically calculated resistivities when determining the current distribution in the CoO/Cu/Pt structures, which appear to be a good approximation.

From the resistivities we calculated from Fuchs-Sondheimer, the sheet resistance of each layer can be obtained as $R_s = \rho/t$. The current distribution between two parallel conducting layers is inversely proportional to their respective sheet resistances, such that:

$$I_{\mathrm{Cu}} = I_{\mathrm{total}} \times \frac{1/R_{\mathrm{s,Cu}}}{1/R_{\mathrm{s,Cu}} + 1/R_{\mathrm{s,Pt}}} = I_{\mathrm{total}} \times \frac{R_{\mathrm{s,Pt}}}{R_{\mathrm{s,Cu}} + R_{\mathrm{s,Pt}}}. \tag{7.3}$$

Using this relation, we find that in the sample with Cu(3 nm)/Pt(2 nm), approximately 82% of the total current flows through the Cu layer. For Cu(6 nm)/Pt(2 nm), this fraction increases to about 94%. These values likely represent lower estimates, since the Cu and Pt layers differ in thickness by a factor of three, and the simplified linear form of the Fuchs-Sondheimer equation tends to underestimate the resistance increase in Pt more strongly than in Cu.

The saturation of the signal amplitudes observed at a Cu thickness of 6 nm, together with the absence of further enhancement at larger thicknesses, indicates that beyond this point the majority of the current already flows through the Cu interlayer. This behavior is consistent with the higher intrinsic conductivity of Cu compared to Pt and supports the quantitative estimates derived above.

We can, thus, conclude that the measured signal is dominated by the OMR, consistent with the MR response in Fig. 7.20(e), which closely resembles that observed in pure CoO/Cu*. Large orbital current, however, cannot be generated in pure Cu, but only from some oxidized form of Cu via the OREE [184]. In the present case, the Cu interlayer is capped by a continuous 2 nm Pt film, which effectively prevents natural surface oxidation, yet a sizable orbital current is still observed. As no evidence of oxidation at the CoO/Cu interface was detected within the experimental

resolution in Sec. 7.1.1, the results indicate that the formation of O-Cu bonds at this interface are sufficient to generate an orbital current through the OREE.

These findings demonstrate that the CoO/Cu interface alone is sufficient for generating large orbital currents and producing a giant OMR, without relying on natural or uncontrolled surface oxidation. In particular, the results suggest that the protective Pt capping layer could, in principle, be replaced by any suitable and inexpensive material that prevents Cu surface oxidation while maintaining efficient orbital current generation. To verify this conjecture, one would need to systematically test alternative capping layers and vary their oxidation barrier and electronic transparency to evaluate whether the resulting OMR amplitude and temperature dependence remain consistent with those observed in CoO/Cu*.

7.4 Conclusion

Driven by the pursuit of faster and more energy-efficient information technologies, recent research has explored new electronic degrees of freedom beyond charge and spin. In this context, OAM has emerged as a powerful alternative for controlling magnetic order and charge transport in solid-state systems.

In this section, we have demonstrated for the first time, that combining an orbital-moment-dominated AFM, CoO, with a dynamic OAM generator, such as Cu* or Cr, gives rise to a giant OMR signal. Remarkably, this effect exceeds the magnitude of conventional SMR in HM-based systems (e.g., CoO/Pt) by two orders of magnitude. This observation establishes a fundamentally different mechanism of magnetotransport, one that does not rely on the interconversion of orbital to spin currents, but instead on a direct coupling between injected orbital currents and the unquenched orbital moments of CoO.

Our results provide compelling evidence that CoO, owing to its large orbital moment, responds far more strongly to orbital excitations than to spin excitations.

In Sec. 7.2, we further showed that this coupling between dynamic OAM and the orbital moments of CoO can also be achieved when replacing Cu* with other orbital-current generators such as Cr or Ti. The overall effect is weaker in these systems, and in the case of Ti even exhibits an opposite MR sign. These findings highlight the sensitivity of the orbital response to the nature of the orbital current source. The microscopic origins of these differences remain an open question and warrant further investigation.

On the other hand, such orbital-driven effects are absent in purely spin-based systems such as hematite ($\alpha - Fe_2O_3$) and YIG, where orbital moments are largely quenched. This contrast reinforces the central conclusion of this chapter: Orbital currents can directly and efficiently couple to unquenched orbital moments, enabling magnetotransport phenomena far beyond the limits of conventional spintronic systems.

Further we show, in Sec. 7.3, how OMR and SMR compete and contribute to the measured MR signal in CoO/Cu/Pt heterostructures. By varying the relative thicknesses of the Cu and Pt layers, the proportion of charge current generating orbital and spin currents, respectively, can be tuned, thereby modulating the overall MR response and eliminating the non-magnetic signal contribution. Since the Cu surface is capped by a continuous Pt layer, we conclude that dynamic OAM can be generated via the OREE exclusively at the CoO/Cu* interface. Our results demonstrate that controlled interface oxidation produces a well-defined Cu* layer that enables reproducible and stable orbital current generation. This insight highlights the potential of CoO/Cu/capping layer structures as model systems for designing robust and well-characterized oxide/metal interfaces for future orbitronic research.

Taken together, these findings establish a new paradigm for orbitronic device engineering. By exploiting the direct orbital-orbital coupling between dynamic OAM and magnetically ordered materials with strong orbital character, it is possible to achieve efficient, tunable, and scalable mechanisms for electrical readout and control of magnetic order, without the need for heavy elements or strong SOC. This underscores the applicability of the discovered mechanism and highlights the potential of giant orbital currents to efficiently detect and potentially also manipulate magnetic order via this novel route. Overall, the interaction mechanisms that arise from the combination of the giant orbital currents generated in Cu* and the large unquenched static OAM in orbital magnets such as CoO could enable the development of all-orbital devices, overcoming the fundamental limitations of conventional SOC-mediated processes.

8 Conclusion and Outlook

The fields of spintronics and orbitronics have undergone remarkable development over the past decade, driven by the pursuit of spin- and orbit-based technologies that are faster, more compact, and more energy-efficient than their charge-based predecessors [38, 412]. Within this evolution, interest in AFMs has shifted from using them merely as passive elements, for instance in exchange-bias stacks, to giving them a central role as active components for information transport, memory, and logic applications [27]. Driven especially by their defining characteristics, such as the absence of a net magnetic moment, AFMs offer inherent advantages including insensitivity to external magnetic fields, the potential for device miniaturization, and ultrafast intrinsic dynamics. At the same time, this very absence of net magnetization poses a major challenge: It renders AFM domain states difficult to control, complicating both deterministic writing and efficient readout. Further, it was found, that in AFMs with large magnetoelasticity, such as CoO, switching effects are dominated by thermally induced mechanisms and large magnetostriction, while the intrinsic advantages such as THz dynamics and the possibility for miniaturization cannot be easily accessed [51, 77, 349].

This work is motivated by the aim of exploiting the advantages of AFMs and by exploring new mechanisms that can address the difficulties inherent to their control. Within this context, the results of this thesis uncover several fundamental insights into how spin and orbital degrees of freedom interact in AFMs and how these interaction mechanisms can be harnessed for future spintronic and orbitronic technologies.

A key insight from this work is that thin-film CoO shows measurable magne-

toelastic coupling, although its influence on the domain structure remains secondary to the intrinsic magnetocrystalline anisotropy. As discussed in Sec. 5, growth induced strain controlled by the oxygen flow during sputtering adjusts the lattice parameter and in this way tunes the Néel-vector orientation. Domain walls induced my optical laser pulses exhibit preferred orientations that are consistent with magnetoelastic effects in the films. On the other hand, geometric confinement and lithographic patterning cause only local perturbations at device edges. This demonstrates that shape anisotropy does not prevail compared to the intrinsic anisotropy of CoO, in contrast to materials such as NiO or CuMnAs. Overall, magnetoelastic coupling is present but modest, and it does not impose meaningful limitations on device design or operation.

While magnetoelastic effects have historically hindered efforts to demonstrate genuine SOT-driven switching in insulating AFMs, this thesis resolves this ambiguity by revealing the coexistence of thermomagnetoelastic and SOT mechanisms in ultrathin CoO/Pt bilayers (Sec. 6). By combining transport measurements with XMLD–PEEM imaging, we show that electrical readout alone can be ambiguous: the apparent SMR sign reversal with current density arises from a heat-assisted thermomagnetoelastic response. Direct imaging resolves the underlying domain rearrangement and separates thermal from non-thermal effects. Strain simulations identify thermomagnetoelastic switching as the dominant mechanism, but the residual domain changes within the current-carrying regions require an additional SOT-driven contribution, which becomes significant in ultrathin ($\approx 2-4$ nm) CoO layers [247]. These findings clarify how thermal and interfacial torque mechanisms coexist in ultrathin CoO and provide a reliable framework for identifying SOT-driven switching in AFMs. Establishing this distinction is essential for designing device structures that can harness interfacial torques instead of relying on thermal effects. More broadly, the demonstrated ability to achieve deterministic and potentially THz-speed switching in a simple CoO/Pt bilayer positions AFMs as practical candidates for future ultrafast and energy-efficient spintronic technologies.

The most significant discovery of this thesis is the observation of giant OMR arising from the direct coupling between orbital currents generated in Cu* and the large unquenched orbital moments in CoO (Sec. 7.1). Our experiments demonstrate that OAM can serve as an efficient carrier of magnetic information, yielding

readout signals two orders of magnitude larger than those achievable via conventional spin-based mechanisms [378]. This establishes a conceptual advance: Orbital currents provide a distinct, highly effective channel for electrical readout and potentially manipulation of magnetic order, complementary to spin currents. Crucially, this coupling does not rely on natural oxidation of Cu. Instead, OAM can directly be generated via the OREE at the CoO/Cu interface [379]. We further show that this mechanism is not limited to Cu*: Orbital currents from Cr or Ti also induce measurable OMR in CoO, albeit with reduced magnitude compared to CoO/Cu* and, in the case of Ti, reversed sign. This sensitivity to the orbital-current source underscores the importance of the interfacial electronic structure, a factor not yet fully understood, but critical for engineering orbital-based devices. In contrast, systems with quenched orbital moments, such as hematite and YIG, exhibit no such orbital-driven magnetotransport, confirming that the effect is uniquely enabled by unquenched orbital moments. Together, these results establish, that orbital currents can couple directly and efficiently to orbital moment-dominated magnets, opening a new pathway for magnetotransport phenomena that transcend the limits of conventional spintronics.

Taken together, the results of this thesis demonstrate that AFM thin films can undergo ultrafast switching and that orbital currents can couple directly to orbital magnetization, a mechanism not previously accessible. This advances the fundamental understanding of AFM dynamics and establishes new design principles for orbitronic devices that operate without relying on spin-to-orbit conversion. They demonstrate how lattice, thermal contributions, spin, and orbital degrees of freedom intersect in determining magnetic functionality, and illustrate pathways for exploiting these couplings in the pursuit of ultrafast and energy-efficient control of magnetic order.

The results presented in this thesis motivate a broad range of future research directions spanning materials science, ultrafast magnetism, and the emerging field of orbitronics. While some aspects, such as modest magnetoelastic coupling in CoO thin films, are likely to primarily refine our understanding of AFM material behavior, the most far-reaching implications arise from the discovery of giant OMR and the demonstration, that orbital currents can directly couple to magnetic order. This establishes a new conceptual and experimental platform with the potential to reshape how information is written, transported, and read in magnetic systems.

Although CoO itself is unlikely to serve as a technological material, owing to its relatively large magnetoelastic coupling, which makes its magnetic state highly sensitive to strain and heating, and low Néel temperature, its value as a model system should not be underestimated. CoO can continue to function as a prototypical insulating AFM for studying spin and orbital transport, switching phenomena, and interfacial physics under conditions where conventional FMs or metallic AFMs complicate the interpretation.

The demonstration that thermomagnetoelastic and SOT-driven switching coexist in ultrathin CoO/Pt bilayers suggests several future directions, particularly toward understanding how interfacial torques evolve when moving beyond conventional spin-orbit physics. While detailed optimization of SOT-based switching in CoO itself may be constrained by the material's intrinsic properties, the methodological approach can readily be transferred to materials with higher ordering temperatures and lower magnetostriction, such as hematite or Mn_2Au. Moreover, the ability to isolate non-thermal torque contributions opens the door to exploring more exotic torque mechanisms, including orbital and multipolar torques.

The most transformative opportunities arise from the discovery of giant OMR. This result demonstrates that orbital currents generated via mechanisms such as the OREE, can couple extremely efficiently to magnets with unquenched orbital moments. In contrast to spin-based mechanisms, which are limited by the magnitude of the SOC [196], orbital currents appear capable of delivering much larger interfacial responses, potentially enabling highly efficient readout and even manipulation of magnetic order [38]. This raises a number of fundamental research questions. For instance, it remains unknown how the order-parameter dynamics differ when driven by OAM compared to spin angular momentum. Theoretical and experimental studies are needed to explore whether OAM and OQP injection lead to qualitatively distinct dynamical regimes, domain-wall velocities, or damping processes, and how these responses depend on the presence of spin-orbital entanglement, crystal-field symmetry, or multipolar interactions. Understanding these regimes will be crucial for developing accurate effective models of orbital transport and for identifying materials where orbital-driven torques may dominate.

An immediate extension of this work is to transfer OMR-based readout and orbital-current injection to technologically more relevant materials. The ideal platform would combine low magnetoelasticity, high ordering temperature, and large

unquenched orbital moments. Several classes of materials stand out as promising candidates: ferrites with partially unquenched orbital degrees of freedom (e.g. $CoFe_2O_4$ or Fe_3O_4) [326, 413]; and certain FMs or noncollinear AFMs such as CoPt alloys [414] or the chiral antiferromagnets Mn_3Sn and Mn_3Ge, which host orbital moments originating from crystal-field asymmetry or multipolar ordering [415–417]. If giant OMR can be realized in such materials, it could enable device-compatible readout schemes that are orders of magnitude more sensitive than spin-Hall-based MR. This would significantly expand the range of viable magnetic memory concepts, including low-power sensors, multi-level memory elements, and hybrid spin-orbital logic devices. Another promising direction concerns the possibility of using orbital currents not only for readout but also for switching. If the coupling strength inferred from OMR measurements reflects a reciprocal symmetry relation, then orbital torques may in principle act on the magnetic order with comparable efficiency. This opens the prospect of developing orbital torque magnetoresistive random-access memory-type devices, in which writing is performed through OAM injection rather than or in combination with spin currents. Such a mechanism could be particularly effective in systems where spin torques are suppressed or inefficient, for example in magnets with weak SOC but large orbital moment. Systematic exploration of interface engineering, orbital transparency, and symmetry-controlled orbital textures will be required to realize such devices experimentally.

Collectively, the findings of this thesis point toward a rapidly expanding landscape in which orbital physics takes on a central role in magnetic transport and control. By combining high-efficiency orbital readout with potentially large orbital torques, next-generation orbitronic systems may achieve unprecedented switching speeds, reduced energy consumption, and new modes of information encoding.

As these avenues are explored, CoO can continue to serve as an essential reference system. Not because it will appear in commercial devices, but because its sizable orbital moment, insulating nature, and tunable thin-film properties make it exceptionally well-suited for disentangling complex mechanisms. Through the insights and techniques developed here, the path is now open to extend these discoveries to a wide range of materials and to harness orbital currents as a foundational element in future magnetic technologies.

Bibliography

[1] R. Landauer, "Information is physical," *Phys. Today*, vol. 44, no. 5, pp. 23–29, 1991.

[2] R. Landauer, "Irreversibility and heat generation in the computing process," *IBM J. Res. Dev.*, vol. 5, no. 3, pp. 183–191, 1961.

[3] C. H. Bennett, "The thermodynamics of computation—a review," *Int. J. Theor. Phys.*, vol. 21, no. 12, pp. 905–940, 1982.

[4] J. Shalf, "The future of computing beyond Moore's Law," *Philos. Trans. R. Soc. A*, vol. 378, no. 2166, p. 20190061, 2020.

[5] International Energy Agency (IEA), "Energy and AI: Executive Summary." https://www.iea.org/reports/energy-and-ai/executive-summary?utm_source=chatgpt.com, 2025. Last accessed: 27 November 2025.

[6] M. T. Takci, M. Qadrdan, J. Summers, and J. Gustafsson, "Data centres as a source of flexibility for power systems," *Energy Rep.*, vol. 13, pp. 3661–3671, 2025.

[7] X. Yuan, J. Liu, S. Sun, X. Lin, X. Fan, W. Zhao, and R. Kosonen, "Data center waste heat for district heating networks: A review," *Renew. Sustainable Energy Rev.*, vol. 219, p. 115863, 2025.

[8] S. Cai and Z. Gou, "Towards energy-efficient data centers: A comprehensive review of passive and active cooling strategies," *Energy Built Environ.*, 2024.

[9] G. Guidi, F. Dominici, J. Gilmour, K. Butler, E. Bell, S. Delaney, and F. J. Bargagli-Stoffi, "Environmental burden of United States data centers in the artificial intelligence era," *arXiv preprint arXiv:2411.09786*, 2024.

[10] G. Akhmat, K. Zaman, T. Shukui, and F. Sajjad, "Does energy consumption contribute to climate change? Evidence from major regions of the world," *Renew. Sustain. Energy Rev.*, vol. 36, pp. 123–134, 2014.

[11] A. Mehonic and A. J. Kenyon, "Brain-inspired computing needs a master plan," *Nature*, vol. 604, no. 7905, pp. 255–260, 2022.

[12] S. Blundell, *Magnetism in condensed matter*. Oxford Master Series in Condensed Matter Physics, New York: Oxford University Press, 2001.

[13] S. Wolf, D. Awschalom, R. Buhrman, J. Daughton, v. S. von Molnár, M. Roukes, A. Y. Chtchelkanova, and D. Treger, "Spintronics: a spin-based electronics vision for the future," *Science*, vol. 294, no. 5546, pp. 1488–1495, 2001.

[14] G. Finocchio, M. Di Ventra, K. Y. Camsari, K. Everschor-Sitte, P. K. Amiri, and Z. Zeng, "The promise of spintronics for unconventional computing," *J. Magn. Magn. Mater.*, vol. 521, p. 167506, 2021.

[15] D. Jo, D. Go, G.-M. Choi, and H.-W. Lee, "Spintronics meets orbitronics: Emergence of orbital angular momentum in solids," *npj Spintronics*, vol. 2, no. 1, p. 19, 2024.

[16] P. Wang, F. Chen, Y. Yang, S. Hu, Y. Li, W. Wang, D. Zhang, and Y. Jiang, "Orbitronics: Mechanisms, materials and devices," *Adv. Electron. Mater.*, vol. 11, no. 5, p. 2400554, 2025.

[17] K. Ando, "Generation and manipulation of current-induced spin-orbit torques," *Proc. Jpn. Acad. B*, vol. 97, no. 9, pp. 499–519, 2021.

[18] E. Díaz, A. Anadón, P. Olleros-Rodríguez, H. Singh, H. Damas, P. Perna, M. Morassi, A. Lemaître, M. Hehn, and J. Gorchon, "Energy-efficient picosecond spin–orbit torque magnetization switching in ferro-and ferrimagnetic films," *Nat. Nanotech.*, vol. 20, no. 1, pp. 36–42, 2025.

[19] H. Hayashi, D. Jo, D. Go, T. Gao, S. Haku, Y. Mokrousov, H.-W. Lee, and K. Ando, "Observation of long-range orbital transport and giant orbital torque," *Commun. Phys.*, vol. 6, no. 1, p. 32, 2023.

[20] M. N. Baibich, J. M. Broto, A. Fert, F. N. Van Dau, F. Petroff, P. Etienne, G. Creuzet, A. Friederich, and J. Chazelas, "Giant magnetoresistance of (001) Fe/(001) Cr magnetic superlattices," *Phys. Rev. Lett.*, vol. 61, no. 21, p. 2472, 1988.

[21] G. Binasch, P. Grünberg, F. Saurenbach, and W. Zinn, "Enhanced magnetoresistance in layered magnetic structures with antiferromagnetic interlayer exchange," *Phys. Rev. B*, vol. 39, no. 7, p. 4828, 1989.

[22] M. Julliere, "Tunneling between ferromagnetic films," *Phys. Lett. A*, vol. 54, no. 3, pp. 225–226, 1975.

[23] J. Katine and E. E. Fullerton, "Device implications of spin-transfer torques," *J. Magn. Magn. Mater.*, vol. 320, no. 7, pp. 1217–1226, 2008.

[24] J. Sun and D. Ralph, "Magnetoresistance and spin-transfer torque in magnetic tunnel junctions," *J. Magn. Magn. Mater.*, vol. 320, no. 7, pp. 1227–1237, 2008.

[25] C. Chappert, A. Fert, and F. N. Van Dau, "The emergence of spin electronics in data storage," *Nat. Mater.*, vol. 6, no. 11, pp. 813–823, 2007.

[26] S. D. Bader and S. S. P. Parkin, "Spintronics," *Annu. Rev. Condens. Matter Phys.*, vol. 1, no. 1, pp. 71–88, 2010.

[27] D. Xiong, Y. Jiang, K. Shi, A. Du, Y. Yao, Z. Guo, D. Zhu, K. Cao, S. Peng, W. Cai, *et al.*, "Antiferromagnetic spintronics: An overview and outlook," *Fundam. Res.*, vol. 2, no. 4, pp. 522–534, 2022.

[28] S. Loth, S. Baumann, C. P. Lutz, D. Eigler, and A. J. Heinrich, "Bistability in atomic-scale antiferromagnets," *Science*, vol. 335, no. 6065, pp. 196–199, 2012.

[29] T. Kampfrath, A. Sell, G. Klatt, A. Pashkin, S. Mährlein, T. Dekorsy, M. Wolf, M. Fiebig, A. Leitenstorfer, and R. Huber, "Coherent terahertz control of antiferromagnetic spin waves," *Nat. Photon.*, vol. 5, no. 1, pp. 31–34, 2011.

[30] P. Wadley, B. Howells, J. Železnỳ, C. Andrews, V. Hills, R. P. Campion, V. Novák, K. Olejník, F. Maccherozzi, S. Dhesi, *et al.*, "Electrical switching of an antiferromagnet," *Science*, vol. 351, no. 6273, pp. 587–590, 2016.

[31] T. Jungwirth, X. Marti, P. Wadley, and J. Wunderlich, "Antiferromagnetic spintronics," *Nat. Nanotechnol.*, vol. 11, no. 3, pp. 231–241, 2016.

[32] Z. Guo, X. Wang, W. Wang, G. Zhang, X. Zhou, and Z. Cheng, "Spin-Polarized Antiferromagnets for Spintronics," *Adv. Mater.*, p. 2505779, 2025.

[33] V. Baltz, A. Manchon, M. Tsoi, T. Moriyama, T. Ono, and Y. Tserkovnyak, "Antiferromagnetic spintronics," *Rev. Mod. Phys.*, vol. 90, no. 1, p. 015005, 2018.

[34] H. Meer, O. Gomonay, A. Wittmann, and M. Kläui, "Antiferromagnetic insulatronics: Spintronics in insulating 3d metal oxides with antiferromagnetic coupling," *Appl. Phys. Lett.*, vol. 122, no. 8, p. 080502, 2023.

[35] T. Tanaka, H. Kontani, M. Naito, T. Naito, D. S. Hirashima, K. Yamada, and J. Inoue, "Intrinsic spin Hall effect and orbital Hall effect in 4*d* and 5*d* transition metals," *Phys. Rev. B*, vol. 77, no. 16, p. 165117, 2008.

[36] H. Kontani, T. Tanaka, D. S. Hirashima, K. Yamada, and J. Inoue, "Giant Orbital Hall Effect in Transition Metals: Origin of Large Spin and Anomalous Hall Effects," *Phys. Rev. Lett.*, vol. 102, no. 1, p. 016601, 2009.

[37] D. Go, D. Jo, C. Kim, and H.-W. Lee, "Intrinsic Spin and Orbital Hall Effects from Orbital Texture," *Phys. Rev. Lett.*, vol. 121, no. 8, p. 086602, 2018.

[38] D. Go, D. Jo, H.-W. Lee, M. Kläui, and Y. Mokrousov, "Orbitronics: Orbital currents in solids," *Europhys. Lett.*, vol. 135, no. 3, p. 37001, 2021.

[39] L. Salemi and P. M. Oppeneer, "First-principles theory of intrinsic spin and orbital Hall and Nernst effects in metallic monoatomic crystals," *Phys. Rev. Mater.*, vol. 6, no. 9, p. 095001, 2022.

[40] Y.-G. Choi, D. Jo, K.-H. Ko, D. Go, K.-H. Kim, H. G. Park, C. Kim, B.-C. Min, G.-M. Choi, and H.-W. Lee, "Observation of the orbital Hall effect in a light metal Ti," *Nature*, vol. 619, no. 7968, pp. 52–56, 2023.

[41] S. A. Nikolaev, M. Chshiev, F. Ibrahim, S. Krishnia, N. Sebe, J.-M. George, V. Cros, H. Jaffrès, and A. Fert, "Large Chiral Orbital Texture and Orbital Edelstein Effect in Co/Al Heterostructure," *Nano. Lett.*, vol. 24, no. 43, pp. 13465–13472, 2024.

[42] D. Go, K. Ando, A. Pezo, S. Blügel, A. Manchon, and Y. Mokrousov, "Orbital pumping by magnetization dynamics in ferromagnets," *Phys. Rev. B*, vol. 111, no. 14, p. L140409, 2025.

[43] Y. Song, J. Tian, F. Zheng, J. Dong, M. Zhu, and J. Zhang, "Inefficiency of orbital Hall effect on the spin torque in transition metal/ferromagnet bilayers," *Phys. Rev. Appl.*, vol. 24, no. 3, p. 034038, 2025.

[44] S. Ding, A. Ross, D. Go, L. Baldrati, Z. Ren, F. Freimuth, S. Becker, F. Kammerbauer, J. Yang, G. Jakob, Y. Mokrousov, and M. Kläui, "Harnessing Orbital-to-Spin Conversion of Interfacial Orbital Currents for Efficient Spin-Orbit Torques," *Phys. Rev. Lett.*, vol. 125, no. 17, p. 177201, 2020.

[45] S. Lee, M.-G. Kang, D. Go, D. Kim, J.-H. Kang, T. Lee, G.-H. Lee, J. Kang, N. J. Lee, Y. Mokrousov, *et al.*, "Efficient conversion of orbital Hall current to spin current for spin-orbit torque switching," *Commun. Phys.*, vol. 4, no. 1, p. 234, 2021.

[46] A. Bose, F. Kammerbauer, R. Gupta, D. Go, Y. Mokrousov, G. Jakob, and M. Kläui, "Detection of long-range orbital-Hall torques," *Phys. Rev. B*, vol. 107, no. 13, p. 134423, 2023.

[47] T. Moriyama, K. Oda, T. Ohkochi, M. Kimata, and T. Ono, "Spin torque control of antiferromagnetic moments in NiO," *Sci. rep.*, vol. 8, no. 14167, p. 14167, 2018.

[48] X. Chen, R. Zarzuela, J. Zhang, C. Song, X. Zhou, G. Shi, F. Li, H. Zhou, W. Jiang, F. Pan, *et al.*, "Antidamping-torque-induced switching in biaxial

antiferromagnetic insulators," *Phys. Rev. Lett.*, vol. 120, no. 20, p. 207204, 2018.

[49] L. Baldrati, O. Gomonay, A. Ross, M. Filianina, R. Lebrun, R. Ramos, C. Leveille, F. Fuhrmann, T. Forrest, F. Maccherozzi, *et al.*, "Mechanism of Néel order switching in antiferromagnetic thin films revealed by magnetotransport and direct imaging," *Phys. Rev. Lett.*, vol. 123, no. 17, p. 177201, 2019.

[50] L. Baldrati, C. Schmitt, O. Gomonay, R. Lebrun, R. Ramos, E. Saitoh, J. Sinova, and M. Kläui, "Efficient spin torques in antiferromagnetic CoO/Pt quantified by comparing field-and current-induced switching," *Phys. Rev. Lett.*, vol. 125, no. 7, p. 077201, 2020.

[51] H. Meer, F. Schreiber, C. Schmitt, R. Ramos, E. Saitoh, O. Gomonay, J. Sinova, L. Baldrati, and M. Kläui, "Direct imaging of current-induced antiferromagnetic switching revealing a pure thermomagnetoelastic switching mechanism in NiO," *Nano Lett.*, vol. 21, no. 1, pp. 114–119, 2020.

[52] J. M. D. Coey, *Magnetism and Magnetic Materials*. Magnetism and Magnetic Materials, Cambridge University Press, 2010.

[53] M. Faraday, "On new magnetic actions, and on the magnetic condition of all matter," *J. Franklin Inst.*, vol. 42, no. 1, pp. 66–69, 1846.

[54] P. Weiss, "La variation du ferromagnétisme avec la température," *Comptes Rendus*, vol. 143, pp. 1136–1139, 1906.

[55] J. A. Ewing, "On the production of transient electric currents in iron and steel conductors by twisting them when magnetised, or by magnetising them when twisted," *Proc. R Soc. London*, vol. 36, no. 228-231, pp. 117–135, 1883.

[56] L. Néel, "Influence des fluctuations du champ moléculaire sur les propriétés magnétiques des corps," in *Ann. phys. (Paris)*, vol. 17, pp. 5–105, 1932.

[57] F. Bitter, "A generalization of the theory of ferromagnetism," *Phys. Rev.*, vol. 54, no. 1, p. 79, 1938.

[58] J. Rodriguez, "Quantized topological point defects in two-dimensional antiferromagnets," *Phys. Rev. B*, vol. 39, no. 4, p. 2906, 1989.

[59] B. Barbara and E. M. Chudnovsky, "Macroscopic quantum tunneling in antiferromagnets," *Phys. Lett. A*, vol. 145, no. 4, pp. 205–208, 1990.

[60] L. Néel, "Propriétés magnétiques des ferrites; ferrimagnétisme et antiferromagnétisme," in *Ann. phys. (Paris)*, vol. 12, pp. 137–198, 1948.

[61] L. Šmejkal, R. González-Hernández, T. Jungwirth, and J. Sinova, "Crystal time-reversal symmetry breaking and spontaneous Hall effect in collinear antiferromagnets," *Sci. Adv.*, vol. 6, no. 23, p. eaaz8809, 2020.

[62] L. Šmejkal, J. Sinova, and T. Jungwirth, "Beyond conventional ferromagnetism and antiferromagnetism: A phase with nonrelativistic spin and crystal rotation symmetry," *Phy. Rev. X*, vol. 12, no. 3, p. 031042, 2022.

[63] L. Šmejkal, J. Sinova, and T. Jungwirth, "Emerging research landscape of altermagnetism," *Phys. Rev. X*, vol. 12, no. 4, p. 040501, 2022.

[64] L. Landau and E. Lifshitz, "On the theory of the dispersion of magnetic permeability in ferromagnetic bodies," in *Perspect. Theor. Phys.*, vol. 169, pp. 51–65, Elsevier, 1992.

[65] C. L. Dennis, R. P. Borges, L. D. Buda, U. Ebels, J. F. Gregg, M. Hehn, E. Jouguelet, K. Ounadjela, I. Petej, I. L. Prejbeanu, *et al.*, "The defining length scales of mesomagnetism: a review," *J. Phys. Condens. Matter*, vol. 14, no. 49, p. R1175, 2002.

[66] E. Gomonay and V. Loktev, "Mechanism of formation of the Equilibrium Domain Structure in Crystals Undergoing Thermoelastic Phase Transitions," *Phys. Solid State*, vol. 47, no. 9, pp. 1755–1760, 2005.

[67] W. Heisenberg, "Mehrkörperproblem und Resonanz in der Quantenmechanik," *Z. Phys.*, vol. 38, no. 6, pp. 411–426, 1926.

[68] P. A. M. Dirac, "On the theory of quantum mechanics," *Proc. R. Soc. London. Ser. A, Contain. Pap. a Math. Phys. Character*, vol. 112, no. 762, pp. 661–677, 1926.

[69] J. H. Van Vleck, "A Survey of the Theory of Ferromagnetism," *Rev. Mod. Phys.*, vol. 17, no. 1, p. 27, 1945.

[70] J. Kanamori, "Theory of the magnetic properties of ferrous and cobaltous oxides, II," *Prog. Theor. Phys.*, vol. 17, no. 2, pp. 197–222, 1957.

[71] C. G. Shull, W. Strauser, and E. Wollan, "Neutron diffraction by paramagnetic and antiferromagnetic substances," *Phys. Rev.*, vol. 83, no. 2, p. 333, 1951.

[72] H. Kramers, "L'interaction entre les atomes magnétogènes dans un cristal paramagnétique," *Physica*, vol. 1, no. 1-6, pp. 182–192, 1934.

[73] P. W. Anderson, "Antiferromagnetism. Theory of superexchange interaction," *Phys. Rev.*, vol. 79, no. 2, p. 350, 1950.

[74] J. H. van Vleck, "On the anisotropy of cubic ferromagnetic crystals," *Phys. Rev.*, vol. 52, no. 11, p. 1178, 1937.

[75] J. Stöhr, "Exploring the microscopic origin of magnetic anisotropies with X-ray magnetic circular dichroism (XMCD) spectroscopy," *J. Magn. Magn. Mater.*, vol. 200, no. 1-3, pp. 470–497, 1999.

[76] P. Bruno, "Tight-binding approach to the orbital magnetic moment and magnetocrystalline anisotropy of transition-metal monolayers," *Phys. Rev. B*, vol. 39, no. 1, p. 865, 1989.

[77] H. Meer, O. Gomonay, C. Schmitt, R. Ramos, L. Schnitzspan, F. Kronast, M.-A. Mawass, S. Valencia, E. Saitoh, J. Sinova, *et al.*, "Strain-induced shape anisotropy in antiferromagnetic structures," *Phys. Rev. B*, vol. 106, no. 9, p. 094430, 2022.

[78] P. Vergallo, B. Karetta, G. Consolo, and O. Gomonay, "Domain-wall orientation in antiferromagnets controlled by magnetoelastic effects," *arXiv preprint arXiv:2301.12539*, 2023.

[79] J. A. Osborn, "Demagnetizing factors of the general ellipsoid," *Phys. Rev.*, vol. 67, no. 11-12, p. 351, 1945.

[80] J. Dubowik, "Shape anisotropy of magnetic heterostructures," *Phys. Rev. B*, vol. 54, no. 2, p. 1088, 1996.

[81] L. D. Landau, "A possible explanation of the field dependence of the susceptibility at low temperatures," *Phys. Z. Sowjet*, vol. 4, p. 675, 1933.

[82] L. Néel, "Théorie du paramagnétisme constant. application au manganése," *C. R. Acad. Sci.*, vol. 203, pp. 304–306, 1936.

[83] C. G. Shull and J. S. Smart, "Detection of antiferromagnetism by neutron diffraction," *Phys. Rev.*, vol. 76, no. 8, p. 1256, 1949.

[84] I. Tsukada, J. Takeya, T. Masuda, and K. Uchinokura, "Two-stage spin-flop transitions in the $S = 1/2$ antiferromagnetic spin chain $BaCu_2Si_2O_7$," *Phys. Rev. Lett.*, vol. 87, no. 12, p. 127203, 2001.

[85] H. Taniguchi, S. Suzuki, T. Arakawa, H. Yoshida, Y. Niimi, and K. Kobayashi, "Fabrication of thin films of two-dimensional triangular antiferromagnet Ag_2CrO_2 and their transport properties," *AIP Adv.*, vol. 8, no. 2, 2018.

[86] W. Xing, L. Qiu, X. Wang, Y. Yao, Y. Ma, R. Cai, S. Jia, X. Xie, and W. Han, "Magnon transport in quasi-two-dimensional van der Waals antiferromagnets," *Phys. Rev. X*, vol. 9, no. 1, p. 011026, 2019.

[87] H. Doki, M. Akazawa, H.-Y. Lee, J. H. Han, K. Sugii, M. Shimozawa, N. Kawashima, M. Oda, H. Yoshida, and M. Yamashita, "Spin thermal Hall conductivity of a kagome antiferromagnet," *Phys. Rev. Lett.*, vol. 121, no. 9, p. 097203, 2018.

[88] K. Kim, S. Y. Lim, J. Kim, J.-U. Lee, S. Lee, P. Kim, K. Park, S. Son, C.-H. Park, J.-G. Park, *et al.*, "Antiferromagnetic ordering in van der Waals 2D magnetic material $MnPS_3$ probed by Raman spectroscopy," *2D Mater.*, vol. 6, no. 4, p. 041001, 2019.

[89] T. Olsen, "Antiferromagnetism in two-dimensional materials: progress and computational challenges," *2D Mater.*, vol. 11, no. 3, p. 033005, 2024.

[90] D. Herrmann-Ronzaud, P. Burlet, and J. Rossat-Mignod, "Equivalent type-II magnetic structures: CoO, a collinear antiferromagnet," *J. Phys. C: Solid State Phys.*, vol. 11, no. 10, p. 2123, 1978.

[91] W. Roth, "Neutron and optical studies of domains in NiO," *J. Appl. Phys.*, vol. 31, no. 11, pp. 2000–2011, 1960.

[92] K. Tomiyasu, T. Inami, and N. Ikeda, "Magnetic structure of CoO studied by neutron and synchrotron x-ray diffraction," *Phys. Rev. B*, vol. 70, no. 18, p. 184411, 2004.

[93] R. Duine, K.-J. Lee, S. S. Parkin, and M. D. Stiles, "Synthetic antiferromagnetic spintronics," *Nat. Phys.*, vol. 14, no. 3, pp. 217–219, 2018.

[94] W. Legrand, D. Maccariello, F. Ajejas, S. Collin, A. Vecchiola, K. Bouzehouane, N. Reyren, V. Cros, and A. Fert, "Room-temperature stabilization of antiferromagnetic skyrmions in synthetic antiferromagnets," *Nat. Mater.*, vol. 19, no. 1, pp. 34–42, 2020.

[95] A. Rajan, T. G. Saunderson, F. R. Lux, R. Y. Díaz, H. M. Abdullah, A. Bose, B. Bednarz, J.-Y. Kim, D. Go, T. Hajiri, *et al.*, "Revealing the higher-order spin nature of the Hall effect in non-collinear antiferromagnet $Mn_3Ni_{0.35}Cu_{0.65}N$," *arXiv preprint arXiv:2304.10747*, 2023.

[96] A. Kohn, A. Kovács, R. Fan, G. McIntyre, R. Ward, and J. Goff, "The antiferromagnetic structures of $IrMn_3$ and their influence on exchange-bias," *Sci. Rep.*, vol. 3, no. 1, pp. 1–7, 2013.

[97] P. Weiss, "L'hypothèse du champ moléculaire et la propriété ferromagnétique," *J. Phys. Theor. Appl.*, vol. 6, no. 1, pp. 661–690, 1907.

[98] B. Barbara, "Louis Néel: His multifaceted seminal work in magnetism," *Comptes Rendus Phys.*, vol. 20, no. 7-8, pp. 631–649, 2019.

[99] F. Bloch, "Zur Theorie des Austauschproblems und der Remanenzerscheinung der Ferromagnetika," *Z. Phys.*, vol. 74, no. 5, pp. 295–335, 1932.

[100] L. Néel, "Energie des parois de Bloch dans les couches minces," *C. R. Acad. Sci.*, vol. 241, no. 6, pp. 533–537, 1955.

[101] H. Kondoh and T. Takeda, "Observation of antiferromagnetic domains in nickel oxide," *J. Phys. Soc. Jpn.*, vol. 19, no. 11, pp. 2041–2051, 1964.

[102] W. J. Ince and A. Platzker, "Antiferromagnetic Domains in $RbMnF_3$," *Phys. Rev.*, vol. 175, no. 2, p. 650, 1968.

[103] F. Spooner and M. Vernon, "Growth, perfection and antiferromagnetic domain structure of epitaxial cobalt oxide," *J. Mater. Sci.*, vol. 4, pp. 734–742, 1969.

[104] B. K. Tanner, "Antiferromagnetic domains," *Contemp. Phys.*, vol. 20, no. 2, pp. 187–210, 1979.

[105] A. Scholl, J. Stöhr, J. Luning, J. W. Seo, J. Fompeyrine, H. Siegwart, J.-P. Locquet, F. Nolting, S. Anders, E. Fullerton, *et al.*, "Observation of antiferromagnetic domains in epitaxial thin films," *Science*, vol. 287, no. 5455, pp. 1014–1016, 2000.

[106] A. V. Goltsev, R. V. Pisarev, T. Lottermoser, and M. Fiebig, "Structure and Interaction of Antiferromagnetic Domain Walls in Hexagonal $YMnO_3$," *Phys. Rev. Lett.*, vol. 90, no. 17, p. 177204, 2003.

[107] A. S. Zimmermann, B. Van Aken, H. Schmid, J.-P. Rivera, J. Li, D. Vaknin, and M. Fiebig, "Anisotropy of antiferromagnetic 180° domains in magnetoelectric $LiMPO_4$ (M= Fe, Co, Ni)," *Eur. Phys. J. B*, vol. 71, no. 3, pp. 355–360, 2009.

[108] B. Náfrádi, T. Keller, F. Hardy, C. Meingast, A. Erb, and B. Keimer, "Magnetostriction and magnetostructural domains in antiferromagnetic $YBa_2Cu_3O_6$," *Phys. Rev. Lett.*, vol. 116, no. 4, p. 047001, 2016.

[109] H. Gomonay and V. M. Loktev, "Magnetostriction and magnetoelastic domains in antiferromagnets," *J. Phys. Condens. Matter*, vol. 14, no. 15, p. 3959, 2002.

[110] Y.-Y. Li, "Domain walls in antiferromagnets and the weak ferromagnetism of $\alpha - Fe_2O_3$," *Phys. Rev.*, vol. 101, no. 5, p. 1450, 1956.

[111] O. Gomonay, S. Kondovych, and V. Loktev, "Shape-induced anisotropy in antiferromagnetic nanoparticles," *J. Magn. Magn. Mater.*, vol. 354, pp. 125–135, 2014.

[112] J. P. Joule, "XVII. On the effects of magnetism upon the dimensions of iron and steel bars," *London, Edinburgh, Dublin Philos. Mag. J. Sci.*, vol. 30, no. 199, pp. 76–87, 1847.

[113] H. A. Pidgeon, "Magneto-striction with special reference to pure cobalt," *Phys. Rev.*, vol. 13, no. 3, p. 209, 1919.

[114] E. W. Lee, "Magnetostriction and magnetomechanical effects," *Reports Prog. Phys.*, vol. 18, no. 1, p. 184, 1955.

[115] B. Karetta, "Antiferromagnetic Domains in Presence of Magnetoelastic Interactions," Master thesis, Johannes Gutenberg University Mainz, 2021.

[116] N. Poulis, J. Van den Handel, J. Ubbink, J. Poulis, and C. Gorter, "On antiferromagnetism in a single crystal," *Phys. Rev.*, vol. 82, no. 4, p. 552, 1951.

[117] C. Gorter and J. Haantjes, "Anti-ferromagnetism at the absolute zero of temperature in the case of rhombic symmetry," *Physica*, vol. 18, no. 5, pp. 285–294, 1952.

[118] P. Anderson, F. Merritt, J. Remeika, and W. Yager, "Magnetic Resonance in $\alpha - Fe_2O_3$," *Phys. Rev.*, vol. 93, no. 4, p. 717, 1954.

[119] F. M. Johnson and A. H. Nethercot Jr, "Antiferromagnetic resonance in MnF_2," *Phys. Rev.*, vol. 114, no. 3, p. 705, 1959.

[120] S. Foner, "High-field antiferromagnetic resonance in Cr_2O_3," *Phys. Rev.*, vol. 130, no. 1, p. 183, 1963.

[121] M. Grzybowski, C. Schippers, O. Gomonay, K. Rubi, M. Bal, U. Zeitler, A. Kozioł-Rachwał, M. Szpytma, W. Janus, B. Kurowska, *et al.*, "Antiferromagnetic hysteresis above the spin-flop field," *Phys. Rev. B*, vol. 107, no. 6, p. L060403, 2023.

[122] E. H. Hall *et al.*, "On a new action of the magnet on electric currents," *Am. J. Math.*, vol. 2, no. 3, pp. 287–292, 1879.

[123] N. Nagaosa, J. Sinova, S. Onoda, A. H. MacDonald, and N. P. Ong, "Anomalous Hall Effect," *Rev. Mod. Phys.*, vol. 82, no. 2, pp. 1539–1592, 2010.

[124] R. E. Prange and S. M. Girvin, *The quantum Hall effect*. Springer, 1987.

[125] D. Xiao, W. Yao, and Q. Niu, "Valley-contrasting physics in graphene: magnetic moment and topological transport," *Phys. Rev. Lett.*, vol. 99, no. 23, p. 236809, 2007.

[126] A. Neubauer, C. Pfleiderer, B. Binz, A. Rosch, R. Ritz, P. Niklowitz, and P. Böni, "Topological Hall effect in the A phase of MnSi," *Phys. Rev. Lett.*, vol. 102, no. 18, p. 186602, 2009.

[127] Y. K. Kato, R. C. Myers, A. C. Gossard, and D. D. Awschalom, "Observation of the spin Hall effect in semiconductors," *Science*, vol. 306, no. 5703, pp. 1910–1913, 2004.

[128] J. Sinova, S. Valenzuela, J. Wunderlich, C. Back, and T. Jungwirth, "Spin Hall effects," *Rev. Mod. Phys*, vol. 87, no. 1213-1260, p. 482, 2015.

[129] E. Saitoh, M. Ueda, H. Miyajima, and G. Tatara, "Conversion of spin current into charge current at room temperature: Inverse spin-Hall effect," *Appl. Phys. Lett.*, vol. 88, no. 18, p. 182509, 2006.

[130] Y. Niimi and Y. Otani, "Reciprocal spin Hall effects in conductors with strong spin–orbit coupling: a review," *Rep. Prog. Phys*, vol. 78, no. 12, p. 124501, 2015.

[131] M. I. Dyakonov and V. Perel, "Current-induced spin orientation of electrons in semiconductors," *Phys. Lett. A*, vol. 35, no. 6, pp. 459–460, 1971.

[132] J. Hirsch, "Spin Hall Effect," *Phys. Rev. Lett.*, vol. 83, no. 9, p. 1834, 1999.

[133] S. Zhang, "Spin Hall effect in the presence of spin diffusion," *Phys. Rev. Lett.*, vol. 85, no. 2, p. 393, 2000.

[134] J. Smit, "The spontaneous Hall effect in ferromagnetics II," *Physica*, vol. 24, no. 1-5, pp. 39–51, 1958.

[135] L. Berger, "Side-jump mechanism for the Hall effect of ferromagnets," *Phys. Rev. B*, vol. 2, no. 11, p. 4559, 1970.

[136] S. Murakami, N. Nagaosa, and S.-C. Zhang, "Dissipationless quantum spin current at room temperature," *Science*, vol. 301, no. 5638, pp. 1348–1351, 2003.

[137] J. Sinova, D. Culcer, Q. Niu, N. Sinitsyn, T. Jungwirth, and A. H. MacDonald, "Universal intrinsic spin Hall effect," *Phys. Rev. Lett.*, vol. 92, no. 12, p. 126603, 2004.

[138] J. Wunderlich, B. Kaestner, J. Sinova, and T. Jungwirth, "Experimental observation of the spin-Hall effect in a two-dimensional spin-orbit coupled semiconductor system," *Phys. Rev. Lett.*, vol. 94, no. 4, p. 047204, 2005.

[139] H. Wang, C. Du, Y. Pu, R. Adur, P. C. Hammel, and F. Yang, "Scaling of spin Hall angle in 3*d*, 4*d*, and 5*d* metals from $Y_3Fe_5O_12$/metal spin pumping," *Phys. Rev. Lett.*, vol. 112, no. 19, p. 197201, 2014.

[140] E. Sagasta, Y. Omori, M. Isasa, M. Gradhand, L. E. Hueso, Y. Niimi, Y. Otani, and F. Casanova, "Tuning the spin Hall effect of Pt from the moderately dirty to the superclean regime," *Phys. Rev. B*, vol. 94, no. 6, p. 060412, 2016.

[141] L. Zhu, D. C. Ralph, and R. A. Buhrman, "Effective spin-mixing conductance of heavy-metal–ferromagnet interfaces," *Phys. Rev. Lett.*, vol. 123, no. 5, p. 057203, 2019.

[142] L. Zhu, L. Zhu, and R. A. Buhrman, "Fully spin-transparent magnetic interfaces enabled by the insertion of a thin paramagnetic NiO layer," *Phys. Rev. Lett.*, vol. 126, no. 10, p. 107204, 2021.

[143] J.-C. Rojas-Sánchez, N. Reyren, P. Laczkowski, W. Savero, J.-P. Attané, C. Deranlot, M. Jamet, J.-M. George, L. Vila, and H. Jaffrès, "Spin pumping and inverse spin Hall effect in platinum: the essential role of spin-memory loss at metallic interfaces," *Phys. Rev. Lett.*, vol. 112, no. 10, p. 106602, 2014.

[144] S.-Y. Huang, X. Fan, D. Qu, Y. Chen, W. Wang, J. Wu, T. Chen, J. Xiao, and C. Chien, "Transport magnetic proximity effects in platinum," *Phys. Rev. Lett.*, vol. 109, no. 10, p. 107204, 2012.

[145] H. Nakayama, M. Althammer, Y.-T. Chen, K.-i. Uchida, Y. Kajiwara, D. Kikuchi, T. Ohtani, S. Geprägs, M. Opel, S. Takahashi, *et al.*, "Spin Hall magnetoresistance induced by a nonequilibrium proximity effect," *Phys. Rev. Lett.*, vol. 110, no. 20, p. 206601, 2013.

[146] P. Bougiatioti, O. Manos, O. Kuschel, J. Wollschläger, M. Tolkiehn, S. Francoual, and T. Kuschel, "Impact of magnetic moment and anisotropy of $Co_{1-x}Fe_x$ thin films on the magnetic proximity effect of Pt," *arXiv preprint arXiv:1807.09032*, 2018.

[147] S. Geprägs, S. Meyer, S. Altmannshofer, M. Opel, F. Wilhelm, A. Rogalev, R. Gross, and S. T. Goennenwein, "Investigation of induced Pt magnetic polarization in $Pt/Y_3Fe_5O_{12}$ bilayers," *Appl. Phys. Lett.*, vol. 101, no. 26, 2012.

[148] S. Geprägs, C. Klewe, S. Meyer, D. Graulich, F. Schade, M. Schneider, S. Francoual, S. P. Collins, K. Ollefs, F. Wilhelm, *et al.*, "Static magnetic proximity effects and spin Hall magnetoresistance in $Pt/Y_3Fe_5O_{12}$ and inverted $Y_3Fe_5O_{12}$/Pt bilayers," *Phys. Rev. B*, vol. 102, no. 21, p. 214438, 2020.

[149] T. Kuschel, C. Klewe, J.-M. Schmalhorst, F. Bertram, O. Kuschel, T. Schemme, J. Wollschläger, S. Francoual, J. Strempfer, A. Gupta, *et al.*, "Static magnetic proximity effect in $Pt/NiFe_2O_4$ and Pt/Fe bilayers investigated by X-ray resonant magnetic reflectivity," *Phys. Rev. Lett.*, vol. 115, no. 9, p. 097401, 2015.

[150] T. Kuschel, C. Klewe, P. Bougiatioti, O. Kuschel, J. Wollschläger, L. Bouchenoire, S. D. Brown, J.-M. Schmalhorst, D. Meier, and G. Reiss, "Static Magnetic Proximity Effect in Pt Layers on Sputter-Deposited $NiFe_2O_4$ and on Fe of Various Thicknesses Investigated by XRMR," *IEEE Trans. Magn.*, vol. 52, no. 7, pp. 1–4, 2016.

[151] M. Valvidares, N. Dix, M. Isasa, K. Ollefs, F. Wilhelm, A. Rogalev, F. Sánchez, E. Pellegrin, A. Bedoya-Pinto, P. Gargiani, *et al.*, "Absence of magnetic proximity effects in magnetoresistive $Pt/CoFe_2O_4$ hybrid interfaces," *Phys. Rev. B*, vol. 93, no. 21, p. 214415, 2016.

[152] Y. A. Bychkov and É. I. Rashba, "Properties of a 2D electron gas with lifted spectral degeneracy," *JETP Lett.*, vol. 39, no. 2, p. 78, 1984.

[153] V. M. Edelstein, "Spin polarization of conduction electrons induced by electric current in two-dimensional asymmetric electron systems," *Solid State Commun.*, vol. 73, no. 3, pp. 233–235, 1990.

[154] A. Manchon, H. C. Koo, J. Nitta, S. M. Frolov, and R. A. Duine, "New perspectives for Rashba spin–orbit coupling," *Nat. Mater.*, vol. 14, no. 9, pp. 871–882, 2015.

[155] J. R. Sánchez, L. Vila, G. Desfonds, S. Gambarelli, J. Attané, J. De Teresa, C. Magén, and A. Fert, "Spin-to-charge conversion using Rashba coupling at the interface between non-magnetic materials," *Nat. Commun.*, vol. 4, no. 1, p. 2944, 2013.

[156] J. Nitta, T. Akazaki, H. Takayanagi, and T. Enoki, "Gate control of spin-orbit interaction in an inverted $In_{0.53}Ga_{0.47}As/In_{0.52}Al_{0.48}$ as heterostructure," *Phys. Rev. Lett.*, vol. 78, no. 7, p. 1335, 1997.

[157] T. Koga, J. Nitta, T. Akazaki, and H. Takayanagi, "Rashba spin-orbit coupling probed by the weak antilocalization analysis in InAlAs/InGaAs/InAlAs quantum wells as a function of quantum well asymmetry," *Phys. Rev. Lett.*, vol. 89, no. 4, p. 046801, 2002.

[158] J.-C. Rojas-Sánchez, S. Oyarzún, Y. Fu, A. Marty, C. Vergnaud, S. Gambarelli, L. Vila, M. Jamet, Y. Ohtsubo, A. Taleb-Ibrahimi, *et al.*, "Spin to charge conversion at room temperature by spin pumping into a new type of topological insulator: α-Sn films," *Phys. Rev. Lett.*, vol. 116, no. 9, p. 096602, 2016.

[159] Q. Song, H. Zhang, T. Su, W. Yuan, Y. Chen, W. Xing, J. Shi, J. Sun, and W. Han, "Observation of inverse Edelstein effect in Rashba-split 2DEG between $SrTiO_3$ and $LaAlO_3$ at room temperature," *Sci. Adv.*, vol. 3, no. 3, p. e1602312, 2017.

[160] A. R. Mellnik, J. Lee, A. Richardella, J. L. Grab, P. J. Mintun, M. H. Fischer, A. Vaezi, A. Manchon, E.-A. Kim, N. Samarth, *et al.*, "Spin-transfer torque generated by a topological insulator," *Nature*, vol. 511, no. 7510, pp. 449–451, 2014.

[161] P. Gambardella and I. M. Miron, "Current-induced spin-orbit torques," *Philos. Trans. R. Soc. A*, vol. 369, no. 1948, pp. 3175–3197, 2011.

[162] V. P. Amin and M. D. Stiles, "Spin transport at interfaces with spin-orbit coupling: Formalism," *Phys. Rev. B*, vol. 94, no. 10, p. 104419, 2016.

[163] C. Heiliger, P. Zahn, and I. Mertig, "Microscopic origin of magnetoresistance," *Mater. Today*, vol. 9, no. 11, pp. 46–54, 2006.

[164] N. Vlietstra, J. Shan, V. Castel, J. Ben Youssef, G. Bauer, and B. Van Wees, "Exchange magnetic field torques in YIG/Pt bilayers observed by the spin-Hall magnetoresistance," *Appl. Phys. Lett.*, vol. 103, no. 3, p. 032401, 2013.

[165] Y.-T. Chen, S. Takahashi, H. Nakayama, M. Althammer, S. T. Goennenwein, E. Saitoh, and G. E. Bauer, "Theory of spin Hall magnetoresistance," *Phys. Rev. B*, vol. 87, no. 14, p. 144411, 2013.

[166] A. Manchon, "Spin Hall magnetoresistance in antiferromagnet/normal metal bilayers," *Phys. Status Solidi - Rapid Res. Lett.*, vol. 11, no. 4, p. 1600409, 2017.

[167] L. Baldrati, A. Ross, T. Niizeki, C. Schneider, R. Ramos, J. Cramer, O. Gomonay, M. Filianina, T. Savchenko, D. Heinze, *et al.*, "Full angular dependence of the spin Hall and ordinary magnetoresistance in epitaxial antiferromagnetic NiO (001)/Pt thin films," *Phys. Rev. B*, vol. 98, no. 2, p. 024422, 2018.

[168] J. Fischer, O. Gomonay, R. Schlitz, K. Ganzhorn, N. Vlietstra, M. Althammer, H. Huebl, M. Opel, R. Gross, S. T. Goennenwein, *et al.*, "Spin Hall magnetoresistance in antiferromagnet/heavy-metal heterostructures," *Phys. Rev. B*, vol. 97, no. 1, p. 014417, 2018.

[169] J. Han, C. Song, F. Li, Y. Wang, G. Wang, Q. Yang, and F. Pan, "Antiferromagnet-controlled spin current transport in $SrMnO_3$/Pt hybrids," *Phys. Rev. B*, vol. 90, no. 14, p. 144431, 2014.

[170] G. R. Hoogeboom, A. Aqeel, T. Kuschel, T. T. Palstra, and B. J. van Wees, "Negative spin Hall magnetoresistance of Pt on the bulk easy-plane antiferromagnet NiO," *Appl. Phys. Lett.*, vol. 111, no. 5, p. 052409, 2017.

[171] B. A. Bernevig, T. L. Hughes, and S.-C. Zhang, "Orbitronics: The intrinsic orbital current in p-doped silicon," *Phys. Rev. Lett.*, vol. 95, no. 6, p. 066601, 2005.

[172] D. Lee, D. Go, H.-J. Park, W. Jeong, H.-W. Ko, D. Yun, D. Jo, S. Lee, G. Go, J. H. Oh, *et al.*, "Orbital torque in magnetic bilayers," *Nat. Commun.*, vol. 12, no. 1, p. 6710, 2021.

[173] B. Thole, P. Carra, F. Sette, and G. van der Laan, "X-ray circular dichroism as a probe of orbital magnetization," *Phys. Rev. Lett.*, vol. 68, no. 12, p. 1943, 1992.

[174] J. H. Van Vleck, *The theory of electric and magnetic susceptibilities*. Oxford University Press, 1932.

[175] O. Dowinton and M. S. Bahramy, "Orbital angular momentum driven anomalous Hall effect," *Phys. Rev. B*, vol. 105, no. 23, p. 235142, 2022.

[176] H. Zheng, "Electronic structure of CoO," *Phys. B: Condens. Matter*, vol. 212, no. 2, pp. 125–138, 1995.

[177] M. Norman, "Orbital polarization and the insulating gap in the transition-metal oxides," *Phys. Rev. Lett.*, vol. 64, no. 10, p. 1162, 1990.

[178] R. Radwanski and Z. Ropka, "Orbital moment in CoO and in NiO," *Phys. B: Condens. Matter*, vol. 345, no. 1-4, pp. 107–110, 2004.

[179] T. Valet and R. Raimondi, "Semiclassical kinetic theory for systems with non-trivial quantum geometry and the expectation value of physical quantities," *Europhys. Lett.*, vol. 143, no. 2, p. 26005, 2023.

[180] T. Valet, H. Jaffres, V. Cros, and R. Raimondi, "Quantum Kinetic Anatomy of Electron Angular Momenta Edge Accumulation," *arXiv preprint arXiv:2507.06771*, 2025.

[181] L. Salemi, M. Berritta, A. K. Nandy, and P. M. Oppeneer, "Orbitally dominated Rashba-Edelstein effect in noncentrosymmetric antiferromagnets," *Nat. Commun.*, vol. 10, no. 1, p. 5381, 2019.

[182] S. Krishnia, Y. Sassi, F. Ajejas, N. Sebe, N. Reyren, S. Collin, T. Denneulin, A. Kovács, R. E. Dunin-Borkowski, A. Fert, J.-M. George, V. Cros, and H. Jaffrès, "Large Interfacial Rashba Interaction Generating Strong Spin–Orbit

Torques in Atomically Thin Metallic Heterostructures," *Nano Lett.*, vol. 23, no. 15, pp. 6785–6791, 2023.

[183] L. Petersen and P. Hedegård, "A simple tight-binding model of spin-orbit splitting of *sp*-derived surface states," *Surf. Sci.*, vol. 459, no. 1-2, pp. 49–56, 2000.

[184] D. Go, D. Jo, T. Gao, K. Ando, S. Blügel, H.-W. Lee, and Y. Mokrousov, "Orbital Rashba effect in a surface-oxidized Cu film," *Phys. Rev. B*, vol. 103, no. 12, p. L121113, 2021.

[185] S. Ding, Z. Liang, D. Go, C. Yun, M. Xue, Z. Liu, S. Becker, W. Yang, H. Du, C. Wang, Y. Yang, G. Jakob, M. Kläui, Y. Mokrousov, and J. Yang, "Observation of the Orbital Rashba-Edelstein Magnetoresistance," *Phys. Rev. Lett.*, vol. 128, no. 6, p. 067201, 2022.

[186] D. Go and H.-W. Lee, "Orbital torque: Torque generation by orbital current injection," *Phys. Rev. Res.*, vol. 2, no. 1, p. 013177, 2020.

[187] G. van der Laan and B. Thole, "Strong magnetic x-ray dichroism in 2*p* absorption spectra of 3*d* transition-metal ions," *Phys. Rev. B*, vol. 43, no. 16, p. 13401, 1991.

[188] P. Santini, S. Carretta, G. Amoretti, R. Caciuffo, N. Magnani, and G. H. Lander, "Multipolar interactions in f-electron systems: The paradigm of actinide dioxides," *Rev. Mod. Phys.*, vol. 81, no. 2, pp. 807–863, 2009.

[189] S. Ding, P. Noël, G. K. Krishnaswamy, N. Davitti, G. Sala, M. Fantauzzi, A. Rossi, and P. Gambardella, "Generation, transmission, and conversion of orbital torque by an antiferromagnetic insulator," *Nat. Commun.*, vol. 16, no. 1, p. 9239, 2025.

[190] T. McGuire and R. Potter, "Anisotropic magnetoresistance in ferromagnetic 3d alloys," *IEEE Trans. Magn.*, vol. 11, no. 4, pp. 1018–1038, 2003.

[191] S. Vélez, V. N. Golovach, A. Bedoya-Pinto, M. Isasa, E. Sagasta, M. Abadia, C. Rogero, L. E. Hueso, F. S. Bergeret, and F. Casanova, "Hanle magnetoresistance in thin metal films with strong spin-orbit coupling," *Phys. Rev. Lett.*, vol. 116, no. 1, p. 016603, 2016.

[192] T. Shiino, S.-H. Oh, P. M. Haney, S.-W. Lee, G. Go, B.-G. Park, and K.-J. Lee, "Antiferromagnetic domain wall motion driven by spin-orbit torques," *Phys. Rev. Lett.*, vol. 117, no. 8, p. 087203, 2016.

[193] J. Železnỳ, H. Gao, K. Vỳbornỳ, J. Zemen, J. Mašek, A. Manchon, J. Wunderlich, J. Sinova, and T. Jungwirth, "Relativistic Néel-order fields induced by electrical current in antiferromagnets," *Phys. Rev. Lett.*, vol. 113, no. 15, p. 157201, 2014.

[194] S. Y. Bodnar, L. Šmejkal, I. Turek, T. Jungwirth, O. Gomonay, J. Sinova, A. Sapozhnik, H.-J. Elmers, M. Kläui, and M. Jourdan, "Writing and reading antiferromagnetic Mn_2Au by Néel spin-orbit torques and large anisotropic magnetoresistance," *Nat. Commun.*, vol. 9, no. 348, p. 348, 2018.

[195] H. V. Gomonay and V. M. Loktev, "Spin transfer and current-induced switching in antiferromagnets," *Phys. Rev. B*, vol. 81, no. 14, p. 144427, 2010.

[196] A. Manchon, J. Železný, I. M. Miron, T. Jungwirth, J. Sinova, A. Thiaville, K. Garello, and P. Gambardella, "Current-induced spin-orbit torques in ferromagnetic and antiferromagnetic systems," *Rev. Mod. Phys.*, vol. 91, no. 3, p. 035004, 2019.

[197] I. Gray, T. Moriyama, N. Sivadas, G. M. Stiehl, J. T. Heron, R. Need, B. J. Kirby, D. H. Low, K. C. Nowack, D. G. Schlom, *et al.*, "Spin Seebeck imaging of spin-torque switching in antiferromagnetic Pt/NiO heterostructures," *Phys. Rev. X*, vol. 9, no. 4, p. 041016, 2019.

[198] C. Schmitt, L. Sanchez-Tejerina, M. Filianina, F. Fuhrmann, H. Meer, R. Ramos, F. Maccherozzi, D. Backes, E. Saitoh, G. Finocchio, *et al.*, "Identifying the domain-wall spin structure in antiferromagnetic NiO/Pt," *Phys. Rev. B*, vol. 107, no. 18, p. 184417, 2023.

[199] B. J. Jacot, G. Krishnaswamy, G. Sala, C. O. Avci, S. Vélez, P. Gambardella, and C.-H. Lambert, "Systematic study of nonmagnetic resistance changes due to electrical pulsing in single metal layers and metal/antiferromagnet bilayers," *J. Appl. Phys.*, vol. 128, no. 17, p. 173902, 2020.

[200] P. Zhang, J. Finley, T. Safi, and L. Liu, "Quantitative study on current-induced effect in an antiferromagnet insulator/Pt bilayer film," *Phys. Rev. Lett.*, vol. 123, no. 24, p. 247206, 2019.

[201] M. Meinert, D. Graulich, and T. Matalla-Wagner, "Electrical switching of antiferromagnetic Mn_2Au and the role of thermal activation," *Phys. Rev. Appl.*, vol. 9, no. 6, p. 064040, 2018.

[202] P. S. Ho and T. Kwok, "Electromigration in metals," *Rep. Prog. Phys*, vol. 52, no. 3, p. 301, 1989.

[203] T. Matalla-Wagner, J.-M. Schmalhorst, G. Reiss, N. Tamura, and M. Meinert, "Resistive contribution in electrical-switching experiments with antiferromagnets," *Phys. Rev. Res.*, vol. 2, no. 3, p. 033077, 2020.

[204] A. Churikova, D. Bono, B. Neltner, A. Wittmann, L. Scipioni, A. Shepard, T. Newhouse-Illige, J. Greer, and G. Beach, "Non-magnetic origin of spin Hall magnetoresistance-like signals in Pt films and epitaxial NiO/Pt bilayers," *Appl. Phys. Lett.*, vol. 116, no. 2, p. 022410, 2020.

[205] F. Schreiber, L. Baldrati, C. Schmitt, R. Ramos, E. Saitoh, R. Lebrun, and M. Kläui, "Concurrent magneto-optical imaging and magneto-transport readout of electrical switching of insulating antiferromagnetic thin films," *Appl. Phys. Lett.*, vol. 117, no. 8, p. 082401, 2020.

[206] P. J. Kelly and R. D. Arnell, "Magnetron sputtering: a review of recent developments and applications," *Vacuum*, vol. 56, no. 3, pp. 159–172, 2000.

[207] A. Scholl, H. Ohldag, F. Nolting, J. Stöhr, and H. A. Padmore, "X-ray photoemission electron microscopy, a tool for the investigation of complex magnetic structures," *Rev. Sci. Instrum.*, vol. 73, no. 3, pp. 1362–1366, 2002.

[208] J. Cramer, *Propagation, manipulation and detection of magnonic spin currents in magnetic oxides and metals.* PhD thesis, Johannes Gutenberg-Universität Mainz, 2018.

[209] A. Ross, *Probing magnetostatic and magnetotransport properties of the antiferromagnetic iron oxide hematite.* PhD thesis, Johannes Gutenberg-Universität Mainz, 2021.

[210] S. M. Czekaj, *Ferromagnetic and antiferromagnetic domain configurations in thin films and multilayers: towards a patterned exchange bias system.* PhD thesis, ETH Zurich, 2007.

[211] S. Reimers, *Antiferromagnetic domain structure in tetragonal CuMnAs films: A picturebook of domains, domain walls and everything in between.* Phd thesis, University of Nottingham, 2022. Available under Creative Commons Attribution License. PDF download available. Supervisors: Kevin Edmonds, Peter Wadley.

[212] H. Meer, *Antiferromagnetic Insulatronics: Control and Manipulation of Magnetic Domains.* Phd thesis, Johannes Gutenberg-Universität Mainz, Mainz, Germany, 2023.

[213] W. Roth, "Magnetic structures of MnO, FeO, CoO, and NiO," *Phys. Rev.*, vol. 110, no. 6, p. 1333, 1958.

[214] R. Powell and W. Spicer, "Optical properties of NiO and CoO," *Phys. Rev. B*, vol. 2, no. 6, p. 2182, 1970.

[215] K. Kim, "X-ray-photoelectron spectroscopic studies of the electronic structure of CoO," *Phys. Rev. B*, vol. 11, no. 6, p. 2177, 1975.

[216] J. Van Elp, J. Wieland, H. Eskes, P. Kuiper, G. Sawatzky, F. De Groot, and T. Turner, "Electronic structure of CoO, li-doped CoO, and $LiCoO_2$," *Phys. Rev. B*, vol. 44, no. 12, p. 6090, 1991.

[217] G. Ghiringhelli, L. Tjeng, A. Tanaka, O. Tjernberg, T. Mizokawa, J. de Boer, and N. Brookes, "*3d* spin-orbit photoemission spectrum of nonferromagnetic materials: The test cases of CoO and Cu," *Phys. Rev. B*, vol. 66, no. 7, p. 075101, 2002.

[218] E. Uchida, N. Fukuoka, H. Kondoh, T. Takeda, Y. Nakazumi, and T. Nagamiya, "Magnetic anisotropy measurements of CoO single crystal," *J. Phys. Soc. Jpn.*, vol. 19, no. 11, pp. 2088–2095, 1964.

[219] S. Saito, K. Nakahigashi, and Y. Shimomura, "X-ray diffraction study on CoO," *J. Phys. Soc. Jpn.*, vol. 21, no. 5, pp. 850–860, 1966.

[220] N. Tombs and H. Rooksby, "Structure of monoxides of some transition elements at low temperatures," *Nature*, vol. 165, no. 4194, pp. 442–443, 1950.

[221] S. Greenwald and J. S. Smart, "Deformations in the crystal structures of antiferromagnetic compounds," *Nature*, vol. 166, no. 4221, pp. 523–524, 1950.

[222] Y.-Y. Li, "Magnetic moment arrangements and magnetocrystalline deformations in antiferromagnetic compounds," *Phys. Rev.*, vol. 100, no. 2, p. 627, 1955.

[223] W. Jauch, M. Reehuis, H. Bleif, F. Kubanek, and P. Pattison, "Crystallographic symmetry and magnetic structure of CoO," *Phys. Rev. B*, vol. 64, no. 5, p. 052102, 2001.

[224] T. Nagamiya and K. Motizuki, "Theory of the magnetic scattering of neutrons by CoO," *Rev. Mod. Phys.*, vol. 30, no. 1, p. 89, 1958.

[225] B. van Laar, "Multi-spin-axis structure for CoO," *Phys. Rev.*, vol. 138, no. 2A, p. A584, 1965.

[226] B. van Laar, "A new interpretation of magnetic anisotropy measurement on CoO single crystals," *J. Phys. Soc. Jpn.*, vol. 20, no. 7, pp. 1282–1283, 1965.

[227] B. van Laar, J. Schweizer, and R. Lemaire, "Neutron-diffraction investigation of CoO single crystals," *Phys. Rev.*, vol. 141, no. 2, p. 538, 1966.

[228] T. Nagamiya, S. Saito, Y. Shimomura, and E. Uchida, "Magnetic structure of CoO," *J. Phys. Soc. Jpn.*, vol. 20, no. 7, pp. 1285–1286, 1965.

[229] K. H. Germann, K. Maier, and E. Strauss, "Linear magnetic birefringence in transition metal oxides: CoO," *Phys. status solidi*, vol. 61, no. 2, pp. 449–454, 1974.

[230] O. Nakanishi and T. Yamada, "Magnetic anisotropy from exchange interaction and magnetic structure of CoO," *J. Phys. Soc. Jpn.*, vol. 36, no. 5, pp. 1315–1321, 1974.

[231] E. Krüger, "Magnetic structure of CoO," *Symmetry*, vol. 13, no. 8, p. 1513, 2021.

[232] E. Krüger, "Magnetic bands producing a monoclinic magnetic structure in NiO, FeO, MnO, and a tetragonal one in CoO," *Symmetry*, vol. 14, no. 7, p. 1285, 2022.

[233] Q. Li, T. Gu, J. Zhu, Z. Ding, J. Li, J. Liang, Y. Luo, Z. Hu, C. Hua, H.-J. Lin, *et al.*, "Multiple in-plane spin reorientation transitions in Fe/CoO bilayers grown on vicinal MgO (001)," *Phys. Rev. B*, vol. 91, no. 10, p. 104424, 2015.

[234] S. Csiszar, M. Haverkort, Z. Hu, A. Tanaka, H. Hsieh, H.-J. Lin, C. Chen, T. Hibma, and L. Tjeng, "Controlling orbital moment and spin orientation in CoO layers by strain," *Phys. Rev. Lett.*, vol. 95, no. 18, p. 187205, 2005.

[235] J. Zhu, Q. Li, J. Li, Z. Ding, C. Hua, M. Huang, H.-J. Lin, Z. Hu, C. Won, and Y. Wu, "Strain-modulated antiferromagnetic spin orientation and exchange coupling in Fe/CoO (001)," *J. Appl. Phys.*, vol. 115, no. 19, 2014.

[236] J. Zhu, Q. Li, J. Li, Z. Ding, J. Liang, X. Xiao, Y. Luo, C. Hua, H.-J. Lin, T. Pi, *et al.*, "Antiferromagnetic spin reorientation transition in epitaxial NiO/-CoO/MgO (001) systems," *Phys. Rev. B*, vol. 90, no. 5, p. 054403, 2014.

[237] W. Cao, J. Li, G. Chen, J. Zhu, C. Hu, and Y. Wu, "Temperature-dependent magnetic anisotropies in epitaxial Fe/CoO/MgO (001) system studied by the planar Hall effect," *Appl. Phys. Lett.*, vol. 98, no. 26, p. 262506, 2011.

[238] M. Grzybowski, C. Schippers, M. Bal, K. Rubi, U. Zeitler, M. Foltyn, B. Koopmans, and H. Swagten, "Electrical switching of antiferromagnetic CoO|Pt across the Néel temperature," *Appl. Phys. Lett.*, vol. 120, no. 12, 2022.

[239] W. Neubeck, C. Vettier, F. De Bergevin, F. Yakhou, D. Mannix, L. Ranno, and T. Chatterji, "Orbital moment determination of simple transition metal oxides using magnetic X-ray diffraction," *J. Phys. Chem. Solids*, vol. 62, no. 12, pp. 2173–2180, 2001.

[240] T. Satoh, R. Iida, T. Higuchi, Y. Fujii, A. Koreeda, H. Ueda, T. Shimura, K. Kuroda, V. Butrim, and B. Ivanov, "Excitation of coupled spin–orbit dynamics in cobalt oxide by femtosecond laser pulses," *Nat. Commun.*, vol. 8, no. 1, p. 638, 2017.

[241] A. Boussendel, N. Baadji, A. Haroun, H. Dreyssé, and M. Alouani, "Effect of substrate strain on calculated magnetic properties and magnetic anisotropy energy of CoO," *Phys. Rev. B*, vol. 81, no. 18, p. 184432, 2010.

[242] M. Ohring, "Chapter 7 - substrate surfaces and thin-film nucleation," in *The Materials Science of Thin Films*, pp. 357–415, Academic Press, 1992.

[243] W. R. Grove, "VII. On the electro-chemical polarity of gases," *Philos. Trans. R. Soc.*, vol. 142, pp. 87–101, 1852.

[244] W. R. Grove, "XXXIII. On some anomalous cases of electrical decomposition," *Philos. Mag.*, vol. 5, no. 31, pp. 203–209, 1853.

[245] V. S. Smentkowski, "Trends in sputtering," *Prog. Surf. Sci.*, vol. 64, no. 1-2, pp. 1–58, 2000.

[246] G. Bräuer, "Magnetron Sputtering," *Comprehensive Materials Processing*, vol. 4, pp. 57–73, 2014.

[247] C. Schmitt, A. Rajan, G. Beneke, A. Kumar, T. Sparmann, H. Meer, B. Bednarz, R. Ramos, M. A. Niño, M. Foerster, *et al.*, "Mechanisms of Electrical Switching of Ultrathin CoO/Pt Bilayers," *Nano Lett.*, vol. 24, no. 5, pp. 1471–1476, 2024.

[248] G. West and P. Kelly, "Influence of inert gas species on the growth of silver and molybdenum films via a magnetron discharge," *Surf. Coatings Technol.*, vol. 206, no. 7, pp. 1648–1652, 2011.

[249] R. Hippler, M. Cada, V. Stranak, and Z. Hubicka, "Time-resolved optical emission spectroscopy of a unipolar and a bipolar pulsed magnetron sputtering discharge in an argon/oxygen gas mixture with a cobalt target," *Plasma Sources Sci. Technol.*, vol. 28, no. 11, p. 115020, 2019.

[250] P. Sigmund, "Theory of sputtering. I. Sputtering yield of amorphous and polycrystalline targets," *Phys. Rev.*, vol. 184, no. 2, p. 383, 1969.

[251] K. Wasa, "2 - Sputtering phenomena," in *Handbook of Sputtering Technology*, pp. 41–75, William Andrew Publishing Oxford, UK, 2 ed., 2012.

[252] K. Wasa, "3 - Sputtering systems," in *Handbook of Sputtering Technology*, pp. 77–139, William Andrew Publishing Oxford, UK, 2 ed., 2012.

[253] T. H. Kim and G. Y. Yeom, "A review of inductively coupled plasma-assisted magnetron sputter system," *Appl. Sci. Converg. Technol.*, vol. 28, no. 5, pp. 131–138, 2019.

[254] J. Musil, P. Baroch, J. Vlček, K. Nam, and J. Han, "Reactive magnetron sputtering of thin films: present status and trends," *Thin solid films*, vol. 475, no. 1-2, pp. 208–218, 2005.

[255] W. D. Sproul, D. J. Christie, and D. C. Carter, "Control of reactive sputtering processes," *Thin solid films*, vol. 491, no. 1-2, pp. 1–17, 2005.

[256] "Bruker D8 Discover." https://www.bruker.com/en/products-and-solutions/diffractometers-and-x-ray-microscopes/x-ray-diffractometers/d8-discover-family/d8-discover.html. Last accessed: 08 December 2025.

[257] M. Deutsch and M. Hart, "Wavelength, energy shape, and structure of the Cu $K\alpha_1$ x-ray emission line," *Phys. Rev. B*, vol. 26, no. 10, p. 5558, 1982.

[258] J. Als-Nielsen and D. McMorrow, "Diffraction by perfect crystals," in *Elements of modern X-ray physics*, pp. 207–238, Cambridge: John Wiley & Sons, 2011.

[259] F. Masiello, G. Cembali, A. I. Chumakov, S. H. Connell, C. Ferrero, J. Härtwig, I. Sergeev, and P. Van Vaerenbergh, "Rocking curve measurements revisited," *Appl. Crystallogr.*, vol. 47, no. 4, pp. 1304–1314, 2014.

[260] J. Als-Nielsen and D. McMorrow, "Refraction and reflection from interfaces," in *Elements of modern X-ray physics*, pp. 69–112, Cambridge: John Wiley & Sons, 2011.

[261] L. Nevot and P. Croce, "Caractérisation des surfaces par réflexion rasante de rayons X. Application à l'étude du polissage de quelques verres silicates," *Revue de Physique appliquée*, vol. 15, no. 3, pp. 761–779, 1980.

[262] M. Ohring, "Chapter 14 - emerging thin-film materials and applications," in *The Materials Science of Thin Films*, pp. 629–683, Academic Press, 1992.

[263] Taiwan Semiconductor Manufacturing Company (TSMC), "3 nm Technology – Logic Technology." https://www.tsmc.com/english/dedicatedFoundry/technology/logic/l_3nm, 2025. Accessed 17 June 2025.

[264] Quantum Design Latin America / Durham Magneto Optics, "MicroWriter ML3." https://www.qd-latam.com/downloads/1/Microwriter-ML3.pdf. Last accessed: 8 July 2025.

[265] B. G. Park, J. Wunderlich, X. Martí, V. Holỳ, Y. Kurosaki, M. Yamada, H. Yamamoto, A. Nishide, J. Hayakawa, H. Takahashi, *et al.*, "A spin-valve-like magnetoresistance of an antiferromagnet-based tunnel junction," *Nat. Mater.*, vol. 10, no. 5, pp. 347–351, 2011.

[266] I. Fina, X. Marti, D. Yi, J. Liu, J. Chu, C. Rayan-Serrao, S. Suresha, A. Shick, J. Železnỳ, T. Jungwirth, *et al.*, "Anisotropic magnetoresistance in an antiferromagnetic semiconductor," *Nat. Commun.*, vol. 5, no. 1, p. 4671, 2014.

[267] M. Grzybowski, P. Wadley, K. Edmonds, R. Beardsley, V. Hills, R. Campion, B. Gallagher, J. S. Chauhan, V. Novak, T. Jungwirth, *et al.*, "Imaging current-induced switching of antiferromagnetic domains in CuMnAs," *Phys. Rev. Lett.*, vol. 118, no. 5, p. 057701, 2017.

[268] P. Wadley, S. Reimers, M. J. Grzybowski, C. Andrews, M. Wang, J. S. Chauhan, B. L. Gallagher, R. P. Campion, K. W. Edmonds, S. S. Dhesi, *et al.*, "Current polarity-dependent manipulation of antiferromagnetic domains," *Nat. Nanotechnol.*, vol. 13, no. 5, pp. 362–365, 2018.

[269] S. Reimers, Y. Lytvynenko, Y. Niu, E. Golias, B. Sarpi, L. Veiga, T. Denneulin, A. Kovacs, R. Dunin-Borkowski, J. Bläßer, *et al.*, "Current-driven writing process in antiferromagnetic Mn_2Au for memory applications," *Nat. Commun.*, vol. 14, no. 1, p. 1861, 2023.

[270] M. Jourdan, J. Bläßer, G. O. Gámez, S. Reimers, L. Odenbreit, M. Fischer, Y. R. Niu, E. Golias, F. Maccherozzi, A. Kleibert, *et al.*, "Identifying switching of

antiferromagnets by spin-orbit torques," *Physical Review B*, vol. 112, no. 10, p. 104408, 2025.

[271] D. Hou, Z. Qiu, J. Barker, K. Sato, K. Yamamoto, S. Vélez, J. M. Gomez-Perez, L. E. Hueso, F. Casanova, and E. Saitoh, "Tunable sign change of spin Hall magnetoresistance in Pt/NiO/YIG structures," *Phys. Rev. Lett.*, vol. 118, no. 14, p. 147202, 2017.

[272] "Keithley Instruments 6221 AC and DC curent source Datasheet." https://download.tek.com/datasheet/6220-6221.pdf. Last accessed: 07 December 2025.

[273] "Keithley Instruments 2182A Nanovoltmeter Datasheet." https://docs.rs-online.com/871d/0900766b8138fb6e.pdf. Last accessed: 07 December 2025.

[274] "Keysight Technologies 34790A Switch Unit Technical Overview." https://www.keysight.com/de/de/assets/7018-06839/technical-overviews/5965-5290.pdf. Last accessed: 07 December 2025.

[275] "Keithley Instruments 2400 SourceMeter Line Datasheet." https://docs.rs-online.com/8b04/0900766b810eb7d7.pdf. Last accessed: 07 Deceber 2025.

[276] "Model 335 Temperature Controller." https://www.lakeshore.com/docs/default-source/product-downloads/lstc_335_l.pdf?sfvrsn=becadb1e_3. Last accessed: 07 December 2025.

[277] "ANRv51/RES/LT/HV - rotator (360°endless)." https://www.attocube.com/downloads/anrv51resuhv-rotator-360-endless.pdf. Last accessed: 07 December 2025.

[278] "ANC350 Piezo Motion und Readout Controller." https://www.attocube.com/downloads/anc350-piezo-motion-and-readout-controller.pdf. Last accessed: 07 December 2025.

[279] G. Schmahl, "X-ray Microscopy," in *RÖNtgen Centennial: X-Rays in Natural and Life Sciences*, pp. 261–285, World Scientific, 1997.

[280] D. A. Shapiro, Y.-S. Yu, T. Tyliszczak, J. Cabana, R. Celestre, W. Chao, K. Kaznatcheev, A. D. Kilcoyne, F. Maia, S. Marchesini, *et al.*, "Chemical composition mapping with nanometre resolution by soft X-ray microscopy," *Nat. Photon.*, vol. 8, no. 10, pp. 765–769, 2014.

[281] P. Willmott, *An Introduction to Synchrotron Radiation: Techniques and Applications*. John Wiley & Sons, 2019.

[282] J. Stöhr, H. Padmore, S. Anders, T. Stammler, and M. Scheinfein, "Principles of X-ray magnetic dichroism spectromicroscopy," *Surf. Rev. Lett.*, vol. 5, no. 06, pp. 1297–1308, 1998.

[283] G. Van der Laan, "Applications of soft x-ray magnetic dichroism," in *J. Phys. Conf. Ser.*, vol. 430, p. 012127, IOP Publishing, 2013.

[284] J. Stöhr and H. C. Siegmann, "Magnetism: From Fundamentals to Nanoscale Dynamics," *Springer Series in Solid-State Sciences, Springer*, 2006.

[285] E. de Smit, J. F. Creemer, H. W. Zandbergen, B. M. Weckhuysen, and F. M. de Groot, "In-situ Scanning Transmission X-ray Microscopy of catalytic materials under reaction conditions," in *J. Phys. Conf. Ser.*, vol. 190, p. 012161, IOP Publishing, 2009.

[286] E. Margui and R. Van Grieken, *X-ray fluorescence spectrometry and related techniques: an introduction*. Momentum press, 2013.

[287] E. Bauer, "Photoelectron microscopy," *J. Phys. Condens. Matter*, vol. 13, no. 49, p. 11391, 2001.

[288] M. Ghidini, F. Maccherozzi, S. S. Dhesi, and N. D. Mathur, "XPEEM and MFM imaging of ferroic materials," *Adv. Electron. Mater.*, vol. 8, no. 6, p. 2200162, 2022.

[289] R. Nakajima, J. Stöhr, and Y. U. Idzerda, "Electron-yield saturation effects in L-edge x-ray magnetic circular dichroism spectra of Fe, Co, and Ni," *Phys. Rev. B*, vol. 59, no. 9, p. 6421, 1999.

[290] J. Stöhr and S. Anders, "X-ray spectro-microscopy of complex materials and surfaces," *IBM J. Res. Dev.*, vol. 44, no. 4, pp. 535–551, 2000.

[291] K. Kanaya, S. Ono, and F. Ishigaki, "Secondary electron emission from insulators," *J. Phys. D: Appl. Phys.*, vol. 11, no. 17, p. 2425, 1978.

[292] H. Ebert, J. Stöhr, S. Parkin, M. Samant, and A. Nilsson, "L-edge x-ray absorption in fcc and bcc Cu metal: Comparison of experimental and first-principles theoretical results," *Phys. Rev. B*, vol. 53, no. 23, p. 16067, 1996.

[293] G. Van der Laan, J. Zaanen, G. Sawatzky, R. Karnatak, and J.-M. Esteva, "Comparison of x-ray absorption with x-ray photoemission of nickel dihalides and NiO," *Phys. Rev. B*, vol. 33, no. 6, p. 4253, 1986.

[294] J. Stöhr, K. Baberschke, R. Jaeger, R. Treichler, and S. Brennan, "Orientation of chemisorbed molecules from surface-absorption fine-structure measurements: CO and NO on Ni (100)," *Phys. Rev. Lett.*, vol. 47, no. 5, p. 381, 1981.

[295] J. Goulon, C. Goulon-Ginet, A. Rogalev, V. Gotte, C. Malgrange, C. Brouder, and C. R. Natoli, "X-ray natural circular dichroism in a uniaxial gyrotropic single crystal of $LiIO_3$," *J. Chem. Phys.*, vol. 108, no. 15, pp. 6394–6403, 1998.

[296] B. Thole, G. Van der Laan, and G. Sawatzky, "Strong magnetic dichroism predicted in the M 4,5 X-ray absorption spectra of magnetic rare-earth materials," *Phys. Rev. Lett.*, vol. 55, no. 19, p. 2086, 1985.

[297] G. Schütz, W. Wagner, W. Wilhelm, P. Kienle, R. Zeller, R. Frahm, and G. Materlik, "Absorption of circularly polarized x rays in iron," *Phys. Rev. Lett.*, vol. 58, no. 7, p. 737, 1987.

[298] G. van der Laan, B. T. Thole, G. A. Sawatzky, J. B. Goedkoop, J. C. Fuggle, J.-M. Esteva, R. Karnatak, J. Remeika, and H. A. Dabkowska, "Experimental proof of magnetic x-ray dichroism," *Phys. Rev. B*, vol. 34, no. 9, p. 6529, 1986.

[299] Y. Yamasaki, Y. Ishii, and N. Sasabe, "Sum rules for x-ray circular and linear dichroism based on complete magnetic multipole basis," *Sci. Technol. Adv. Mater.*, no. just-accepted, p. 2513217, 2025.

[300] I. P. Krug, *Magnetic Proximity Effects in Highly-ordered Transition Metal Oxide Heterosystems - A Study by Soft-x-ray Photoemission Microscopy*, vol. 2. Forschungszentrum Jülich GmbH Zentralbibliothek Verlag, 2008.

[301] Y. Wu, Y. Zhao, E. Arenholz, A. Young, B. Sinkovic, C. Won, and Z. Qiu, "Analysis of x-ray linear dichroism spectra for NiO thin films grown on vicinal Ag (001)," *Phys. Rev. B*, vol. 78, no. 6, p. 064413, 2008.

[302] C. Schmitt, L. Baldrati, L. Sanchez-Tejerina, F. Schreiber, A. Ross, M. Filianina, S. Ding, F. Fuhrmann, R. Ramos, F. Maccherozzi, *et al.*, "Identification of Néel Vector Orientation in Antiferromagnetic Domains Switched by Currents in NiO/Pt Thin Films," *Phys. Rev. Appl.*, vol. 15, no. 3, p. 034047, 2021.

[303] E. Arenholz, G. van der Laan, R. V. Chopdekar, and Y. Suzuki, "Angle-dependent Ni^{2+} x-ray magnetic linear dichroism: interfacial coupling revisited," *Phys. Rev. Lett.*, vol. 98, no. 19, p. 197201, 2007.

[304] Y. Wu, B. Sinkovic, C. Won, J. Zhu, Y. Zhao, and Z. Qiu, "Experimental study of the x-ray linear dichroism of NiO films grown on Fe (001)," *Phys. Rev. B*, vol. 85, no. 13, p. 134436, 2012.

[305] P. Kuiper, B. G. Searle, P. Rudolf, L. Tjeng, and C. Chen, "X-ray magnetic dichroism of antiferromagnet Fe_2O_3: the orientation of magnetic moments observed by Fe 2p x-ray absorption spectroscopy," *Phys. Rev. Lett.*, vol. 70, no. 10, p. 1549, 1993.

[306] A. Yaresko, A. Perlov, V. Antonov, and B. Harmon, "Band-structure theory of dichroism," in *Magnetism: A Synchrotron Radiation Approach*, pp. 121–141, Springer, 2006.

[307] O. Amin, A. Dal Din, E. Golias, Y. Niu, A. Zakharov, S. Fromage, C. Fields, S. Heywood, R. Cousins, F. Maccherozzi, *et al.*, "Nanoscale imaging and control of altermagnetism in MnTe," *Nature*, vol. 636, no. 8042, pp. 348–353, 2024.

[308] H. Ohldag, G. Van Der Laan, and E. Arenholz, "Correlation of crystallographic and magnetic domains at Co/NiO (001) interfaces," *Phys. Rev. B*, vol. 79, no. 5, p. 052403, 2009.

[309] S. Czekaj, F. Nolting, L. Heyderman, P. Willmott, and G. Van Der Laan, "Sign dependence of the x-ray magnetic linear dichroism on the antiferromagnetic spin axis in $LaFeO_3$ thin films," *Phys. Rev. B*, vol. 73, no. 2, p. 020401, 2006.

[310] F. P. Chmiel, N. Waterfield Price, R. D. Johnson, A. D. Lamirand, J. Schad, G. van der Laan, D. T. Harris, J. Irwin, M. S. Rzchowski, C.-B. Eom, *et al.*, "Observation of magnetic vortex pairs at room temperature in a planar $\alpha - Fe_2O_3$/Co heterostructure," *Nat. Mater.*, vol. 17, no. 7, pp. 581–585, 2018.

[311] H. Bulou, L. Joly, J.-M. Mariot, and F. Scheurer, "X-ray sources at large-scale facilities," in *Magnetism and Accelerator-Based Light Sources*, pp. 1–38, Springer Nature, 2021.

[312] E. Longhi, P. Bencok, A. Dobrynin, E. Rial, A. Rose, P. Steadman, C. Thompson, A. Thomson, and H. Wang, "Developments in polarization and energy control of APPLE-II Undulators at Diamond Light Source," in *J. Phys. Conf. Ser.*, vol. 425, p. 032011, IOP Publishing, 2013.

[313] M. Hand, H. Wang, F. Maccherozzi, M. Apollonio, J. Zhu, S. S. Dhesi, and K. Sawhney, "Quantitative investigation of linear arbitrary polarization in an APPLE-II undulator," *J. Synchrotron Radiat.*, vol. 25, no. 2, pp. 378–384, 2018.

[314] S. Anders, H. A. Padmore, R. M. Duarte, T. Renner, T. Stammler, A. Scholl, M. R. Scheinfein, J. Stöhr, L. Séve, and B. Sinkovic, "Photoemission electron microscope for the study of magnetic materials," *Rev. Sci. Instrum.*, vol. 70, no. 10, pp. 3973–3981, 1999.

[315] S. Y. Bodnar, M. Filianina, S. Bommanaboyena, T. Forrest, F. Maccherozzi, A. Sapozhnik, Y. Skourski, M. Kläui, and M. Jourdan, "Imaging of current induced Néel vector switching in antiferromagnetic Mn_2Au," *Phys. Rev. B*, vol. 99, no. 14, p. 140409, 2019.

[316] B. Gilbert, R. Andres, P. Perfetti, G. Margaritondo, G. Rempfer, and G. De Stasio, "Charging phenomena in PEEM imaging and spectroscopy," *Ultramicroscopy*, vol. 83, no. 1-2, pp. 129–139, 2000.

[317] S. Nepijko, N. Sedov, and G. Schönhense, "Measurement of magnetic fields and domain structures using a photoemission electron microscope," in *Advances in Imaging and Electron Physics*, vol. 113, pp. 205–248, Elsevier, 2000.

[318] L. Aballe, M. Foerster, E. Pellegrin, J. Nicolas, and S. Ferrer, "The ALBA spectroscopic LEEM-PEEM experimental station: layout and performance," *J. Synchrotron Radiat.*, vol. 22, no. 3, pp. 745–752, 2015.

[319] F. Kronast, J. Schlichting, F. Radu, S. Mishra, T. Noll, and H. Dürr, "Spin-resolved photoemission microscopy and magnetic imaging in applied magnetic fields," *Surface and Interface Analysis*, vol. 42, no. 10-11, pp. 1532–1536, 2010.

[320] Helmholtz-Zentrum Berlin, "SPEEM – Photoemission Electron Microscope at UE49-PGM (HZB)." https://www.helmholtz-berlin.de/pubbin/igama_output?gid=1688&modus=einzel&sprache=en&gid=1688. Last accessed: 8 July 2025.

[321] Y. Niu, N. Vinogradov, A. Preobrajenski, C. Struzzi, B. Sarpi, L. Zhu, E. Golias, and A. Zakharov, "MAXPEEM: a spectromicroscopy beamline at MAX IV laboratory," *J. Synchrotron Radiat.*, vol. 30, no. 2, pp. 468–478, 2023.

[322] A. Goswami, "Thin Film," in *Thin Film Fundamentals*, pp. 1–48, New age international publishers, 1996.

[323] M. Ohring, "Why are thin films different from the bulk?," in *Laser-Induced Damage in Optical Materials: 1993*, vol. 2114, pp. 624–639, SPIE, 1994.

[324] W. Gil, D. Görlitz, M. Horisberger, and J. Kötzler, "Magnetoresistance anisotropy of polycrystalline cobalt films: Geometrical-size and domain effects," *Phys. Rev. B*, vol. 72, no. 13, p. 134401, 2005.

[325] M. Yamanouchi, A. Jander, P. Dhagat, S. Ikeda, F. Matsukura, and H. Ohno, "Domain structure in CoFeB thin films with perpendicular magnetic anisotropy," *IEEE Magn. Lett.*, vol. 2, pp. 3000304–3000304, 2011.

[326] F. Eskandari, S. Porter, M. Venkatesan, P. Kameli, K. Rode, and J. Coey, "Magnetization and anisotropy of cobalt ferrite thin films," *Phys. Rev. Mat.*, vol. 1, no. 7, p. 074413, 2017.

[327] R. Denecke, M. Welke, P. Huth, J. Gräfe, K. Brachwitz, M. Lorenz, M. Grundmann, M. Ziese, P. D. Esquinazi, E. Goering, *et al.*, "Magnetic anisotropy in thin layers of (Mn, Zn)Fe_2O_4 on $SrTiO_3$ (001)," *Phys. Stauts Solidi B*, vol. 257, no. 7, p. 1900627, 2020.

[328] G. Garreau, S. Hajjar, J. Bubendorff, C. Pirri, D. Berling, A. Mehdaoui, R. Stephan, P. Wetzel, S. Zabrocki, G. Gewinner, *et al.*, "Growth and magnetic anisotropy of Fe films deposited on Si (111) using an ultrathin iron silicide template," *Phys. Rev. B*, vol. 71, no. 9, p. 094430, 2005.

[329] I. Marozau, P. T. Das, M. Döbeli, J. G. Storey, M. A. Uribe-Laverde, S. Das, C. Wang, M. Rössle, and C. Bernhard, "Influence of La and Mn vacancies on the electronic and magnetic properties of $LaMnO_3$ thin films grown by pulsed laser deposition," *Phys. Rev. B*, vol. 89, no. 17, p. 174422, 2014.

[330] J. Vila-Fungueiriño, C. T. Bui, B. Rivas-Murias, E. Winkler, J. Milano, J. Santiso, and F. Rivadulla, "Thermodynamic conditions during growth determine the magnetic anisotropy in epitaxial thin-films of $La_{0.7}Sr_{0.3}MnO_3$," *J. Phys. D: Appl. Phys.*, vol. 49, no. 31, p. 315001, 2016.

[331] A. Beiranvand, E. Rivasto, H. Huhtinen, and P. Paturi, "Strain-Induced Domain Structure and Its Impact on Magnetic and Transport Properties of $Gd_{0.6}Ca_{0.4}MnO_3$ Thin Films," *ACS Omega*, vol. 6, no. 50, pp. 34572–34579, 2021.

[332] X. Portier, E. Millon, V. Demange, S. Ollivier, M. Guilloux-Viry, M. Nistor, C. Hebert, C. Cachoncinlle, and J. Perrière, "Growth and magnetic properties of iron-based oxide thin films deposited by pulsed laser deposition at room temperature," *Appl. Phys. A*, vol. 130, no. 7, p. 502, 2024.

[333] T. Phillips and R. White, "Single-ion magnetostriction in the iron group monoxides from the strain dependence of electron-paramagnetic-resonance spectra," *Phys. Rev.*, vol. 153, no. 2, p. 616, 1967.

[334] T. Hibma and M. W. Haverkort, "Antiferromagnetic Oxide Films on Nonmagnetic Substrates," in *Magnetic Properties of Antiferromagnetic Oxide Materials: Surfaces, Interfaces, and Thin Films*, pp. 99–142, Wiley Online Library, 2010.

[335] L. Lünenbürger, "Correlation of structure and magnetic properties in antiferromagnetic CoO thin films," Bachelor thesis, Johannes Gutenberg University Mainz, 2024.

[336] L. Micus, "Tuning Structural and Magnetic Properties of Cobalt Oxide Thin Films by Varying Oxygen Flow During Sputtering," Bachelor thesis, Johannes Gutenberg University Mainz, 2025.

[337] C. D. Stanciu, F. Hansteen, A. V. Kimel, A. Kirilyuk, A. Tsukamoto, A. Itoh, and T. Rasing, "All-optical magnetic recording with circularly polarized light," *Phys. Rev. Lett.*, vol. 99, no. 4, p. 047601, 2007.

[338] S. Alebrand, A. Hassdenteufel, D. Steil, M. Cinchetti, and M. Aeschlimann, "Interplay of heating and helicity in all-optical magnetization switching," *Phys. Rev. B*, vol. 85, no. 9, p. 092401, 2012.

[339] S. Mangin, M. Gottwald, C. Lambert, D. Steil, V. Uhlíř, L. Pang, M. Hehn, S. Alebrand, M. Cinchetti, G. Malinowski, *et al.*, "Engineered materials for all-optical helicity-dependent magnetic switching," *Nat. Mater.*, vol. 13, no. 3, pp. 286–292, 2014.

[340] M. S. El Hadri, M. Hehn, G. Malinowski, and S. Mangin, "Materials and devices for all-optical helicity-dependent switching," *J. Phys. D: Appl. Phys.*, vol. 50, no. 13, p. 133002, 2017.

[341] A. V. Kimel and M. Li, "Writing magnetic memory with ultrashort light pulses," *Nat. Rev. Mater.*, vol. 4, no. 3, pp. 189–200, 2019.

[342] C. Tzschaschel, K. Otani, R. Iida, T. Shimura, H. Ueda, S. Günther, M. Fiebig, and T. Satoh, "Ultrafast optical excitation of coherent magnons in antiferromagnetic NiO," *Phys. Rev. B*, vol. 95, no. 17, p. 174407, 2017.

[343] N. Kanda, T. Higuchi, H. Shimizu, K. Konishi, K. Yoshioka, and M. Kuwata-Gonokami, "The vectorial control of magnetization by light," *Nat. Commun.*, vol. 2, no. 1, p. 362, 2011.

[344] P. Němec, M. Fiebig, T. Kampfrath, and A. V. Kimel, "Antiferromagnetic opto-spintronics," *Nat. Phys.*, vol. 14, no. 3, pp. 229–241, 2018.

[345] A. Kimel, A. Kirilyuk, A. Tsvetkov, R. Pisarev, and T. Rasing, "Laser-induced ultrafast spin reorientation in the antiferromagnet $TmFeO_3$," *Nature*, vol. 429, no. 6994, pp. 850–853, 2004.

[346] S. Wust, C. Seibel, H. Meer, P. Herrgen, C. Schmitt, L. Baldrati, R. Ramos, T. Kikkawa, E. Saitoh, O. Gomonay, *et al.*, "Indirect optical manipulation of the antiferromagnetic order of insulating NiO by ultrafast interfacial energy transfer," *arXiv preprint arXiv:2205.02686*, 2022.

[347] E. Rongione, O. Gueckstock, M. Mattern, O. Gomonay, H. Meer, C. Schmitt, R. Ramos, T. Kikkawa, M. Mičica, E. Saitoh, J. Sinova, *et al.*, "Emission of coherent THz magnons in an antiferromagnetic insulator triggered by ultrafast spin-phonon interactions," *Nat. Commun.*, vol. 14, no. 1, p. 1818, 2023.

[348] P. Stremoukhov, A. Safin, S. Nikitov, A. Kirilyuk, *et al.*, "Phononic manipulation of antiferromagnetic domains in NiO," *New J. Phys.*, vol. 24, no. 2, p. 023009, 2022.

[349] H. Meer, S. Wust, C. Schmitt, P. Herrgen, F. Fuhrmann, S. Hirtle, B. Bednarz, A. Rajan, R. Ramos, M. A. Niño, *et al.*, "Laser-induced creation of antiferromagnetic 180-degree domains in NiO/Pt bilayers," *Adv. Funct. Mater.*, vol. 33, no. 21, p. 2213536, 2023.

[350] J. L. Ross, P.-I. Gavriloaea, F. Freimuth, T. Adamantopoulos, Y. Mokrousov, R. F. Evans, R. Chantrell, R. M. Otxoa, and O. Chubykalo-Fesenko, "Ultrafast antiferromagnetic switching of Mn_2Au with laser-induced optical torques," *npj Comput. Mater.*, vol. 10, no. 1, p. 234, 2024.

[351] P. Sarte, S. Wilson, J. Attfield, and C. Stock, "Magnetic fluctuations and the spin–orbit interaction in Mott insulating CoO," *J. Phys. Condens. Matter*, vol. 32, no. 37, p. 374011, 2020.

[352] G. Cardone, J. Schindelin, J. Eglinger, and M. Hiner, "Directionality." https://imagej.net/plugins/directionality, 2018. Last accessed: 23 June 2025.

[353] S. Reimers, O. Gomonay, O. J. Amin, F. Krizek, L. X. Barton, Y. Lytvynenko, S. F. Poole, V. Novák, R. P. Campion, F. Maccherozzi, *et al.*, "Magnetic domain

engineering in antiferromagnetic CuMnAs and Mn_2Au," *Phys. Rev. Appl.*, vol. 21, no. 6, p. 064030, 2024.

[354] T. Kawahara, K. Ito, R. Takemura, and H. Ohno, "Spin-transfer torque RAM technology: Review and prospect," *Microelectron. Reliab.*, vol. 52, no. 4, pp. 613–627, 2012.

[355] B. Dieny, I. L. Prejbeanu, K. Garello, P. Gambardella, P. Freitas, R. Lehndorff, W. Raberg, U. Ebels, S. O. Demokritov, J. Akerman, *et al.*, "Opportunities and challenges for spintronics in the microelectronics industry," *Nat. Electron.*, vol. 3, no. 8, pp. 446–459, 2020.

[356] Y. Huai *et al.*, "Spin-transfer torque MRAM (STT-MRAM): Challenges and prospects," *AAPPS Bull.*, vol. 18, no. 6, pp. 33–40, 2008.

[357] Y. Cheng, S. Yu, M. Zhu, J. Hwang, and F. Yang, "Electrical Switching of Tristate Antiferromagnetic Néel Order in $\alpha - Fe_2O_3$ Epitaxial Films," *Phys. Rev. Lett.*, vol. 124, no. 2, p. 027202, 2020.

[358] P. Zhang, C.-T. Chou, H. Yun, B. C. McGoldrick, J. T. Hou, K. A. Mkhoyan, and L. Liu, "Control of Néel Vector with Spin-Orbit Torques in an Antiferromagnetic Insulator with Tilted Easy Plane," *Phys. Rev. Lett.*, vol. 129, no. 1, p. 017203, 2022.

[359] C. F. Schippers, M. J. Grzybowski, K. Rubi, M. E. Bal, T. J. Kools, R. A. Duine, U. Zeitler, and H. J. Swagten, "Disentangling electrical switching of antiferromagnetic NiO using high magnetic fields," *Phys. Rev. B*, vol. 106, no. 17, p. 174434, 2022.

[360] M. Yang, Q. Li, T. Wang, B. Hong, C. Klewe, Z. Li, X. Huang, P. Shafer, F. Zhang, C. Hwang, *et al.*, "Current switching of the antiferromagnetic Néel vector in Pd/CoO/MgO (001)," *Phys. Rev. B*, vol. 106, no. 21, p. 214405, 2022.

[361] T. Wu, H. Chen, T. Ma, J. Xu, and Y. Wu, "Current-density-modulated antiferromagnetic domain switching revealed by optical imaging in the Pt/CoO (001) bilayer," *Phys. Rev. Appl.*, vol. 21, no. 4, p. 044054, 2024.

[362] F. Schreiber, H. Meer, C. Schmitt, R. Ramos, E. Saitoh, L. Baldrati, and M. Kläui, "Magnetic sensitivity distribution of Hall devices in antiferromagnetic switching experiments," *Phys. Rev. Appl.*, vol. 16, no. 6, p. 064023, 2021.

[363] "COMSOL Multiphysics® v. 5.4." https://www.comsol.com, COMSOL AB. "Heating-Circuit".

[364] M. N. Baibich, J. M. Broto, A. Fert, F. N. Van Dau, F. Petroff, P. Etienne, G. Creuzet, A. Friederich, and J. Chazelas, "Giant Magnetoresistance of (001)Fe/(001)Cr Magnetic Superlattices," *Phys. Rev. Lett.*, vol. 61, no. 21, pp. 2472–2475, 1988.

[365] G. Binasch, P. Grünberg, F. Saurenbach, and W. Zinn, "Enhanced magnetoresistance in layered magnetic structures with antiferromagnetic interlayer exchange," *Phys. Rev. B*, vol. 39, no. 7, pp. 4828–4830, 1989.

[366] I. M. Miron, K. Garello, G. Gaudin, P.-J. Zermatten, M. V. Costache, S. Auffret, S. Bandiera, B. Rodmacq, A. Schuhl, and P. Gambardella, "Perpendicular switching of a single ferromagnetic layer induced by in-plane current injection," *Nature*, vol. 476, no. 7359, pp. 189–193, 2011.

[367] S. Bhatti, R. Sbiaa, A. Hirohata, H. Ohno, S. Fukami, and S. Piramanayagam, "Spintronics based random access memory: a review," *Mater. Today*, vol. 20, no. 9, pp. 530–548, 2017.

[368] A. Fert, V. Cros, and J. Sampaio, "Skyrmions on the track," *Nat. Nanotechnol.*, vol. 8, no. 3, pp. 152–156, 2013.

[369] K. Everschor-Sitte, J. Masell, R. M. Reeve, and M. Kläui, "Perspective: Magnetic skyrmions—Overview of recent progress in an active research field," *J. Appl. Phys.*, vol. 124, no. 24, p. 240901, 2018.

[370] X. Zhang, M. Ezawa, and Y. Zhou, "Magnetic skyrmion logic gates: conversion, duplication and merging of skyrmions," *Sci. Rep.*, vol. 5, no. 1, p. 9400, 2015.

[371] J. Grollier, D. Querlioz, K. Y. Camsari, K. Everschor-Sitte, S. Fukami, and M. D. Stiles, "Neuromorphic spintronics," *Nat. Electron.*, vol. 3, no. 7, pp. 360–370, 2020.

[372] T. da Câmara Santa Clara Gomes, Y. Sassi, D. Sanz-Hernández, S. Krishnia, S. Collin, M.-B. Martin, P. Seneor, V. Cros, J. Grollier, and N. Reyren, "Neuromorphic weighted sums with magnetic skyrmions," *Nat. Electron.*, vol. 8, no. 3, pp. 204–214, 2025.

[373] G. Beneke, T. B. Winkler, K. Raab, M. A. Brems, F. Kammerbauer, P. Gerhards, K. Knobloch, S. Krishnia, J. H. Mentink, and M. Kläui, "Gesture recognition with Brownian reservoir computing using geometrically confined skyrmion dynamics," *Nat. Commun.*, vol. 15, no. 1, p. 8103, 2024.

[374] K.-J. Lee, V. Cros, and H.-W. Lee, "Electric-field-induced orbital angular momentum in metals," *Nat. Mater.*, vol. 23, no. 10, pp. 1302–1304, 2024.

[375] A. Johansson, B. Göbel, J. Henk, M. Bibes, and I. Mertig, "Spin and orbital Edelstein effects in a two-dimensional electron gas: Theory and application to $SrTiO_3$ interfaces," *Phys. Rev. Res.*, vol. 3, no. 1, p. 013275, 2021.

[376] I. Lyalin, S. Alikhah, M. Berritta, P. M. Oppeneer, and R. K. Kawakami, "Magneto-optical detection of the orbital Hall effect in chromium," *Phys. Rev. Lett.*, vol. 131, no. 15, p. 156702, 2023.

[377] J. C. Idrobo, J. Rusz, G. Datt, D. Jo, S. Alikhah, D. Muradas, U. Noumbe, M. V. Kamalakar, and P. M. Oppeneer, "Direct observation of nanometer-scale orbital angular momentum accumulation," *arXiv preprint, arXiv:2403.09269*, 2024.

[378] C. Schmitt, S. Krishnia, M. Zeer, E. Galíndez-Ruales, M. Loyal, J. Köhler, L. Micus, T. Kikkawa, H. Arisawa, T. Denneulin, *et al.*, "Giant orbital magnetoresistance in the antiferromagnet CoO driven by dynamic orbital angular momentum interaction," 2025. Under review.

[379] C. Schmitt, E. Galíndez-Ruales, H. Meer, S. Krishnia, T. Kikkawa, E. Saitoh, T. Kuschel, and M. Kläui 2026. Under preparation.

[380] S. Fukami, K.-J. Lee, and M. Kläui, "Challenges and opportunities in orbitronics," *arXiv preprint arXiv:2509.23954*, 2025.

[381] S. Krishnia, B. Bony, E. Rongione, L. M. Vicente-Arche, T. Denneulin, A. Pezo, Y. Lu, R. E. Dunin-Borkowski, S. Collin, A. Fert, J.-M. George,

N. Reyren, V. Cros, and H. Jaffrès, "Quantifying the large contribution from orbital Rashba–Edelstein effect to the effective damping-like torque on magnetization," *APL Mater.*, vol. 12, no. 5, p. 051105, 2024.

[382] G. Sala and P. Gambardella, "Giant orbital Hall effect and orbital-to-spin conversion in $3d$, $5d$, and $4f$ metallic heterostructures," *Phys. Rev. Res.*, vol. 4, no. 3, p. 033037, 2022.

[383] R. Gupta, C. Bouard, F. Kammerbauer, J. O. Ledesma-Martin, A. Bose, I. Kononenko, S. Martin, P. Usé, G. Jakob, M. Drouard, *et al.*, "Harnessing orbital Hall effect in spin-orbit torque MRAM," *Nat. Commun.*, vol. 16, no. 1, p. 130, 2025.

[384] R. Lebrun, A. Ross, S. Bender, A. Qaiumzadeh, L. Baldrati, J. Cramer, A. Brataas, R. Duine, and M. Kläui, "Tunable long-distance spin transport in a crystalline antiferromagnetic iron oxide," *Nature*, vol. 561, no. 7722, pp. 222–225, 2018.

[385] S. Das, A. Ross, X. Ma, S. Becker, C. Schmitt, F. van Duijn, E. Galindez-Ruales, F. Fuhrmann, M.-A. Syskaki, U. Ebels, V. Baltz, A.-L. Barra, H. Chen, G. Jakob, S. Cao, J. Sinova, O. Gomonay, R. Lebrun, and M. Kläui, "Anisotropic long-range spin transport in canted antiferromagnetic orthoferrite $YFeO_3$," *Nat. Commun.*, vol. 13, no. 1, p. 6140, 2022.

[386] C. T. Chen, Y. U. Idzerda, H.-J. Lin, N. V. Smith, G. Meigs, E. Chaban, G. H. Ho, E. Pellegrin, and F. Sette, "Experimental Confirmation of the X-Ray Magnetic Circular Dichroism Sum Rules for Iron and Cobalt," *Phys. Rev. Lett.*, vol. 75, no. 1, pp. 152–155, 1995.

[387] S. Krishnia, L. Vojáček, T. d. C. S. C. Gomes, N. Sebe, F. Ibrahim, J. Li, L. M. Vicente-Arche, S. Collin, T. Denneulin, R. E. Dunin-Borkowski, S. A. Nikolaev, P. Ohresser, N. Jaouen, A. Thiaville, A. Fert, H. Jaffrès, M. Chshiev, N. Reyren, and V. Cros, "Interfacial spin-orbitronic effects controlled by different oxidation levels at the Co/Al interface," *Phys. Rev. Appl.*, vol. 24, no. 2, p. 024055, 2025.

[388] W. Wang, T. Wang, V. P. Amin, Y. Wang, A. Radhakrishnan, A. Davidson, S. R. Allen, T. J. Silva, H. Ohldag, D. Balzar, B. L. Zink, P. M. Haney, J. Q.

Xiao, D. G. Cahill, V. O. Lorenz, and X. Fan, "Anomalous spin-orbit torques in magnetic single-layer films," *Nat. Nanotechnol.*, vol. 14, no. 9, pp. 819–824, 2019.

[389] S. Krishnia, E. Haltz, L. Berges, L. Aballe, M. Foerster, L. Bocher, R. Weil, A. Thiaville, J. a. Sampaio, and A. Mougin, "Spin-Orbit Coupling in Single-Layer Ferrimagnets: Direct Observation of Spin-Orbit Torques and Chiral Spin Textures," *Phys. Rev. Appl.*, vol. 16, no. 2, p. 024040, 2021.

[390] R. Abrudan, J. Miguel, M. Bernien, C. Tieg, M. Piantek, J. Kirschner, and W. Kuch, "Structural and magnetic properties of epitaxial Fe/ CoO bilayers on Ag (001)," *Phys. Rev. B*, vol. 77, no. 1, p. 014411, 2008.

[391] F. De Groot and A. Kotani, *Core level spectroscopy of solids*. CRC press, 2008.

[392] G. van der Laan, "Magnetic linear X-ray dichroism as a probe of the magnetocrystalline anisotropy," *Phys. Rev. Lett.*, vol. 82, no. 3, p. 640, 1999.

[393] J. Kim, P. Sheng, S. Takahashi, S. Mitani, and M. Hayashi, "Spin Hall Magnetoresistance in Metallic Bilayers," *Phys. Rev. Lett.*, vol. 116, no. 9, p. 097201, 2016.

[394] S. R. Marmion, M. Ali, M. McLaren, D. A. Williams, and B. J. Hickey, "Temperature dependence of spin Hall magnetoresistance in thin YIG/Pt films," *Phys. Rev. B*, vol. 89, no. 22, p. 220404, 2014.

[395] A. Shitade, H. Watanabe, and Y. Yanase, "Theory of orbital magnetic quadrupole moment and magnetoelectric susceptibility," *Phys. Rev. B*, vol. 98, no. 2, p. 020407, 2018.

[396] J.-Y. Yoon, P. Zhang, C.-T. Chou, Y. Takeuchi, T. Uchimura, J. T. Hou, J. Han, S. Kanai, H. Ohno, S. Fukami, and L. Liu, "Handedness anomaly in a non-collinear antiferromagnet under spin–orbit torque," *Nat. Mater.*, vol. 22, no. 9, pp. 1106–1113, 2023.

[397] L. Pauw, "A method of measuring specific resistivity and Hall effect of discs of arbitrary shape," *Philips Res. Rep.*, vol. 13, no. 1, pp. 1–9, 1958.

[398] I. V. Solovyev, A. I. Liechtenstein, and K. Terakura, "Is Hund's Second Rule Responsible for the Orbital Magnetism in Solids?," *Phys. Rev. Lett.*, vol. 80, no. 26, pp. 5758–5761, 1998.

[399] S. Han, D. Jo, I. Baek, S. Cheon, P. M. Oppeneer, and H.-W. Lee, "Harnessing magnetic octupole Hall effect to induce torque in altermagnets," *Phys. Rev. Lett.*, vol. 135, no. 7, p. 076705, 2025.

[400] R. Sun, Y. Nabei, A. McConnell, X. Zhang, A. Comstock, H. Jones, R. Gyawali, Y. Xiong, Z. Wang, J. Liu, *et al.*, "Determination of orbital relaxation in Ti/Ni heterostructure via orbital pumping," *J. Appl. Phys.*, vol. 138, no. 12, p. 123905, 2025.

[401] G. Rollmann, A. Rohrbach, P. Entel, and J. Hafner, "First-principles calculation of the structure and magnetic phases of hematite," *Phys. Rev. B*, vol. 69, no. 16, p. 165107, 2004.

[402] A. Ross, R. Lebrun, C. Ulloa, D. A. Grave, A. Kay, L. Baldrati, F. Kronast, S. Valencia, A. Rothschild, and M. Kläui, "Structural sensitivity of the spin Hall magnetoresistance in antiferromagnetic thin films," *Phys. Rev. B*, vol. 102, no. 9, p. 094415, 2020.

[403] S. Pütter, S. Geprägs, R. Schlitz, M. Althammer, A. Erb, R. Gross, and S. T. Goennenwein, "Impact of the interface quality of Pt/YIG (111) hybrids on their spin Hall magnetoresistance," *Appl. Phys. Lett.*, vol. 110, no. 1, 2017.

[404] M. Althammer, A. V. Singh, T. Wimmer, Z. Galazka, H. Huebl, M. Opel, R. Gross, and A. Gupta, "Role of interface quality for the spin Hall magnetoresistance in nickel ferrite thin films with bulk-like magnetic properties," *Appl. Phys. Lett.*, vol. 115, no. 9, 2019.

[405] J. Fontcuberta, H. B. Vasili, J. Gàzquez, and F. Casanova, "On the role of interfaces on spin transport in magnetic insulator/normal metal heterostructures," *Adv. Mater. Interfaces*, vol. 6, no. 15, p. 1900475, 2019.

[406] S. Catalano, J. M. Gomez-Perez, M. X. Aguilar-Pujol, A. Chuvilin, M. Gobbi, L. E. Hueso, and F. Casanova, "Spin Hall magnetoresistance effect from a

disordered interface," *ACS Appl. Mater. Interfaces*, vol. 14, no. 6, pp. 8598–8604, 2022.

[407] K. Fuchs, "The conductivity of thin metallic films according to the electron theory of metals," in *Mathematical Proceedings of the Cambridge Philosophical Society*, vol. 34, pp. 100–108, Cambridge University Press, 1938.

[408] E. H. Sondheimer, "The mean free path of electrons in metals," *Adv. Phys.*, vol. 50, no. 6, pp. 499–537, 2001.

[409] D. Lide, "CRC Handbook of Chemistry and Physics 85th Ed CRC Press," *Boca Raton*, pp. 8–141, 2004.

[410] D. Gall, "Electron mean free path in elemental metals," *J. Appl. Phys.*, vol. 119, no. 8, 2016.

[411] S. Dushenko, M. Hokazono, K. Nakamura, Y. Ando, T. Shinjo, and M. Shiraishi, "Tunable inverse spin Hall effect in nanometer-thick platinum films by ionic gating," *Nat. Commun.*, vol. 9, no. 1, p. 3118, 2018.

[412] A. Hirohata, K. Yamada, Y. Nakatani, I.-L. Prejbeanu, B. Diény, P. Pirro, and B. Hillebrands, "Review on spintronics: Principles and device applications," *Journal of Magnetism and Magnetic Materials*, vol. 509, p. 166711, 2020.

[413] D. Huang, C. Chang, H.-T. Jeng, G. Guo, H.-J. Lin, W. Wu, H. Ku, A. Fujimori, . f. Y. Takahashi, and C. Chen, "Spin and orbital magnetic moments of Fe_3O_4," *Phys. Rev. Lett.*, vol. 93, no. 7, p. 077204, 2004.

[414] I. Galanakis, M. Alouani, and H. Dreysse, "Spin-axis-dependent magnetic properties of FePt and CoPt," *Phys. B: Condens. Matter*, vol. 320, no. 1-4, pp. 221–225, 2002.

[415] N. Ito and K. Nomura, "Anomalous Hall effect and spontaneous orbital magnetization in antiferromagnetic Weyl metal," *J Phys. Soc. Jpn.*, vol. 86, no. 6, p. 063703, 2017.

[416] S. Sakamoto, T. Higo, M. Shiga, K. Amemiya, S. Nakatsuji, and S. Miwa, "Observation of spontaneous x-ray magnetic circular dichroism in a chiral antiferromagnet," *Phys. Rev. B*, vol. 104, no. 13, p. 134431, 2021.

[417] M. dos Santos Dias, J. Bouaziz, M. Bouhassoune, S. Blügel, and S. Lounis, "Chirality-driven orbital magnetic moments as a new probe for topological magnetic structures," *Nat. Commun.*, vol. 7, no. 1, p. 13613, 2016.

A Sample preparation

A.1 Sample Growth

The epitaxial MgO(001)//CoO thin films used for the work in this thesis have been grown using reactive magnetron sputtering in the ULVAC QAM4 chamber in the Saitoh Laboratory in Tokyo, Japan, via an automatic sputtering process. The recipe used mainly follows the recipe established by -, similar to previous studies [50], and only individual parameters were adjusted in order to ensure high quality sample growth. The author was supported by - in the sample growth. Here, we briefly discuss the growth procedure of the AFM CoO films and outline the basic steps.

To achieve high-quality films, new MgO(001) substrates from MaTeck are used. To avoid oxidation, the samples are stored in a argon glove box prior to deposition and air exposure is minimized. For the sputtering process the substrate surface is cleaned by blowing it with nitrogen gas and then the substrate is placed face-down on the Cu-sample holder. Once the pressure in the load lock falls below $5 \cdot 10^{-4}$ Pa the sample is transferred to chamber 2, in which magnetic materials such as Co, Ni and Fe are sputtered. This chamber is connected to chamber 1 (for non-magnetic) materials and chamber 4 via a central transfer chamber.

CoO is deposited by reactive magnetron sputtering with O_2 at elevated temperatures. The base pressure in the chamber was $p_2 < 1.2 \cdot 10^{-5}$ Pa.

I. The MgO substrates were pre-annealed at a temperature of $T_{\mathrm{MgO}} = 770\,^{\circ}\mathrm{C}$ for 50 minutes. The temperature of the chamber was for this raised to $T_{\mathrm{Ch}_2} = 970\,^{\circ}\mathrm{C}$.

II. The deposition temperature of the CoO is $T_{\mathrm{MgO}} = 430\,^{\circ}\mathrm{C}$. Therefore, the temperature of the chamber was lowered to $T_{\mathrm{Ch_2}} = 573\,^{\circ}\mathrm{C}$.

III. A sample holder rotation of 10 rpm is initialized, if the linear shutter is not to be used for the deposition process. Several steps are now conducted in order to start the sputtering process.

   (a) Pre-sputtering: With a closed shutter, a 10 s long pre-sputtering step is performed in order to clean the target surface from potential oxidation. $V_{\mathrm{DC}} = 20\,\mathrm{W}$, Ar flow: 15 sccm

   (b) Initiating the Co sputtering: For 300 s, Co is sputtered to ensure the sputtering process starts without problems. The shutter is still closed and in case problems should occur, the process can be restarted. $V_{\mathrm{RF}} = 150\,\mathrm{W}$, Ar flow: 15 sccm

   (c) Deposition: If everything went well, now the actual deposition process is started. The shutter is opened and oxygen is introduced into the chamber. The default oxygen flow is 2.0 sccm, however this was varied for some samples to investigate the effect of the oxygen flow rate on the crystallographic and magnetic order of the CoO films. $V_{\mathrm{RF}} = 150\,\mathrm{W}$, Ar flow: 15 sccm

IV. After the deposition, the heater shuts down. Once the temperature in the chamber is below $T_{\mathrm{Ch_2}} < 500\,^{\circ}\mathrm{C}$, the holder is automatically transferred to chamber 4 for faster cool down.

V. The HM was deposited at room temperature in the chamber for non-magnetic materials. For that, the sample was transferred into chamber 1, once the substrate was cooled down. A DC voltage of $V_{\mathrm{DC}} = 20\,\mathrm{V}$ was applied for the growth of Pt as well as for Cu, Cr and Ti.

An overview on the samples grown during this thesis is shown in 🕮 labbook experiment ID 6817.

A.2 Lithography Recipes

In this section of the appendix, details of the patterning process used for the preparation of the samples used in this thesis will be provided.

A.2.1 Sample Cleaning

I. Immerse sample in acetone for 180 s in an ultrasonic bath

II. Immerse sample in isopropyl alcohol for 180 s in an ultrasonic bath

III. Dry sample with nitrogen gas

A.2.2 Resist Spin-Coating

To pattern the structures used in this thesis, different resists were used depending on the setup used for the lithographic process. When doing EBL and optical lithography using a Cr mask the resist AR-N7520.17 was used along with the developer AR300-47. The details for spin coating are given below, resulting in a film thickness of ≈ 400 nm.

Step	Time	Speed	Acceleration
Prespin	1 s	500 rpm	500 rpm/s
Main	60 s	4000 rpm	4000 rpm/s

After the spin-coating process, the sample is soft-baked for 60 s on a hot plate at 85 °C and afterwards is left to cool down and stabilize for 60 s. As the substrates used in this work were insulating, for EBL the spin-coating of a conductive resist ARPC 5090 was required to avoid charging during the lithography. This resist can be removed with H_2O after the lithography process.

Step	Time	Speed	Acceleration
Main	60 s	3000 rpm	3000 rpm/s

After spin-coating, the sample was left to rest for 2 minutes and then was soft-baked for 2 minutes at 90 °C.

For the samples that were patterned via optical lithography with the Micro3-Writer, the positive resist ma-P 1215 was used along with the developer AR300-46. The details for spin-coating are given below.

Step	Time	Speed	Acceleration
Prespin	2 s	500 rpm	500 rpm/s
Main	45 s	3000 rpm	3000 rpm/s

Afterwards, the sample was left to rest for 1 minute and then was soft-baked at 100 °C for 1 minute.

A.2.3 Lithographic Process

The lithographic process using the different available setups is detailed below.

A.2.3.1 Optical Lithography with a Cr Mask

For the optical lithography process, the sample was brought into soft contact with the optical mask and was exposed to UV light for 10 s. As the samples used for this work were highly transparent, black foam was placed under the sample to prevent backscattering of the UV light and to improve the resolution of the structures.

A.2.3.2 Optical Lithography Using the Micro3Writer

When doing the optical lithography using the Micro3Writer, the exposure was done with a dose of 110 mJ/cm^2. To ensure good resolution, autofocussing was enabled and performed for every writefield.

A.2.3.3 Electron Beam Lithography

Acceleration voltage and aperture size were chosen depending on the feature size that was patterned. The dose required to expose the resist is depending on the acceleration voltage as well as potential additional exposure caused by proximity effects between separated structures.

For Hall structures, acceleration voltages of 20 kV, aperture size of 30 µm and dosages of 335 $\mu C/cm^2$ were used. For contact pads, this was changed to acceleration voltages of 10 kV, aperture size of 120 µm and dosages of 110 $\mu C/cm^2$.

A.2.4 Development

After the lithographic process, the samples were developed. If the lithography was performed using EBL the conductive resist was first removed by immersing the sample in deionized water for 30 s and then dried with nitrogen gas. For the development step itself, the samples were immersed in a beaker with the corresponding developer, depending on the resist used. If the negative resist AR-N7520.17 was used, the sample was developed in the developer AR300-47 for 150 s. For the positive resist ma-P 1215, the sample was developed in ARN300-46 for 30 s. To break the development step, in both cases the samples were immersed in high-purity water for 20 s and dried with nitrogen gas afterwards. The outcome of the development process was checked with an optical microscope and, if necessary, additional development was performed or the whole process was repeated.

A.2.5 Etching

The unprotected regions of the sample have been removed by ion beam etching using an Ionsys500 ion etcher with an argon plasma. The etching has been performed with a dose of $\approx 356\,\mu A/cm^2$. If a certain etching depth (down to a certain material) was desired, the etching was performed under an angle of 55° using an endpoint-detector. In case the etching depth did not matter but only the conducting material layers were supposed to be removed, the etching was performed under an angle of 90° for 60 s. This was done in two steps of 30 s each to avoid heating effects. Afterwards, the resist can be removed by the above described cleaning process.

B Results

B.1 Giant Orbital Magnetoresistance

B.1.1 Magnetoresistance Measurements on CoO/Cu(t)/Pt

The transverse MR measurements were performed on seven samples with Cu thicknesses varying between 0 nm and 6 nm in 1 nm steps and on an additional sample with 25 nm Cu interlayer to check for saturation of the signal as a function of Cu thickness. The acquired angular-dependent MR curves are shown in Fig. B.1. One can see that, as pointed out in Sec. 7.1.3, the sinusoidal component of the signal continuously transitions from a maximum at 45° to a minimum. The hysteresis curve reverses with the first nm of Cu and becomes more pronounced with increasing Cu layer thickness.

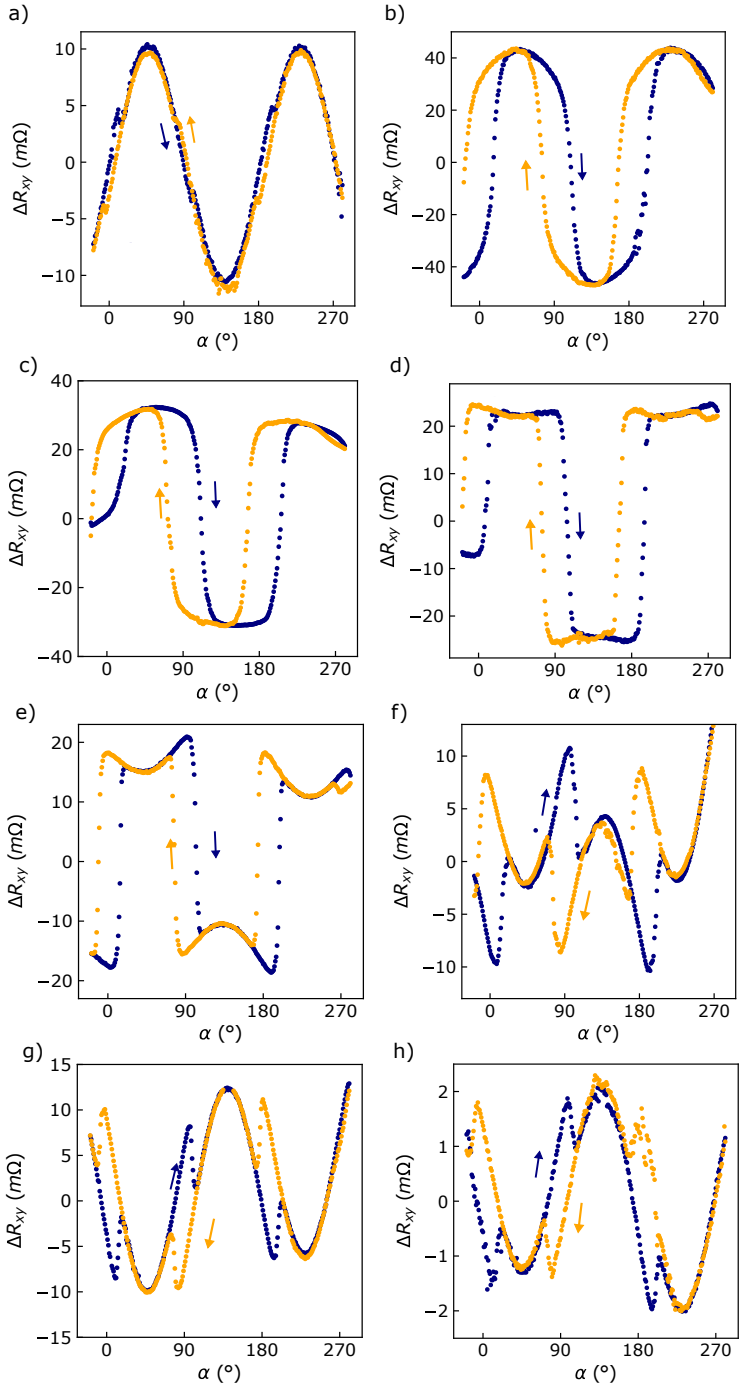

Figure B.1: Angular dependent transverse SMR for several samples with different Cu interlayer thickness t = (a) 0 nm, (b) 1 nm, (c) 2 nm, (d) 3 nm, (e) 4 nm, (f) 5 nm, (g) 6 nm, (h) 25 nm.

C Other information

C.1 Contributions

In this section details of the contributions of the author and co-workers to the projects presented in this work are given. If not noted otherwise, the co-workers are from JGU Mainz.
Names of co-workers are removed due to data privacy reasons.

C.1.1 Characterization of CoO Thin Films

I. Sample growth by the author, - and - supported by -, - and - under the supervision of -. Additional Ru deposition by -.

II. XRD and XRR measurements by - and - supported by - and -.

III. Laser irradiation at TU Kaiserslautern by - under the guidance of - and-. Details can be found in labbook experiment ID 6565.

IV. Device fabrication and design by the author and -.

V. Sample annealing by the author.

VI. Imaging during beamtimes was lead by the author, supported by -, -, -, -, - and the beamline scientist -.

VII. Data evaluation by the author.

C.1.2 Electrical Switching in Ultrathin CoO/Pt Bilayers

I. Sample growth by the author and - supported by - under the supervision of -.

II. Device fabrication and design by the author and -.

III. Electrical measurements by the author.

IV. XMLD-PEEM imaging during beamtime by -, -, - and -, supported by the the beamline scientists: - and -. With remote support from the author.

V. Birefringence imaging by the author.

VI. COMSOL simulations by the author supported by -.

VII. Data evaluation by the author supported by -.

VIII. Manuscript writing by the author and - with input from all co-authors.

C.1.3 Giant Orbital Magnetoresistance in CoO

I. Sample growth by the author and - supported by - and - under the supervision of -.

II. Device fabrication and design by the author and -.

III. Electrical measurements on CoO and hematite crystals by the author, assisted by - and -.

IV. Electrical measurements on YIG crystals by -.

V. XRD and XRR measurements by the author supported by -.

VI. STEM and EELS measurements by - and -, supervised by -.

VII. XMLD-PEEM imaging during beamtime by the author, -, - and -, supported by the the beamline scientist -.

VIII. Data evaluation by the author and - with inputs from -, -, - and -. Details can be found in 🕮 labbook experiment ID 14102 and 🕮 labbook experiment ID 6243, with all relevant samples linked within the experimental report.

IX. Theoretical calculations and simulations by -, -, -, -, - and -.

X. -, -, - and - prepared the $\alpha - Fe_2O_3/Cu$ sample.

XI. Manuscript writing by the author, -, -, - and - with input from all co-authors.

C.2 Use of Artificial Intelligence

Table C.1: Use of AI tools in the context of this thesis.

AI tool	**Used for**	**Reason**	**Where or when**
Connected Papers	Literature research	To find relevant papers	To find further connected papers throughout the thesis
Perplexity AI	Literature research	To find relevant papers	Finding relevant papers for the theory and methods section
DeepL Translate	First translation of the abstract into German	Have an identical abstract version in German and English	Abstract and Kurzzusammenfassung
KI-Chat@JGU	Improving language flow and syntax	Better readability	Throughout the thesis wherever results were discussed
ChatGPT	Improving language flow and syntax; improving LaTex formatting	Better readability	Throughout the thesis when there were no results discussed

C.3 List of Publications

1. L. Baldrati, C. Schmitt, O. Gomonay, R. Lebrun, R. Ramos, E. Saitoh, J. Sinova, and M. Kläui, "Efficient Spin Torques in Antiferromagnetic CoO/Pt Quantified by Comparing Field- and Current-Induced Switching," *Phys. Rev. Lett.*, vol. 125, p. 077201, 2020.

2. F. Schreiber, L. Baldrati, C. Schmitt, R. Ramos, E. Saitoh, R. Lebrun, and M. Kläui "Concurrent magneto-optical imaging and magneto-transport readout of electrical switching of insulating antiferromagnetic thin films," *Appl. Phys. Lett.*, vol 117, p. 082401, 2020.

3. H. Meer, F. Schreiber, C. Schmitt, R. Ramos, E. Saitoh, O. Gomonay, J. Sinova, L. Baldrati, and M. Kläui, "Direct Imaging of Current-Induced Antiferromagnetic Switching Revealing a Pure Thermomagnetoelastic Switching Mechanism in NiO," *Nano Lett.*, vol. 21, pp. 114-119, 2020.

4. C. Schmitt, L. Baldrati, L. Sanchez-Tejerina, F. Schreiber, A. Ross, M. Filianina, S. Ding, F. Fuhrmann, R. Ramos, F. Maccherozzi, D. Backes, M. -A. Mawass, F. Kronast, S. Valencia, E. Saitoh, G. Finocchio, and M. Kläui, "Identification of Néel Vector Orientation in Antiferromagnetic Domains Switched by Currents in NiO/Pt Thin Films," *Phys. Rev. Appl.*, vol. 15, p. 034047, 2021.

5. F. Schreiber, H. Meer, C. Schmitt, R. Ramos, E. Saitoh, L. Baldrati, and M. Kläui, "Magnetic Sensitivity Distribution of Hall Devices in Antiferromagnetic Switching Experiments," *Phys. Rev. Appl.*, vol. 16, p. 064023, 2021.

6. H. Meer, O. Gomonay, C. Schmitt, R. Ramos, L. Schnitzspan, F. Kronast, M. -A. Mawass, S. Valencia, E. Saitoh, J. Sinova, L. Baldrati, and M. Kläui, "Strain-induced shape anisotropy in antiferromagnetic structures," *Phys. Rev. B,* vol. 106, p. 094430, 2022.

7. S. Das, A. Ross, X. X. Ma, S. Becker, C. Schmitt, F. Van Duijn, E. F. Galíndez-Ruales, F. Fuhrmann, M. -A. Syskaki, U. Ebels, V. Baltz, A. -L. Barra, H. Y. Chen, G. Jakob, S. X. Cao, J. Sinova, O. Gomonay, R. Lebrun, and M. Kläui, "Anisotropic long-range spin transport in canted antiferromagnetic orthoferrite $\mathbf{YFeO_3}$," *Nat. Commun.*, vol. 13, p. 6140, 2022.

8. E. Rongione, O. Gueckstock, M. Mattern, O. Gomonay, H. Meer, C. Schmitt, R. Ramos, T. Kikkawa, M. Mičica, E. Saitoh, J. Sinova, H. Jaffrès, J. Mangeney, S. T. B. Goennenwein, S. Geprägs, T. Kampfrath, M. Kläui, M. Bargheer, T. S. Seifert, S. Dhillon, and R. Lebrun, "Emission of coherent THz magnons in an antiferromagnetic insulator triggered by ultrafast spin-phonon interactions," *Nat. Commun.*, vol. 14, p. 1818, 2023.

9. C. Schmitt, L. Sanchez-Tejerina, M. Filianina, F. Fuhrmann, H. Meer, R. Ramos, F. Maccherozzi, D. Backes, E. Saitoh, G. Finocchio, L. Baldrati, and M. Kläui, "Identifiying the domain wall spin structure in current-induced switching of antiferromagnetic NiO/Pt," *Phys. Rev. B*, vol. 107, p. 184417, 2023.

10. H. Meer, S. Wust, C. Schmitt, P. Herrgen, F. Fuhrmann, S. Hirtle, B. Bednarz, A. Rajan, R. Ramos, M. A. Niño, M. Foerster, F. Kronast, A. Kleibert, B. Rethfeld, E. Saitoh, B. Stadtmüller, M. Aeschlimann, and M. Kläui, "Laser-Induced Creation of Antiferromagnetic 180-Degree Domains in NiO/Pt Bilayers," *Adv. Funct. Mater.*, vol. 33, p. 2213536, 2023.

11. S. Koraltan, C. Schmitt, F. Bruckner, C. Abert, K. Prügl, M. Kirsch, R. Gupta, S. Zeilinger, J. M. Salazar-Mejía, M. Agrawal, J. Güttinger, A. Satz, G. Jakob, M. Kläui, D. Suess, "Single-device offset-free magnetic field sensing with tunable sensitivity and linear range based on spin-orbit torques," *Phys. Rev. Appl.*, vol. 4, p. 044079, 2023.

12. C. Schmitt, A. Rajan, G. Beneke, A. Kumar, T. Sparmann, H. Meer, B. Bednarz, R. Ramos, M. A. Niño, M. Foerster, E. Saitoh, and M. Kläui, "Mechanisms of electrical switching of ultra-thin CoO/Pt bilayers," *Nano Lett.*, vol. 24, pp. 1471-1476, 2024.

13. E. F. Galíndez-Ruales, R. González-Hernández, C. Schmitt, S. Das, F. Fuhrmann, A. Ross, E. Golias, A. Akashdeep, L. Lünenbürger, E. Baek, W. Yang, L. Šmejkal, V. Krishna, R. Jaeschke-Ubiergo, J. Sinova, A. Rothschild, C. -Y. You, G. Jakob, and M. Kläui, "Revealing the Altermagnetism in Hematite via XMCD Imaging and Anomalous Hall Electrical Transport," *Adv. Mater.*, vol. 37, pp. e05019, 2025.

14. A. Akashdeep, E. M. Ababneh, C. Schmitt, E. F. Galíndez-Ruales, F. Fuhrmann, T. Kuschel, M. Kläui, V. Amin and G. Jakob, "Angle-dependent magnetoresistance induced by interface-generated spin current in RuO_2/permalloy heterostructures," *Phys. Rev. Appl.*, vol.24, p. 054018, 2025.

15. S. Wust, C. Seibel, H. Meer, P. Herrgen, C. Schmitt, L. Baldrati, R. Ramos, T. Kikkawa, E. Saitoh, O. Gomonay, J. Sinova, Y. Mokrousov, H. C. Schneider, M. Kläui, B. Rethfeld, B. Stadtmüller, and M. Aeschlimann, "Indirect optical manipulation of the antiferromagnetic order of insulating NiO by ultrafast interfacial energy transfer," *arXiv*, 2205.02686, 2022.

16. M. Weber, S. Wust, L. Haag, A. Akashdeep, K. Leckron, C. Schmitt, R. Ramos, T. Kikkawa, E. Saitoh, M. Kläui, L. Šmejkal, J. Sinova, M. Aeschlimann, G. Jakob, B. Stadtmüller, and H. C. Schneider, "All optical excitation of spin polarization in d-wave altermagnets," *arXiv, 2408.05187*, 2024.

17. E. F. Galíndez-Ruales, W. Yang, T. Dannegger, M. Kundu, J. Köhler, C. Schmitt, F. Fuhrmann, A. Akashdeep, D. Tran, X. Ma, G. Jakob, S. Cao, U. Nowak and M. Kläui, "Altermagnetic magnon transport in the *d*-wave altermagnet $LuFeO_3$," *arXiv, 2508.14569*, 2025.

18. C. Schmitt, S. Krishnia, M. Zeer, E. F. Galíndez-Ruales, M. Loyal, J. Köhler, L. Micus, T. Kikkawa, H. Arisawa, T. Denneulin, A. Kovács, R. Xu, D. Tran, F. Kronast, D. Go, L. V. Pourovskii, R. E. Dunin-Borkowski, T. Kuschel, M. Ležaić, J. Sinova, E. Saitoh, G. Jakob, O. Gomonay, Y. Mokrousov and M. Kläui, "Giant orbital magnetoresistance in the antiferromagnet CoO driven by dynamic orbital angular momentum interaction," (under review), 2025.

19. C. Schmitt, E. F. Galíndez-Ruales, H. Meer, S. Krishnia, T. Kikkawa, E. Saitoh, T. Kuschel and M. Kläui, "Interfacial Orbital Rashba Edelstein Effect in CoO/Cu/Pt trilayers," (under preparation), 2025.

C.4 Acknowledgements

Removed due to data privacy

Removed due to data privacy

C.5 Curriculum Vitae

Removed due to data privacy